INVESTIGATION OF NEURAL CORRELATES BETWEEN PERCEPTION OF PAIN AND HEMODYNAMIC RESPONSE MEASURED IN THE PRE-FRONTAL CORTEX USING FUNCTIONAL NEAR INFRA-RED SPECTROSCOPY

by

VENKATAGIRI KRISHNAMURTHY

Presented to the Faculty of the Graduate School of

The University of Texas at Arlington in Partial Fulfillment

of the Requirements

for the Degree of

DOCTOR OF PHILOSOPHY

THE UNIVERSITY OF TEXAS AT ARLINGTON

August 2011

DEDICATION

This dissertation work is dedicated to my parents and all the teachers in my life.

ACKNOWLEDGEMENTS

With deepest gratitude, I would first like to thank my dissertation supervisor, Dr. Hanli Liu, for stepping up to mentor me in 2008, and support me to finish up my doctoral studies. Without her constant push, I do not think I could have finished as much as I did within the last two years. I am grateful to Dr. Liu for supporting me with assistantships and fellowships throughout these years. I am also deeply indebted to Dr. Khosrow Behbehani as our department Chair, for co-advising me. His patient demeanor and words of wisdom have made me a more professional individual.

Along with Dr.Liu and Dr. Behbehani, I would also like to thank my committee members, Dr. Georgios Alexandrakis, Dr. Yuan Bo Peng, Dr. Frank Andrew Kozel and Dr. Pablo A. Mora for their time and patience in helping me steer my dissertation work with a focused and strong scientific foundation. I am also deeply indebted to Dr. Nancy Rowe for patiently guiding me through the statistical analysis and running the SAS models for this dissertation work.

I started my Ph.D. studies under the guidance of Dr. Richard W. Briggs. He taught me the baby steps of research: literature survey, critiquing scientific work, approaching a problem with a scientific logic, and design of experiments. He is exemplary in the department of professionalism, work ethics and principles, and I have great respect for him as a person and a scientist.

The Gulf War Neuroimaging lab at UTSW was a terrific congregation of world class, highly trained and bright researchers from all different fields; we had physicists, chemists, engineers, neurologists, epidemiologists, psychiatrists, psychologists, radiologists, and statisticians. It was an excellent platform for a budding researcher such as me to absorb knowledge. My personal thanks and best wishes goes out to all of them with whom I worked day in and day out, sharing their knowledge and experience. Specifically, my deepest appreciation goes out to Dr. Kaundinya Gopinath and Dr. Thomas C. Ferree for their excellent work ethics and

rigorous scientific approach. At the Biomedical Optics lab, I am indebted to all of the students who volunteered as subjects for my experiments. My deepest gratitude and best wishes go out to Venki and Sabin for being a great help in conducting my experiments. I am also deeply thankful to Dr. Fenghua Tian who gave me a jump start in carrying out optical measurements and data analysis.

I would also like to thank all the staff of our department on both UTA and UTSW campuses, the Graduate school, and the Registrar's office for promptly taking care of all my paper work. I am also indebted and thankful to Ken and Charlene at the Bursar's for being very kind and supportive at times when I needed it the most!

Throughout these years, my parents have been a constant support, giving inspirational pieces of advice, words of wisdom, and motivation. I appreciate the highest level of importance they always held for knowledge and hence encouraging me to pursue this path of seeking knowledge. I am indebted for their selfless attitude and patience to see me go through school for all these years. I am also deeply indebted to the kind support that I got from my sister Rashmi, brother-in-law Madhukara and Uncle Gopal when I needed it the most. Thanks for being with me always.

In this journey of my doctoral studies, the most memorable moment of my life came when I met the love of my life, Lisa Krishnamurthy. She has been a bundle of energy for me, constantly encouraging and supporting me towards excellence. She has been there for me in all possible ways with love, patience, and always with a smile. She is my brilliant physicist. I have no doubt in my mind that we have a bright future and I love you!

December 1, 2010

ABSTRACT

INVESTIGATION OF NEURAL CORRELATES BETWEEN PERCEPTION OF PAIN AND HEMODYNAMIC RESPONSE MEASURED IN PRE-FRONTAL CORTEX USING FUNCTIONAL NEAR INFRA-RED SPECTROSCOPY

Venkatagiri Krishnamurthy, Ph.D.

The University of Texas at Arlington, 2011

Supervising Professor: Hanli Liu

Perception of pain is multi-dimensional, comprising three major psychological dimensions: sensory-discriminative, motivational-affective and cognitive-evaluative. This dissertation study investigates the cognitive evaluation of pain, by acquiring functional Near Infra-Red Spectroscopic (fNIRS) measurements from the prefrontal cortex (PFC) areas, during mechanical and thermal pain stimulation induced on the subject's volar forearm. Clustered-wise analysis on the oxy-hemoglobin (HbO) response from specific PFC areas was followed by categorizing the resulting HbO response into early (0.1-12sec) and late (12.1-25sec) phases. For each respective phase, regression analysis was carried between the HbO-derived parameters and behaviorally measured pain rating.

The major findings of this study include: (1) across both 41℃ and 48℃ thermal stimulation, significant ΔHbO deactivation was observed during the late phase, in the left hemispheric (LH) anterior PFC (aPFC) or Brodmann area 10 (BA 10). (2) Significant correlates of pain rating were observed in the LH prefrontal areas: (a) under mechanical stimulation, early phase HbO-derived peak intensity (PI) from LH aPFC correlated with the pain rating. (b) Under

both 41℃ and 48℃ thermal stimulation, late phase HbO-derived PI from the LH dorsolateral PFC (DLPFC or BA 46) showed correlation with the pain rating. (3) The significant correlates observed from the right hemispheric (RH) PFC were: (a) under mechanical stimulation, early phase HbO-derived FWHM from the RH aPFC correlated with the pain rating. (b) Under 41℃ thermal stimulation, late phase HbO-derived PI from the RH DLPFC area correlated with the pain rating. (4) The late phase HbO-derived time to peak from LH aPFC reflected cognitive discrimination of two different pain levels (41℃ and 48℃).

The observed trend for ΔHbO activation and deactivation could possibly be due to synaptic-induced vasodilation and vasoconstriction leading to increased or decreased blood oxygenation to the localized PFC areas. Due to a limited subject pool, the findings listed above demand further corroboration.

TABLE OF CONTENTS

LIST OF FIGURES

LIST OF TABLES

CHAPTER 1

INTRODUCTION

Pain is a universal sensation, experienced by everyone in slightly different forms. In the wide spectrum of its causes, this unpleasant feeling could be evoked from external causes such as a prick or touching a hot pan. Internally, we feel pain in the form of headaches, chest pain, and muscle cramps. Pain is an alert signal that demands our attention. It allows us to realize that something within the body is not normal and needs further care. This alert system is manipulated as a function of external and internal triggers, coupled with the state of mind. According to Wall and Melzack, pain is a multi-dimensional experience that is functionally categorized into sensory, adaptive, and affective components (McMahon & Koltzenberg, 2005).

The pain experience and subjective assessment of pain varies greatly among people. Past experiences and current motivational states shape the painful episode. Counter intuitively, pain perception does not directly reflect incoming signals from primary sensory neurons (McMahon & Koltzenberg, 2005). In psychological studies, behavioral measures are gathered by asking the patient or subject to rate their feelings based on a specific scale. This approach is useful in the clinical setting to assess a patient's perceived amount of pain. However, behavioral measures do not point to the specific brain areas involved in cognitive or affective phenomenon during distress or injury. Hence, several researchers have taken the progressive step of combining behavioral measures with the spatio-temporal aspects of brain activity available through neuroimaging.

An exciting and relatively new neuroimaging tool is the Diffuse Optical Tomography (DOT) which is an extension of the Near InfraRed Spectroscopy (NIRS) technique. In 1977, Jobsis, et al. showed the feasibility of applying near-infrared optical techniques towards bio-medical applications (Jobsis, 1977). Three decades since then, researchers have developed the technology for brain related studies. Some inherent advantages of NIRS over other currently available neuroimaging tools such as PET and fMRI are its cheap, mobile, and accessible method of acquiring brain hemodynamics.

An increased availability of brain imaging techniques has developed into a search for the 'state' that relates neural basis to conscious experience. Simply measuring a biophysical phenomenon is not satisfactory; it is necessary to mesh the biophysical component to the behaviorally measured conscious state of an experience using a quantitative approach. A 'neural correlate' is defined as a 'state' based on a specific biophysical sub-system of the brain whose presence regularly correlates with the specific content of experience (Chalmers, 1996). By providing an input that creates a state, such as the experience of pain, the subsequent physiological reaction, such as the hemodynamic response, should consistently correlate with the behavioral measure in order to have an adequate neural correlate. Simply put, the neural correlate provides an interface between the conscious state and the measurable.

In many subject populations, it is difficult to objectively quantify the pain level. These subject populations include patients under anesthesia, neonates, amputees, and burn patients. The challenge also largely depends upon the subject's conscious or unconscious state of mind and the level of developed cognitive functions. Some patient populations are addicted to pain medication, which causes difficulty in objectively diagnosing the level of pain, if any. Hence it is pertinent to identify objective measures that characterize pain for diagnostic and therapeutic interventions.

Given that pain is a subjective experience, it is challenging to quantify a state based on a specific biophysical sub-system of the brain whose presence regularly correlates with the pain experience. Although recent studies are showing that the prefrontal cortex plays an important role in the cognitive and emotional aspects of pain, the scientific community still lacks a good

understanding of the underlying neurophysiology and different cognitive roles shared by the prefrontal areas under a task or stimulation. The motivation was to deduce logical inferences for physiological cause for cognitive aspects of pain in the prefrontal areas based on the fNIRS hemodynamic measurements carried out in this study.

Measuring pain objectively is a necessity for the medical and patient community. Functional NIRS is a promising technology as it provides several advantages such as non-invasiveness, inherently non-ionizing radiation, patient-friendliness (unlike MRI where the patients frequently complain about claustrophobia, limited bore size of the scanner, and the need to lie rigid in the scanner to minimize motion artifacts), portability and low cost electronics compared to MRI. Hence, the goal of this dissertation work is to develop novel methods to quantify neural correlates between pain perception and fNIRS measurements acquired from the prefrontal areas.

CHAPTER 2

PRINCIPLES OF NEAR INFRARED SPECTROSCOPY AND DIFFUSE OPTICAL TOMOGRAPHY

2.1 Light: Some Basic Concepts

Light is the bearer of information in Near Infrared Spectroscopy (NIRS) and Diffuse Optical Tomography (DOT). By understanding the nature of light, the information gathered during a DOT experiment can be unraveled and interpreted. Electromagnetic (EM) radiation comes in all types and flavors. From the highly energetic Gamma rays to the monstrous Radio waves, EM waves are classified in a continuous spectrum.

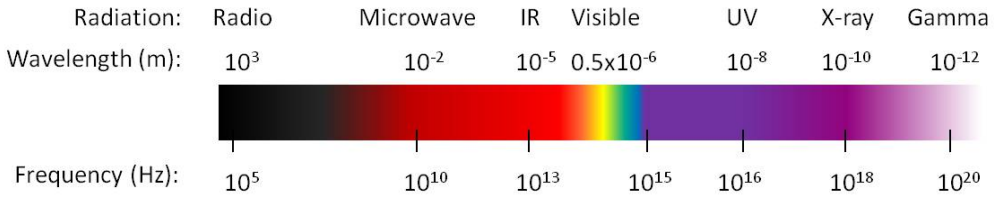

Figure 2-1: The spectrum of light for which common sources and detectors exist.

Though this entire spectrum is composed of photons, what humans perceive as ‘light’ is a small band of wavelengths from 430 nm to 690 nm (Halliday & Resnick, 1962). This comprises the visible spectrum. Beyond these wavelengths, the average human eye is not sensitive to the photon. For reasons explained later in this chapter, the visible spectrum is not of interest to the Diffuse Optics that are utilized in the experiments reported in Chapters 5, 6, and 7. Instead, we must step a slight notch to the left of the visible in Figure 2-1 into the Near Infrared (NIR).

As seen in Figure 2-1, wavelength and frequency both describe types of EM radiation. This stems from the fact that the speed of light in free space is a constant, and by convention is denoted by the letter c and has a value of 3 ×10^8 m/s. The frequency, ν in Hertz (s^{-1}), and wavelength, λ in meters, are related by the speed of light:

$$c = \nu\lambda \qquad 2.1$$

This generally describes any wave composed of one frequency, except that its velocity of propagation may be different from c. Specifically, EM waves are composed of orthogonal electric and magnetic waves. In turn, the direction of propagation is orthogonal to both the electric and magnetic field oscillations, as can be seen in Figure 2-2.

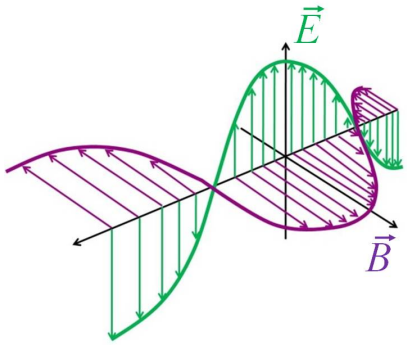

Figure 2-2: Electromagnetic radiation. The Electric and Magnetic fields oscillate orthogonal to each other.

Moreover, light exhibits what is called the particle-wave duality (Krane, 1998); light exists simultaneously as a particle and a wave. Thus, light is also referred to as quantized bundles of energy, called photons. The energy of the photon is a product of Plank's constant and the light's frequency.

$$E = h\nu \qquad 2.2$$

Throughout this chapter, I will use both models of light interchangeably, depending on which is more applicable and easily understood.

2.2 Reflection, Refraction, and Absorption

In geometric optics, it is assumed that light travels in a straight line as it passes through a homogeneous substance, until it meets another medium or if the substance is not regular in space or time (Serway & Jewett, 2004).

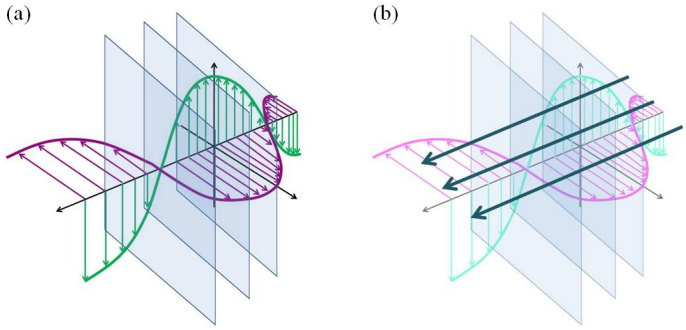

Figure 2-3: (a) EM radiation is approximately a plane wave and (b) can furher be described via the ray approximation.

As depicted in Figure 2-3(a), EM radiation is approximately a plane wave, where the plane describes the amplitude of the wave and lies perpendicular to the direction of propagation. If we draw an arrow from one point in a plane to an adjacent point in the next plane, that arrow points in the direction of propagation. This is the ray approximation of light, where any EM radiation can be approximated by a ray pointing in the direction of travel (Serway & Jewett, 2004).

If a light source strikes an object and changes its direction, so that it remains in the original medium, the light is said to be reflected. Without proof, the law of reflection states that the angle of incidence, as measured from the normal of the interface, equals the angle of reflection as measured from the normal. This phenomenon is depicted in Figure 2-4 (b), where $\theta = \theta'$ (Hecht & Zajac, 1997).

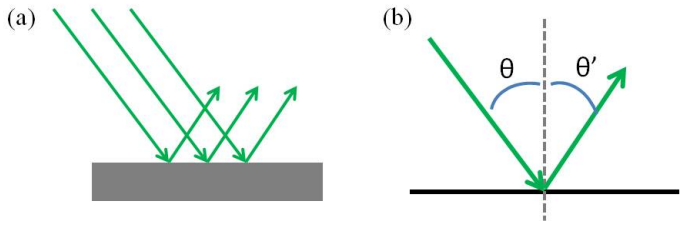

Figure 2-4: (a) specular reflection of a collimated beam of light where (b) the angle of incidence and the angle of reflection are equal.

As depicted in Figure 2-4 (a), specular reflection occurs when the reflected light beam travels in only one direction (Serway & Jewett, 2004). This is possible when the surface of the interface has deformities that are less than the wavelength of the light projected onto it (Wolff, 1994). But in a *Diffuse* Optics experiment, the medium has deformities larger than the wavelength of the light (Wolff, 1994). This causes most of the light to enter the subsurface of the medium, where the light scatters more, until it exits the medium.

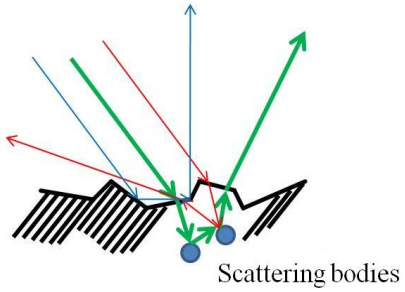

Figure 2-5: Diffuse reflectance causes the light to be reflected at many angles.

As can be seen in Figure 2-5, the light must enter the medium to reflect diffusely. Thus, to better understand diffuse reflectance, we must also touch upon refraction. Let us think about a plane wave with wave number $k_1 = 2\pi/\lambda_1$ incident on an interface of two optically different media. This results in a reflected wave and a transmitted (or refracted) wave, as seen in Figure 2-6.

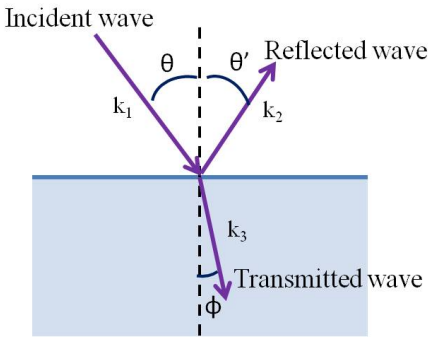

Figure 2-6: The resulting reflected and transmitted waves from a single incident wave on an interface of two optically different media.

Incident wave: $e^{i(\boldsymbol{k_1}\cdot\boldsymbol{r}-\omega t)}$ 2.3

Reflected wave: $e^{i(\boldsymbol{k_2}\cdot\boldsymbol{r}-\omega t)}$ 2.4

Transmitted wave: $e^{i(\boldsymbol{k_3}\cdot\boldsymbol{r}-\omega t)}$ 2.5

As the electromagnetic wave propagates, it carries information both through space and time (Fowles, 1989). This dependence is explicit in the set of equations above describing the incident, reflected, and transmitted waves. For this to hold true at the boundary, the following relation must be satisfied:

$$e^{i(\boldsymbol{k_1}\cdot\boldsymbol{r}-\omega t)} = e^{i(\boldsymbol{k_2}\cdot\boldsymbol{r}-\omega t)} = e^{i(\boldsymbol{k_3}\cdot\boldsymbol{r}-\omega t)} \quad 2.6$$

At the boundary, the ωt term is equal for all three wave components, such that this reduces to the requirement that:

$$\boldsymbol{k_1}\cdot\boldsymbol{r} = \boldsymbol{k_2}\cdot\boldsymbol{r} = \boldsymbol{k_3}\cdot\boldsymbol{r} \quad 2.7$$

Now, two vectors that are joined by one point are explicably coplanar. Thus, we could arbitrarily define the incident and reflected rays as lying in the same plane. In fact, all three waves are coplanar, as shown in Figure 2-6.

Moreover, since the incident and reflected waves are in the same medium (where the wave numbers equal each other), we have:

$$k_1 r \sin\theta = k_2 r \sin\theta' \quad 2.8$$

$$\theta = \theta' \quad 2.9$$

So the Law of Reflection is reaffirmed. As for the refracted wave, the change in medium governs a change in the wave number. A different way of seeing this is by taking a ratio of the velocity of light with respect to vacuum and the medium the light is traveling in. By invoking Equation 2.1, and by replacing the velocity c with a medium-dependent velocity u, while recalling that $k_1 = 2\pi/\lambda_1$ and $\omega = 2\pi\nu$, we have:

$$\frac{\lambda_1}{2\pi} = \frac{u_1}{2\pi\nu} \quad 2.10$$

$$\frac{1}{k_1} = \frac{u_1}{\omega} \quad 2.11$$

$$k_1 \sin\theta = k_3 \sin\phi \quad 2.12$$

$$\frac{k_1}{k_3} = \frac{\omega/u_1}{\omega/u_3} = \frac{c/u_1}{c/u_3} = \frac{n_1}{n_3} = \frac{\sin\phi}{\sin\theta} \quad 2.13$$

$$n_1 \sin\theta = n_3 \sin\phi \quad 2.14$$

Equation 2.15 depicts the Snell's Law. Conceptually, it implies that the angle of the transmitted light's trajectory is determined by the medium (index of refraction), and by the angle of the incident light. If the light is entering a more dense substance (e.g. air → water) the light will bend towards the normal. However, if the situation is reversed (e.g. water → air), then the light will bend away from the normal.

The phenomenon of refraction is important to diffuse reflectance concepts; light must enter the medium if diffuse reflectance is to take place. When light enters a medium it will be refracted, and continue on its new trajectory, until it encounters a scattering body or an absorber. For the sake of simplicity, a scattering body is a spherical object with a diameter of approximately one wavelength that scatters electromagnetic waves elastically. In a dispersive, turbid medium, the photon will scatter many times in a random walk fashion, without much loss of energy. Sometimes, a photon will encounter an absorbing chromophore and be "annihilated," which means that the photon has transferred its energy to the absorbing molecule in the form of thermal energy. Thus, as light travels through a dispersive medium, it dually experiences scattering and attenuation. As will be discussed in the next section, this causes the signals that have passed through tissue to be very small.

2.3 Light Interaction with Tissue

When light interacts with tissue, ray geometry is no longer an appropriate description for the behavior of light. Inherently, the scattering of light through thick, dense tissue calls for a modification of the theory to account for multiple scatterings (Frostig, 2009). By injecting light into a medium and measuring the exiting photons at some other point, we can deduce the scattering and absorption properties of the medium. That is to say, the substance between source and detector is treated as a black-box, whose properties must be inferred by providing a known input and quantifying the measured output. In contrast, it is possible to calculate the optical output from

the black box with *apriori* knowledge of the scattering and absorption properties. Both models are used in optical imaging, and are known as the inverse and forward problem, respectively.

2.3.1 Forward and Inverse Problem

In the forward problem, it is assumed that the absorption coefficient μ_a and the reduced scattering coefficient μ_s' of a substance are known. If a known light source of amplitude I_0 with wavelength λ is injected into the substance, we can calculate the expected output amplitude I of the light (S. R. Arridge & Schweiger, 1997). The forward problem is often used as a means to predict measured output, where a computational or experimental phantom has been constructed with the desired μ_a and μ_s'. Conversely, if the properties of the diffusive medium are not known, then the inverse problem is utilized. In the inverse problem there is a known light source I_0 and a measured output I, and the reduced scattering and absorption coefficients are deduced from this information. The inverse problem is used to quantify the unknown optical properties in a given organ, such as the brain.

2.3.2 Photon Migration in the tissue

Photons entering tissue will start performing a random walk, as they refract and encounter many scattering bodies. When we collect a photon at the detector, we must have some idea of where the photon started and has been in order to make inferences. Recall that this is termed the inverse problem. The known input for the experiments delineated in this dissertation is a continuous wave diode laser source, incident onto the tissue.

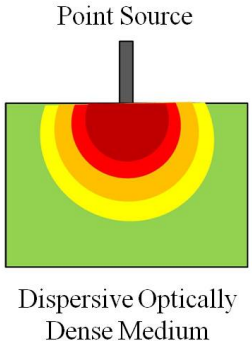

Figure 2-7: A point source will create a radial outflow of photons into the dispersive medium. Most photons are scattered away or absorbed.

The overall propagation of photons in the tissue can be described by the photon diffusion approximation (Equation 2.17), provided that the rate of scattering is much greater than absorption. Since the photons are not guided and are blind to the position of the detector, most photons are never collected. As can be seen in Figure 2-7, as the photons scatter and undergo diffuse processes, their outflow is assumed to be radial. The diffusion equation below describes the propagation of diffuse photons (D. Boas, 1997).

$$-D\nabla^2\Phi(r,t) + u\mu_a\Phi(r,t) + \frac{\partial\Phi(r,t)}{\partial t} = uS(r,t) \qquad 2.15$$

The photon fluence at position r and time t, $\Phi(r,t)$, is proportional to the number of photons within a volume. The distribution of source photons within a voxel at position r and time t is represented by $S(r,t)$ and is multiplied by the photon's velocity through the medium, u. The diffusion coefficient D, given by Equation 2.16, describes the rate of diffusion of the photons expressed in cm^2/s.

$$D = \frac{u}{3(\mu_s^{'} + \mu_a)} \cong \frac{u}{3\mu_s^{'}}, \qquad for\ \mu_s^{'} \gg \mu_a \qquad 2.16$$

$$\mu_s^{'} = (1-g)\mu_s \qquad 2.17$$

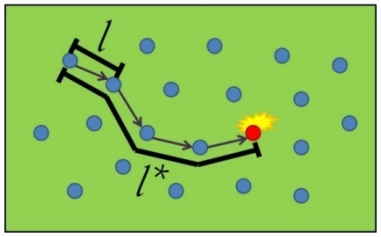

Figure 2-8: Photons in tissue experience scattering and absorption. The blue shapes represent scattering bodies, and the red shape represents an absorber. The scattering length l is inversely proportional to the scattering coefficient. The absorption length is inversely proportional to the absorption coefficient.

Since the absorption coefficient μ_a follows the relationship $\mu_a(\lambda) \propto \epsilon(\lambda)C$, it physically is represented by the inverse of the absorption length l^*. The scattering coefficient μ_s is the inverse of the scattering length l. Figure 2-8 shows the concept of scattering and absorption length. The

reduced scattering coefficient μ_s' is defined in Equation 2.17, where the value $g = \langle \cos\theta \rangle$ is the anisotropy factor (commonly determined to be greater than 0.9 for most of the tissues), and describes how isotropic the scattering will occur. A value of $g = 1$ is defined as complete forward scattering, where the average cosine of the scattering angle θ is one. A value of $g = 0$ is defined as complete isotropic scattering, where the cosine of the scattering angle θ has averaged to zero. Thus, an anisotropic value of 0.9 implies a great amount of forward scattering in tissue, and points to the fact that a multitude of scattering events must occur before a true random walk is established for the photons (D. A. Boas, Dale, & Franceschini, 2004). The scattering of a photon within tissue is often modeled with the Henyey-Greenstein function:

$$p(\cos\theta) = \frac{1}{4\pi} \frac{1 - g^2}{(1 + g^2 - 2g\cos\theta)^{\frac{2}{3}}} \qquad 2.18$$

The absorption coefficient, μ_a, describes the loss of intensity due to absorption and is proportional to the chromophore extinction coefficient and the chromophore concentration. Moreover, μ_a is dependent on the source wavelength, which arises from the wavelength dependency of the extinction coefficient (***ε***). Figure 2-9(b) shows the extinction coefficients, as measured by Cope (Cope, 1991), of oxy- and deoxy-hemoglobin. Near-Infrared Spectroscopy is sensitive to the changes of oxy-hemoglobin (*HbO*) and deoxy-hemoglobin (*Hb*). The photon wavelength (*λ*) dependent absorption coefficient is proportional to a linear combination of the absorbing chromophores (Huppert, Franceschini, & Boas, 2009). The relationship between the absorption coefficient to the spectroscopic measured change in detected intensity will be described in section 2.3.4

$$\mu_a(\lambda) = \epsilon_{HbO}(\lambda)[HbO] + \epsilon_{Hb}(\lambda)[Hb] \qquad 2.19$$

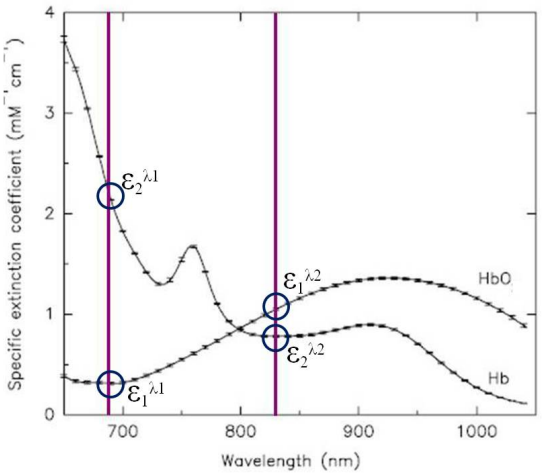

Figure 2-9 The extinction coefficients of HbO and Hb as a function of wavelength as measured in newborn infants by [Cope dissertation]. Note: the vertical lines depict the wavelengths used in the CW5 hardware (690 nm and 830 nm).

2.3.3 Why Consider a Semi-Infinite Medium?

A medium which is bound on one side and infinite in all other directions is considered semi-infinite. Treating the air-tissue interface as infinite would result in major discrepancies between theory and experimental data (David A Boas, 1996). This is especially true of light entering or exiting a diffusive medium (such as tissue) to or from a non-diffusive medium (such as air). In order to reconcile theory and experiment, an approximation is made for photons traveling through a dispersive medium, called the photon diffusion equation, given in Equation 2.17. The solution to the photon diffusion equation is geometry dependent and solutions often do not exist. However, it has been solved for a semi-infinite medium, given here (Frostig, 2009):

$$\Delta OD = \frac{1}{2}\sqrt{\frac{3\,\mu_s'}{\mu_a}}\left(1 - \frac{1}{1 + L\sqrt{3\mu_s'\mu_a}}\right)\Delta\mu_a L \qquad 2.20$$

The existence of a solution as indicated in Equation 2.20 implies that the hemoglobin concentration changes can be quantified from the NIRS measurements (Frostig, 2009).

2.3.4 Modified Beer-Lambert Law

The traditional method of modeling the detected light intensity I after it has passed through a dispersive medium with source intensity I_0 is the Beer-Lambert law. An off-shoot of this

theory, the Modified Beer-Lambert law, describes the electromagnetic attenuation as it travels through a highly scattering medium, such as tissue (Frostig, 2009).

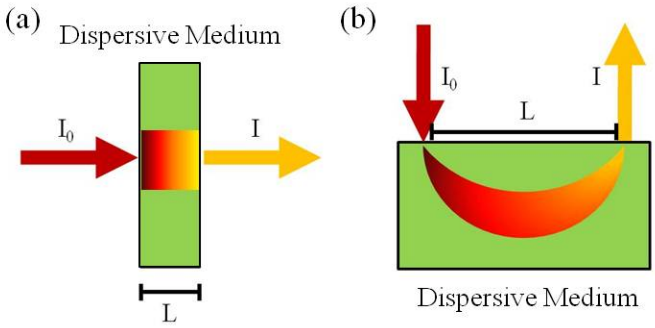

Figure 2-10: Conceptual diagrams depicting (a) Beer-Lambert Law and (b) Modified Beer-Lambert Law. Note: I_0 = input intensity, I = output intensity, L = path length which must be corrected for in (b).

The Beer-Lambert Law (BLL) is a staple of optics. As seen in Figure 2-10(a), if a known intensity of light (I_0) is incident onto a dispersive medium, the light will traverse the medium and exit with some intensity (I). The output intensity can be modeled by the relationship shown in equation 2.21 where ε is the extinction coefficient, L is the effective average path length and C is the chromophore concentration. From Equation 2.19, we observed that the absorption coefficient (μ_a) is a function of extinction coefficient (ε) and the chromophore concentration (*Hb* or *HbO*). Substituting equation 2.19 in Equation 2.22, we observe that the measured OD is related to the absorption coefficient (μ_a), extinction coefficient (ε) and the chromophore concentration (*Hb* or *HbO*) through the natural logarithm function. Equation 2.23 shows the generalized linear relationship between spectroscopic measured change in detected intensity (ΔOD) and the change in absorption coefficient ($\Delta\mu_a$) and the effective path length factor (L). Note that all the parameters are wavelength dependent.

$$I = I_0 e^{-\epsilon CL} = I_0 e^{-\mu_a L} \tag{2.21}$$

$$OD = -\ln\left(\frac{I}{I_0}\right) = \epsilon CL = \mu_a L \tag{2.22}$$

$$\Delta OD(t,\lambda) = -\ln\left(\frac{I(t,\lambda)}{I_0(\lambda)}\right) = \Delta\mu_a(t,\lambda)L(\lambda) \tag{2.23}$$

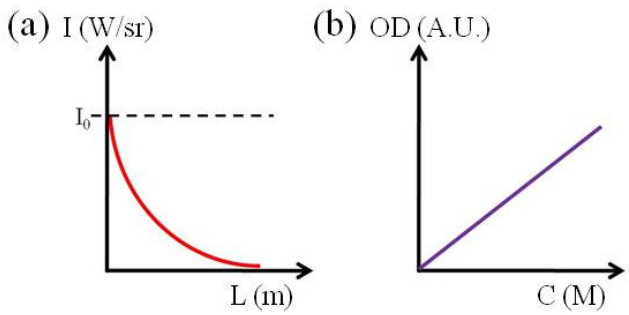

Figure 2-11: (a) The intensity of light as a function of path length and (b) the linear relationship between optical density and chromophore concentration.

As light travels through a medium, it is assumed that the surviving intensity decays mono-exponentially. The amount of decay depends on the path length traversed by the light (L), whereas the rate of decay depends on the amount of absorbing chromophore that exists in the medium (C), and the extinction coefficient of those chromophores (ϵ). The optical density, or absorption, of a medium is a linear function of the concentration of chromophores, given by the BLL in Equation 2.23. Thus, if the path length and absorbing species is known, one can deduce the concentration of the absorber by calculating the optical density from the input and output light intensities. Recall that this is the inverse problem approach to Near Infrared Spectroscopy.

If the light enters a semi-infinite bound scattering medium, it can only be measured on the same boundary as the incident light. Notice from Figure 2-10 that the BLL and the MBLL both use the measure L for the length between incident (source) and output (detected) light. For the BLL, it is assumed that the light traveled the approximate distance of L. However, in the MBLL scenario, the light path dips into the medium, later returning to the surface after undergoing multiple scattering. This causes the photons to travel a much greater path length than L. Hence, the optical path length that the light traverses must be corrected for the light scattering effects.

$$OD = -\ln\left(\frac{I}{I_0}\right) = \epsilon CLB + G \qquad 2.24$$

The path length correction factor (B) corrects for the increased distance traversed by the photons due to the multiple scatterings within the medium, and G corrects for probe geometry and loss of intensity at the boundary. Since DC-based NIRS cannot measure absolute values of

absorbing chromophores, the focus is on quantifying a change in OD. It is assumed that during the fNIRS based experiment, the parameters B and G will not change (Frostig, 2009) as long as the source-detector geometry remains fixed. Thus a change in optical density results solely from a change in chromophore concentration as shown by the equation below.

$$\Delta OD = \epsilon \Delta C L B = \Delta \mu_a L B \qquad 2.25$$

Moreover, if more than one absorbing chromophore exists within the dispersive medium, the change in optical density will depend on a linear combination of respective extinction coefficients and the related chromophore concentration as shown in Equation 2.26.

$$\Delta OD = [\epsilon_1 \Delta C_1 + \epsilon_2 \Delta C_2] B L \qquad 2.26$$

It is necessary to have two equations to solve for two unknowns. In order to predict the two concentration levels (that is *Hb* and *HbO*), two sources of light with different wavelengths are used. Recall from the previous section that the behavior of light is dependent on its wavelength. This is true for both scattering and absorption, such that a wavelength dependence is placed upon $\Delta OD, \epsilon,$ and B. The following is a derivation of the concentration changes that can be inferred from MBLL by using two sources of light with different wavelengths:

$$\begin{aligned} \Delta OD^{\lambda_1} &= \left[{\epsilon_1}^{\lambda_1} \Delta C_1 + {\epsilon_2}^{\lambda_1} \Delta C_2\right] B^{\lambda_1} L \\ \Delta OD^{\lambda_2} &= \left[{\epsilon_1}^{\lambda_2} \Delta C_1 + {\epsilon_2}^{\lambda_2} \Delta C_2\right] B^{\lambda_2} L \end{aligned} \qquad 2.27$$

$$\Delta C_1 = \frac{1}{{\epsilon_1}^{\lambda_2}} \left(\frac{\Delta OD^{\lambda_2}}{B^{\lambda_2} L} - {\epsilon_2}^{\lambda_2} \Delta C_2 \right) \qquad 2.28$$

$$\frac{\Delta OD^{\lambda_1}}{B^{\lambda_1} L} = {\epsilon_1}^{\lambda_1} \left[\frac{1}{{\epsilon_1}^{\lambda_2}} \left(\frac{\Delta OD^{\lambda_2}}{B^{\lambda_2} L} - {\epsilon_2}^{\lambda_2} \Delta C_2 \right) \right] + {\epsilon_2}^{\lambda_1} \Delta C_2 \qquad 2.29$$

$$\frac{\Delta OD^{\lambda_1}}{B^{\lambda_1} L} - \frac{{\epsilon_1}^{\lambda_1}}{{\epsilon_1}^{\lambda_2}} \frac{\Delta OD^{\lambda_2}}{B^{\lambda_2} L} = \Delta C_2 \left[{\epsilon_2}^{\lambda_1} - \frac{{\epsilon_1}^{\lambda_1}}{{\epsilon_1}^{\lambda_2}} {\epsilon_2}^{\lambda_2} \right] \qquad 2.30$$

$$\Delta C_2 = \left[\frac{1}{{\epsilon_1}^{\lambda_2}{\epsilon_2}^{\lambda_1} - {\epsilon_1}^{\lambda_1}{\epsilon_2}^{\lambda_2}}\right] \cdot \left[{\epsilon_1}^{\lambda_2}\frac{\Delta OD^{\lambda_1}}{B^{\lambda_1}L} - {\epsilon_1}^{\lambda_1}\frac{\Delta OD^{\lambda_2}}{B^{\lambda_2}L}\right]$$

$$\Delta C_1 = \left[\frac{1}{{\epsilon_1}^{\lambda_2}{\epsilon_2}^{\lambda_1} - {\epsilon_1}^{\lambda_1}{\epsilon_2}^{\lambda_2}}\right] \cdot \left[{\epsilon_2}^{\lambda_1}\frac{\Delta OD^{\lambda_2}}{B^{\lambda_2}L} - {\epsilon_2}^{\lambda_2}\frac{\Delta OD^{\lambda_1}}{B^{\lambda_1}L}\right] \quad 2.31$$

Conditions may now be placed on the experimental set-up based on Equation 2.32. The measured concentration changes (that is ΔC_1 and ΔC_2) is heavily dependent on the inverse of ${\epsilon_1}^{\lambda_2}{\epsilon_2}^{\lambda_1} - {\epsilon_1}^{\lambda_1}{\epsilon_2}^{\lambda_2}$. Thus, to obtain stable solutions, the two wavelengths of the sources must be chosen wisely such that the net result of ${\epsilon_1}^{\lambda_2}{\epsilon_2}^{\lambda_1} - {\epsilon_1}^{\lambda_1}{\epsilon_2}^{\lambda_2}$ does not yield to zero. Figure 2-9(a) shows a cartoon of the relationship between extinction coefficient and the wavelength of the light being absorbed by the chromophore. If the wavelengths are chosen too close together, then the resulting ${\epsilon_1}^{\lambda_2}{\epsilon_2}^{\lambda_1} - {\epsilon_1}^{\lambda_1}{\epsilon_2}^{\lambda_2}$ will be very small causing unstable solutions. The wavelengths also cannot be chosen too far apart either due to the constraints of the optical window. The optimal selection of wavelengths would be to choose one on each side of the isobestic point (that is 800nm) as shown in Figure 2-9.

2.3.5 The Optical Window

The absorption coefficients of HbO and Hb are too large for wavelengths shorter than 650 nm (Cope, 1991). This means that light shorter than 650 nm is heavily attenuated by biological tissue, and will mostly be extinguished before exiting the tissue. By examining Figure 2-9(b), it is tempting to choose wavelengths above 900 nm. However, another absorber comes into play at these wavelengths: water. As can be seen in Figure 2-12, the extinction coefficient of water rapidly rises above 900 nm, such that light at these wavelengths is also largely attenuated. The optimal range of wavelengths to measure biological tissue is between 650 and 900 nm to obtain the greatest amount of contrast while maintaining the largest penetration depth for the light to travel.

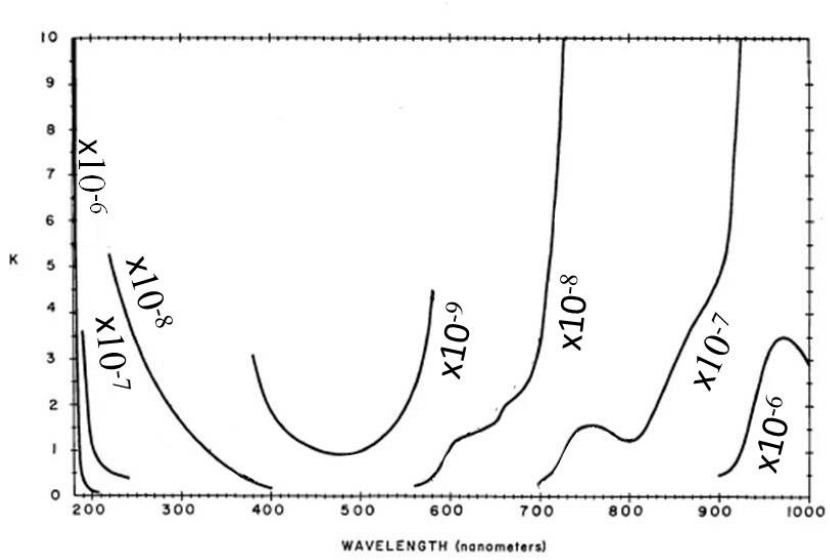

Figure 2-12: The extinction coefficient (K) of water as a function of wavelength as compiled by Hale and Querry (Hale & Querry, 1973). Note: In the range of 200 to 1000 nm, water displays varying degrees of opacity. In the UV and NIR range, water absorbs EM waves 1000 times more readily than that for visible light between 390 and 560 nm.

2.3.6 Red Shift in Diffuse Reflectance

Because wavelengths shorter than 800 nm are more greatly attenuated by HbO, those wavelengths are less likely to survive the trip from source to detector. If light that is not monochromatic is injected into biological tissue, it will undergo an apparent 'red shift'. This is not because of the well-known Doppler shift, since there is no moving target. Rather, this is because the red wavelengths have survived the trip through the tissue, and other colors have been extinguished due to large absorption. If we use monochromatic light, no red-shift, only attenuation will be observed.

2.3.7 From Diffusion Equation to y=Ax

As was mentioned previously, the diffusion equation describes the propagation of diffuse photons. In order to apply the diffusion theory to fNIRS and DOT, the Rytov approximation assumes that the diffuse photon fluence is given by:

$$\Phi(r_s, r_d) = \Phi_{inc}(r_s, r_d) e^{\Phi_{sc}(r_s, r_d)} \qquad 2.32$$

Where Φ_{inc} is the diffuse photon fluence measured without homogeneities, and Φ_{sc} is the scattered photon fluence (D. Boas, 1997). The r_s denotes the source position, and r_d denotes the detector position. The Rytov approximation allows a first order linear approximation to the diffusion equation, which gives the scattered wave as:

$$\Phi_{sc}(r_s, r_d) = \frac{-1}{\Phi_{inc}(r_s, r_d)} \int \Phi_{inc}(r_s, r_d) L(r) G(r_s, r_d) dr \qquad 2.33$$

The Green's function solution, given by $G(r_s, r_d)$, is the solution to the diffusion equation for a spatially uniform background (D. Boas, 1997). The operator $L(r)$ describes the spatially varying absorption and reduced scattering coefficients, and contains the information we seek. Measurement of Φ_{sc} happens at the detector, the solution to G exists for a semi-infinite medium, and the source fluence Φ_{inc} can be calculated, such that an inversion of Equation 2.34 gives the varying absorption and scattering characteristics of the tissue. Usually, the Rytov approximation is broken down into discrete components and implemented in matrix form:

$$\boldsymbol{y}_{N\times 1} = \boldsymbol{A}_{N\times M} \boldsymbol{x}_{M\times 1} \qquad 2.34$$

Where $\boldsymbol{y}$ is an $N \times 1$ column vector containing the measured change in light intensity, $\boldsymbol{A}$ is the $N \times M$ photon sensitivity matrix, and $\boldsymbol{x}$ is an $M \times 1$ column matrix that describes the volume perturbation in absorption and scattering coefficient.

2.3.8 Solving for y=Ax

It is the vector $\boldsymbol{x}$ that we wish to solve for, which mandates that the matrix $\boldsymbol{A}$ must be inverted successfully. However, this is easier said than done. Consider the example depicted in Figure 2-13, where one measurement (y_1) is responsible for quantifying 72 perturbations ($x_1, x_2, \ldots, x_{72}$). Since the light traverses only some of the tissue voxels, it is possible to quantify the properties of those tissue voxels that the light has passed through, shown in dark gray units in Figure 2-13. Even so, there are not enough equations for the amount of unknowns, such that the

entire problem is underdetermined and ill-posed as the problem arises from lack of unique solution (i.e. have many solutions).

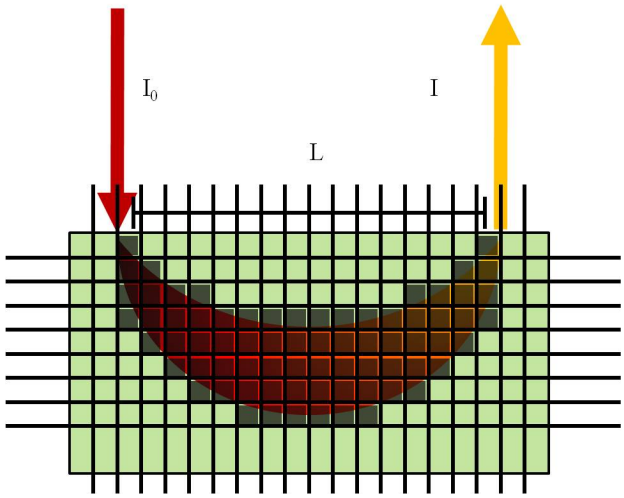

Figure 2-13: For the sake of analysis, the tissue can be thought of many discrete 3 dimensional components called voxels. Each voxel contains its own $\Delta\mu_a$ perturbation that we wish to quantify. For this example, one measurement covers 72 voxels.

Usually more than one source detector pair are chosen, hence increasing the number of unknowns that need to be inversely determined. The generalized matrix form of this situation is as shown below:

$$\begin{bmatrix} y_1 \\ \vdots \\ y_N \end{bmatrix} = \begin{bmatrix} a_{11} & \cdots & a_{1M} \\ \vdots & \ddots & \vdots \\ a_{N1} & \cdots & a_{NM} \end{bmatrix} \cdot \begin{bmatrix} x_1 \\ \vdots \\ x_M \end{bmatrix}, \qquad M > N \tag{2.35}$$

Where M is the number of unknowns and N is the number of measurements. Equation 2.36 is a set of linear equations that can be solved using a linear regression model. The vector y contains the measured ΔOD values, or the observations. The vector x contains the perturbations, $\Delta\mu_a$, or predictors. The sensitivity matrix A represents the independent variables that link the measured output with the desired predictors.

In order to solve for the unknown values in vector x, the sensitivity matrix must be inverted. However, since the problem is underdetermined (i.e. the matrix A is not square), the true inverse of A does not exist. To overcome this obstacle, the Moore-Penrose generalized inversion is implemented (D. A. Boas, Dale, et al., 2004):

$$\hat{\boldsymbol{x}} = \boldsymbol{A^T}(\boldsymbol{AA^T} + \alpha s_{\max}\boldsymbol{I})^{-1}\boldsymbol{y} \quad 2.36$$

The parameter I is the identity matrix, A^T is the transpose of A, $\alpha = 10^{-3}$ is the regularization parameter, and s_{max} is the maximum eigenvalue of AA^T. This regularization approach is computationally intensive and sensitive to noise (D. A. Boas, Dale, et al., 2004). Hence, the interpolated backprojection is another widely employed scheme in optical imaging (Walker, Fantini, & Gratton, 1997). Equation 2.37 below shows the interpolated backprojection scheme where the diagonal matrix S column normalizes the sensitivity matrix A (D. A. Boas, Dale, et al., 2004).

$$\hat{\boldsymbol{x}} = (\boldsymbol{AS})^T\boldsymbol{y} \quad 2.37$$

2.4 CW Hardware

A continuous wave (CW) system in optics refers to a source that is continually on. In other words, the light source is not pulsed in an on/off fashion. The frequency of a CW system can be modulated at frequencies not higher than a few 10 kHz (Frostig, 2009). A CW point source injects photons into a light scattering medium in a radial fashion, such that most photons are either scattered away from or absorbed before they reach the detector. However, a CW system is more easily implemented and much more cost effective than its frequency domain and time domain siblings. The CW-based fNIRS system used for this dissertation study is the TechEn CW5 (TechEn Inc, Milford, MA), as described in the next section.

2.4.1 Instrumentation of CW5

The standard CW5 hardware comes equipped with 32 sources and 32 detectors. Each light source is square-wave frequency modulated between 6.4 kHz and 12.6 kHz in steps of 200 Hz (Franceschini, Joseph, Huppert, Diamond, & Boas, 2006). The 32 distinct modulated frequencies of the sources are controlled by a system reference clock. The diode laser sources consist of sixteen sources emitting at 690 nm and the remaining sixteen emitting at 830 nm. The system is mounted with 32 light sources as transmitting channels. However, depending on the user's probe design, only a desired number of laser sources may be enabled by transmitting serial bit data transmission to the system.

The 690 and 830nm laser sources have a maximum power output of 9 mW and 3mW respectively. The laser sources are calibrated using an OPHIR PD200 optical power meter. The operator also can tweak the potentiometer next to each laser source made accessible in the transmitter card to change the laser intensity. One calibration procedure is to confirm whether the laser can emit optical power of about 3mW by placing a detector at a distance of 1cm from the front of the laser diode (TechEn, 2006).

The source light is incident on the sample, and allowed to traverse the medium. The diffuse reflectance is then detected with an avalanche photodiode (APD). The APD relies on the principle of the photoelectric effect to convert the analog electromagnetic radiation to an analog current. Following the conversion, the signal is initially high pass filtered at 500 Hz to remove low frequency noise from interference sources such as room light and electronic 1/*f* noise. After high-pass filtering, the signals on the analog-to-digital (A/D) converter are matched to the acquisition levels by a programmable gain control. Finally, the signal is low-pass filtered at 16 kHz to prevent aliasing during digital sampling (Franceschini, et al., 2006). Each detector signal is sampled at 41.7 kHz and the sampled data is stored in a PC. A block diagram of this process can be seen in Figure 2-14 (Franceschini, et al., 2006). Each of the eight laser modules consists of a card that houses four diode lasers. Each of the sixteen detector modules contains two detectors. See Figure 2-15 for the panel layout. Laser sources and avalanche detectors mounted on the front panel shown in Figure 2-15 are coupled to the fiber optic cables using SMA connectors.

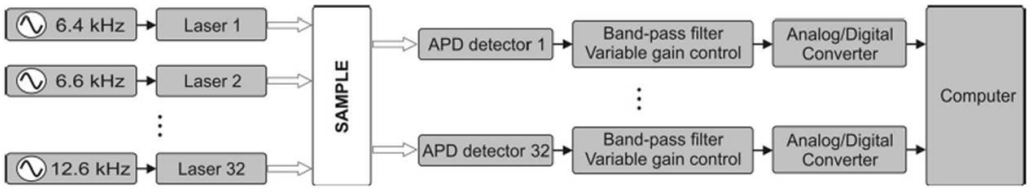

Figure 2-14: Block diagram of CW5 as proposed by (Franceschini, et al., 2006).

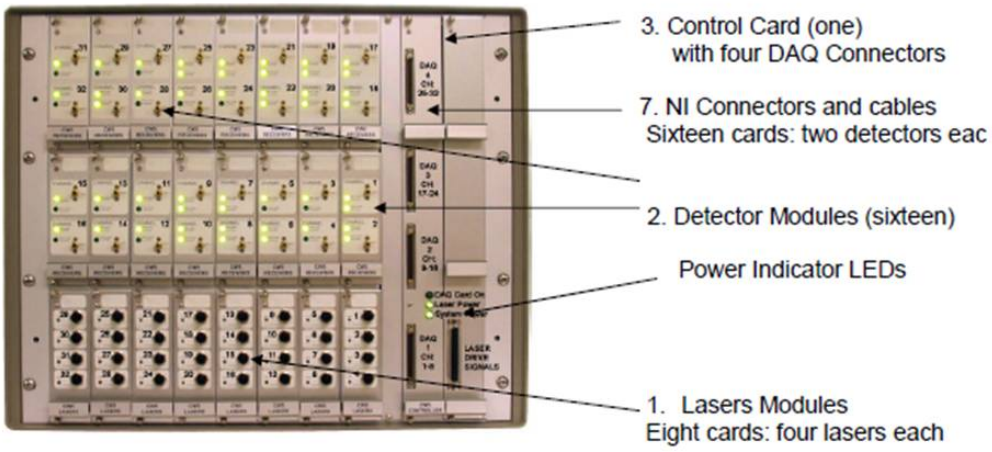

Figure 2-15: CW5 source and detector panel (TechEn, 2006).

Functioning of the hardware and data pre-processing is controlled via the appropriate MATLAB code installed on the PC. The MATLAB code may require further modification depending on the user's probe geometry configuration. Please refer to Appendix A for the source code that enabled operation of the CW5 probe geometry used in experiments detailed in Chapters 5, 6, and 7.

2.4.2 CW-5 Instrument Calibration

The system should frequently be tested for quality assurance. Typical interferences may arise from electronic leakage, light leakage and aliasing. Calibration assures that such noise is minimized and the acquired signal is in the desired range. Some of the basic and quick calibration tests are: (1) laser frequency test, which ascertains that the laser source is modulated at an accurate frequency. (2) Noise floor test for system error and light leakage. (3) Solid phantom test to check for aliasing due to electronic leakage and (4) Drift test to make sure that signal drift is less than 1% over a continuous 10min data acquisition. Although, these calibration tests need not be carried out before each data acquisition, it is highly recommended to frequently calibrate the instrument per the decision of the user and recommendations described in the manual (TechEn, 2006).

2.4.2.1 Laser Frequency Test

This test is carried out to observe if the laser sources are initiated to the correct frequency. The probe set-up must be mounted on a solid phantom. It is desirable that the optical properties of the solid phantom are comparable to the target tissue medium. The instrument should be switched on, and the data viewing should be set to the “Log Fourier” mode. The detectors are then set to record the first 5 channels. Now, by selecting the “source” mode, laser source 1 should be turned on and a visible spike in signal amplitude should be observed. Following this, the second laser source 2 should be turned on and we should be able to view a higher spike frequency compared to that of source 1. Then the laser source 1 should be turned off followed by turning on laser source 3. The resulting spike frequency for laser source 3 should be higher than that of laser source 2. If the laser source is not assigned the correct frequency, then the instrument power should be turned-off for a few seconds and turned back on again. The power cycle should be able to reset the laser frequency dividers. This procedure should be repeated for all laser sources. Ideally, as explained above, there should be an increase in spike frequency as a function of laser source number.

2.4.2.2 Noise Floor Test

The purpose of the noise floor calibration test is to observe spurious noise levels in response to electronic leakage and system error. The desired probe geometry should be mounted on the solid phantom as described in the previous sub-section. A single detector should be covered by black tape. Now, the data display should be in the “Log Fourier” mode and the sources should be turned on. If the noise floor as a function of frequency looks flat, then it is assumed that no spurious signal is observed at that detector. However, if a spurious peak is observed, then it could possibly be due to light leakage. If multiple spurious peaks are found, there might be a potential problem due to misbehaving electronic components. This procedure should be repeated for each detector by masking it with black tape as explained above. If a detector has noise leakage, it is not reliable, and must be sent back to the company for further testing and repair.

2.4.2.3 Harmonics or Aliasing Test

The desired probe geometry should be mounted on the solid phantom as described in the above two sub-sections. However, for this calibration test, all the detectors except for the one detector with the highest signal should be blocked with a black tape. The sources should be turned on for a few minutes and then recording should be carried for 30 seconds. The Fourier spectra should be inspected for each channel at each of the detectors. Ideally, the spike in signal amplitude for the detector under test should display the laser modulated frequency. However, the Fourier spectra for rest of the detectors that were blocked should look flat. If the Fourier spectrum at the detector that was not taped shows peaks at frequencies other than that of the laser modulated frequency, then we observe aliasing or harmonics which is undesirable. In this situation, the specific detector cannot be used and must to be shipped back to the company for further testing and repair.

2.4.2.4 Drift Test

According to the instrumentation manual, the acceptable drift for the CW-5 instrument is 1% over a 10 minute data acquisition (TechEn, 2006). In order to test for drift, the solid phantom should be mounted with the desired probe geometry. The laser sources must be on for one hour prior to this test to allow for the instrument to warm up. The data recording should be carried out for 10min, during which the instrumentation and the set-up should be untouched and stable. After demodulation, the variation within the demodulated signals should be less than or equal to the manual specification of 1%. If the drift is not within the specifications, it can be eliminated during further analysis by tuning the band-pass filter to an appropriate cut-off frequency.

2.5 Software: HomER

The bulk of the analysis presented in this dissertation was carried out with an open source Graphical User Interface (GUI)-based data processing software called HomER, which runs on the MATLAB platform. HomER is an acronym for Hemodynamic optically measured Evoked Response, and allows the user to analyze time series optical data on the individual or group level (Huppert, Diamond, Franceschini, & Boas, 2009). HomER is virtually compatible with

any existing NIRS and DOT acquisition system, including the CW5. The user has a large range of versatility in specifying acquisition parameters, including probe geometry and source wavelength.

Initially, the probe geometry is imported, and sources and detectors are defined by the user. This means that the data format *'.cw5*' is converted into the *'.nirs*' format which is accepted by HomER's GUI interface. Appendix A in this dissertation shows the MATLAB code that is modified to the needs of probe geometry designed for this dissertation work. The codes shown in Appendix A also down-sample the acquired data to 10 time points/sec.

At the first organizational level of HomER, individual data files (or runs) can visually be eyeballed for huge spiky artifacts or low SNR. The user has the option to disable certain channels with high artifacts or low SNR. However, caution is warranted to not disable too many channels as that would lead to a lower statistical power. The selected, visually 'good' channels are subjected to filtering, removing instrumentation noise, and physiological noise and motion artifacts. More details on physiological noise and its influence on the hemodynamic sensitivity will be discussed in section 2.6.4 Once the raw data is filtered, the oxy- and deoxy- and total-hemoglobin concentration are extracted, which are quantified based on the fundamental principle of MBLL and relevant physical factors such as extinction coefficient, differential path- length factor (DPF), and partial volume effects. The extinction coefficient has been addressed in Section 2.3.2 . More details on the importance of DPF, and partial volume in enhancing the sensitivity and subsequent quantification will be described in the Section 2.6 .

At the second level of HomER, the user can graphically view the filtered ΔC (concentration) as a function of time for a time-series analysis. Depending on the experimental protocol design, the time points that define the baseline and each functional block can be entered by the user. The software also allows for visualization of each block in the entire time-series, and allows the user to disable any blocks that look noisy. Again, at this step, caution is warranted that disabling too any blocks would reduce the 'functional' power. Finally, the functional hemodynamic response can be computed in one of two ways: (1) block averaging or (2) finite impulse response. Both analysis methods are calculated using the ordinary least squares method (T. J. Huppert, et al., 2009). Depending on the protocol design, the software also makes available

several advanced averaging features available. The concepts of experimental design, data pre-processing and statistical analysis for functional brain imaging studies are complex and cannot be completely addressed in this dissertation. Readers are suggested to refer to (Huettel, Song, & McCarthy, 2008) for fundamental concept based details.

At the third organizational level of HomER, the user has the feature to obtain reconstructed images for each type of the task-induced ΔC (concentration changes). The software has two options for reconstruction algorithms: (1) Backprojection and (2) Regularized-inversion. A brief technical description on these algorithms are described in sub-sections 2.3.7 and 2.3.8 In addition, the limitations of these algorithms and its quantification accuracy of the optical properties from the reconstructed images are described in section 2.6 Finally, the option of region-of-interest (ROI) comparison at this level circumvents the possibility of inter-subject registration issues (Frostig, 2009). The statistical criteria for ROI are based on either the *T*-statistics calculated from the effects of the functional model or the *F*- test statistics describing the ability of the model to fit the data (T. J. Huppert, et al., 2009).

This section has briefly described the features of HomER and has tagged its functioning back to the underlying physical principles. More details on HomER based data processing and its validation pertaining to this dissertation work will be described in the following chapters that are associated directly to each of the specific aims. For further details on HomER, the readers are referred to read Ted Huppert's recently published journal article (T. J. Huppert, et al., 2009).

2.6 Limitations and Sensitivity of DOT

2.6.1 Limitations: Penetration Depth

Mansouri et al. 2010 recently published depth sensitivity of DOT using the Henyey-Greenstein function and Monte Carlo simulations. As can be seen in Figure 2-16, the probability density of the photons trajectory through the tissue is a banana shape. Recall from Figure 2-7 that a point source creates a radial outflow of photons, and that most photons are scattered away from the detector. However, the light that does travel between source and detector has the most probable pathways as depicted in Figure 2-16. This pathway is often referred to the 'banana

shape', because of its close resemblance to the fruit. Mansouri et al. concluded that as the source detector separation becomes larger, the depth sensitivity goes up, but with a rapid decrease in SNR. In order to reach the cortical regions, which is approximately 2 cm below the scalp, the source-detector separation must be greater than 2 cm. However, to measure a reasonable signal, this distance must be less than 4 cm. Thus, DOT and NIRS measurements are most likely sensitive to the first 5 mm of grey matter without any additional depth reconstruction algorithms. This is not too detrimental since most brain activity is performed at this structural level (Frostig, 2009).

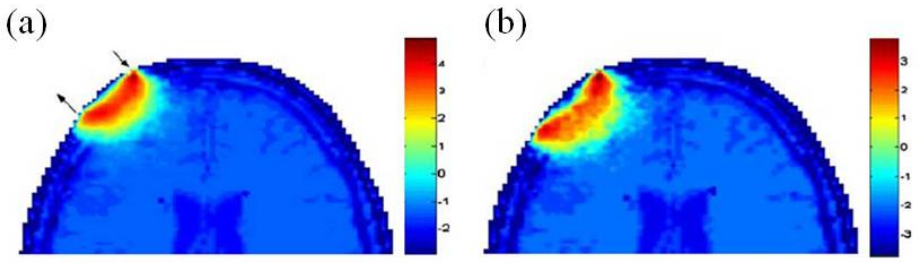

Figure 2-16: Results depicting the probability density for photon trajectory with (a) 2 cm source detector separation and (b) 3.3 cm source detector separation (Mansouri, L'Huillier J, Kashou, & Humeau, 2010).

2.6.2 Differential Path-length Factor (DPF) Sensitivity

The Modified Beer-Lambert Law (MBLL) accounts for the increased distance of travel for the photon as it scatters through a dispersive medium. This "modification," or adjustment, in path length for a semi-infinite medium is embodied in the Differential Path length Factor (DPF) or *B* that is based on Equation 2.20.

As discussed throughout this chapter, at different wavelengths, light behaves differently in subtle ways. The absorption of a photon has wavelength dependence, since the extinction coefficient is a function of wavelength. Complementing this trend, scattering is also wavelength dependent which imposes a dependence of *B* on scattering. The coefficient *B* also depends on the source-detector separation, since the probable photon trajectory will change with a change in L (path length). Equation 2.20 describes the solution for B under the condition of semi-infinite slab geometry.

From several optical studies, it has been established that DPF is critical to be included in the derivation of clinically relevant parameters such as cerebral blood flow and cerebral blood volume. Essenpreis et.al 1993 experimentally showed that DPF has wavelength dependence. Along with its spectral dependence, the DPF also depends on inter-subject variation leading to a ±10% variability in quantitative measurements (Essenpreis, et al., 1993).

2.6.3 Limitations: Reconstruction

The first diffuse optical images of brain activation were published in 1995. The initial approach of quantification was to measure the hemodynamic response with individual pairs of sources and detectors and interpolate the response between measured channels (Franceschini, Toronov, Filiaci, Gratton, & Fantini, 2000). The resolution of this analysis is comparable to the source detector separation, and quantitative accuracy is compromised due to the underdetermined and ill-posed problem with the inverse method approach for reconstruction (Simon R Arridge, 1999). A brief description of the under-determined and ill-posed issues originating from the linearized inverse method is given in sections 2.3.7 and 2.3.8 .

The probe geometry design also plays an important role in the reconstruction sensitivity due to its resulting spatial resolution. Given the NIR technological limitations, David Boas concluded that a hexagonal geometry is the best available option (D. A. Boas, Chen, Grebert, & Franceschini, 2004). In addition to the probe geometry, the image performance also depends on the position of the absorber relative to the sources and detectors. When the absorption change occurs in a region that is equally sampled by neighboring measurements, it leads to spatial ambiguity due to reduced image amplitude and spatial blurring. This problem was shown to be ameliorated by the addition of overlapping measurements from the next nearest neighbor channels (D. A. Boas, Chen, et al., 2004).

2.6.4 Hemodynamic Sensitivity

In Section 2.3.8 , it was discussed that the image reconstruction process is ill-posed, leading to errors in the hemodynamic characterization. In an effort to reduce both spatial and concentration estimation errors, optical sources centered at 690 nm and 830 nm is shown to be

optimal (Siegel, Culver, Mandeville, & Boas, 2003). It is believed that a source wavelength of 690 nm is preferable to 780 nm when paired with an 830 nm source for DOT based studies (Strangman, Franceschini, & Boas, 2003; Yamashita, Maki, & Koizumi, 2001). In addition, features with high absorbance such as large blood vessels can absorb nearly all of the local incident flux, thus reducing NIRS signal sensitivity in those areas. This means that most NIRS and DOT based measurements are uniformly sensitive to vessels smaller than the optical absorption length, with sensitivity progressively decreasing for larger vessels (Liu, Chance, Hielscher, Jacques, & Tittel, 1995).

The estimation of true concentration also depends on the partial path-length factor. The equivalent of the same parameter in DOT is referred to the partial volume error. The partial volume error depends on the position of the absorber relative to the positions of the source and detector, depth of the absorber, spatial extent of the absorption change, and optical properties of the cortical tissue (D. A. Boas, Dale, et al., 2004). An analytical approach solving for the dependence of these parameters can be carried out using the photon diffusion equation (Strangman, et al., 2003). However, the experimental approach still faces many challenges when attempting to address these issues. Thus, to increase the vascular sensitivity further work must be done in order to improve the depth resolution and partial volume correction in the reconstructed images.

One of the celebrated features of DOT is the non-invasive nature of capturing measurements on the patient's scalp. However, this benefit also creates new challenges. The practical limitation such as a reduced signal-to-noise ratio due to the overlying scalp and skin, the skull thickness and the shape of the head cannot be discounted (Feng, et al., 2001). One approach of increasing depth sensitivity is to incorporate a spatial prior from structural MRI to enhance the DOT measured brain activation (D. A. Boas, Chen, et al., 2004).

Further, the sensitivity to weaker brain activation signals is corrupted by interference from the systemic physiological signals such as cardiac pulsations, respiration, and blood-pressure variations, including Mayer waves. The temporal variation of these systemic signals can be as large as 10% (Theodore J. Huppert, et al., 2009). For comparison, fMRI studies have shown that

task-induced changes in brain activation only account for a 5% change for strong finger-tapping stimuli, and is even smaller for other types of stimuli (Huettel, et al., 2008). Hence, to improve the optically measured hemodynamic sensitivity, it is necessary to develop signal processing methods that can distinguish the different source signals both spatially and temporally. A recent approach utilizes Principal Component Analysis (PCA) (Franceschini, et al., 2006) to determine the principle spatial components of the spatio-temporal covariance of the baseline optical data. Using this information, the entire data is globally filtered for systemic signal variation. Unfortunately, the cross-correlation between independent systemic physiological measures and brain activation is not well understood. Moreover, a quantitative metric approach based on rigorous models (Buxton & Frank, 1997) is a challenging problem since it requires experimental validation.

2.7 Topography versus Tomography in Diffuse Optics

In the Greek derived word 'tomography', *tomo* means slices and *graphy* implies pictures or images. Whereas, in the word 'topography' *topo* means place and again *graphy* means image. Tomography incorporates three-dimensional volumetric imaging, wherein two-dimensional images are obtained by slices at defined depths. This concept originates from the field of X-Ray and Computerized Tomography (CT), and has been translated to PET, SPECT and MRI based medical imaging applications. Both tomography and topography are utilized in optical imaging. In general, the method used depends on the researcher's application and the hypothesis under investigation.

In typical diffuse optical imaging, a grid of light sources and detectors is positioned on the head of the subject. Each pair of sources and detectors is typically referred to as an 'optode'. The arrangement of the optodes on the head determines the depth-sensitivity of the measurements from the underlying cortical tissue as a function of the distance between the source-detector pair. In the case of true tomographic imaging, a dense array of optodes and overlapping measurements covering the sample volume are used to obtain uniform spatial coverage and the best possible spatial resolution (D. A. Boas, Dale, et al., 2004). Typically, for a tomographic probe

to function, light from sources located at various distances must be detected by a single detector. This collection of overlapping measurements requires detectors with a high dynamic range (Zeff, White, Dehghani, Schlaggar, & Culver, 2007) or fast source-switching schemes (Barbour, Graber, Pei, Zhong, & Schmitz, 2001).

Tomographic imaging such as in DOT is cumbersome and very sensitive to instrumentation signal-to-noise ratio. Hence, most diffuse optical imaging is based on point source measurement imaging, such as NIRS, compromising uniformity and spatial resolution (Theodore J. Huppert, et al., 2009). Topographic imaging based NIRS incorporates less denser optodes giving rise to a lower spatial resolution. In addition, post hoc analysis approaches such as overlapping the measurements from the adjacent channels cannot be efficiently carried out with a lesser dense optode array. Hence, the sensitivity to the depth and also the hemodynamic changes is compromised in the NIRS based topographic imaging.

CHAPTER 3

COGNITIVE ASPECTS OF PAIN

3.1 Background

According to Wall and Melzack 1965, pain is a multi-dimensional experience that encompasses sensory, emotional and cognitive components. It can also be termed as a universal experience encountered by all vertebrates, specifically humans. The interest to understand emotional and cognitive components has increased immensely in the last few decades. Antonio Damasio 2003, a well-known neuroscientist, opinionated that the sensory systems are better understood than the affective systems. Along the same line, William Willis 1995 advocated that affective components of pain deserve more experimental study for clinical relevance. The relative lack of neurobiological understanding of the emotional and cognitive components of pain can be attributed to the non-accessibility of subjective states in non-verbal organisms. Fortunately, the advent of brain imaging with a multimodal approach has permitted a dramatic improvement in the understanding of the complex interactions among affective, sensory, cognitive and behavioral mechanisms during pain.

If the pain reported by a patient cannot be objectively confirmed, is judged to be disproportionate to physical pathology, or if the pain complaint is recalcitrant to appropriate treatment, it is often assumed that psychological factors play a causal role. The determination of whether the reported pain is disproportionate is purely a subjective decision by an external observer. This simply means that there is no way to objectively determine pain level and administer appropriate treatment.

Investigation towards the cognitive-behavioral perspective of pain was initiated, and to some extent conceptually conceived by Meichenbaum and Turk in the 1970s. They characterized the cognitive factors underpinning pain with some key assumptions. The assumptions are: (1) humans are active processors of information and not passive reactors, and (2) that human thought processes are influenced by mood, physiology, environmental factors and behavior. Although the conceptual framework and models proposed by Turk and others propelled the psychological aspects, understanding of the neurobiological substrate that lead to the cognitive components of pain is lacking.

Early pain studies using neuroimaging were carried out using PET (Jones, Brown, Friston, Qi, & Frackowiak, 1991; Talbot, et al., 1991) and later with functional MRI (Apkarian, Darbar, Krauss, Gelnar, & Szeverenyi, 1999; L. R. Becerra, et al., 1999; Davis, Wood, Crawley, & Mikulis, 1995). Most of these earlier studies focused on the primary somatosensory cortex S1 (Apkarian, Bushnell, Treede, & Zubieta, 2005; L. Becerra, et al., 2006; Christian Maihofner, Handwerker, & Birklein, 2006). However, most of these studies pointed to a lack of consistent activation in S1. This has been attributed to cognitive modulation, inhibitory processes and methodological differences (Bushnell, et al., 1999). Since then, other areas of the brain have come under investigation during pain administration. The putative role of the frontal lobe has been linked to memory, executive functioning (C. Maihofner, Schmelz, Forster, Neundorfer, & Handwerker, 2004), cognitive and emotional responses (Kong, et al., 2006; Lorenz, Minoshima, & Casey, 2003), placebo response (Wager, et al., 2004), altered activations in chronic pain (Witting, Kupers, Svensson, & Jensen, 2006), and morphological changes (Apkarian, et al., 2004).

Although pain processing involves a network of cortical and sub-cortical areas, most of the earlier fMRI studies focused on “what” and “where” of the functional networks. It appears perhaps that in addition to “what” and “where” systems, the “how much” system that gives rise to subjective perception of pain needs to be explored. A theoretical approach in this direction was shown in (V. Walsh, 2003), but technological advances in brain imaging now allow experimental work to explore the “how much” module of the pain network (Baliki, Geha, & Apkarian, 2009).

However, the role played by the prefrontal areas in the “how much” module of the pain network is still not well understood. Recent fMRI reports have shown the role of the medial prefrontal area (Kong, et al., 2006) in pain encoding and cognitive evaluation, and the role of the dorsolateral prefrontal area (Wiech, et al., 2006) in expected and perceived control over pain. These studies are grounds to further explore the prefrontal areas, specifically BA 46 (dorsolateral prefrontal) and BA 10 (anterior prefrontal) areas, in the cognitive evaluation of pain using diffuse optical tomography. In the following sections, neuroanatomical and neurophysiological features of BA 9 and 10 will be described, along with their role played in the cognitive aspects of pain.

3.2 Cytoarchitecture of the Prefrontal Cortex

Cytoarchitecture is defined as the package or arrangement of the cells in a tissue; specific interest being the nerve cells in the cerebral cortex. Microscopic examination, such as histology, is a scientific landmark and allows for a better understanding of the details at the cellular level.

The prefrontal cortex is essential for complex cognitive processing, but a good understanding of its functions is lacking. According to Fuster, the cortex of the mammalian brain is conventionally defined by two criteria: the cytoarchitecture and the connectivity (Fuster, 2002). The earliest human cytoarchitectural study was reported in the early 19th Century by Korbinian Brodmann (Brodmann, 1908). Since then, neuroanatomic (Pandya D.N., 1987), neurophysiological (di Pellegrino & Wise, 1991), and neurocircuitry (Pandya D.N., 1987) studies suggest that the prefrontal cortex should be subdivided into structural and functional sub-regions. At the same time, functional neuroimaging emerged in the 1980s, which incorporated much of Brodmann’s cytoarchitectonic work by adopting Brodmann areas into Talairach and Tournox based stereotaxic brain atlas. The figure below shows a lateral view of the cytoarchitectonic map of the human cerebral cortex.

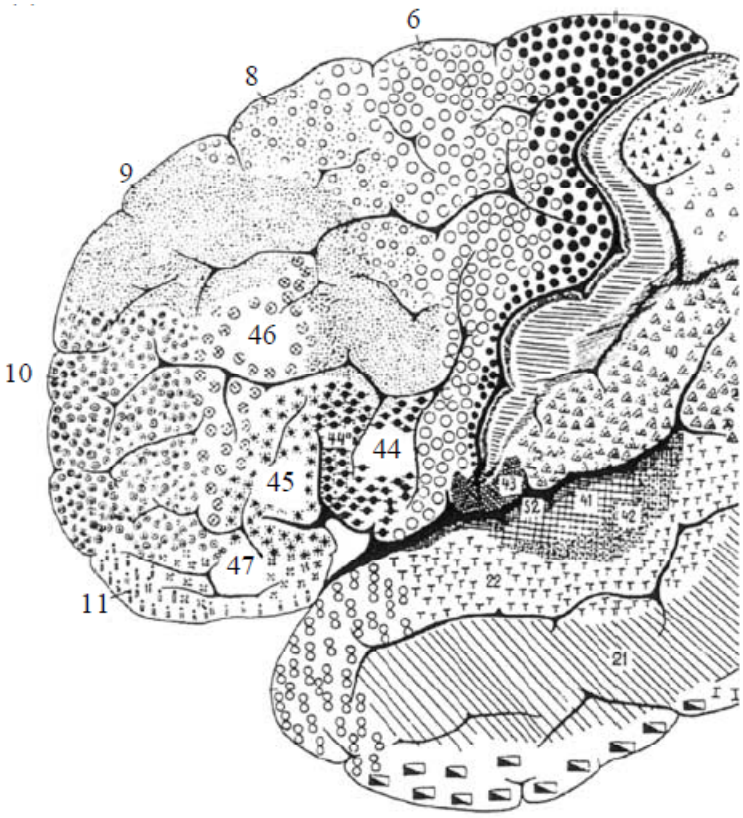

Figure 3-1: Brodmann cytoarchitectonic map of human cerebral cortex from a lateral view. The different pattern in the figure depicts different cellular types. Their granulation is used for sub-dividing and demarcating the Brodmann areas (Brodmann, 1909). This figure is reproduced from (M. Petrides, 2005).

In the context of neuroimaging, statistically significant 'functional' voxels are co-registered to structural brain areas to implicate regions that show significant task-induced functional changes. Thus, cytoarchitecture and accurate representation and demarcation of cortical areas are essential to the neuroimaging field.

3.2.1 Anterior Prefrontal Cortex

According to Burgess et.al, Brodmann area 10 is the least understood cortical area, both anatomically and functionally (Burgess, Gilbert, & Dumontheil, 2007). A detailed cytoarchitectonic study on medial and orbito-medial prefrontal areas in monkeys has concluded that experimental work on monkeys can be applied to humans (Ongur, Ferry, & Price, 2003). Another group carried

out comparative cytoarchitectonic study between monkeys and humans, specifically for BA 10 (Semendeferi, Armstrong, Schleicher, Zilles, & Van Hoesen, 2001).

As can be seen in Figure 3-1, BA 10 is dorsally bound by granular BA 9 (dorsolateral prefrontal cortex), caudally by BA 46 (dorsolateral prefrontal cortex), and ventrally by BA 45 (orbito-medial prefrontal cortex). It has been reported that BA 10 is the largest, single architectonic region of the PFC (Ongur, et al., 2003). Moreover, BA10 is relatively larger than its counterpart in any closely related primates (Semendeferi, et al., 2001). From an evolution perspective, this area has developed relatively recently, and has led some researchers to hypothesize that BA10 might play a role in higher-cognitive functions in humans. Interestingly, BA10 has a lower cell density in humans. This architecture allows for more connections with other cortical and sub-cortical areas involved in complex cognitive tasks (Semendeferi, et al., 2001).

3.2.2 Dorsolateral Prefrontal Cortex

The dorsolateral prefrontal cortex (DLPFC), in a broader and conservative sense, maps to BA 9 and 46, shown in Figure 3-1. However, a recent work by Petridis disagrees with the classical architectonic map of Brodmann (M. Petrides, 2005). In the human brain, BA 9 refers to both the cortical area over the superior frontal gyrus and a large part of cortical area caudal to BA 46. Thus, BA9 occupies the middle frontal gyrus, separating BA 46 and BA 8. Petridis' careful work on monkeys shows that the portion of BA 9 on the middle frontal gyrus shares a well-developed layer IV with BA 46. However, the latter can be discriminated by the presence of large, deeply stained pyramidal neurons (M. Petrides, 2005). They also report that comparing the architecture of the monkey and human prefrontal cortex, only a limited region of Brodmann area 46 has similarities to BA 46 of the human brain. Thus, they designated mid-dorsolateral prefrontal cortex as area 9/46. Now, the previously designated area 9 by Brodmann has been reconstituted as area 9/46. It has architecture similar to area 46 and extends along the same gyrus. Thus, BA 9/46 extends lateral to BA 9 which is on the superior frontal gyrus. Figure 3-2 below shows the revised cytoarchitectonic map which demarcates the area 9/46 (Michael Petrides & Pandya, 1994).

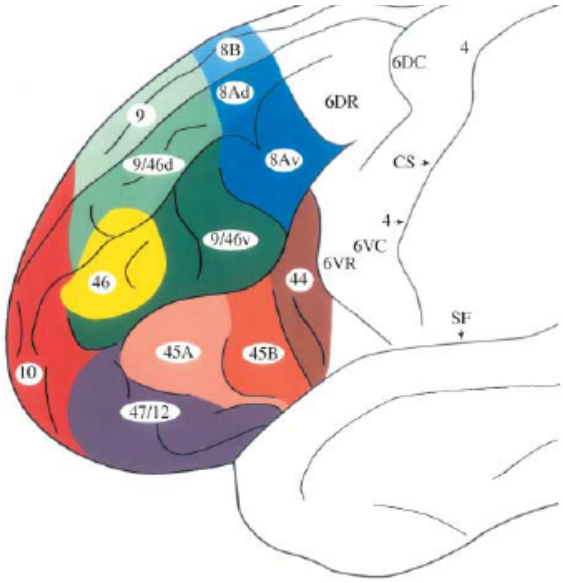

Figure 3-2: Revised cytoarchitectonic map of human prefrontal cortex by (Michael Petrides & Pandya, 1994).Note: VR: ventral rostral; VC: ventral caudal; DR: dorsal rostral; A and B: sub-divisions of an area; d: dorsal; v: ventral; and the numbers denote the architectonic areas. This figure is reproduced from (M. Petrides, 2005).

BA 9, BA 10 and area 9/46 receive their multimodal input from the superior sulcal cortex, the rostral superior temporal gyrus, the anterior and posterior cingulate cortex, and the retrosplenial cortex. It has been observed that these areas maintain preferential connections with temporal areas, and with paralimbic areas such as the cingulate, the retrosplenial and the rostral temporal cortex.

3.3 Cognitive Factors in Pain

The theoretical framework developed by Meichenbaum and Turk (Meichenbaum & Turk, 1976) characterizes the cognitive-behavioral perspective of pain perception and tolerance. Their key assumptions were briefly mentioned in Section 3.1 . Additional assumptions they describe are (a) that behavior is reciprocally determined by the person and environmental factors, (b) that people 'learn' adaptive ways of thinking, reacting, and behaving and (c) that people are capable as 'active agents' to react and change maladaptive thoughts, feelings and behavior. These assumptions are relevant to the cognitive-behavioral perspective. Patients suffering from chronic

pain harbor negative expectations about their ability to control certain motor skills, and foster negative beliefs that they have limited ability to exert control over their pain. Such negative, maladaptive appraisals about the situation and personal efficacy reinforce the experience of demoralization, inactivity and overreaction to nociceptive stimulation. Although this work focuses mainly on the cognitive-evaluative aspects of pain, the following sub-sections will discuss several cognitive factors that shape the perception of the pain experience.

3.3.1 Personal Beliefs about Pain

Clinicians report that patients with similar pain histories may differ greatly in their beliefs about their pain. Ideally, the objective cause of the painful event should be explored, but the emotions and behavior that influence the interpretation of events cannot be ruled out (McMahon & Koltzenberg, 2005). In addition to the causal role of pain, beliefs about the ability to control pain are important to patients coping with pain. Experimental studies show that the conviction of personal control can ameliorate the negative experience of experimentally induced nociception (Jensen & Karoly, 1991).

The concept of belief is very important in understanding the pain rating outcome, which is discussed in Section 3.5 . Personal beliefs and thoughts employed during exposure to painful stimulation have been related to pain tolerance and pain intensity ratings (Spanos, Radtke-Bodorik, Ferguson, & Jones, 1979). Clinical studies have shown that in chronic pain patients, the presence of catastrophic thoughts and convictions of helplessness, and the absence of coping thoughts and convictions of resourcefulness have been associated with higher levels of pain and an inability to use resources such as the health care system (D. A. Walsh & Radcliffe, 2002).

The beliefs about pain not only shape the capability to function during pain, but also the response to treatment, and the adherence to self-management of activities and disability (Kerns & Rosenberg, 2000). Newton and Barbaree's innovative experimental study show that patients who exhibit a positive shift in cognitive appraisal also report a lower rating of pain intensity (Newton C.R., 1987). This implies that successful rehabilitation induces a cognitive shift from beliefs about helplessness and passivity to resourcefulness and coping abilities, irrespective of pain.

3.3.2 Self Efficacy

In addition to belief, another closely related factor is self-efficacy, which reflects the level of control over adverse stimuli. According to Bandura et.al 1987, self-efficacy expectation is defined as a personal conviction that one can successfully execute a course of action to produce a desired outcome in a given situation. The self-efficacy factor not only affects the coping efforts related to pain perception and behavior, but also the related physiological variables underlying the processing and perception of pain (Bandura, O'Leary, Taylor, Gauthier, & Gossard, 1987).

3.3.3 Catastrophizing Factor

Experimental studies on normal volunteers and patient populations have shown that pain tolerance and subsequent cognitive evaluation of pain are influenced by the catastrophizing factor. 'Catastrophizing' consists of extremely negative thoughts about one's plight, such that a minor problem is misinterpreted as a major catastrophe (Turk, Meichenbaum, & Genest, 1983). Cognitive-behavioral based treatment has shown reduction in catastrophizing factor, resulting in an increased pain tolerance. These experimental psychological studies show that a reduced catastrophizing factor is related to the evaluation of perceived pain intensity and physical impairment.

3.3.4 Attention

Pain is an alert signal that demands our attention. It allows us to realize that something within the body is not normal and needs further care. This alert system manipulates itself in different ways as a function of external or internal factors that caused its trigger, coupled with the state of mind. Hayes et al. 1981 have shown that focusing attention towards painful stimuli increases the neuronal spiking activity in monkey's brain stem as compared to that of focusing attention away from the painful stimuli. Recent BOLD fMRI studies have also shown that focused attention towards painful stimuli activates the peri-acqueductal gray (PAG) area, while distraction

from painful stimuli activates other cortical and sub-cortical areas involved in the pain matrix (Bantick, et al., 2002; Tracey, et al., 2002).

3.3.5 Memory in Pain

Subjective assessment of pain stimuli is highly variable, since it is shaped by past experiences and current motivational states. It has also been reported that pain perception does not directly reflect incoming signals from the primary sensory neurons (McMahon & Koltzenberg, 2005). Magnitude estimation or evaluation of pain intensity requires mapping of nociceptive signals to some kind of neural construct with numerosity representation (Piazza, Pinel, Le Bihan, & Dehaene, 2007). Recent reports propose different brain regions that are involved in integrating magnitudes from multiple sensory modalities and its transformation to pain perception (Baliki, et al., 2009; Piazza, et al., 2007; V. Walsh, 2003). Researchers have proposed the use of classical psychophysical studies to define the properties of perception. In one seminal study (Miller, 1956), Miller showed that humans can identify only one of the seven different sensory stimuli. This demonstration lead some to hypothesize that working memory has limited capacities in processing information (Cowan, 2001).

Several studies based on autobiographical memory tasks have shown that patients not only rely and focus on negative experiences while in a state of pain, but also during a pain-free state of experience. This becomes more complicated when memories of pain in the non-conscious state of mind also manifest themselves into pain-enhancing and pain-maintaining roles in the conscious state of mind.

3.4 Anticipation

According to Wall and Melzack (McMahon & Koltzenberg, 2005), anticipation and its associated distress is also an emotional factor in the context of pain. The temporal variation of emotions for different painful conditions have been categorized into potential antecedents, comorbid states, and consequences (McMahon & Koltzenberg, 2005). Anticipatory distress is observed to be the consequent emotion of antecedents such as fear and anxiety under both phasic and acute painful conditions.

Anticipatory stress can be deemed both positive and negative. Anticipatory stress can aid a person in pain to seek help, enhances problem-solving behavior, and also triggers the patient's coping skills to deal with post-operative distress. In contrast, the negative dimension of high level anticipatory stress is its adverse, post-operative experiences (Palermo & Drotar, 1996), excessive emotional reactions (Crombez, Eccleston, Baeyens, & Eelen, 1998), somatic preoccupation and increased dependency on healthcare (Reesor & Craig, 1988), and behavioral disorganization (Sullivan & D'Eon, 1990). Psychological research work on fear, the catastrophizing factor, and cognitive-behavioral interventions (Vlaeyen, De Jong, Onghena, Kerckhoffs-Hanssen, & Kole-Snijders, 2002) have played a significant role in alleviating pain-related distress and disability. In recent years, the emergence of functional brain imaging modalities have allowed further exploration of the brain areas involved in cognitive-emotional factors underlying pain modulation (Porro, et al., 2002) (Wager, et al., 2004). Although the main focus of this dissertation work investigates the cognitive evaluation of pain, exploratory work towards the interaction between cognitive evaluation and anticipatory stress is also carried out to understand the role of prefrontal areas in cognitive evaluation and anticipatory aspects of pain.

3.5 Pain Rating Scales

It is essential to determine the intensity, perceptual qualities, and time course of a patient's pain. This allows clinicians to evaluate the cause of the pain, and to determine an effective treatment. Since the beginning of the 20th century, research in pain has been dominated by the concept that pain is purely a sensory experience. Paradoxically, the behavioral or 'verbal' feedback has always been that it is an unpleasant experience. To consider just the sensory aspect of pain is purely one-dimensional and an incomplete approach to understanding pain or to design an effective treatment. These considerations propelled researchers such as Wall and Melzack in the 1960s to create a new scientific framework for pain which comprised of three major psychological dimensions: sensory-discriminative, motivational-affective, and cognitive-evaluative (Melzack & Wall, 1965).

To this date, clinicians utilize the cognitive-evaluative dimension of pain through verbal rating scales, numerical rating scales, and visual analog scales. Verbal rating scales typically consist of a series of verbal pain descriptors in an ordered form (Jensen M.P., 2001). Numerical rating scales typically consist of a series of numbers ranging from 0 to 10 or 0-100 with the extreme numbers indicating the contrasting experience. Typically 0 is rated as no pain, and 10 (or 100) are rated as excruciating pain. Subjects or patients choose the number that best corresponds to their pain intensity in their 'current' state of mind. Unfortunately, this one-dimensional measure of pain cannot capture the complexity of the pain experience (de, Davies, & Chadury, 2000).

A typical visual analog scale (VAS) consists of a 10-cm horizontal or vertical line with the two end points labeled 'no pain' or 'excruciating pain'. The subjects or patients are instructed to place a mark on the 10-cm line that corresponds to their pain level in their 'current' state of mind. The distance, in centimeters, between the lower ends of the scale to the patient's marked point linearly translates to the numeric index of the pain severity. Some key advantages offered by VAS are minimal intrusiveness, greater sensitivity to detect intervention-based changes in pain, and conceptual simplicity (McMahon & Koltzenberg, 2005). However, VAS also has disadvantages. Namely, it has lower sensitivity and causes more errors compared to the verbal scale in elderly patients (Gagliese & Melzack, 1997). It is also more difficult to administer in patients with perceptual-motor problems, patients with comprehension disability, lack of comprehension ability such as neonates, and the VAS is impractical in clinical situations when immediate patient response may not be possible..

The major disadvantage with the numerical or visual scale is that they are one-dimensional, whereas the perception of pain is multi-dimensional. Brain imaging techniques allow a look at the brain noninvasively. This allows digging into the root-problem by attempting to identify the cause of pain, and allows an objective quantification of the pain experience.

3.6 Mapping Cognitive Aspects of Pain to BA 46 and BA 10

Previous sections briefly glimpsed over the cytoarchitecture of prefrontal areas whose role are least understood in the cognitive aspects of pain processing. In addition, important cognitive factors associated with pain identified from psychological studies were also discussed. Moreover, the current practical approaches of pain rating and its cognitive evaluative foundation was explored. However, we learned that this method is one-dimensional, and cannot probe into the root-cause of the problem. With this background, it is time to delve into the futuristic and promising neuroimaging work, where we map the cognitive aspects of pain to the brain area or network that mediates the induced perception.

3.6.1 BA 10 Role in Cognitive Aspects of Pain

Pain related responses in the PFC, specifically dorso-medial prefrontal areas, have received relatively little attention to date. Lesion studies in monkey reported that the dorso-medial PFC may lead to an attention related motor deficit as a function of aversion to painful stimuli (Lucchetti, Lui, & Bon, 1998). Thus, this area is considered to monitor and respond to stimuli according to their affective valence. Other reports have shown the involvement of the medial PFC in anticipation (Porro, et al., 2002), pain encoding, and pain intensity evaluation (Kong, et al., 2006).

The role of BA 10 in cognitive or affective aspects of pain is least understood. Recent fMRI reports have shown that BA 10 has the overlapping role of both cognitive evaluation of pain intensity and sensory encoding (Kong, et al., 2006). From a physiological perspective, Kong et al. also reported deactivation of the BOLD response in medial prefrontal areas under noxious thermal stimuli (Kong, et al., 2010). Deactivation in medial prefrontal areas was also reported under mechanical stimulation using fMRI techniques (Lui, et al., 2008). Pain related hypoactive state in BA 10 has been reported in patients with somatoform pain disorder (Gundel, et al., 2008).

3.6.2 BA 46 Role in Cognitive Aspects of Pain

Several recent PET and fMRI reports show that the DLPFC is involved in the perception of intensity and unpleasantness (Lorenz, et al., 2003). Specifically, the right DLPFC is responsible

for monitoring sensory comparisons and response selection (Oshiro, Quevedo, McHaffie, Kraft, & Coghill, 2009). The DLPFC also has a marked difference in the perception of pain between genders (Moulton, Keaser, Gullapalli, Maitra, & Greenspan, 2006). The key observation is that the dorsolateral area is shown activated in several experimentally induced thermal stimulation studies. Although it is not known if the DLPFC only activates under thermal stimulation, it has been shown that the right DLPFC is involved in the discrimination of pain intensity, a non-spatial aspect of pain (Oshiro, et al., 2009).

In Section 3.3 , the ability of self-efficacy in voluntary and conscious controlled form to attenuate pain-induced aversive emotional reactions was discussed. Recent fMRI studies have also shown mediation of right DLPFC in the analgesic effect of expected and perceived control over pain (Wiech, et al., 2006). During the task of cognitive evaluation of pain, it is not only important to understand the brain processing behind the pain rating, but also to understand the processing behind the performance of the task. Kong et al. (Kong, et al., 2006) in their fMRI study, have shown that the DLPFC is activated during the performance of the pain rating task.

Hence, advanced neuroimaging tools have facilitated our understanding of the prefrontal areas, specifically in the cognitive and affective aspects of pain. More work and cross-validation is necessary to further explore the functionality of this area for better clinical treatment.

CHAPTER 4

STEERING NIRS TOWARDS THE COGNITIVE ASPECTS OF PAIN

4.1 Background

Studies on pain processing and its mechanisms are no longer confined to animal models and lesion studies with the recent development of neuroimaging tools. However, this field has barely scratched the surface of possibilities. The scientific community still lacks a good understanding of the role played by several cortical areas, such as the prefrontal areas, during a painful experience. From an engineering perspective, we lack any single stand alone tool that is non-invasive and non-ionizing, which provides good spatial and temporal resolution simultaneously.

One emerging neuroimaging modality is functional near-infrared spectroscopy (fNIRS) (D. A. Boas, Dale, et al., 2004; Chance, Zhuang, UnAh, Alter, & Lipton, 1993; Villringer & Chance, 1997). Near-infrared (NIR) light scatters through biological tissue up to several centimeters, and is predominantly absorbed by hemoglobin chromophores for a certain 'optical window'. Due to light absorption and scattering, the outgoing signal intensity is attenuated. This attenuation is quantified by measuring the attenuation changes with respect to baseline at two or more wavelengths. The principles that govern diffuse reflectance experiments and light-interaction with tissue is detailed in Chapter 2.

Although functional MRI is the gold standard for non-invasive brain imaging studies, Huppert, et al. showed that fNIRS also provides a comparable measure of cerebral hemodynamics with an improved temporal resolution (Huppert, Hoge, Diamond, Franceschini, & Boas, 2006). Moreover, fNIRS can provide an objective measure for neurologic and psychiatric

applications comparable to fMRI, with an advantage of simplicity, portability, and insensitivity to motion artifacts (Irani, Platek, Bunce, Ruocco, & Chute, 2007). Becerra, et al. published the earliest report measuring signal changes using DOT in the frontal and sensory cortices for innocuous mechanical and noxious thermal stimulation (L. Becerra, et al., 2008). Their report was a proof of principle, showing that DOT can be utilized for pain related applications. From a scientific and technological standpoint, it was necessary to verify their work. The focus of this chapter is to steer the DOT technology towards objectively quantifying pain perception. In this guiding process, it is imperative to validate some of the fundamental concepts such as baseline stability, expectation values of concentration changes to verify HomER derived calculations, to validate the depth simulated by HomER, and to interpret the physiology of the observed results.

4.2 Becerra et al. DOT Study on Pain

The primary focus of the Becerra, et al. 2008 study was to explore the feasibility of DOT to detect changes in the brain under noxious pain stimuli. Figure 4-1 depicts the average response from selected channels in the frontal area, as reported by Becerra et al. (L. Becerra, et al., 2008). Note that the ΔHbO change on the contra-lateral side shows a biphasic response, where there is an early deactivation followed by activation in the late phase.

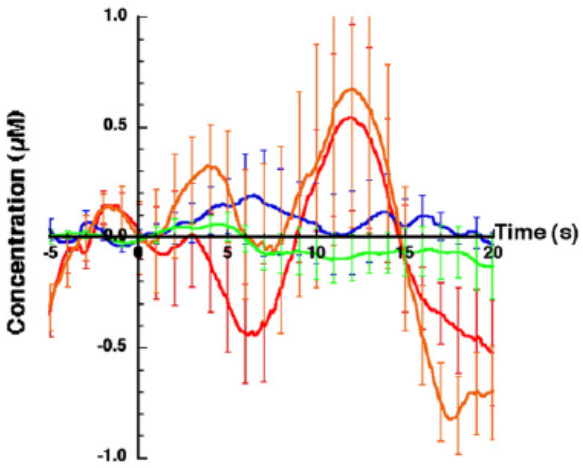

Figure 4-1: Average response ± std. error from the frontal area in response to 46℃ thermal stimuli from Becerra et.al. Note: Red: contra HbO; orange: ipsi HbO; blue: Contra HbR and green: ipsi HbR change (L. Becerra, et al., 2008).

In the subsequent chapters, innovative experimental methods and results for both mechanical and thermal noxious stimulation will be discussed. It is important to note that Becerra et al. incorporated an event-related protocol utilizing 46℃ thermal stimuli to induce pain.

4.3 Analytical Derivation for Pain-induced ΔHbO Magnitude Range

The primary focus of this dissertation will be to quantify pain perception using diffuse optical measurements. The details on quantification and related methodologies are described in Chapter 5. Extracting the ΔHbO concentration from the detected ΔOD (optical density) based on the Modified Beer-Lambert Law (MBLL) is the basis for fNIRS and fDOT. The theoretical framework for this extraction of chromophore concentration change is laid out in Section 2.3.4 .

The primary software utilized for this work, HomER (T. J. Huppert, et al., 2009), is detailed in Section 2.5 . This open-source software has been gaining popularity in the optical imaging field due to its user-friendly graphical interface. Becerra et.al (L. Becerra, et al., 2008) documented using HomER for their data analysis, and they quote a ΔHbO change in the range of -1 to 1 μM, as can be seen in Figure 4-1. Quantification of a statistically significant functional episode depends on the range of ΔHbO change. Thus, it is imperative to verify the observed ΔHbO ranges independent of HomER derived values. In order to verify the HomER derived ΔHbO range, pain-induced ΔHbO ranges will be analytically derived based on the MBLL theoretical framework. A randomly chosen random data set under mechanical noxious stimuli was imported into HomER, and a specific channel in the aPFC area was chosen, as shown in Figure 4-2(a). The raw ΔOD data was band-pass filtered at cut-off frequencies between 0.01 and 0.4Hz. The filtered ΔOD values obtained from the 830 nm and 690 nm sources are shown in Figure 4-2(b) and Figure 4-2(c) respectively.

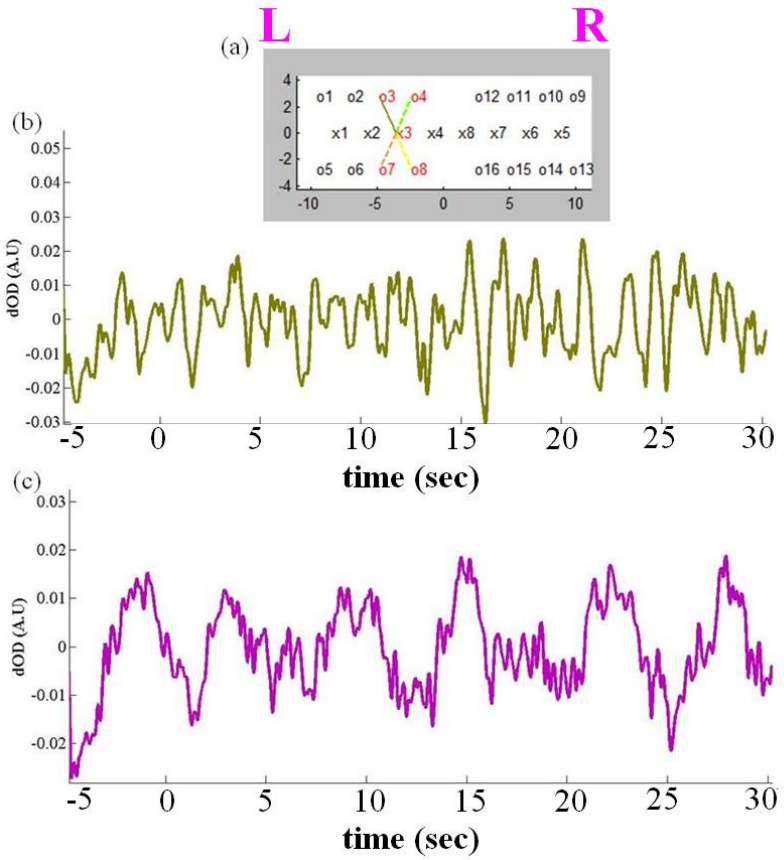

Figure 4-2: Filtered ΔOD changes from subject S01 from a channel in left hemispheric aPFC area. (a) Probe geometry from which solid line shows selected channel and dotted lines show disabled channels. (b) ΔO.D from 830nm (c) ΔOD from 690 nm. Note: L: Left hemisphere; R: Right hemisphere.

Consider the ΔOD value at an arbitrarily time point = ~16.3sec for both source wavelengths. This time point in the ΔHbO plot shows a peak. Subsequent quantification detailed in the specific aims relies on peak activation/deactivation. The ΔOD values at time point = 183 for each source wavelength are:

$$\Delta OD^{690} = -0.0163, \qquad \Delta OD^{830} = -0.0220 \tag{4.1}$$

Extinction coefficient values (ϵ) at each source wavelength and for each chromophore species are taken from Cope's dissertation (Cope, 1991):

$$\epsilon_{HbO}^{690} = 320\, M^{-1}cm^{-1}, \qquad \epsilon_{HbO}^{830} = 1050.8\, M^{-1}cm^{-1} \tag{4.2}$$

$$\epsilon_{HbR}^{690} = 1827.2\ M^{-1}cm^{-1}, \qquad \epsilon_{HbR}^{830} = 780.4\ M^{-1}cm^{-1} \tag{4.3}$$

The unit-less differential path length factor (B) is in the range of 5-6 according to (Frostig, 2009). For this derivation, the value of B = 6 was arbitrarily chosen. The probe geometry has a source-detector separation (L) of 2.5 cm.

$$\Delta C_1 = \left[\frac{1}{{\epsilon_1}^{\lambda_2}{\epsilon_2}^{\lambda_1} - {\epsilon_1}^{\lambda_1}{\epsilon_2}^{\lambda_2}}\right] \cdot \left[{\epsilon_2}^{\lambda_1}\frac{\Delta OD^{\lambda_2}}{B^{\lambda_2}L} - {\epsilon_2}^{\lambda_2}\frac{\Delta OD^{\lambda_1}}{B^{\lambda_1}L}\right] \tag{4.4}$$

$$\Delta HbO = \left[\frac{1}{\epsilon_{HbO}^{830}\epsilon_{HbR}^{690} - \epsilon_{HbO}^{690}\epsilon_{HbR}^{830}}\right] \cdot \left[\epsilon_{HbR}^{690}\frac{\Delta OD^{830}}{BL} - \epsilon_{HbR}^{830}\frac{\Delta OD^{690}}{BL}\right] \tag{4.5}$$

$$\Delta HbO = \frac{1}{(1050.8\ M^{-1}cm^{-1})(1827.2\ M^{-1}cm^{-1}) - (320\ M^{-1}cm^{-1})(780.4\ M^{-1}cm^{-1})} \cdot \left[(1827.2\ M^{-1}cm^{-1})\frac{-0.0220}{6 \cdot 2.5\ cm} - (780.4\ M^{-1}cm^{-1})\frac{-0.0163}{6 \cdot 2.5\ cm}\right] \tag{4.6}$$

$$\boxed{\Delta HbO = -1.09673 \times 10^{-6}\ \mathrm{M}} \tag{4.7}$$

Equation 4.7 shows the resultant ΔHbO change obtained from the analytical derivation utilizing MBLL. Note that the resultant ΔC is in the μM range, which corroborate Becerra's results shown in Figure 4-1. Thus, HomER derived ΔC values are reliable, and will be used for quantification throughout the specific aims.

4.4 Resting-state Baseline Stability

In functional brain imaging studies, the experiments are typically designed with a contrasting resting-state baseline, interspersed with a task-induced activity (Huettel Scott A, 2008). This allows the measurement of relative changes in the hemodynamic response due to a task. In the conscious state of mind, brain activity and the physiology is continuous, and cannot be in an absolute zero state. Thus, the experimental goal is to induce a change, or perturbation, in the neuronal and subsequent vascular response. This change results in an activation or deactivation of the measured hemodynamic response with respect to resting-state baseline. Typically, a resting-state baseline is measured when the subject or patient is resting comfortably

in a supine or reclined position, eyes closed, without a task or induced stimuli, whereas the baseline refers to the period of time prior to stimulation in task or stimulation-based protocols.

It is clear that the experimentally measured baseline for a stimulus-based study must be stable. In order to validate the stability of fNIRS acquired baseline, two measurements of resting-state baseline were taken for approximately 6 minutes. The measurements were obtained from the prefrontal area. The acquired data was down sampled to 25 Hz. The raw data was pre-processed to reduce physical and physiological artifacts using a band-pass filter with cut-off of frequencies [0.01 - 0.4] Hz. The filtered ΔHbO data from the aPFC area was parsed into blocks (each block of 35 sec long) and then block-averaged. The raw and block-averaged resting-state ΔHbO for the two subjects are shown in Figure 4-3 and Figure 4-4 respectively.

Qualitative inspection of filtered ΔHbO data from Figure 4-3(a) and Figure 4-4(a), show consistent concentration changes in the order of magnitude of 10^{-5} M. Even during the resting-state, the brain is involved in some processing and hence we observe some ups and downs in the entire acquisition of 6 minutes. The baseline can be quantitatively analyzed by block averaging several blocks (each block of 35 sec long) obtained by parsing out the 6 minutes of data as shown in Figure 4-5. The rationale was to maintain consistency with the pain-protocol design of 35 sec functional blocks, detailed in Chapters 5, 6, and 7. Note that the ΔHbO concentration change for subject-1 as shown in Figure 4-3(b), and subject-2, as shown in Figure 4-4(b), has an order of magnitude of 10^{-6}. The plots show the average response from 3 channels covering the anterior prefrontal area. Error bars denote the standard deviation across the 3 channels. In order to be consistent with the data analysis for specific aims of this dissertation study, 4 channels were initially chosen from the aPFC area. However, visual inspection of raw data displayed one noisy channel which was disabled, resulting in an average over 3 channels. From diffusion theory, choosing only one channel is not an optimal approach because the SNR from one channel is suboptimal. The sensitivity to detected photons or the SNR can be increased by averaging across neighboring channels. The fluctuating error bars in Figure 4-5 show that a long resting state baseline measurement cannot be expected to remain stable due to spontaneous neuronal activity.

Spontaneous neuronal activity is a new direction that neuroscientists have undertaken in the recent years. Functional MRI studies have shown that fluctuations in BOLD signals correlate with underlying slow fluctuations in the neuronal signal; particularly the local field potential in the gamma band (Shmuel & Leopold, 2008). Essentially, the spontaneous brain activity reflect the coherent neuronal activities during resting state that are topologically organized both at spatial and temporal scales supporting global computation and information integration in the absence of specific stimuli (He, et al., 2009). These results show that resting-state baseline studies are helpful for scientific hypothetical testing that involves spontaneous brain activity and associated functional connectivity between different cortical and sub-cortical areas in the absence of any stimuli. However, studies that involve hypothetical testing for significant relative changes in response to a stimuli, such as the one in this dissertation study, the protocol design for baseline (acting as no-stimuli or contrasting condition), should be in the range of seconds such that the quantification for relative changes are reliable.

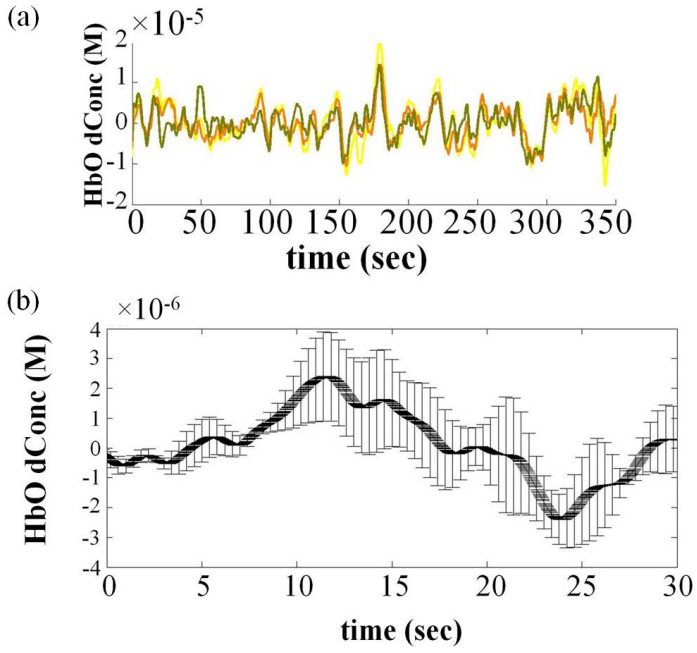

Figure 4-3: Resting-state baseline measurement from subject-1. (a) Filtered HbO response from 3 neighboring channels from the right aPFC during the ~ 6minute long resting state condition. (b) Block averaged HbO response from (a) where error bars show the standard deviation across the 3 channels.

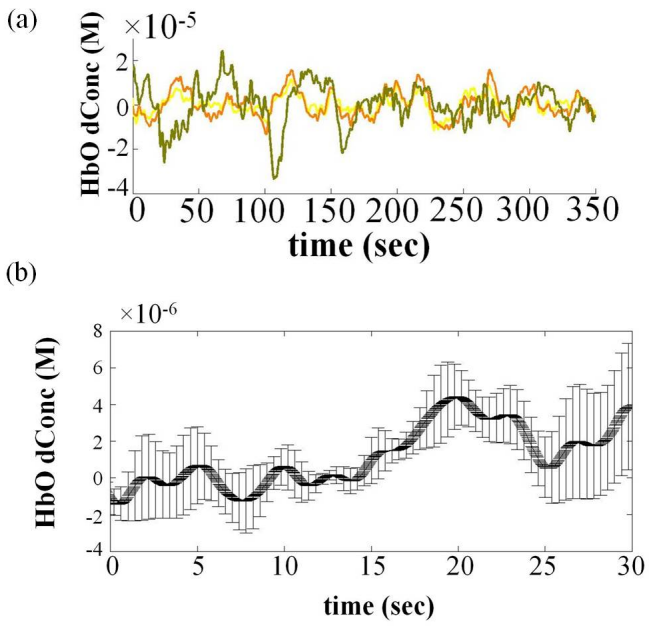

Figure 4-4: Resting-state baseline measurement from subject-2. (a) Filtered HbO response from 3 neighboring channels from the right aPFC during the ~ 6minute long resting state condition. (b) Block averaged HbO response from (a) where error bars show the standard deviation across the 3 channels.

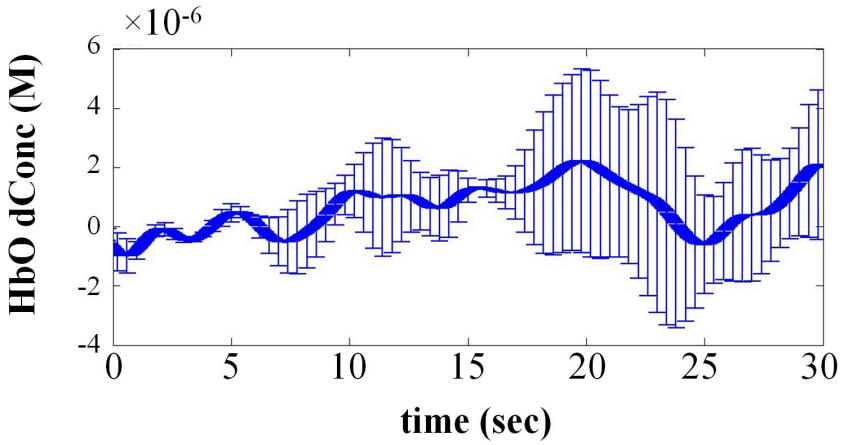

Figure 4-5: Group averaged (*N*=2) resting-state baseline measurement from the above two subjects. Note: error bars show the standard deviation across the 2 subjects.

4.5 Evaluation of 'Depth' Setting in HomER using a Laboratory Phantom

Unlike MRI, DOT lacks spatial specificity and depth sensitivity. The software package HomER allows image reconstruction of the hemodynamic response to be carried out at a user-

chosen depth. However, it is imperative to test if the real depth is truly depicted. In order to know the approximate depth of a specific cortical area, a human brain atlas must be surveyed. Atlas based depiction (Mai, Assheuer, & Paxinos, 1997) gives a classical approach of correlated studies between medical images and post mortem tissue *in situ*. Atlas based depiction also includes photographs of a cross-sectional brain and MRIs of the same brain *in vitro* with *in vivo* images from living individuals. Based on (Mai, et al., 1997), Brodmann area 9 and 10, which are specific areas of interest for this study, fall within the 2cm depth that a near-infrared diffuse optics experiment can detect.

In order to evaluate the quality of HomER generated fNIRS images, experiment based on a depth imaging protocol was undertaken using laboratory phantom. A high density optical imager (DYNOT or DYnamic Near-Infrared Optical Tomography) that functions on the same principle of continuous-wave diffused optics was used for this experiment. DYNOT (NIRx Inc, Gen Head, NY) incorporates laser sources that emit light at wavelengths of 730 and 850nm.

A thin capillary glass tube with a diameter of ~1mm was covered with a black electrical tape, acting as an absorbing object as shown in Figure 4-6(a). It was then secured in a holder attached to a vertically moving scale. An intralipid solution with reduced scattering coefficient of 10 cm^{-1} was freshly prepared in the container. The taped glass tube was placed in the container at an angle of ~45º. Finally the probe was placed on the surface of the intralipid solution, as shown in Figure 4-6(b). Figure 4-6(c) shows the dense array optodes geometry that had a rectangular geometry with a 1cm separation between the optodes along the *x*- axis and a 2cm separation along the *y*- axis.

Figure 4-6: Experimental setup to study the depth-dependent fNIRS based image reconstruction based on HomER. (a) A thin black-taped capillary tube was placed at an angle of ~45º (b) positioning of a high density probe array for the imaging experiment (c) probe geometry for the measurements; optode separation of 2 cm along the *x*-axis and 1cm along the *y*-axis.

Figure 4-7 shows the simple protocol designed to carry out depth imaging. Initially, the taped glass tube is placed at the bottom of the intralipid filled container (5cm). This is considered as the 'baseline' measurement since the sensitivity at that depth is assumed to be poor. While using a timer, the capillary tube is manually raised to desired depths that simulate 'activation' measurements. The measured data was imported into HomER for pre-processing and reconstruction of the images.

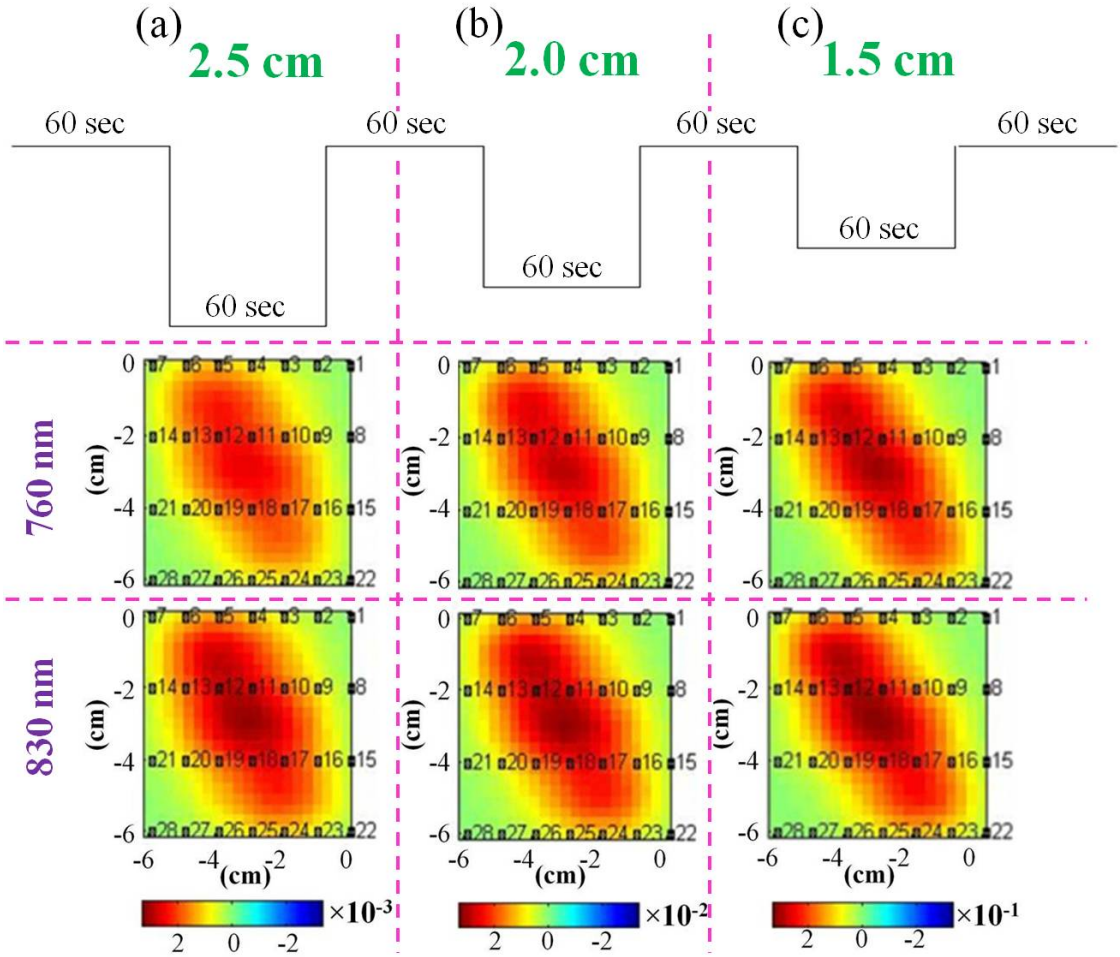

Figure 4-7: A simple protocol to probe depth of the embedded black absorber. The time period to collect the data for the baseline and activation at each specific depth were designed for 60 sec. The three different depths measured were 2.5, 2, and 1.5 cm. Backprojection based reconstructed images at different depths are shown in: (a) 2.5 cm (b) 2 cm (c) 1.5 cm. Note: the color bar indicates absorption level. Red indicates higher absorption while blue indicates the opposite.

Figure 4-7 shows the backprojection-based ΔOD reconstructed images obtained for both the wavelengths at different depths. Since the capillary tube was not filled with blood, Hb or HbO concentration changes were not extracted. The reconstructed images for 760nm show that the magnitude of ΔOD drops as a function of increasing depth. In other words, as the depth increases, the magnitude of ΔOD decreased by a factor of 10. However, the reconstructed images at the longer wavelength of 830nm do not show clear differences between different depths.

Although in realistic human measurements, we do not know the true depth for absorbing chromophores, a depth setting at 2cm will be chosen for all the specific aims of this dissertation work. The reason for not choosing 1.5 cm as the depth parameter was that it leads to closer proximity to the scalp. The physiological changes in the scalp might possibly corrupt the cortical hemodynamic activity of interest and hence reducing the SNR of interest.

However, it has to be noted from the above discussion that the depth parameter in HomER was set at the true depth of the absorber. Although it would be scientifically meaningful to explore the outcome for depth parameter set at different values other than the true depth, given the nature of diffuse optics theory and the limitations of reconstruction algorithms, we assume that it would not add any valuable information in terms of depth sensitivity.

The theoretical aspects of MBLL applied to biological tissues were described in section 2.3 . In the context of DOT, an important parameter of interest is the differential path length correction factor (B), as it accounts for scattering behavior of photons propagating in the tissue. The images shown in Figure 4-7 represent the OD changes at different depths. For the purposes of ΔOD quantification, the path length factor does not come into picture. However, since our interest lies in quantification for hemoglobin concentration changes, based on MBLL theory, the path length correction factor becomes critical for accurate quantification for concentration changes within a tissue volume. For image reconstruction, the B factor eliciting the spatially varying absorption and scattering aspects are incorporated into linear models such as Born or Rytov approximations. Image reconstruction algorithms such as the backprojection algorithm, is based on Born or Rytov approximations. As discussed in section 2.6.3 , typical linearized

reconstruction algorithms such as backprojection suffer from under-determined and ill-posed problems. Furthermore, a previous simulation study (D. Boas, 1997) has shown that the accuracy for quantification from images based on first order Born or Rytov approximation reduces as these algorithms compromise the accuracy compared to rigorous analytical solutions.

In general for diffuse optical imaging, the 2-D based backprojection and regularized inversion algorithms are not sensitive to the depth accuracy. These algorithms provide a lateralized 2-D slab image at an artificially set depth. Moreover, these algorithms result in absorption sensitivity being pulled over to the superficial areas. Hence in recent years, researchers have come up with advanced and improvised techniques to enhance the sensitivity of absorption at different depths through laboratory phantoms experiments (Niu, Tian, Lin, & Liu, 2010).

4.6 Invasive Optical Study by Devor et al. to Investigate Negative HbO Response

It is challenging to explore and understand the underlying physiology via non-invasive methods. Thus, invasive studies are carried out on animals to help scientists and researchers understand the mechanisms of observed brain activity.

In the BOLD fMRI community, an intriguing mystery has been the negative BOLD response. The earliest seminal work in this direction was shown in (Shmuel, et al., 2002). Although, this ground breaking work provided an experimental understanding of the negative BOLD response, 2-3 plausible physiological causes were not disentangled in their study. Devor et al. took an aggressive step to explore the negative BOLD response aspect further by using multimodal optical techniques on rat's somatosensory area and electrically stimulating the rat's forepaw. The key results of their work that allow physiological interpretation of the negative BOLD response are shown in Figure 4-8 and Figure 4-9.

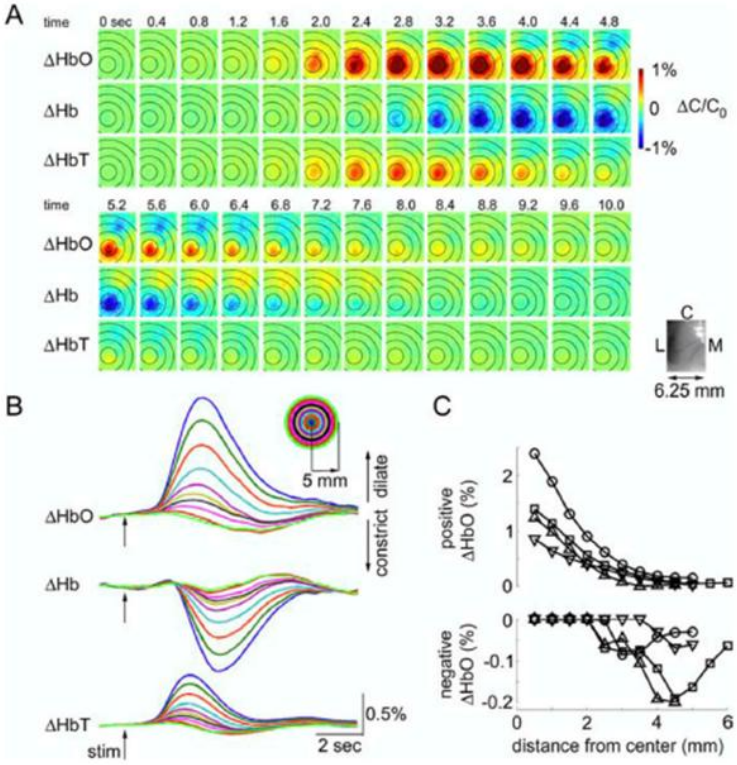

Figure 4-8: The figure is reproduced from the journal article (Devor, et al., 2007). See the text for a brief description. For details please refer to the respective figure caption from the same journal article.

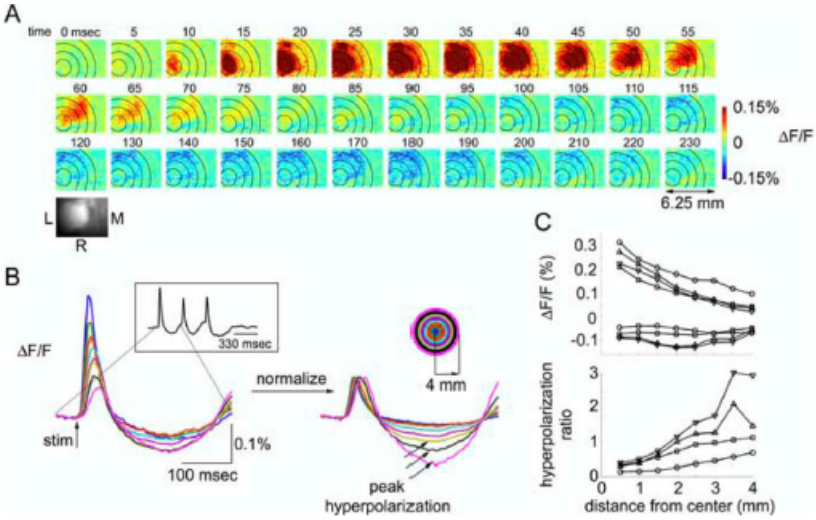

Figure 4-9: The figure is reproduced from (Devor, et al., 2007). See the text for a brief description. For details please refer to the respective figure caption from the same journal article.

Figure 4-8(A) shows Devor et al.'s spectroscopic measurements, depicting a center-surround antagonistic pattern in ΔHbO. At the center there is an increase in ΔHbO, while at a distance of 4 mm from the center; there is a negative ΔHbO, as shown in the bottom graph of Figure 4-8(c). Devor also carried out two photon microscopy to measure the arterial diameter changes and observed vasodilation during ΔHbO increase and vasoconstriction during negative ΔHbO. Figure 4-9 shows Devor's voltage-sensitive fluorescence dye measurements of neuronal activity. Figure 4-9(A) shows the center-surround antagonistic pattern, where increased ΔF/F (higher activation) was observed in the center due to depolarization, while at a distance of 4mm, hyperpolarization was observed.

The above results from Devor et al.'s work show that specific neurotransmitter and neuropeptide release due to synaptic transmission initiates arterial dilation and constriction, where the neuronal activity can be differentially engaged in the center and in the surrounding cortical columns. Their multi-modal measurements show that an evoked decrease in ΔHbO could possibly be due to arterial constriction and inhibitory poly-synaptic activity.

4.7 Hypothesis and Specific Aims

The following section describes the goals and specific aims to identify correlates of pain from cortical responses to nociceptive inputs by using functional Near InfraRed Spectroscopy (fNIRS). The *hypothesis* of this study is that **functional Near InfraRed Spectroscopy (fNIRS) has the feasibility to identify neural correlates between the hemodynamic response in the pre-frontal cortex and pain perception under mechanical and thermal stimulations**. The *specific aims* are:

Specific Aim 1: Quantify neural correlates between oxy-hemoglobin concentration changes and cognitive evaluation of pain intensity under noxious mechanical (pinch) stimulation. Using a continuous wave (CW) fNIRS imager, measurements will be collected from the subject's pre-frontal cortex. The mechanical pain is induced on healthy, right-handed subject's non-dominant volar forearm, followed by pain rating.

Specific Aim 2: Quantify neural correlates between oxy-hemoglobin concentration changes and cognitive evaluation of pain intensity under noxious thermal stimulation. Using CW fNIRS imager, measurements will be collected from the subject's pre-frontal cortex. The pain is induced on right-handed, healthy subject's dominant volar forearm by thermal stimulation at 48℃, followed by pain rating.

Specific Aim 3: Investigate the detectability of fNIRS and the role of pre-frontal cortex to differentiate pain intensity. Using CW fNIRS imager, measurements will be collected from the subject's pre-frontal cortex. The pain is induced on right-handed, healthy subject's dominant volar forearm by thermal stimulation at 41℃ and 48℃ sep arately, each followed by pain rating.

The primary interest of a bioengineer is to develop and enhance the existing technology for a better scientific understanding of the underlying biological phenomena that transform and extend directly to clinical applications. The above hypothesis and specific aims are laid out from a technical perspective to explore the feasibility of the fNIRS technology to objectively quantify pain perception in normal healthy subjects. However, the *scientific working hypothesis for this study is that a positive/negative correlation exists between subjective pain ratings and quantified HbO changes measured from the pre-frontal areas in healthy normal subjects.* In order to methodically test the above scientific hypothesis for each of the specific aims, the sub-hypotheses and associated statistical methods, results and discussion for each of the specific aims are laid out in Chapters 5 -7.

CHAPTER 5

NEURAL CORRELATES OF NOXIOUS MECHANICAL PAIN STIMULATION

5.1 Current Understanding

Exposing subjects to painful stimuli while imaging brain function is a new technique of exploring pain. Becerra et al. (L. Becerra, et al., 2008) are the first to date to test the feasibility of measuring brain activity using fDOT in response to applied thermal pain stimulation. However, in clinical settings, patients are more likely to be exposed to mechanical pain, such as invasive surgical procedures, rather than thermal pain. Since these surgical procedures are often performed under anesthesia, this could result in pain which has not been quantified. Moreover, research on mechanical pain stimulation on animal models has proven difficult since design of cognitive behavioral paradigms to obtain pain rating is complicated due to the animal's inability to communicate verbally. Becerra, et al. (L. Becerra, et al., 2008) reported negative contra lateral activation of HbO in frontal areas due to painful thermal stimulation. In addition, (L. Becerra, et al., 2008) focused only on changes in HbO in response to pain, and did not correlate HbO changes to behavioral measures.

The motivations of this specific aim are multipronged. First, the results reported in (L. Becerra, et al., 2008) are validated using mechanical stimulation, rather than thermal stimulation. Secondly, ΔHbO is quantified, followed by correlation of the quantified ΔHbO parameters with subjective pain rating. This is carried out to identify specific (anterior and dorsolateral) pre-frontal areas' role in cognitive evaluation of pain perception.

5.2 Sub-hypotheses

The major specific aim undertaken in this chapter is to quantify neural correlates between oxy-hemoglobin concentration changes and cognitive evaluation of pain intensity under noxious mechanical (pinch) stimulation. In order to methodically investigate the above specific aim, it is broken down in to sub-hypotheses as follows:

1. Within the selected subject pool, pinch stimulation will cause HbO change in the **anterior prefrontal cortex (BA 10)** during the **early (0.1 to 12sec)** and **late phase (12.1 to 25sec)** of the pinch stimulation**.** Pinch-induced HbO changes are significantly different from the **baseline (-5 to 0sec)** HbO changes.
2. During the **early phase (0.1 to 12sec)** of pinch stimulation**,** the mean estimates from statistical testing for sub-hypothesis 5.2.1 show HbO deactivation in both left and right hemispheric **anterior prefrontal cortex**. The HbO-derived parameters **(PI and FWHM)** from the early phase have a **significant correlation** with the behaviorally measured **pain rating**.
3. **HbO-quantified PI and FWHM** from both the left and right hemispheric **anterior prefrontal cortex** reflect the cognitive evaluation of pain perception. They are **not affected by anticipation** in response to the first pain stimulus.
4. Within the selected subject pool, pinch stimulation will cause HbO change in the **dorsolateral prefrontal cortex (BA 46)** during the **early (0.1 to 12sec)** of the pinch stimulation**.** Pinch-induced HbO changes are significantly different from the **baseline (-5 to 0sec)** HbO changes.

5.3 Methods

In this section and affiliated sub-sections, the details on subjects, experimental protocol design, data acquisition, and data analysis for this specific aim are described.

5.3.1 Subjects

Eight healthy volunteers were recruited through local advertisements. All the subjects chosen were right handed. The subject group comprised of 6 males and 2 females in the age

range of 20-35 years. Subjects with a history of neurological trauma and psychiatric or neurological disorders were excluded. Subjects who were on any psychoactive or pain medications were also excluded from the study. Written informed consent was obtained from all subjects as per the guidelines set by the University of Texas at Arlington Institutional Review Board, who reviewed and approved this study.

5.3.2 Experimental Protocol

The block design paradigm is shown in Figure 5-1. Prior to the experiment, the area for pain stimulation was marked out on the subject's non-dominant volar forearm, at the center of subject's arm length, between elbow and wrist. The subject was asked to look at this marked area prior to starting the experiment. They were then instructed to close their eyes during the experiment and focus their attention on the marked area. The pinch stimulation was induced using a sterile plastic bag clip, which caused pain without inducing an allergic skin reaction. The operator practiced the pinching action with the bag clip several times prior to the experiment to ensure consistency of pain induction. The protocol consisted of a 30 second pre- and post baseline. Each functional block comprised of 10 sec mechanical (pinch) stimulation, followed by 25 sec of recovery period. In total, the entire protocol comprised of 8 functional blocks that lasted for 340 sec. For analysis purposes, in each of the 10+25=35 sec blocks, the last 5 seconds is considered as the baseline for the subsequent block, except for the eighth block. Hence, the length of the 'functional' block comprises 30 seconds. The 8 block design provided a balance between sufficient statistical power and the subject's comfort level. The stimulation period of 10 seconds causes an 'early response' to the pain, while the resting period of 25 seconds explores the 'late response' to the pain. Immediately following the protocol, subjects were asked to rate the pain intensity of the stimuli in a Likert 11-point scale (0: no pain, 10: excruciating pain).

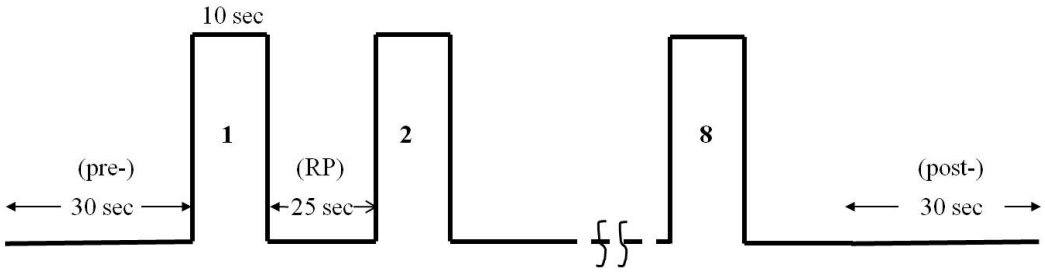

Figure 5-1: A schematic for block-design paradigm. The protocol incorporated 8 blocks of 10 sec stimulation and 25 sec recovery period (RP). The protocol also incorporated a 30sec pre- and post baseline.

5.3.3 Data Acquisition

Figure 5-2 shows the probe design and experimental setup for this study. The optical data was acquired using a multichannel CW optical imager (CW-5, TechEn Inc., Milford, MA) that emits two wavelengths of light at 690 nm and 830 nm. More details on this equipment are described in Chapter 2 and in (Franceschini, et al., 2006). The probe geometry comprised of 8 pairs of sources and 16 detectors, with a nearest source-detector separation of 2.5 cm. Source fibers delivering the 690 nm wavelength were paired with those emitting 830 nm, which together formed one “optode”. The detailed calibration procedures required for CW-5 is described in section 2.4.2 . The instrument was tested for any necessary calibration procedures, such that the acquired signals were in the desired range before carrying out human measurements. The probe was secured to the subject’s forehead using Velcro, with the bottom row detectors placed 0.5 cm above the eyebrow line to avoid muscle movement artifacts. The hair covering the subject’s forehead scalp area was brushed aside before placing the probe on the subject’s forehead. After placing the probe on the subject’s forehead, remaining strands of hair, if any, blocking the optodes were brushed aside to obtain cleaner signals. The probe mounted on the forehead was finally wrapped with a black head band to secure it further at the subject’s comfort level, and to minimize interference from any extraneous ambient light sources. Subjects sat comfortably in a reclined position during the experiment. After the initial setup, all the room lights were turned off and the gain settings for each channel were calibrated to the desired range.

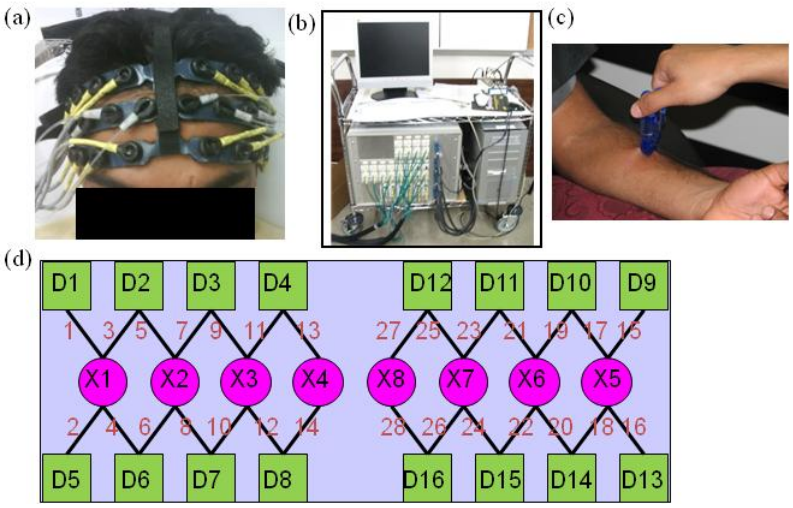

Figure 5-2: Experimental setup. (a) Probe placement on the subject's forehead. (b) CW-5 imager (c) pinching action at the marked area on non-dominant volar forearm. (d) Probe geometry. Note: pink circles: sources; green boxes: detectors; thin black lines: channels.

5.3.4 Data Analysis

5.3.4.1 Pre-processing

Data analysis was carried out using the open source software HomER (T. J. Huppert, et al., 2009), which is supported by the MATLAB (Mathworks, Natick, MA) platform. The data pre-processing incorporated two basic steps: (i) Filtering and (ii) Averaging of the ΔOD signals. Each individual data set was filtered using a low pass frequency cutoff at 0.4 Hz and high pass cutoff at 0.01 Hz to minimize physiological noise. Further, the highest variance (up to two) components were filtered off using Principle Component Analysis (PCA) technique. PCA primarily minimizes global artifacts due to motion, and has proven useful in other functional NIR studies (Franceschini, et al., 2006). If visual inspection of epochs of data showed noise on more than one channel that was not removed after the filtering process, then those specific noisy epochs (maximum up to two epochs) were manually disabled.

5.3.4.2 Clustered-wise Analysis

In the clustered-wise analysis, several neighboring channels are spatially grouped together to enhance the SNR for reliable results (Zhang, et al., 2011). In this study, all the

channels except for those covering the area of interest were manually disabled in the HomER software. For the aPFC area, 4 channels were enabled one each side of the probe geometry (2 sources, and 2 detectors), as can be seen in Figure 5-3(a). Clustered channel analysis of the DLPFC area consisted of enabled channels from sources 1 and 5 (1 sources and 4 detectors on each side of the probe geometry), as shown in Figure 5-3(b), disabling the remaining channels. Figure 5-3 shows the 4 channels covering ipsi aPFC (shown by red) and contra aPFC (shown by blue) that were spatially averaged for each individual data set. Similarly, ipsi DLPFC (shown by red) and contra DLPFC (shown by blue) were spatially averaged for each individual subject. For each functional block, 5 seconds before the stimulation is defined as the 'relative' baseline for that functional block. The functional block is set to 30 sec, which comprises the 10 sec stimulation followed by a 20 sec resting period.

Spatial averaging is followed by temporal averaging across the 8 functional blocks to obtain one averaged temporal response. This temporal response consists of a 5 sec averaged baseline and 30 sec averaged activation response for each individual subject. Each subject's block-averaged temporal response is group-averaged to obtain a grand-average temporal response (*N*=8). The grand-average temporal response is shown in Figure 5-6(b) for aPFC.

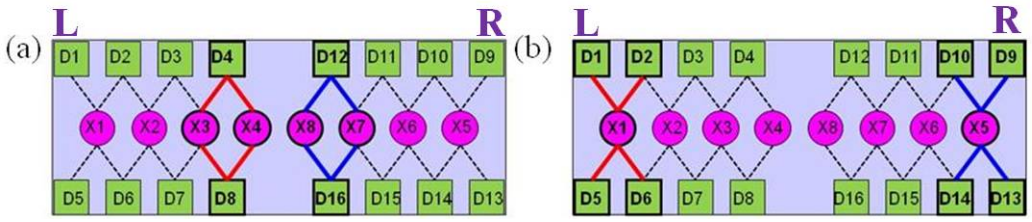

Figure 5-3: Clustered-wise channels covering (a) anterior PFC where solid red lines: ipsi aPFC (that is X3-D4, X4-D4, X3-D8, X4-D8) and solid blue lines: contra aPFC (that is X8-D12, X7-D12, X8-D16, X7-D16) (b) dorsolateral PFC where solid red lines: ipsi DLPFC (that is X1-D1, X1-D2, X1-D5, X1-D6) and solid blue lines: contra DLPFC (that is X5-D10, X5-D9, X5-D14, X5-D13). Note: Pink circles: sources; green boxes: detectors; dashed lines: disabled channels.

5.3.4.3 Quantification for HbO-derived Parameters

The temporal ΔHbO data, initially processed in HomER, was exported to MATLAB for quantification. Figure 5-4 is a graphical sketch of the HbO response as a function of time. Depicted in this cartoon are the HbO-derived parameters that will be extracted from the

hemodynamic response. Each individual data set was divided into an 'early' (0.1-12 sec) and a 'late' (12.1-25 sec) response. Separate extraction of the HbO-derived parameters is performed for the early and late response. The time to peak (ttp) was calculated from time 0, when the stimulation was initiated, to the time of the maximum peak/dip (that is maximum concentration change in either positive or negative direction with respect to the baseline) of the HbO response. This is shown by the segment AB for the early phase and the segment AF for the late phase in the Figure 5-4 below. The peak intensity was derived as the signed absolute maximum value with respect to the average preceding baseline as shown by segments EB and FI for early and late phase respectively. Finally, full-width half maxima were derived with respect to the peak intensity value as shown by segments CD and FI for early and late phase respectively. The MATLAB code used for the quantification purpose is shown in Appendix B.

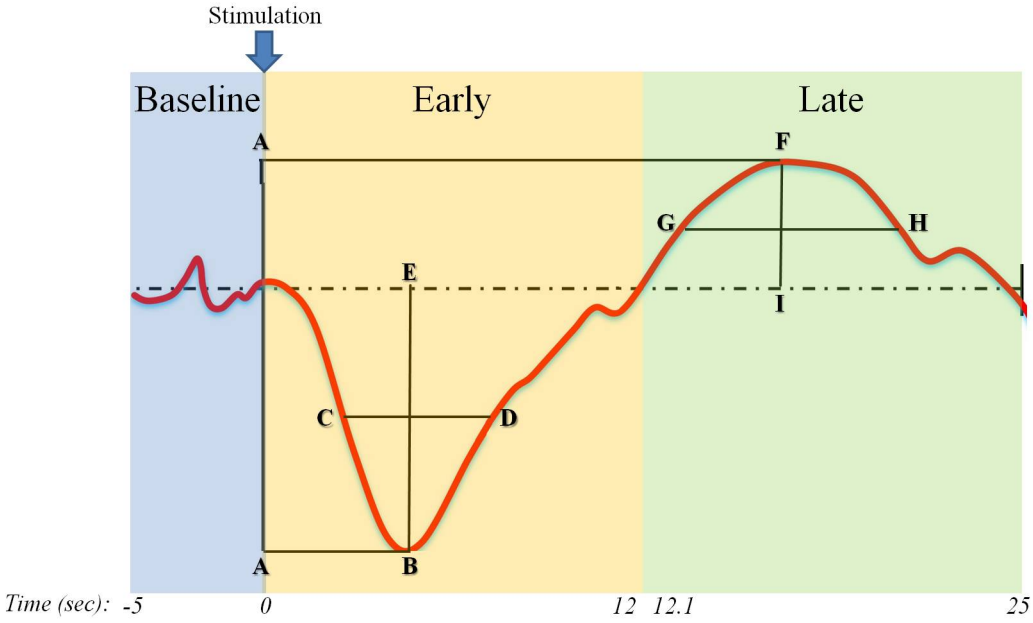

Figure 5-4: Graphical sketch describing the quantification steps on ΔHbO temporal data. The blue shade denotes the baseline (-5 to 0sec); beige shade denotes the early phase (0.1 to 12 sec) and the green shade denotes the late phase (12.1 to 25sec). The segments shown within the early phase are AB: time to peak (ttp); CD: full-width half maxima (FWHM); EB: Peak Intensity (PI). The segments shown within the late phase are AF: ttp; GH: FWHM; and FI: PI.

5.3.4.4 General Linear Mixed Model

In functional brain imaging, only relative changes can be quantified with respect to the baseline. Thus, it is imperative to test for the significance of activation/deactivation with respect to the baseline. Typically, significance of activation or deactivation with respect to the baseline is carried out using standard t-test (Tian, Chance, & Liu, 2009; Tian, Sharma, Kozel, & Liu, 2009) in the functional NIRS field.

Due to the nature of simultaneous and repeated measurements on each subject, an inherent temporal and spatial correlation may exist between the acquired data points. Since univariate tests such as t-test requires independence and identical distribution of the observations, t-test would not be an optimal method to statistically test the significance of stimulus-induced changes. Thus an advanced statistical approach such as linear mixed modeling was incorporated to test for the significance between the pain-induced and baseline (no-stimulation) HbO responses measured from the two cortical areas. Thus, for a repeated measure's design which measures the variables of interest more than once on each subject, the model accounts for the correlation among the repeated measures on the same subjects. Thus, the parameter estimates and the estimates of their standard errors are more accurate and thus the significance tests are more accurate. A brief theoretical description of the principle behind general linear mixed modeling is described below.

General Linear Mixed models are essentially linear statistical models that are effective to explore the variability in heterogeneous data. Mathematically, this model is a generalization of combined ANOVA, variance component model (VARCOMP) and regression model (Demidenko, 2004). In classical statistics, the observations drawn from a subject are assumed to be identical and independently distributed. However, mixed modeling can be extended to complex and multi-level data such as the one in this study where we have repeated measurements from each subject in which we assumed that the data points can be correlated within a cortical area and also between the cortical areas. The generalized equation for a linear mixed model is given by:

$$Y = X\beta + Z\gamma + \varepsilon \qquad 5.1$$

In the above equation, *Y* denotes the HbO measurements, X is a matrix of fixed effects, Z is a matrix of random effects and ε is a random error term. For our purposes, Z is zero and there is no matrix of random effects. That is, General Linear Mixed Models for repeated measures are models of the form

$$f\left(\overline{x_{ij}}\right) = \beta_0 + \beta_1 x_{ij1} + \beta_2 x_{ij2} + \Lambda + \beta_p x_{ijp} + \varepsilon_{ij} \qquad 5.2$$

where $f\left(\overline{x_{ij}}\right)$ represents the value of the dependent variable corresponding to the values of the independent variables $\overline{x_{ij}} = \left(x_{ij1}, x_{ij2}, \mathrm{K}\ , x_{ijp}\right)$, where *i=1*,……, *m* is the subject while *j=1*,….,*p* is the observation within each subject. The process of fitting the mixed model estimates the parameters, $\beta_0, \beta_1, \Lambda\ , \beta_p$, and their standard errors. The model has a deterministic part

$f\left(\overline{x_{ij}}\right) = \beta_0 + \beta_1 x_{ij1} + \beta_2 x_{ij2} + \Lambda + \beta_p x_{ijp}$ and a random part ε_{ij}. The deterministic part is used to estimate the value of $f\left(\overline{x_{ij}}\right)$ for specific values of $\overline{x_{ij}} = \left(x_{ij1}, x_{ij2}, \mathrm{K}\ , x_{ijp}\right)$. The estimates of $\beta_0, \beta_1, \Lambda\ , \beta_p$ and their standard errors are also used to construct the F-statistics and t-statistics which are used to perform the significance tests which determine which independent variables account for variation in the dependent variable.

Scientifically, the interest of this study was to make inferences of pain-induced changes only within the subject population recruited for this study. This essentially accounts for only the *fixed effects* of the stimulation-induced changes (Friston, Holmes, Price, Buchel, & Worsley, 1999). From a mathematical perspective, an important assumption for fixed effect model is that the βs are non-random. However, if β is assumed to be random, then the "random effect" comes into the model which is shown by γ and associated design matrix *Z* in the above Equation 5.1. This scientifically translates to introduction of subject-to-subject variability within the stimulus-induced responses. In other words, the random effects would account towards inferences that generalize to the larger population from which the sample subjects were randomly chosen for a specific study (Friston, et al., 1999). In the light of a small subject pool recruited for this study, our focus was limited to draw inferences only in respect to the randomly selected subject pool, which lead us to the fixed effects model.

In a general linear mixed model, the variance of the observations (*V*) is composed of two parts: (a) the residual variation that is manifested in the distribution of the model errors (that is ε's). In other words, $Var(\varepsilon) = S$ is typically referred to as the within-subject variation. (b) the random effect variation associated with Z. Let us denote the random effects as δ and $Var(\delta) = D$ that reflects the between-subject variation. Hence the variance of the observed response (V) is given by:

$$V = ZDZ' + S \qquad 5.3$$

Typically various mathematical assumptions are assumed for the matrices *D* and *S* depending on the structure of the data. Since the focus of this study was to investigate the fixed effects, the covariance matrix *D* associated with random effects is assumed to be zero. As far as the covariance matrix *S* is concerned, *compound symmetry* structure was undertaken in this study. This structure assumes that the observations within and between the clusters are equally correlated irrespective of the spatial and /or temporal distance between the observations. The compound symmetry structure has two unknown parameters: one that models for a common correlation (σ_1); and the other that models for the residual or the unexplained variance (σ_1+σ^2). For example, if we consider a vector of 4 observations within each subject, then the covariance matrix S for the *i*th subject looks like:

$$Var(\epsilon_i) = S_i = \begin{bmatrix} \sigma^2 + \sigma_1 & \sigma_1 & \sigma_1 & \sigma_1 \\ \sigma_1 & \sigma^2 + \sigma_1 & \sigma_1 & \sigma_1 \\ \sigma_1 & \sigma_1 & \sigma^2 + \sigma_1 & \sigma_1 \\ \sigma_1 & \sigma_1 & \sigma_1 & \sigma^2 + \sigma_1 \end{bmatrix} \qquad 5.4$$

Basically from Equation 5.4, we can notice that this model assumes the residual variance to be the same within a condition (that is pain or no-pain). Although the equation above describes the structure for S only for an *i*th subject, the residual variance and the correlation is assumed to be the same across all the subjects included in the analysis. In other words, this implies that the fixed effect due to pain or no-pain is the same both between the subjects and between trials within subjects. The variance-covariance of *Y* is estimated using the reduced or restricted maximum likelihood (REML) method. Unlike the maximum likelihood estimation, where

estimators are obtained by maximizing the whole likelihood function, REML estimators are obtained by maximizing the likelihood function to that part in the linear model that is invariant to the fixed effects. In other words, the REML estimates the variance components of *Y* by maximizing the likelihood function of a set of error contrasts given by $C = HY$ where *H* is a matrix whose columns are orthogonal to the fixed effects parameters in *β*. The set of error contrasts *C* produces a likelihood that does not depend on the fixed effects parameters in *β* but instead restricted only to the variance components in *V*. Once the variance parameters in *V* are estimated, the fixed effects model coefficients are estimated by,

$$b = \left(X'\hat{V}^{-1}X\right)^{-1}X'V^{-1}y \qquad 5.5$$

and the estimated variance-covariance matrix of *b* is given by

$$\widehat{Var(b)} = \left(X'\hat{V}^{-1}X\right)^{-1} \qquad 5.6$$

The estimated standard errors of the regression coefficients *b* that comprises of $\beta_0, \beta_1, \Lambda\ , \beta_p$, are the square roots of the diagonal elements of the Equation 5.6 above. The estimates of $\beta_0, \beta_1, \Lambda\ , \beta_p$ and their standard errors are also used to construct the F-statistics and t-statistics which are used to perform the significance tests which determine which independent variables account for variation in the dependent variable.

Further, in order to obtain robust standard errors of the estimates, typically one does not know the true correlation (σ_1) is in the S matrix. The numerical approach of iteratively estimating the regression coefficients also provides iterative estimation for correlation based on the underlying structure assumed for *S*. It has to be noted that in practical situations, if the distribution of residuals or model error (ε) violates conditions such as normality, then the standard errors for estimates would be incorrect and misleading. In order to overcome this problem, robust estimation of *V* is empirically derived from the data using the robust or empirical estimator. If the reader is interested in further mathematical details on robust or empirical estimator, it can be found elsewhere (Myers, Montgomery, Vining, & Robinson, 2010).

In this dissertation work, the baseline was consistently set to 5 sec for statistical comparison purposes. The baseline fixed at 5sec allows for using the entire 5sec for statistical comparison and hence preventing any bias that may appear if the baseline time points change with different lengths of quantified stimulation time period (that is FWHM). To extract the stimulus-induced activation/deactivation HbO changes, as shown in Figure 5-4, a time bin of length equal to the FWHM encompassing the peak activation/deactivation were obtained and the ΔHbO values within the FWHM time period were compared with the ΔHbO values from the baseline. Finally, linear mixed model as described above is employed to statistically compare the baseline and stimulus-induced HbO changes. The linear mixed modeling analysis was implemented using the SAS (SAS Institute Inc., Cary, N.C) software.

5.3.4.5 Linear Regression

In order to obtain correlates between the HbO-derived parameters and pain rating (sub-hypothesis 5.2.3), linear regression was carried out between the behaviorally measured subjective pain rating and the quantified ΔHbO parameters. Linear regression is a statistical approach of obtaining a relationship between two set of variables wherein, based on the derived equation, an estimate of one unknown variable can be calculated if the other variable is given. In other words, in the absence of any one of the two variables, the unknown variable can be estimated from the equation, provided that the other variable is known. The generalized linear regression is given by

$$y_i = X_i\beta + \epsilon_i \qquad 5.7$$

In this context, y_i (dependent variable) describes the pain rating and X_i (independent variable) is given by the HbO-derived parameters (PI or FWHM) wherein '*i*' denotes the subject or data set. In this way, it can be tested whether the stand-alone HbO-derived parameters acquired via fNIRS can be utilized to estimate cognitive evaluation of pain. The parameter β is the vector of regression coefficients that are typically estimated using the least squares method. Finally, ε_i is the vector of error or noise that is assumed to be random and uncorrelated with the regressors X_i. The assumption of no correlation between regressors and error term is very important in least

square estimation, since any correlation would result in poor estimation of β. Two other important assumptions for linear regression are normality and homoscedasticity of y_i, which are statistically tested using Shapiro-Wilk and Brown-Forsythe test respectively. The significance of relationship between the two variables was tested using *F*-statistics wherein the resulting *p*-value is compared to a critical value of 0.05. A *p*-value of less than 0.05 implies a significant relationship between the two variables and vice versa. In conjunction with *F*-statistics, the strength of the relationship between the two variables, or the coefficient of determination (R^2) was also computed in this study. Regression analyses, and all the associated statistical tests, were implemented using Sigma Plot 11.0 (Systat Inc., San Jose, CA) software.

5.3.4.6 Image Reconstruction

HomER software was used in this study for the purpose of image reconstruction of the HbO concentration changes. Backprojection method, which is a linearized algorithm, was employed for reconstruction. A brief technical background on the backprojection method was described in section 2.3.8 . The image reconstruction is carried out on both the block and group averaged HbO data. Individual images are generated for 'early' and 'late' responses by appropriately setting the temporal length at 0.1-12sec for early and 12.1-25 sec for late response. For 2-D imaging, the pixel size was set to 0.96cm in the *x* direction and 0.28cm in the *y* direction. The depth for absorption was set to 2cm from the scalp contact. Thus, the reconstructed image represents a 2-D slab of HbO changes at a 2cm depth from the scalp.

5.3.4.7 Anticipation

Anticipation and anticipatory stress is an affective factor that might have significant interaction with the cognitive response to painful stimulus. Since the primary interest of this specific aim is to elucidate the role of aPFC in cognitive evaluation of pain, it is important to explore if any bias due to anticipatory stress exists. Especially the response to the first painful stimulus could be reflected in the cognitive evaluation due to higher anticipation. In order to separate out the role of anticipation in response to the first stimulus, the first functional block in the raw data was disabled, as shown in Figure 5-5, followed by temporal block averaging the

remaining 7 functional blocks from each subject. The temporal averaging was followed by group temporal averaging across all the subjects (*N*=8).

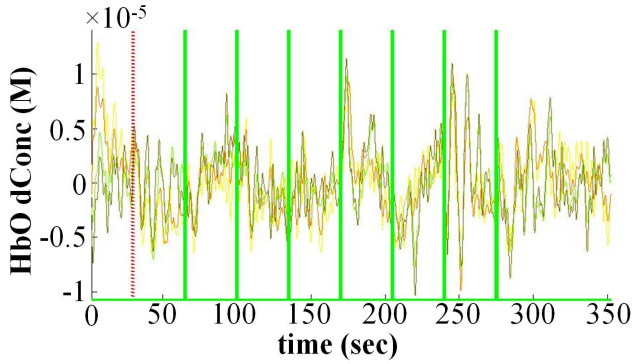

Figure 5-5: Sample raw data from a subject wherein the first block was disabled to explore anticipatory effects. Note: dotted red line: disabled block; solid green lines: enabled blocks. Raw data shown here is derived from clustered-wise channels from the contra aPFC area.

In the above mentioned approach, there are two key assumptions. The first assumption is that the anticipation in response to the first stimulus is higher compared to that of the remaining stimuli. The second assumption is that by disabling the first block, the anticipation effects are significantly minimized. Although this approach is arguably a sub-optimal experimental approach to investigate the role played by anticipation in pain perception, it shed some light on the anticipatory effect in fNIRS data based on block designed protocols.

In order to explore the interaction of anticipation with cognitive evaluation, each subject's block averaged (number of blocks = 7) HbO response was quantified for PI and FWHM without the first block. It is imperative to understand if HbO-derived parameters correlate solely with the cognitive aspects or if there is any interaction of cognitive evaluation with anticipation as seen through the HbO-derived parameters. Statistical tests were carried out to compare the HbO-derived parameters with and without the first block to investigate for interaction between anticipation and cognitive evaluation.

5.4 Results

The following analyzed data is comprised of results from the clustered-wise analysis and reconstructed images. Details of the methodology were described in the previous data analysis

section of this chapter. The motivation here is to quantify fNIRS measured parameters that correlate with the subjective pain rating, which leads to an objective quantification of pain perception using fNIRS.

5.4.1 Anterior Pre-frontal Cortex

Figure 5-6(a) shows the selected channels covering the anterior PFC (aPFC or BA 10). This cortical area was chosen because recent fMRI studies have shown the role of aPFC in the cognitive processing of pain intensity (Kong, et al., 2010; Kong, et al., 2006; Lui, et al., 2008). The average temporal response over the four channels from aPFC is depicted in Figure 5-6(b). Note that during the pinching stimulation (shown by the shaded box), the ΔHbO plot shows a trend for bilateral deactivation, followed by a slow recovery during the recovery period. Significant changes in de-oxy hemoglobin (ΔHbR) were not observed in this data. Moreover, the total hemoglobin (HbT), which is a linear combination of ΔHbO and ΔHbR, followed the temporal trend of HbO. The temporal profile of HbO, as shown in Figure 5-6(b), is consistent with the results reported in (L. Becerra, et al., 2008), even though Becerra et al. used thermal stimulation at 46℃ to induce pain.

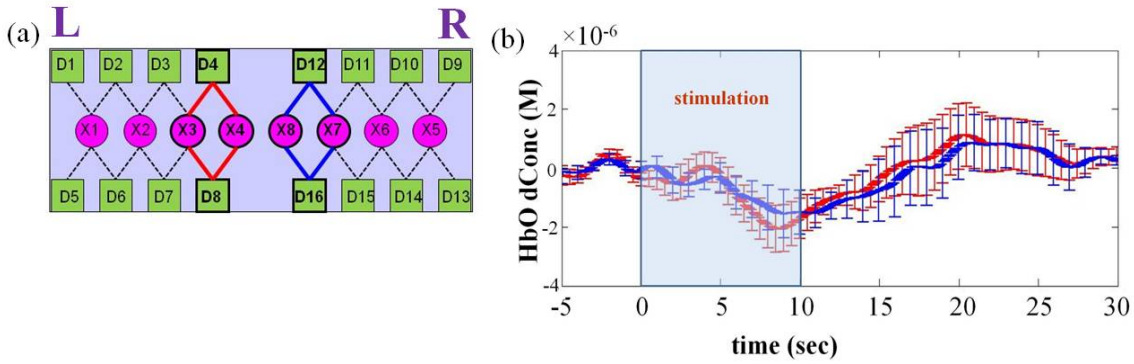

Figure 5-6: (a) Channels covering anterior PFC (b) Grand averaged temporal plots along with the standard error shown by the error bars. The grand average included averaging across the 8 blocks for each subject, followed by group temporal averaging across the 8 subjects. Note: pink circles: sources; green box: detectors; dashed line: disabled channels; solid red line: ipsi aPFC; solid blue line: contra aPFC; L: Left hemisphere; R: Right hemisphere.

5.4.1.1 Significance of Pinch-induced HbO Changes

The activation/deactivation changes observed in the temporal response need to be statistically verified for significance with respect to the baseline. In section 5.3.4.4 the detailed methods for statistical testing of significance in activation/deactivation is delineated. Briefly, the baseline time length was set at 5 sec. The data sampling rate was set at a down-sampled rate of 10 data points/sec. Thus, baseline consisted of a time bin of 50 data points. The time period of the functional block (30sec) was split into early (0.1-12sec) and late phase (12.1-25sec) in order to explore the immediate and delayed hemodynamic response. In section 5.3.4.3 , a generalized description of quantification for FWHM was described. The FWHM within the early and late phase was extracted for both ipsi- and contra- response, as shown in Figure 5-4. For accurate quantification of FWHM from the late phase, the 25-30sec time window which is defined here as the post-baseline, and considered as dummy from a 'functional' perspective, was incorporated if necessary.

The data points from the baseline and from the pinch-induced early and late phase for each subject (N=8) were laid out continuously on a spread sheet and imported into the SAS software for mixed modeling analysis. The SAS code and results from the mixed modeling analysis for comparison between the baseline and pinch-induced HbO changes are shown in Appendix C. Figure 5-7 below summarizes the mean estimates and associated standard errors for both baseline and pinch-induced HbO changes from the aPFC cortical area.

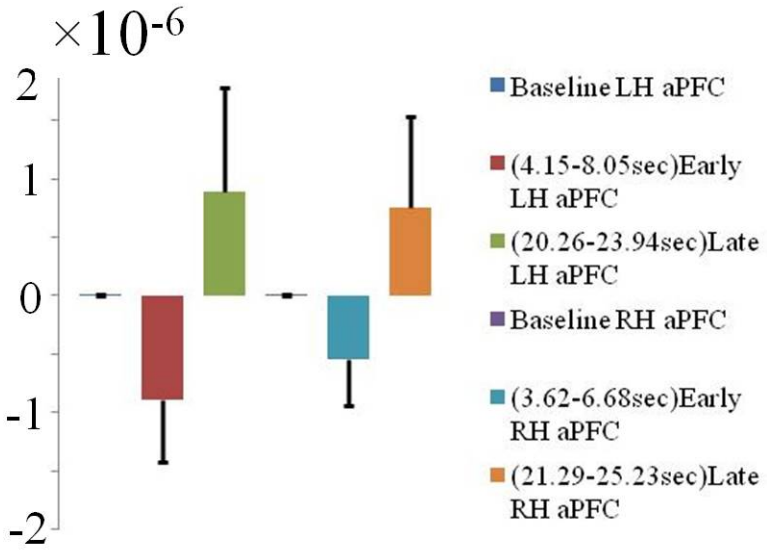

Figure 5-7: Summary of mean estimates and standard errors obtained for the baseline and pinch-induced HbO changes in the aPFC area using Linear Mixed Model. Note: The baseline was fixed at -5 to 0sec.

From Figure 5-7, we observe that for both LH and RH aPFC, the baseline mean estimates for HbO changes were very small in the range of 10^{-9} M. The mean estimates for the pinch-induced changes were in the range of 10^{-7} M. This implies that pinch stimulation induced a change in the HbO response magnitude by an order of 100. Specifically, we can also observe that the mean estimates for pinch-induced change during the early phase are -8.89×10^{-7} and -5.45×10^{-7} in the LH and RH aPFC respectively. Comparing these values to the respective baseline values, we observe that the stimulus-induced HbO change shows a trend for deactivation in response to the pinch stimulation. Since both the LH and RH aPFC show a trend for negative HbO changes with respect to the baseline, we can deduce that bilateral deactivation were observed during the early phase while a trend for bilateral activation was observed during the late phase.

The next important step was to investigate the significance of pinch-induced changes with respect to the baseline. The observed p-values shown in Table 5-1 were obtained from the linear mixed model analysis for comparison between baseline and pinch-induced HbO changes. From Table 5-1, we can clearly notice that significant pinch-induced HbO changes were not

observed with respect to the baseline. This could probably be due to the small size of the subject pool and in addition, in this preliminary study, we did not consider the between-subject variability or the random effects.

Table 5-1: Summary of significance of pinch-induced HbO changes with respect to the baseline in the aPFC area. Note: The critical value for significance is 0.05; LS stands for least square and the baseline was fixed at -5 to 0sec.

Baseline/Stimulation comparison	**LS Mean Difference (M)**	**Std. Error (M)**	**Pr > |t|**	**Significantly Induced Change**
LH aPFC (t=4.15 to 8.05 sec)$_{early}$	-8.97×10^{-7}	5.28×10^{-7}	$p = 0.094$	No change
LH aPFC (t=20.26 to 23.94 sec)$_{late}$	8.85×10^{-7}	8.66×10^{-7}	$p = 0.322$	No change
RH aPFC (t=3.62 to 6.68 sec)$_{early}$	-5.47×10^{-7}	3.96×10^{-7}	$p = 0.172$	No change
RH aPFC (t=21.29 to 25.23 sec)$_{late}$	7.53×10^{-7}	7.79×10^{-7}	$p = 0.337$	No change

5.4.1.2 Correlates for Cognitive Evaluation

The key observation from Figure 5-7 was that a trend for ΔHbO deactivation was observed during the early phase. As mentioned earlier, the deactivation observed was in the range of 10^{-7} which is lower in magnitude by order of 100 compared to the baseline. Although from Table 5-1 we observe that significance was not observed ($p>0.05$), from a neurophysiological perspective, it was intriguing to observe negative HbO response in response to pinch stimulation and if it is associated with cognitive aspects of pain perception. Hence, the HbO-derived parameters were quantified from the early phase as shown in Figure 5-8. As previously observed through linear mixed model estimates, we observed a trend for bilateral deactivation in the aPFC area as shown in Figure 5-8(b). Full-width half maximum of the HbO response was another HbO-derived parameter that would be useful in reflection of pain level perceived by the subject. In order to test the sub-hypothesis 5.2.2, PI and FWHM would be the two HbO-derived parameters that would be regressed with the behaviorally measured pain rating.

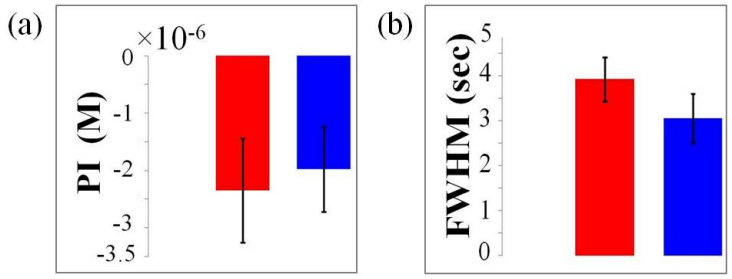

Figure 5-8: Comparison of average HbO-derived parameters from early (0.1-12 sec) response between ipsi and contra aPFC. (a) peak intensity (b) full-width half maxima. Note: error bar indicates the standard error across the subjects.

Figure 5-9 below shows the linear regression results between quantified HbO parameters extracted from aPFC and the behaviorally measured subjective pain rating for early and late response at the group level. Pain rating was considered as the dependent variable, and the HbO-derived parameters were considered as the independent variables. The following Equations (5.1-5.3) show the linear relationship between rating and (1) contra aPFC peak intensity (p=0.025, r = 0.773, R^2=0.597); (2) ipsi aPFC peak intensity (p=0.023, r = 0.777, R^2=0.604) and (3) contra aPFC fwhm (p=0.004, r = -0.875, R^2=0.765) respectively. Each regression fitting passed the Shapiro-Wilk normality test and the constant variance test.

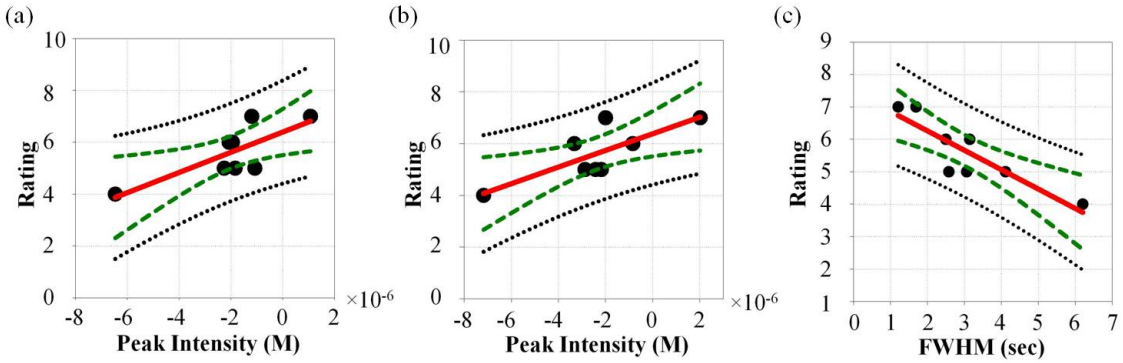

Figure 5-9: Linear regression between subjective pain rating and early HbO-derived parameters. (a) peak intensity in contra aPFC (p= 0.025) (b) peak intensity in ipsi aPFC (p= 0.023) (c) full-width half maxima in contra aPFC (p=0.004). Note: solid black dots denote raw data; thick red lines denote the regression line; dashed dark green lines denote the 95% confidence interval for regression; and dotted black lines denote the 95% confidence interval for raw data.

Equations 5.1 and 5.2 mathematically describe the linear relationship between pain rating and peak intensity (PI) in contra- and ipsi aPFC. In the equations below, '*E*' denotes the early response. The two equations showed that the intercepts were similar and paired t-test between the contra and ipsi slopes also did not had any statistical significance. Now moving on to equation 5.3, it shows the linear relationship between rating and FWHM derived from contra lateral activation. Ipsi aPFC derived early phase FWHM did not show significant correlation with rating. The regression analysis was also carried out on late phase derived parameters, and the results are shown in Figure 5-10. The *F*-statistics analysis did not show significant *p-value* for regression between rating and 'late' phase HbO-derived parameters.

$$Rating = 6.4 + 3.9 \times 10^5 * PI\_\_E\_\_contra\ aPFC \quad 5.8$$

$$Rating = 6.4 + 3.21 \times 10^5 * PI\_\_E\_\_\text{ipsi}\ aPFC \quad 5.9$$

$$Rating = 7.46 - 0.59 * \text{fwhm}\_\_E\_\_\text{contra}\ aPFC \quad 5.10$$

From Figure 5-9 regression plots, for example from Figure 5-9(a), the question arose whether the left-most extreme data point was an outlier and further if this data point were excluded from the regression analysis, would the correlation relationship still hold good. To explore this for contra aPFC PI, the left-most extreme data point (subject S20) was excluded and similar regression analysis was carried out with the remaining 7 data points. The resulting correlation (r = 0.6) was still positive between rating and contra aPFC with a p=0.153 and R^2=0.361. Similar kind of analysis was carried out for ipsi aPFC PI. Excluding the left-most extreme data point (subject S20), the resulting correlation (r = 0.6) was positive with a significance of p=0.154 and R^2=0.36. Finally, for contra aPFC FHWM, the negative correlation (r = -0.82) between rating and FWHM was consistent after excluding the same left-most extreme data point as described above. The resulting significance from *F*-statistics after excluding the left-most extreme data point was p=0.025, R^2= 0.67.

The above analysis helped in exploring the robustness of the relationship between the variables involved in the regression analysis. It has to be noted that in this preliminary study, the subject pool was relatively small. Despite this limitation, excluding one data point that appeared to be an outlier resulted in similar correlation between pain rating and the HbO-derived parameters.

This implies that the relationship between the pain rating and HbO-derived parameters is robust in this preliminary study.

It has to be noted that from Table 5-1 that significant pinch-induced HbO changes were not observed in both early and late phase with respect to the baseline. However, from the above results, we can observe that significant pain-correlates were obtained from the early phase HbO response. From a scientific perspective, this also raises our interest to investigate whether the HbO activation observed during the late phase resulted in any significant relationship with the behaviorally measured pain rating. Similar to the above procedure, the HbO-derived parameters were quantified from the late phase HbO response and regressed with the behaviorally measured pain rating. Figure 5-10 below shows that the resulting regression between late phase HbO-derived parameters and pain rating do not have a significant relationship. Hence these results all together support the sub-hypothesis 5.2.2 that only the early phase HbO-derived parameters has a significant relationship with the behaviorally measured pain rating and hence reflecting the cognitive evaluation of pain perception.

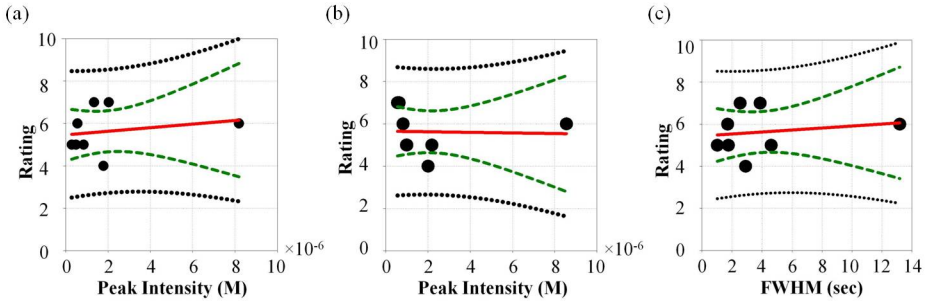

Figure 5-10: Linear regression between subjective pain rating and late HbO-derived parameters. (a) peak intensity in contra aPFC (p= 0.622, r = 0.21) (b) peak intensity in ipsi aPFC (p= 0.934, r = 0.03) (c) full-width half maxima in contra aPFC (p=0.680, r = 0.17). Note: solid black dots denote raw data; thick red lines denote the regression line; dashed dark green lines denote the 95% confidence interval for regression; and dotted black lines denote the 95% confidence interval for raw data.

5.4.2 Are the Correlates from aPFC Biased by Anticipation?

In order to explore the anticipatory effects, the clustered-wise analysis on aPFC derived HbO response were obtained as shown in Figure 5-11 and Figure 5-12. The difference between the two temporal plots is that one includes the first block into the block averaging (shown by red

and blue line) while the other does not include the first block into the block averaging (shown by pink and teal line). However, the two temporal plots show the grand average across all the 8 subjects. From section 5.4.1 , the HbO-derived parameters PI and FWHM from the early response correlated with pain rating. Hence, the same HbO-derived parameters (that is PI and FWHM) were extracted from grand averaged temporal plots wherein the first block was excluded from block averaging. Table 5-2 below shows the paired *t*-test comparison between PI and FWHM values for with and without the first block. Preceding the paired *t*-test, Shapiro-Wilk test for normality was carried out and the data held true for normality which is an important assumption for parametric statistical tests. The resulting *p-value* (greater than 0.05) as shown in Table 5-2 implies that the higher anticipation in response to the first stimulus did not interfere with the cognitive evaluation of pain. This result asserts the previous observation that the correlates (that is PI and FWHM) obtained from aPFC solely reflects cognitive evaluation of pain.

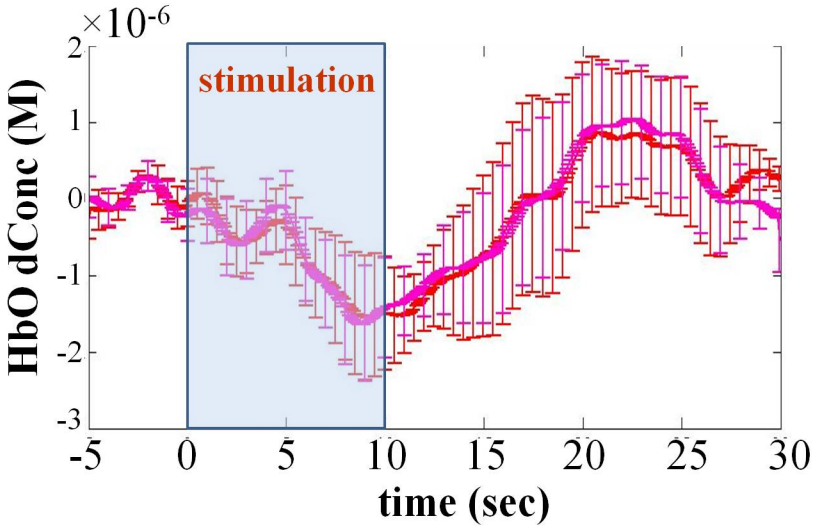

Figure 5-11: Grand averaged ΔHbO temporal plots (*N*=8) with and without the first block included into the block averaging to explore the anticipation effect in *contra* aPFC. Note: solid red line: first block included; solid pink line: first block excluded; error bars denote the standard error across the subjects.

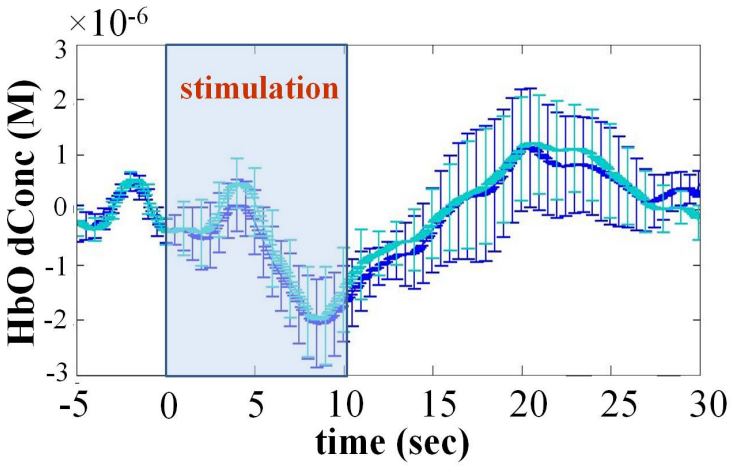

Figure 5-12: Grand averaged ΔHbO temporal plots (*N*=8) with and without the first block included into the block averaging to explore the anticipation effect in *ipsi* aPFC. Note: solid blue line: first block included; solid teal line: first block excluded; error bars denote the standard error across the subjects.

Table 5-2: Comparison of the HbO-derived parameters (PI and FWHM) extracted from with and without first block to explore anticipation effect. The critical value for significance is set at 0.05

w/ and w/o first block comparison	**Side of the brain**	**Paired t-test**
PI _Early	Contra-lateral	p = 0.453
FWHM_Early	Contra-lateral	p = 0.483
PI _Early	Ipsi-lateral	p = 0.320
FWHM_Early	Ipsi-lateral	p = 0.390

5.4.3 HbO Changes in Dorsolateral Pre-frontal Cortex

Clustered-wise analysis was also carried out for selected channels covering the dorsolateral pre-frontal areas as shown in Figure 5-3(b). Figure 5-13 shows the grand averaged temporal plots along with the standard error for both contra (blue) and ipsi (red) dorsolateral areas. In the plots, the baseline is shown between -5 and 0 sec, the stimulation is given from 0 to 10 sec and, the resting period is between 10 and 30 sec. The first step was to investigate whether the activation from dorsolateral area is significantly different from the baseline. In order to execute this, FWHM was extracted from the early phase which was 3.59 sec for ipsi DLPFC and 4.1sec for contra DLPFC respectively. Linear mixed modeling analysis was carried out to test whether the pinch-induced HbO changes in the DLPFC area was significantly different from the

associated baseline during the early phase. The reason only early phase was chosen was that from section 5.4.1.2 , we observed that for the aPFC area, significant pain-correlates were obtained only from the early phase. Since simultaneous measurements were obtained from the DLPFC along with the aPFC area, it was important to investigate whether the early phase HbO response from the DLPFC area was involved in the cognitive evaluation of the pain perception.

From Figure 5-13 and Figure 5-14, we can clearly observe that the pinch-induced HbO changes were not significant with respect to the baseline. Although we observe a trend for activation in both LH and RH DLPFC, the standard errors are relatively larger compared to the mean estimates. The statistical comparison between estimates for baseline and pinch-induced HbO changes resulted in a p-value of 0.91 and 0.85 for LH and RH DLPFC using the linear mixed model analysis. Further details of these results can also be found in Appendix C.

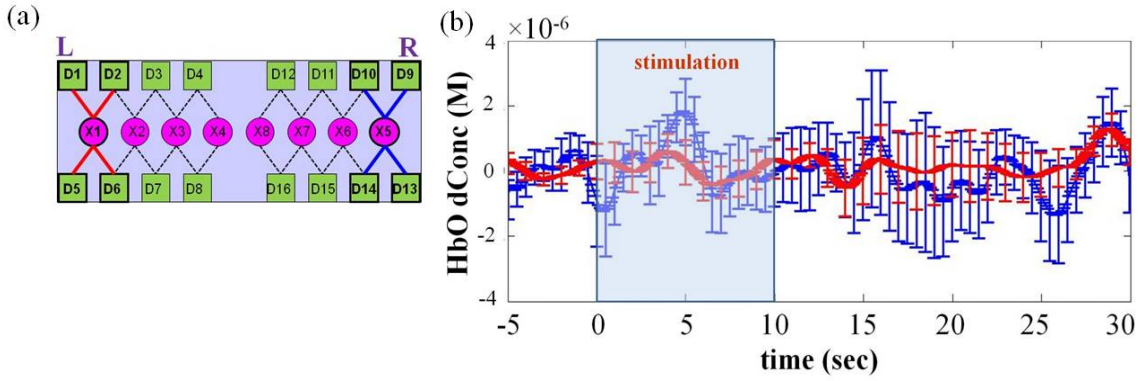

Figure 5-13: (a) Channels covering dorsolateral PFC (b) Grand averaged temporal plots along with the standard error shown by the error bars. The grand average included averaging across the 8 blocks for each subject, followed by group temporal averaging across the 8 subjects. Note: solid red line: ipsi aPFC; solid blue line: contra aPFC; L: Left hemisphere; R: Right hemisphere.

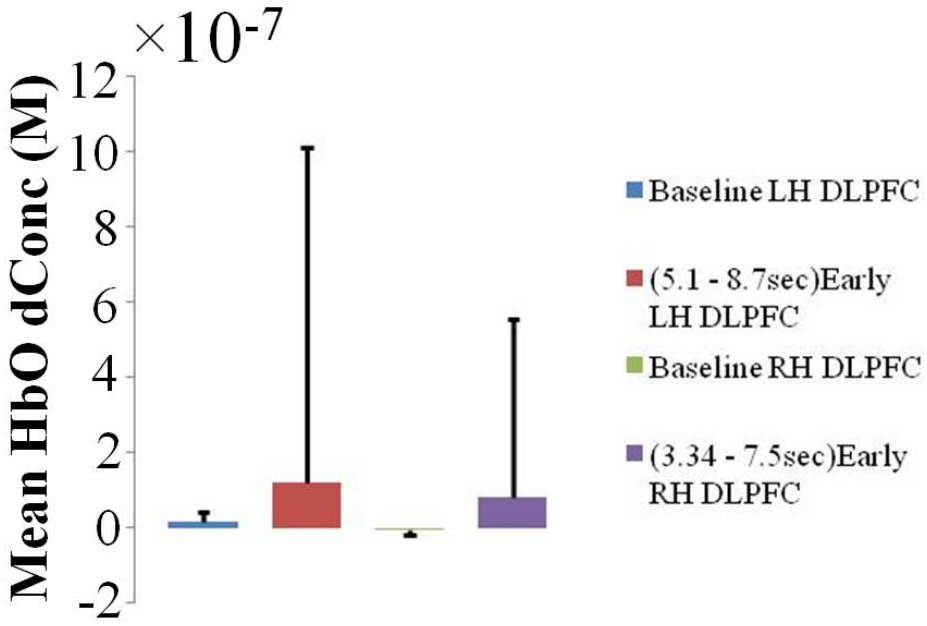

Figure 5-14: Summary of mean estimates and standard errors obtained for the baseline and pinch-induced HbO changes in the DLPFC area using Linear Mixed Model. Note: The baseline was fixed at -5 to 0sec.

Further, linear regression was carried out between pain rating and HbO-derived parameters (PI and FWHM) extracted from early response (0.1-12sec). The statistical results showed p=0.439, r=0.32, R^2=0.102 for HbO-derived FWHM from ipsi DLPFC; p=0.139, r=0.57, R^2=0.326 for HbO-derived FWHM from contra DLPFC; p=0.542, r=0.26, R^2=0.06 for HbO-derived PI from ipsi DLPFC; and p=0.863, r=0.07, R^2=0.005 for HbO-derived PI from contra DLPFC. The resulting p-values and goodness of fit did not show significance implying that early phase of HbO response from the DLPFC does not significantly correlate with the pain rating.

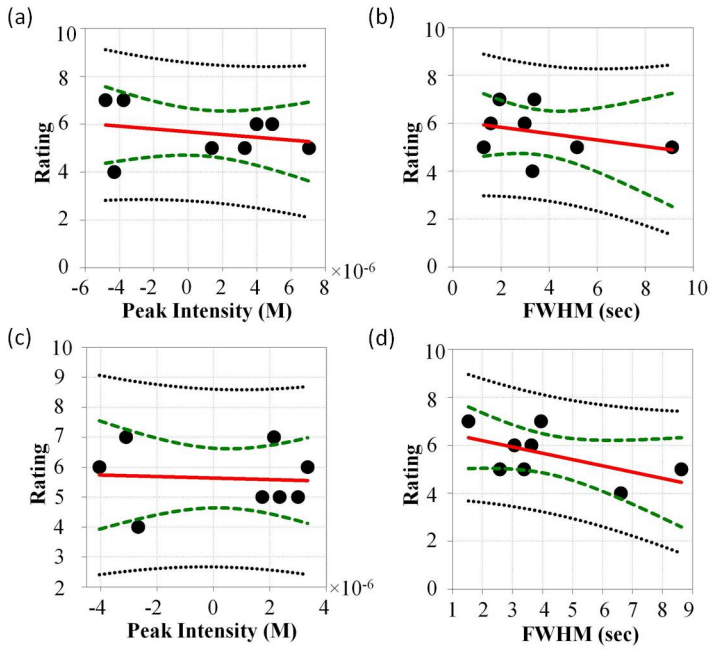

Figure 5-15: Linear regression between subjective pain rating and HbO-derived parameters from DLPFC early response. (a) peak intensity in ipsi DLPFC (p= 0.542, r=0.26) (b) FWHM in ipsi DLPFC (p= 0.439, r=0.32) (c) peak intensity in contra DLPFC (p=0.863, r=0.07) (d) FWHM in contra DLPFC (p= 0.139, r=0.57). Note: solid black dots denote raw data; thick red lines denote the regression line; dashed dark green lines denote the 95% confidence interval for regression ; and dotted black lines denote the 95% confidence interval for raw data.

The above results showing no significance between the baseline and pinch-induced HbO changes during the early phase clearly indicates that the results from this study do not support our sub-hypothesis 5.2.4. In addition, no significant relationship was observed between the HbO-derived parameters from the early phase and the behaviorally measured pain rating. This further confirms that in this study, the HbO changes measured from the DLPFC area in response to pinch stimulation do not reflect cognitive evaluation of the pain perception.

5.4.4 Significant Difference between aPFC and DLPFC HbO Changes

Sub-hypotheses 5.2.1 and 5.2.4 were solely based on investigating the significance of pinch-induced HbO changes with respect to baseline in the aPFC and DLPFC areas respectively. We observed from Table 5-1 and section 5.4.3 that no significance was observed between the baseline and pinch-induced HbO changes in the aPFC and DLPFC areas. However, given that we obtained measurements simultaneously from both the aPFC and DLPFC areas, inherently

there exists correlation between the measurements from the two different cortical areas for each subject. This was modeled in the covariance structure of the linear mixed model by assuming equi-correlation between all the measurements which refers to the compound symmetry structure.

From Table 5-3, we observe that there was no significance (p>0.05) between the HbO changes from aPFC and DLPFC areas due to pinch stimulation. Specifically, we had to focus on the early phase HbO changes from the aPFC area (shown by yellow shade in Table 5-3) as we observed from section 5.4.1.2 that the HbO-derived parameters from the aPFC early phase, significantly correlated with the pain rating. We observe that there is no significant difference between the estimates from the early phase LH/RH aPFC areas and the early phase LH/RH DLPFC HbO changes. Non-significance could possibly be due to the limited size of our subjects and the variability between the subjects. However, it could also be possible that both the areas are coherently involved to some extent in the processing of pain. These possibilities need further investigation that is currently not investigated in this study.

Table 5-3: Summary of significance between pinch-induced HbO changes from aPFC and DLPFC areas. Note: LH: Left hemispheric; RH: Right hemispheric; LS: Least square; the yellow shade indicates the areas and associated phase from which significant correlates were obtained in section 5.4.1.2 .

aPFC	DLPFC	LS Mean Difference (M)	Std. Error (M)	Pr > |t|
LH_{early}	LH_{early}	-1×10^{-6}	9.39×10^{-7}	0.287
LH_{late}	LH_{early}	7.73×10^{-7}	1.04×10^{-6}	0.461
RH_{early}	LH_{early}	6.65×10^{-7}	9.18×10^{-7}	0.4717
RH_{late}	LH_{early}	-6.35×10^{-7}	9.45×10^{-6}	0.504
LH_{early}	RH_{early}	-9.72×10^{-7}	7.03×10^{-7}	0.172
LH_{late}	RH_{early}	8.11×10^{-7}	1.18×10^{-6}	0.494
RH_{early}	RH_{early}	-6.27×10^{-7}	6.73×10^{-7}	0.355
RH_{late}	RH_{early}	6.72×10^{-7}	1.11×10^{-6}	0.547

5.4.5 Summary of pain-correlates for Pinch Stimulation

Table 5-4 below summarizes the correlates between the HbO-derived parameters and the behaviorally measured pain rating under the pinch stimulation. One of the key observations is that the correlates were observed only during the early phase of the aPFC area. Further from Table 5-1, we observed a trend for early phase HbO deactivation in the aPFC area. This implies

that from this preliminary study, the negative HbO changes observed in the aPFC area through fNIRS measurements; reflect the cognitive evaluation of pain perception. Another key observation is that a positive correlation was observed between PI and the pain rating in both LH and RH aPFC areas; while a negative correlation was observed between FWHM and the pain rating only in the RH aPFC area. Finally, the DLPFC area did not show any significant correlates during the early phase while the late phase was not investigated in this study as visual inspection from Figure 5-13(b) for the HbO changes during the late phase did not show significance with respect to the baseline.

Table 5-4: Summary of *significant* correlates between ΔHbO-derived parameters and pain rating under mechanical stimulation. Note: RH: right hemispheric; LH: left hemispheric; (+): positive correlation; (-): negative correlation; --: no correlates; N/I: not investigated; PI: ΔHbO-derived Peak Intensity; FWHM: ΔHbO-derived full-width half maxima.

	Early phase	**Late phase**
RH aPFC	(+) PI (-) FWHM	--
LH aPFC	(+) PI	--
RH DLPFC	--	N/I
LH DLPFC	--	N/I

5.4.6 Reconstructed Images

Figure 5-16(a) and (b) shows the HbO reconstructed images obtained for early and late response respectively. In order to obtain the temporally averaged image, for early phase, the temporal averaging was carried out between 0.1-12sec, and for late phase, the temporal averaging was carried out across 12.1-25sec. First off, focusing on aPFC areas (selected channels as shown in Figure 5-3(a)), a trend for bilateral deactivation (shown by blue) was observed during the early response while in the same area; the late response showed activation (shown by red). From clustered-wise analysis, the HbO-derived parameters from the early response (peak intensity and FWHM) derived from ipsi aPFC correlated with pain rating. Figure 5-16(a) for early response also showed a trend for bilateral deactivation in aPFC implying that we observe consistent results. The correlates obtained from regression analysis also implied that deactivation in ΔHbO reflects the pain perception and cognitive evaluation of pain level. The DLPFC area appears to have a bilateral activation during the early phase. However, for the late

phase, there is no clear pattern observed in this area. This observation is in agreement with the clustered-wise analysis where significant changes was not observed in response to the stimulation.

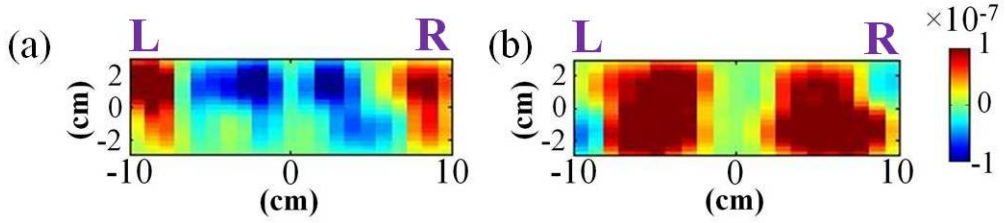

Figure 5-16: Reconstructed ΔHbO images in (a) early response (b) late response for mechanical stimulation. Note: the color bar range shows blue for deactivation and red for activation; the image for early response is the temporal average across 0.1-12sec while that for late response is the temporal average across 12.1-25sec; L: left hemisphere and R: right hemisphere.

5.5 Discussion

The specific aim delineated in this chapter focused on the HbO changes in response to mechanical stimulation. The major goals of this specific aim were: (1) To investigate whether the pinch-induced HbO changes were significant with respect to the baseline in both aPFC and DLPFC areas. (2) Given the preliminary nature of this study with only 8 recruited subjects, obtain the correlates between behaviorally measured pain rating and HbO-derived parameters. (3) The final major goal was to test the robustness of the correlates in reflecting the cognitive evaluation of pain perception.

In functional brain imaging, the 'functional' response of interest is always extracted and interpreted with respect to contrasting experimental conditions. Since the induced responses are relative, it is imperative to test for significance between the experimentally induced contrasting conditions. Thus, in a standard two-condition blocked design, it has been shown in fMRI literature (Huettel Scott A, 2008) that standard *t*-test is sufficient to evaluate whether the difference between the two conditions is large compared to the measure of the variability in the data. Although univariate tests, such as the *t*-test, are considered as a justifiable approach to perform statistical comparison between task and no-task conditions (Huettel Scott A, 2008); (Tian, Chance, et al., 2009), such tests have limitations. For example, the *t*-test is inappropriate

for exploring the precise timing of activation, since it combines data from all time points within a condition. Further, we also need to keep in mind that *t*-test only finds the differences between the means of the two distributions while it is insensitive to the differences in their variability.

Given that this study involved repeated measurements, univariate tests were not the optimal approach as it assumes independence between the measurements. Hence, we relied on a more robust general linear mixed model approach to test the significance between baseline and pinch-induced HbO changes. The mixed model is an extension of fixed effect model wherein the model allows for estimation of between-subjects variance at the group level (Beckmann, Jenkinson, & Smith, 2003). However in this study, the random effects were not investigated as the degree of freedom to estimate robust error variance is small due to the small size of subject pool. Within the fixed effect model, it comes down to the choice of the investigator to appropriately model the covariance structure of the residuals. In this study compound symmetry was chosen as it is mathematically a simple and parsimonious model that assumes equal correlation between the measurements within a cluster (cortical area) and across the subjects. Although compound symmetry has also been undertaken in other studies (Ng, et al., 2010), from a practical perspective, first order autoregressive model, AR (1), is another reasonable choice. However in this study, since the preprocessing data analysis step involved high-pass filtering of the raw data, AR(1) was not an optimal choice as one of the recent journal article has shown that estimation of covariance using AR(1) is not robust if the covariance is estimated after the filtering step (Mumford & Nichols, 2008).

Hence, linear mixed model was employed in this study to statistically compare the mean estimates between the baseline and pinch-induced HbO changes. This statistical test essentially becomes the key for drawing inferences on sub-hypotheses 5.2.1 and 5.2.4. The details on SAS code and the SAS output can be found in Appendix C. Figure C-1 and Figure C-2 in the same appendix show the histogram and normal probability plot for the residuals from mixed modeling analysis. Visual inspection of these figures show that the histogram looks close to a normal curve and the normal probability plot appears close to straight line. Since the residuals

follow the normal distribution, this verifies that the data set meets the general requirement of a linear mixed model.

The aPFC cortical area displays interesting trends in response to mechanical stimulation. From Figure 5-6(b) and Figure 5-7, a trend for HbO deactivation was observed in both right hemispheric (RH/contra) and left hemispheric (LH/ipsi) aPFC during the early phase. However, statistical comparison between the least square means of the baseline and pinch-induced HbO changes did not result in significance (p>0.05) as observed in Table 5-1 . This observation leads to the inference that the results from this specific aim do not support the sub-hypothesis 5.2.1. However, recent fMRI reports have also shown negative BOLD response under mechanical (Lui, et al., 2008) and thermal stimulation (Kong, et al., 2010; Moulton, et al., 2006) in the same area. In addition, the deactivation observed during the early phase was bilateral in the aPFC. Similar results have also been reported in studies using PET (Peyron, Laurent, & Garcia-Larrea, 2000) and fMRI (Kong, et al., 2006; Lui, et al., 2008; Peyron, et al., 2000). The underpinning neurophysiology behind the negative HbO phenomenon is explained in section 8.5 . As far as DLPFC is concerned, the results from Figure 5-14 show that the standard errors are larger compared to the estimates and further no significance was observed between the early phase pinch-induced HbO activation and the baseline. Hence from our study we observe that DLPFC does not result in significant HbO changes in response to pinch stimulation.

A recent fMRI study (Kong, et al., 2006) has shown that the aPFC is involved in the cognitive evaluation of pain intensity. From Table 5-1, we observed that the pinch-induced HbO changes during the early phase were not significant with respect to the baseline. However, given that this is a preliminary study with only limited subjects, it was interesting to observe a trend for HbO deactivation in response to pinch stimulation. From Figure 5-7, we can observe that the mean estimates for pinch-induced HbO changes are larger in magnitude (in the negative direction) than the baseline by an order of 100. Further from the same Figure 5-7, the standard errors are also relatively smaller compared to respective mean estimates. From a scientific perspective, we were interested to investigate the cause for HbO deactivation and if it has any role in cognitive evaluation of pain. Hence, linear regression analysis was carried between

behaviorally measured pain rating and HbO-derived parameters quantified from the early phase in the aPFC area. Interestingly, a significant positive relationship was observed between the pain rating and HbO-derived PI in both RH and LH aPFC. In addition, a significant inverse relationship was observed between the pain rating and HbO-derived FWHM only in the RH aPFC. Since both HbO-derived PI and FWHM from RH aPFC correlated with the behaviorally measured pain rating, the right hemisphere has a higher significant role in the processing of cognitive evaluation of pain under mechanical stimulation. These observations support our sub-hypothesis 5.2.2 that a significant relationship exists between the fNIRS based HbO-derived parameters and the behaviorally measured pain rating.

This preliminary study also investigated the potential application of ΔHbO reconstructed images in the pain studies. The reconstructed image for the early phase shown in Figure 5-16 displaying a trend for bilateral deactivation in the aPFC area was consistent with the clustered-wise analysis. The DLPFC areas showed bilateral activation during the early phase while a clear pattern was not observed during the late phase. This observation from ΔHbO reconstructed images was in agreement with the clustered-wise analysis, where significance was not observed between the baseline and stimulation induced HbO changes in the DLPFC area. The drawbacks associated with the backprojection algorithm as applied to fNIRS were discussed in section 2.6.3 . Hence, further development in reconstruction algorithms is necessary to enhance the absorption sensitivity and improve the accuracy for quantitative imaging. Imaging-based Region of Interest (ROI) analysis would be more useful as it is a less cumbersome approach compared to the clustered-wise analysis. In this aspect, advanced statistical approaches are necessary to extract a ROI and to correct for intra and inter-subject variability.

A recent fMRI study has shown that the aPFC is also involved in the processing of anticipation in response to painful stimulation (Porro, et al., 2002). Since the correlates for cognitive evaluation were obtained from the aPFC area, it was necessary to test whether the correlates were biased by anticipatory stress in response to the painful stimuli. Statistical results shown in Table 5-2 indicate that no significant difference was observed between the HbO-derived parameters, with and without the first block, implying that the subject's higher anticipation in

response to the first pain stimulus did not interfere with the cognitive evaluation of pain. Further, the fMRI studies have also shown that habituation and anticipation is an inherent confounding factor of blocked-design protocol (Rosen, Buckner, & Dale, 1998). Since this study incorporated a block design, further experimental investigation incorporating event-related or mixed design (Huettel Scott A, 2008) is necessary to disentangle the anticipatory stress factor from other cognitive factors.

In conclusion, a trend for bilateral HbO deactivation was observed in the aPFC area during the stimulation, from which two HbO-derived parameters significantly correlated with the behaviorally measured pain rating. Further, anticipation did not interfere with the cognitive evaluation from the measured aPFC HbO responses, solidifying the result that the correlates obtained for cognitive evaluation are robust. Finally, the DLPFC was not observed to have significance in the processing of pain perception under mechanical stimulation. The investigation for correlates under a different type of pain stimuli other than mechanical, such as thermal, are described in the following chapters.

CHAPTER 6

NEURAL CORRELATES OF 48℃ THERMAL PAIN STIMULATION

6.1 Current Understanding

In the previous chapter, the feasibility of fNIRS to quantify pain perception under mechanical stimulation was explored. Further, to test the robustness of fNIRS and the methodologies, thermal pain stimulation will be incorporated in this study. From a scientific perspective, the interest was to investigate the role of pre-frontal cortex in the emotional and cognitive processing of pain experience under thermal stimulation.

Although there have been several PET and fMRI studies carried out on pain perception in normal and patient population, as reviewed in (Peyron, et al., 2000), the first study using DOT towards pain measurements was carried out Becerra et.al (L. Becerra, et al., 2008). Becerra et.al work did not focus on quantifying the cognitive and emotional aspects of pain perception.

Further, in one of our previous studies (Krishnamurthy, Kavuri, Tian, & Liu, 2010), the feasibility of a high density optical imager was explored to measure pain induced changes. However, in that study the protocol incorporated baseline at room temperature (25℃), while the noxious stimuli were set at 48℃. Our results from this previous study (Krishnamurthy, et al., 2010) also show bilateral activity in the aPFC area. However, one of the major drawbacks of our previous study was that the probe holder of the high density optical imager was heavy as reported by the subjects. From a scientific standpoint, the interest was to measure changes in reference to baseline set to body temperature (35℃) instead of room temperature (25℃).

The motivation of this specific aim was to explore the feasibility of NIRS for quantification of pain perception under noxious thermal stimulation. Moreover, a new aspect of correlating

optical measurements with the clinically standard psychological assessment was explored. The rationale was that the quantified correlates attribute the processing of specific pain dimensions to prefrontal substrate in the brain's pain circuitry.

6.2 Sub-hypotheses

The major specific aim undertaken in this chapter is to quantify neural correlates between oxy-hemoglobin concentration changes and cognitive evaluation of pain intensity under noxious thermal stimulation. In order to methodically investigate the above specific aim, it is broken down in to sub-hypotheses as follows

1. Within the selected subject pool, **48℃** thermal stimulation will cause HbO change in the **anterior prefrontal cortex (BA 10)** during the **early (0.1 to 12sec)** and **late phase (12.1 to 25sec)** of the stimulation**.** 48℃-induced HbO changes are significantly different from the **baseline (-5 to 0sec)** HbO changes.
2. During the **late phase (12.1 to 25sec)** of the **48℃** thermal stimulation**,** the mean estimates from statistical testing for sub-hypothesis 6.2.1 show HbO deactivation in the **anterior prefrontal cortex**. The HbO-derived parameter **(PI and FWHM)** from the late phase has a **significant correlation** with the behaviorally measured **pain rating**.
3. Within the selected subject pool, **48℃** thermal stimulation will cause HbO change in the **dorsolateral prefrontal cortex (BA 46)** during the **early (0.1 to 12sec)** and **late phase (12.1 to 25sec)** of the thermal stimulation**.** 48℃-induced HbO changes are significantly different from the **baseline (-5 to 0sec)** HbO changes.
4. During the **late phase (12.1 to 25sec)** of the **48℃** thermal stimulation**,** the mean estimates from statistical testing for sub-hypothesis 6.2.3 show HbO activation in the **dorsolateral prefrontal cortex**. The HbO-derived parameter **(PI and FWHM)** from the late phase has a **significant correlation** with the behaviorally measured **pain rating**.

5. **HbO-quantified PI** from the **left hemispheric anterior prefrontal cortex** reflects the cognitive evaluation of pain perception. It is **not affected by anticipation** in response to the first pain stimulus.

6.3 Methods

In this section and subsections, the details on subjects, experimental protocol design, data acquisition and data analysis tailored towards this specific aim are described.

6.3.1 Subjects

Six healthy, right handed volunteers were recruited through local advertisements. The subject group was comprised of 4 males and 2 females within an age range of 20-35 years. Subjects with a history of neurological trauma, psychiatric or neurological disorders were excluded. Subjects who were on any psychoactive or pain medications were also excluded from the study. Written informed consent was obtained from all the subjects as per the guidelines set by the University of Texas at Arlington Institutional Review Board, who reviewed and approved this study. Out of the 6 subjects, the data from one subject was very noisy and hence it was dropped out from data analysis and statistical inference.

6.3.2 Experimental Protocol

In order to induce noxious painful heat stimuli, the thermal stimulator (model: Pathway ATS, Medoc Inc., Haifa, Israel) was used in this study. The thermode (3×3 cm^2) was strapped on to the subject's dominant volar forearm, at about 10-13cm from the elbow. Figure 6-1 shows the overall experimental setup. Figure 6-1(a) shows the overall experimental setup, the thermode strapped to the volar forearm right above marked area is shown in Figure 6-1(b), and the thermal stimulator used for pain delivery is shown in Figure 6-1(c). To induce noxious pain within the subject's comfort level, the thermode was strapped on to the subject's dominant volar forearm (approximately close to the marked area) followed by slowly increasing the temperature in unit steps until the subject's tolerable pain threshold was attained. The bearable range was determined to be 45 - 48℃ across the recruited subjects. Hence the stimulus delivery for the

actual experiment was fixed at 48℃ across all the subjects. It has to be noted that 48℃ was way below the maximum temperature (that is 52℃) that the FDA approved Pathway stimulator thermode can deliver. This step of estimating subjective pain threshold was carried out before the actual experiment. If any specific volunteer pain threshold was determined to be less than the range of 45-48℃, then that specific volunteer was not recruited to continue with the experiment.

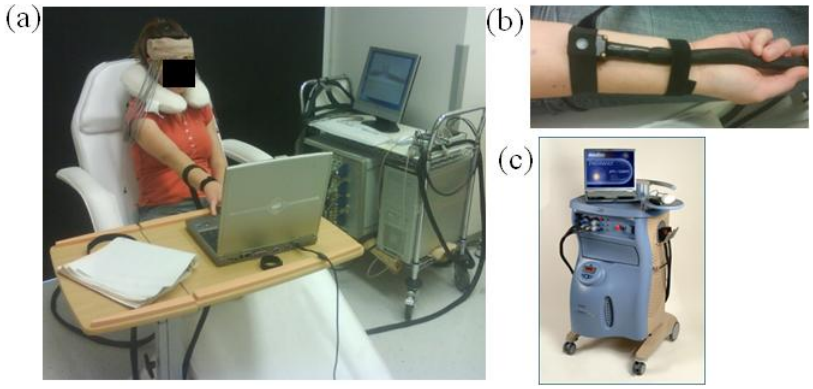

Figure 6-1:Experimental setup. (a) shows the subject with probe on and wrapped with gauze. The CW imager can be seen to the right and the laptop is placed in front subject for psychological rating. (b) the thermode is strapped on marked area on subjects volar forearm. (c) Pathway stimulator for thermal stimulation.

Figure 6-2 shows the experimental protocol that was based on blocked design. The protocol comprised of 8 functional blocks, each with a block length of 35 sec. Each functional block sub-comprised of 10 sec of pain delivery via thermode followed by 25 sec resting period. For pain delivery during each functional block, the thermode's rise and fall time was set at 3℃/sec, resulting in approximately 1.33 sec of noxious pain delivery at 48℃. The baseline and resting period temperature was set at 35℃, and the pre- and post-baseline time length was designed for 30 sec. During the optical measurements, the subjects were instructed to keep their eyes closed and to focus on the marked area of their volar forearm. It has to be noted that the protocol design shown below (Figure 6-2) was tailored to the same parameters as that of the mechanical (pinch) protocol design described in section 5.3.2

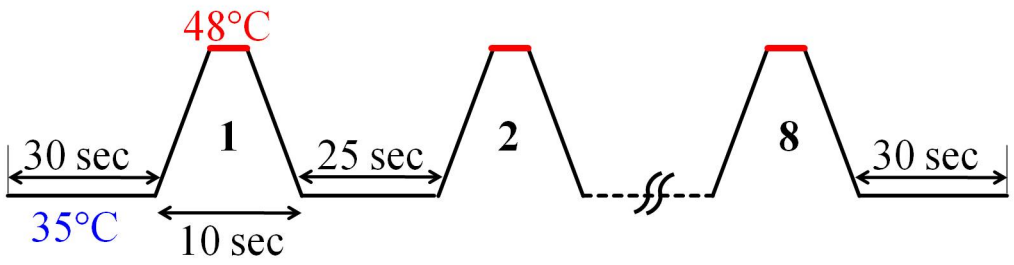

Figure 6-2: A schematic for block-design protocol. The protocol incorporated 8 blocks of 10 sec stimulation and 25 sec recovery period. The stimulation block comprised a linear rise and fall slope of 3℃/sec; the stimulation at 48℃ was appli ed for 1.33 sec. The protocol begins and ends with 30 sec pre- and post baseline during which thermode is set at 35℃.

Immediately following the experimental protocol, the subjects were asked to rate their pain level through the AVAS software. The experimental setup in Figure 6-1(a) shows the laptop placed comfortably in front of the subject for the purpose of rating. When the subjects walked into the experiment room, they were given clear instructions about the study, and they received training through the pain rating training module made available on the AVAS software. They practiced through the training modules until they were comfortable with the rating procedure they were required to do immediately following the experimental measurements. The pain rating displayed on the laptop through the AVAS software had the standard rating of 0-100 (0: no pain, 100: excruciating pain). A thick black line of 10cm long was displayed in the center of the screen. The subjects had to click the cursor anywhere on the thick black line, denoting their rating, which was automatically saved into an EXCEL worksheet. On the vertical thick black line, the bottom of the line displayed the level of 0, while the top displayed 100. More details on Adaptive Visual Analog Scale (AVAS) software is described elsewhere (Marsh-Richard, Hatzis, Mathias, Venditti, & Dougherty, 2009).

6.3.3 Data Acquisition

The details on data acquisition were previously described in section 5.3.3 . The goal of this specific aim was to validate the observations from mechanical (pinch) stimulation study using a different mode of pain delivery which was the thermal stimulation. For consistency purposes,

the data acquisition was carried out with the same probe design and acquisition procedures as described in section 5.3.3 .

6.3.4 Data Analysis

As explained above, the goal was to have consistent methodologies for scientific comparison between mechanical and thermally induces pain perception. Hence, similar data analysis procedures as described in sub-sections under section 5.3.4 were implemented in this study.

6.4 Results

The following analyzed data is comprised of results from the clustered-wise analysis method and supporting reconstructed images. Details of the methodology are described in the data analysis section of the previous chapter. The motivation here is to quantify NIRS measured parameters that correlate with subjective pain perception in response to noxious thermal stimuli at 48℃, which leads to objective quantification of pa in perception using NIRS.

6.4.1 Anterior Prefrontal Cortex (BA 10)

Figure 6-3(a) shows the selected channels of the aPFC area used in cluster-wise analysis. The sources covering the aPFC are denoted by the pink circles outlined in bold (from left to right: X3, X4, X8, and X7). The detectors collecting the signals from the aPFC are shown as solid green boxes, outlined in bold (from left to right, top to bottom: D4, D12, D8, and D16). The black, dashed lines denote the channels disabled for clustered-wise analysis of the aPFC. The red solid lines show the channels of contra-aPFC (X3-D4, X4-D4, X3-D8, X4-D8), and the solid blue lines show the channels of ipsi-aPFC (X8-D12, X7-D12, X8-D16, X7-D16).

Figure 6-3(b) below shows the averaged temporal plots from the aPFC (BA 10) area. Note that in response to the noxious heat stimuli, late phase from both ipsi and contra aPFC undergoes HbO deactivation (Figure 6-3 (b)). The statistical verification of the above statement is explored in the following sub-section.

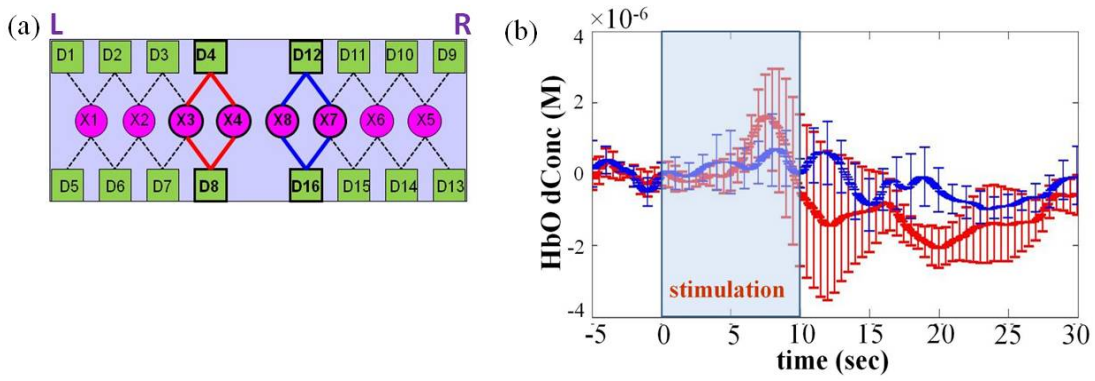

Figure 6-3: (a) Channels covering anterior PFC (b) Grand averaged temporal plots along with standard deviation shown by the error bars. The grand average included averaging across the 8 blocks for each subject, followed by group temporal averaging across the 5 subjects. Note: pink circles: sources; green box: detectors; dashed line: disabled channels; solid red line: contra aPFC; solid blue line: ipsi aPFC; L: left hemisphere and R: right hemisphere.

6.4.1.1 Significance of 48℃-induced HbO Changes

The activation/deactivation changes observed in the temporal response need to be statistically verified for significance with respect to the associated baseline. In section 5.3.4.5 , the methodological details for statistical test for significance between the baseline and the pain-induced HbO changes were explained. The baseline time length was set at 5 sec (that is -5 to sec). The data sampling rate was set at a down-sampled rate of 10 data points/sec. This implied that for baseline, a time bin of 50 data points were obtained. The key focus of this dissertation work is to quantify ΔHbO changes. Hence, the time period that comprised of FWHM time period encompassing PI during activation/deactivation was compared with that of the baseline. The FWHM within the early (0.1-12sec) and late phase (12.1-25sec) was extracted for both ipsi- and contra- response as shown in Figure 5-4. For late phase, if necessary, the last 5sec of the functional block, that is 25-30sec, was incorporated for accurate quantification of the FWHM.

The data points from the baseline and from the 48℃-induced early and late phase HbO changes associated with the aPFC for each subject (*N*=5) were laid out continuously on a spread sheet and imported into the SAS software for mixed modeling analysis. The SAS code and results from the mixed modeling analysis for comparison between the baseline and 48℃-induced HbO changes are shown in Appendix D. Figure 6-4 below summarizes the mean estimates and

associated standard errors for both baseline and 48℃-induced HbO changes from the aPFC cortical area.

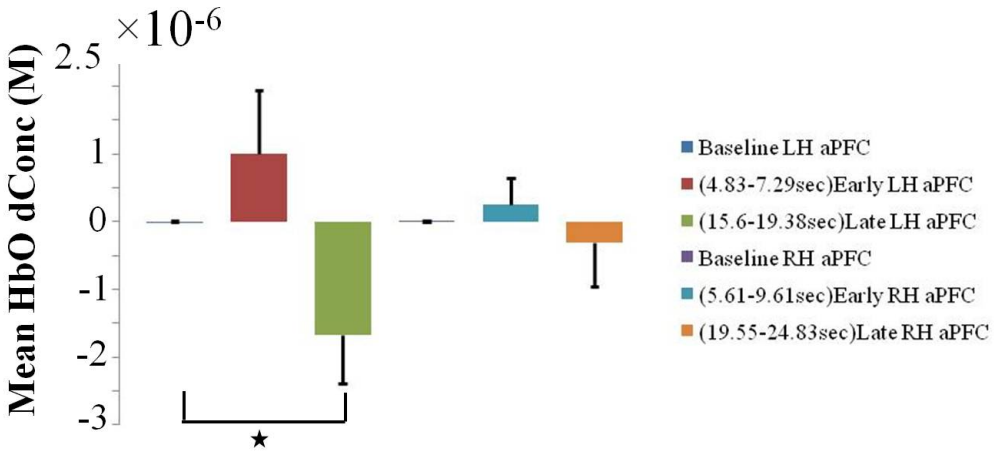

Figure 6-4: Summary of mean estimates and standard errors obtained for the baseline and 48℃-induced HbO changes in the aPFC area using Linear Mixed Model. Note: The baseline was fixed at -5 to 0sec and the * indicates significant difference at 0.05.

The mean estimates for the baseline from both LH and RH aPFC were observed in the range of 10^{-11} M. Similarly from Figure 6-4, the mean estimates for the 48℃-induced changes were in the range of 10^{-6} M in the LH aPFC and 10^{-7} M in the RH aPFC respectively. This implies that 48℃ thermal stimulation induced a change in t he HbO response magnitude by an order of at least 10000. Specifically, we can also observe that the mean estimates for 48℃-induced change during the late phase are -1.68×10^{-6} M and -3.05×10^{-7} M in the LH and RH aPFC respectively. Comparing these values to the respective baseline values, we can clearly observe that the stimulus-induced HbO changes show a trend for deactivation in response to the 48℃ thermal stimulation. Since both the LH and RH aPFC show negative HbO changes with respect to the baseline, we can deduce that a trend for bilateral deactivation was observed in the aPFC area during the late phase while a trend for bilateral activation was observed during the early phase.

The next important step was to investigate the significance of 48℃-induced changes with respect to the baseline. The observed p-values shown in Table 6-1 were obtained from the linear mixed model analysis for comparison between baseline and 48℃-induced HbO changes. From

Table 6-1, we can clearly notice that significant 48℃-induced HbO changes were not observed with respect to the baseline except for the late phase in the LH aPFC area. This could probably be due to the small size of subject pool and also that in this preliminary study; we did not consider the between-subject variability or the random effects. However, it was promising to find late phase significance with respect to the baseline and hence the late phase of the HbO changes from the aPFC will be continued with further analyses for quantification for PI and FWHM and its correlation with cognitive evaluation of pain perception.

Table 6-1: Summary of significance for 48℃-induced HbO changes with respect to the baseline. Note: The critical value for significance is 0.05 and the green shade indicates the observed significance; LS stands for least square and the baseline was fixed at -5 to 0sec.

Baseline/Stimulation comparison	LS Mean Difference(M)	Std. Error (M)	Pr > |t|	Significantly Induced Change
LH aPFC (t=4.83 to 7.29 sec)$_{early}$	1.00×10^{-6}	9.47×10^{-7}	$p = 0.294$	No change
LH aPFC (t=15.6 to 19.38 sec)$_{late}$	-1.68×10^{-6}	6.98×10^{-7}	**$p = 0.021$**	Deactivation
RH aPFC (t=5.61 to 9.61 sec)$_{early}$	2.45×10^{-7}	3.98×10^{-7}	$p = 0.542$	No change
RH aPFC (t=19.55 to 24.83 sec)$_{late}$	-3.06×10^{-7}	6.42×10^{-7}	$p = 0.636$	No change

6.4.1.2 Correlates for Cognitive Evaluation from aPFC

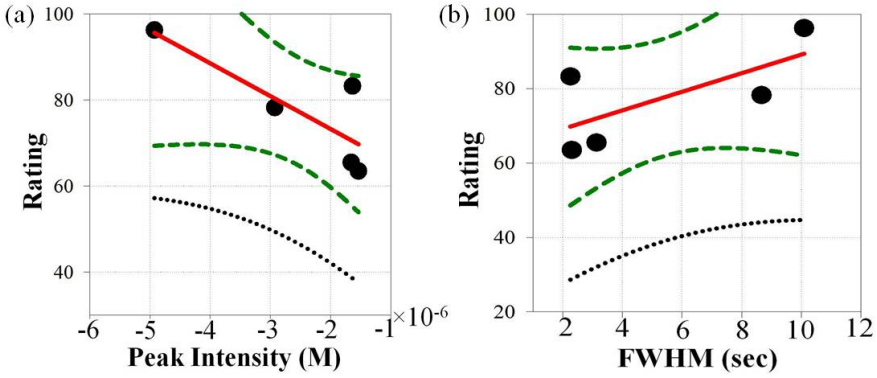

Figure 6-5: Linear regression between subjective pain rating and HbO-derived parameters from the *late* phase of LH aPFC. (a) Peak Intensity (p=0.086) (b) FWHM (p=0.187).Note: solid black dots denote raw data ; thick red lines denote the regression line ; dashed dark green lines denote the 95% confidence interval for regression ; and dotted black lines denote the 95% confidence interval for raw data.

From Figure 6-4, statistical significance was observed between baseline and late phase LH aPFC HbO changes. Hence the group level linear regression was carried out between the late

phase HbO-derived PI and FWHM extracted from the LH aPFC and subjective pain rating. As shown in Figure 6-5, for linear regression, pain rating was considered as the dependent variable and PI as the independent variable. Equation 6.2 below show the linear relationship between pain rating and late phase HbO-derived FWHM from ipsi-aPFC (p=0.187, r=0.7, R^2=0.49). Similarly, Equation 6.3 shows the relationship between pain rating and the late phase HbO-derived PI from ipsi-aPFC (p=0.086, r=0.82 R^2=0.68). Each of the regression fittings passed the Shapiro-Wilk normality test and constant variance test.

$$Rating(48℃) = 64.14 + 2.49 * FWHM\_late\_\text{ipsi } aPFC \quad 6.1$$

$$Rating(48℃) = 57.95 - 7.64 \times 10^6 * PI\_late\_\text{ipsi } aPFC \quad 6.2$$

From Table 6-1, we can observe that 48℃ stimulatio n induced significant HbO changes only during the late phase of LH aPFC. However, the quantified parameters (that is PI and FWHM) from the late phase HbO changes does not show a significant relationship with the cognitive evaluation of pain. From this study with a limited number of subjects (N=5), we observe a significance of p=0.086 for ΔHbO-derived PI and pain rating, and a significance of p=0.187 for HbO-derived FWHM and pain rating. From the regression plots, for example in Figure 6-5(a), the question arises whether the left-most extreme data point is an outlier. Further, if this data point is excluded from the regression analysis, would the correlation relationship still hold good. To explore this question, the left-most extreme data point (subject S28) was excluded and similar regression analysis was carried out with the remaining 4 data points. The resulting correlation was still negative between pain rating and late PI from ipsi aPFC (p=0.58 and R^2=0.176).

Although from Table 6-1, there was no significance observed between late phase HbO changes from RH aPFC, it was still imperative to explore whether the ΔHbO derived parameters from the RH aPFC significantly correlated with the pain rating. Table 6-2 below summarizes the correlation coefficient (r) and significance (p-value) for ΔHbO derived parameters from both LH and RH aPFC. We observe from the table below that no significant correlation was observed between ΔHbO derived parameters from the RH aPFC and pain rating. However, a strong correlation was observed between pain rating and HbO-derived PI from LH aPFC (r=0.82), pain rating and HbO-derived FWHM from LH aPFC (r=0.7), pain rating and HbO-derived FWHM from

RH aPFC (r=0.62). These results indicate that further investigation is necessary to validate the correlation observed from the current results in order to enhance the confidence that these HbO-derived parameters significantly reflect cognitive evaluation of pain perception.

Table 6-2: Summary of significance and correlation coefficient obtained for relationship between HbO-derived parameters from the late phase of aPFC and pain rating. Note: r: correlation coefficient obtained from linear regression analysis; p: significance of relationship between the two variables shown within the square brackets [].

Cortical area	**[Peak Intensity, Pain Rating]**	**[FWHM, Pain Rating]**
LH aPFC	r = 0.82	r = 0.70
	p = 0.086	p = 0.187
RH aPFC	r = 0.17	r = 0.62
	p = 0.779	p = 0.262

6.4.2 Dorsolateral Prefrontal Cortex (BA 46)

Figure 6-6(a) shows the selected channels of the DLPFC area used in cluster-wise analysis. The sources covering the DLPFC are denoted by the pink circles outlined in bold (from left to right: X1 and X5). The detectors collecting the signals from the DLPFC are shown as solid green boxes, outlined in bold (from left to right, top to bottom: D1, D2, D10, D9, D5, D6, D14, D13). The black, dashed lines denote the channels disabled for clustered-wise analysis of the DLPFC. The red solid lines show the channels of contra-DLPFC (X1-D1, X1-D2, X1-D5, X1-D6), and the solid blue lines show the channels of ipsi-DLPFC (X5-D10, X5-D9, X5-D14, X5-D13).

Figure 6-6(b) below shows the averaged temporal plots from the DLPFC (BA 10) area. Visual inspection of the temporal response shows that the early phase from both ipsi and contra DLPFC had a trend for ΔHbO deactivation while a trend for ΔHbO activation was observed during the late phase. The statistical verification of the above statement is explored in the following sub-section.

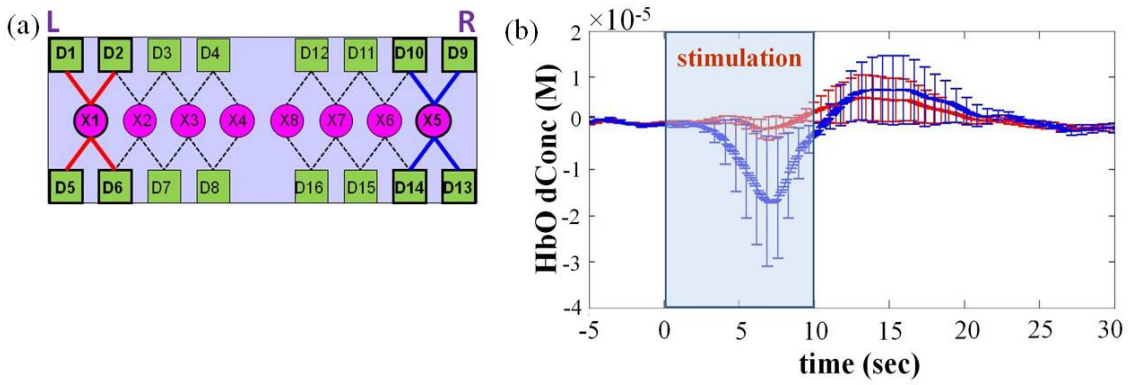

Figure 6-6: (a) Channels covering dorsolateral PFC (b) Grand averaged temporal plots along with standard deviation shown by the error bars. The grand average included averaging across the 8 blocks for each subject, followed by group temporal averaging across the 5 subjects. Note: pink circles: sources; green box: detectors; dashed line: disabled channels; solid red line: contra DLPFC; solid blue line: ipsi DLPFC; L: left hemisphere and R: right hemisphere.

6.4.2.1 Significance of 48℃-induced HbO Changes

The key focus of this dissertation work was to quantify the ΔHbO changes. Hence, the time period that comprised of FWHM time period encompassing PI during the stimulation-induced HbO changes was compared with that of the baseline. The FWHM within the early (0.1-12sec) and late phase (12.1-25sec) was extracted for both ipsi- and contra- response as shown within parentheses in Figure 6-7. For late phase, if necessary, the last 5sec of the functional block, that is 25-30sec, was incorporated for accurate quantification of the FWHM.

The data points from the baseline and from the 48℃-induced early and late phase HbO changes associated with the DLPFC for each subject (N=5) were laid out continuously on a spread sheet and imported into the SAS software for mixed modeling analysis. The SAS code and results from the mixed modeling analysis for comparison between the baseline and 48℃-induced HbO changes are shown in Appendix D. Figure 6-7 below summarizes the mean estimates and associated standard errors for both baseline and 48℃-induced HbO changes from the DLPFC area.

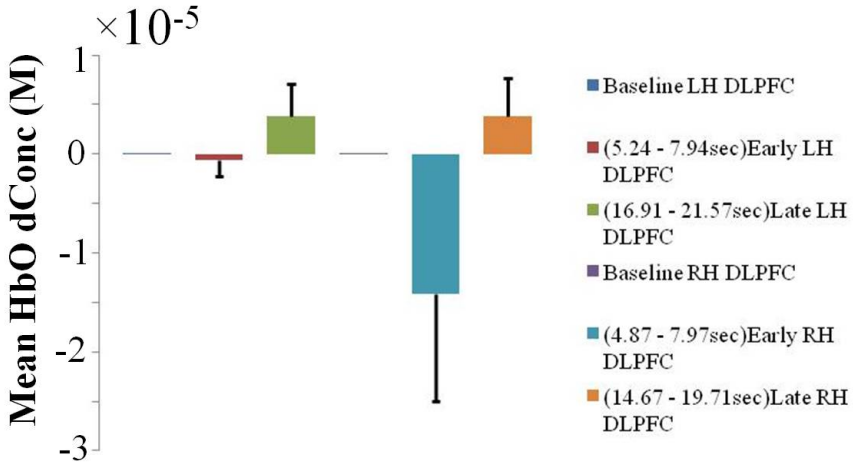

Figure 6-7: Summary of mean estimates and standard errors obtained for the baseline and 48℃-induced HbO changes in the DLPFC area using Linear Mixed Model. Note: The baseline was fixed at -5 to 0sec.

The baseline mean estimate for the LH DLPFC was found in the range of 10^{-10} M and that for the RH DLPFC was observed in the range of 10^{-9} M. From Figure 6-7, it can also be observed that the standard error for baseline HbO changes were higher by an order of 10 compared to the mean estimates. The mean estimates for the 48℃ -induced changes, specifically in the late phase HbO changes, were in the range of 10^{-6} M in both the LH and RH DLPFC. This implies that 48℃ thermal stimulation induced a change in the HbO response magnitude by an order of at least 1000. The mean estimates for 48℃-induced HbO change during the late phase were 3.79×10^{-6} M and 3.86×10^{-6} M in the LH and RH DLPFC respectively. Comparing these values to the respective baseline values, we can clearly observe that the 48℃ stimuli induced activation in the ΔHbO response. Since both the LH and RH DLPFC show activation with respect to the baseline, we can deduce that bilateral activation was observed in the DLPFC area in response to 48℃ thermal stimulation during the late phase of the stimulation.

The next important step was to investigate the significance of 48℃ -induced changes with respect to the baseline in the DLPFC area. The observed p-values shown in Table 6-3 were obtained from the linear mixed model analysis for comparison between the baseline and 48℃-induced HbO changes. From Table 6-3, we can clearly notice that significant 48℃-induced HbO

changes were not observed with respect to the baseline in the DLPFC area. This could probably be due to the small size of subject pool and also that in this preliminary study; we did not consider the between-subject variability or the random effects.

Table 6-3: Summary of significance of 48℃-induced HbO changes with respect to the baseline in the DLPFC area. Note: The critical value for significance is 0.05; LS stands for least square and the baseline was fixed at -5 to 0sec.

Baseline/Stimulation comparison	LS Mean Difference(M)	Std. Error (M)	Pr > |t|	Significantly Induced Change
LH DLPFC (t=5.24 to 7.94 sec)$_{early}$	-6.51×10^{-7}	1.57×10^{-6}	$p = 0.679$	No change
LH DLPFC (t=16.91 to 21.57 sec)$_{late}$	3.79×10^{-6}	3.26×10^{-6}	$p = 0.252$	No change
RH DLPFC (t=4.87 to 7.97 sec)$_{early}$	-1.41×10^{-5}	1.09×10^{-5}	$p = 0.203$	No change
RH DLPFC (t=14.67 to 19.71 sec)$_{late}$	3.85×10^{-6}	3.78×10^{-6}	$p = 0.315$	No change

6.4.2.2 Correlates for Cognitive Evaluation from DLPFC

From Table 6-3 above, we observed that there was no significant HbO changes induced in the DLPFC area in response to the 48℃ thermal stimuli. Although the late phase does not show significant HbO changes, the mean estimates showing the magnitude change (Figure 6-7) are larger than that from the baseline by an order of at least 1000. Further, the standard errors for the late phase HbO changes are smaller compared to the stimulation-induced mean estimates. Given the preliminary nature of this study and that we had only 5 subjects; correlation between the ΔHbO-derived parameters (that is PI and FWHM) and the behaviorally measured pain rating was investigated in this study. The following figures below show the regression between HbO-derived PI and FWHM and pain rating during the late phase.

As shown in Figure 6-8, for linear regression, pain rating was considered as the dependent variable and PI as the independent variable. Equation 6.3 below show the linear relationship between pain rating and late phase HbO-derived FWHM from ipsi/LH DLPFC (p=0.280, r=0.6, R^2=0.37). Similarly, Equation 6.3 shows the relationship between pain rating and the late phase HbO-derived PI from ipsi/LH DLPFC (p=0.045, r=0.89 R^2=0.79). Each of the regression fittings passed the Shapiro-Wilk normality test and constant variance test.

$$Rating(48℃) = 62.15 + 3.01 * FWHM\_late\_\text{ipsi DL}PFC \quad 6.3$$

$$Rating(48℃) = 71.45 + 1.07 \times 10^{6} * PI\_late\_\text{ipsi DL}PFC \quad 6.4$$

From Table 6-3, we can observe that 48℃ stimulation induced HbO changes were not significant in the late phase of the DLPFC area. However, the quantified parameters (that is PI) from the late phase HbO changes from LH DLPFC show a significant relationship with the cognitive evaluation of pain. From this study with a limited number of subjects (N=5), we observe a significance of p=0.045 for ΔHbO-derived PI and pain rating, and a significance of p=0.280 for HbO-derived FWHM and pain rating. Unlike the mechanical stimulation, it was interesting to observe that significant correlates were observed in the DLPFC area in response to thermal stimuli. From the regression plots, for example in Figure 6-8(a), the question arises whether the right-most extreme data point is an outlier. Further, if this data point is excluded from the regression analysis, would the correlation relationship still hold good. To explore this question, the right-most extreme data point (subject S28) was excluded and similar regression analysis was carried out with the remaining 4 data points. The resulting relationship was a significant positive correlation between pain rating and late PI from the LH DLPFC (p=0.036, r =0.96 and R^2=0.93).

From Table 6-3, we observed that there was no significance observed between late phase stimulation-induced HbO changes from the RH DLPFC area. Since we investigated for correlates from the LH DLPFC area that also did not had significant HbO changes in response to the thermal stimuli, it was imperative to explore whether the ΔHbO derived parameters from the RH DLPFC significantly correlated with the pain rating. Table 6-4 below summarizes the correlation coefficient (r) and significance (p-value) for ΔHbO derived parameters from both LH and RH DLPFC. We observe from the table below that no significant correlation was observed between ΔHbO derived parameters from the RH DLPFC and pain rating.

Table 6-4: Summary of significance and correlation coefficient obtained for relationship between HbO-derived parameters from the *late* phase of DLPFC and pain rating. Note: *r*: correlation coefficient obtained from linear regression analysis; *p*: significance of relationship between the two variables shown within the square brackets []; the critical value for significance is 0.05 and the green shade indicates the observed significance.

Cortical area	[Peak Intensity, Pain Rating]	[FWHM, Pain Rating]
LH DLPFC	$r = 0.89$	$r = 0.6$
	$p = 0.045$	$p = 0.280$
RH DLPFC	$r = 0.81$	$r = 0.13$
	$p = 0.092$	$p = 0.837$

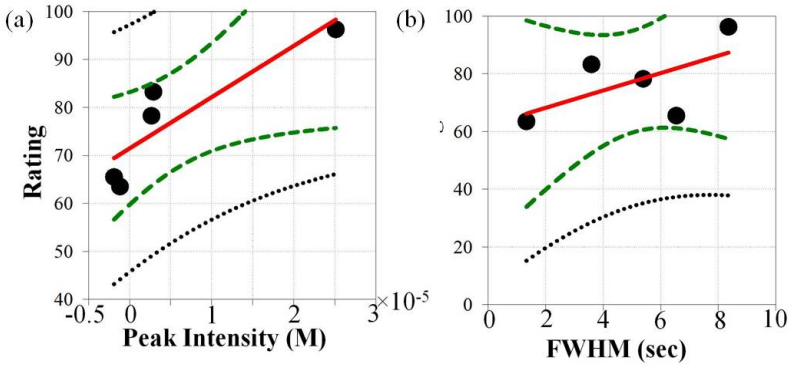

Figure 6-8: Linear regression between subjective pain rating and HbO-derived parameters from the late phase of LH DLPFC. (a) Peak Intensity (p=0.045) (b) FWHM (p=0.280).Note: solid black dots denote raw data ; thick red lines denote the regression line ; dashed dark green lines denote the 95% confidence interval for regression ; and dotted black lines denote the 95% confidence interval for raw data.

6.4.3 Are the Correlates from the LH aPFC Biased by Anticipation?

Similar to the mechanical stimulation as described in the previous chapter, the anticipation effects on cognitive evaluation of pain was explored in this specific aim. Since aPFC has been reported to also play a role in processing the anticipatory effects (Porro, et al., 2002), we undertook the investigation to explore whether anticipation affected the correlates obtained for cognitive evaluation of pain in the aPFC area. The details on approach taken to explore the anticipation effect are described in section 5.3.4.7 .

Although we did not find significant correlates from the late phase of LH aPFC, the stimulation-induced HbO changes were significant with respect to the baseline (Table 6-1). Therefore, it is necessary to tease out the anticipation effects on the correlates from the LH aPFC

area. Thus, the PI was derived from the LH aPFC derived grand averaged HbO response, where the first block was excluded, and statistically compared with the HbO-derived PI, where the first block was included. In Figure 6-9 below, the solid pink temporal plot shows the block averaged temporal HbO response (average of 2nd through the 8th functional block) along with standard error mean. The analysis for anticipation effects as described in section 5.3.4.7 was carried out on the LH aPFC derived HbO measurements (that is with the first block disabled and averaging of the remaining blocks). A paired t-test between the PI (with and without the first block included) values resulted in a significance of p=0.213. The p-value greater than 0.05 between the mean values for PI implied that anticipation did not influence the cognitive evaluation of pain reflected through PI.

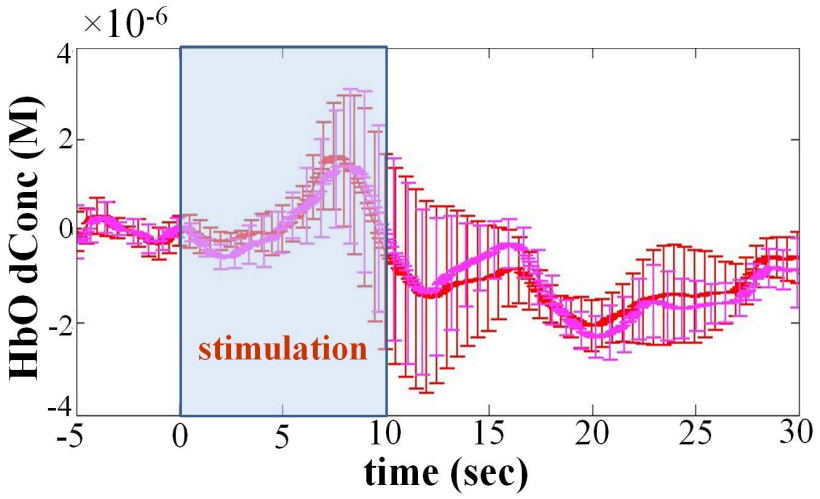

Figure 6-9: Grand averaged ΔHbO temporal plots (N=5) with and without the first block included into the block averaging to explore the anticipation effect in *ipsi/LH* aPFC. Note: solid red line: first block included; solid pink line: first block excluded; error bars denote the standard error mean across the subjects.

6.4.4 Significant Difference between aPFC and DLPFC HbO Changes

Sub-hypotheses 6.2.1 and 6.2.3 were solely based on investigating the significance of 48℃-induced HbO changes with respect to baseline in the aPFC and DLPFC areas respectively. We observed from Table 6-1 and Table 6-3 that significance was observed between the baseline and 48℃-induced HbO changes only in the LH aPFC area. However, given that we obtained measurements simultaneously from both the aPFC and DLPFC areas, we assume that inherently

there exists a correlation between the measurements from the two different cortical areas for each subject. This was modeled in the covariance structure of the linear mixed model by assuming equi-correlation between all the measurements which refers to the compound symmetry structure.

From Table 6-1, we observe that there was significance (p<0.05) between the HbO changes before and after the thermal stimuli only during the late phase of the aPFC area. Further, from Table 6-4, we observed significant correlation between HbO-derived PI quantified from the late phase of the LH DLPFC area. Since our interest in this study was to quantify correlates, we focused on the late phase HbO changes from the DLPFC area (shown by yellow shade in Table 6-5). We observe that there is no significant difference between the estimates from the late phase of aPFC and the late phase of DLPFC HbO changes. Non-significance could possibly be due to the limited size of our subjects and the variability between the subjects. However, it could also be possible that both the areas are coherently involved to some extent in the processing of pain. These possibilities need further investigation that is currently not investigated in this study.

Table 6-5: Summary of significance between 48℃-ind uced HbO changes from aPFC and DLPFC areas. Note: LH: Left hemispheric; RH: Right hemispheric; LS: Least square; the yellow shade indicates the areas and associated phase from which significant correlates were obtained in section 6.4.2.2 .

aPFC	DLPFC	LS Mean Difference(M)	Std. Error(M)	Pr > |t|
LH_{late}	LH_{late}	-5.47×10^{-6}	3.92×10^{-6}	p=0.169
RH_{late}	LH_{late}	4.1×10^{-6}	3.58×10^{-6}	p=0.258
LH_{late}	RH_{late}	-5.53×10^{-6}	4.44×10^{-6}	p=0.219
RH_{late}	RH_{late}	-4.16×10^{-6}	4.1×10^{-6}	p=0.316

6.4.5 Summary of Correlates

Table 6-6 below summarizes the correlates between the HbO-derived parameters and the behaviorally measured pain rating under the 48°C thermal stimulation. One of the key observations is that the correlates were observed only during the late phase of the DLPFC area. Further from Figure 6-7, we observed a trend for late phase ΔHbO activation in the DLPFC area. This implies that from this preliminary study, the HbO activation observed in the DLPFC area through fNIRS measurements; reflect the cognitive evaluation of pain perception.

Table 6-6: Summary of *significant* correlates between ΔHbO-derived parameters and pain rating under 48℃ thermal stimulation. Note: RH: right hem ispheric; LH: left hemispheric; (+): positive correlation; (-): negative correlation; --: no correlates; PI: ΔHbO-derived Peak Intensity.

	Early phase	**Late phase**
RH aPFC	--	--
LH aPFC	--	--
RH DLPFC	--	--
LH DLPFC	--	(+)PI

6.4.6 Reconstructed ΔHbO Images

Reconstructed ΔHbO images are very helpful in displaying scientifically meaningful, yet intuitive, information readily in the clinical environment. However, the current results are limited by a small subject pool and by the inherent drawbacks of backprojection algorithm as applied to diffuse optical imaging.

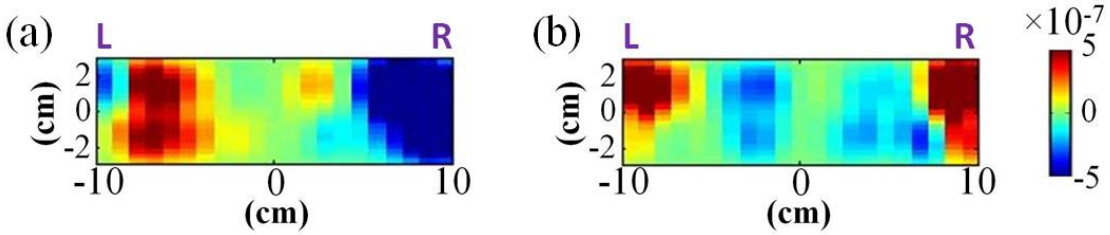

Figure 6-10: Reconstructed ΔHbO images in (a) early response (b) late response for 48℃ thermal stimulation. Note: the color bar range shows blue for deactivation and red for activation; the image for early response is the temporal average across 0.1-12sec while that for late response is the temporal average across 12.1-25sec; L: left hemisphere and R: right hemisphere.

Figure 6-10(a) and 6-8(b) show the ΔHbO reconstructed images for the early and late phase respectively. Visual inspection of the aPFC area (selected channels as shown in Figure 5-3(a)), from the above figure show a weak ΔHbO activation (shown by yellow) in the ipsi aPFC during the early response while in the same area, ΔHbO deactivation (shown by blue) was observed during the late phase. At this point, it is important to recall that for mechanical stimulation, a trend for ΔHbO deactivation was observed during the early phase (Figure 5-16) while here, a trend for HbO deactivation was found during the late phase. This shows that reconstructed images are helpful in finding the similarities and differences between different

studies in an intuitive fashion. Figure 6-10(b) shows bilateral ΔHbO activation (shown by red) during the late phase and a strong ΔHbO deactivation in the right DLPFC (selected channels as shown in Figure 5-3(b)) during the early phase. It was promising to observe that the above observations from preliminary reconstructed images corroborate with the clustered-wise analysis on channels covering specific cortical (that is aPFC and DLPFC) areas.

6.5 Discussion

The specific aim delineated in this chapter focused on HbO changes in response to 48℃ thermal stimulation. The major goals of this specific aim were: (1) to investigate whether the 48℃-induced HbO changes were significant with respect to the baseline in both the aPFC and DLPFC areas. (2) Given the preliminary nature of this study with only 5 recruited subjects, obtain the correlates between behaviorally measured pain rating and the HbO-derived parameters (that is PI and FWHM) from the aPFC and DLPFC areas. (3) The final major goal was to test the robustness of the correlates in reflecting the cognitive evaluation of pain perception.

Section 6.2 describes the major sub-hypotheses that were investigated for this specific aim. In the first two sub-hypotheses we focused on significance of 48℃-induced HbO changes in the aPFC area and whether the correlates quantified from the same area significantly reflects cognitive evaluation of pain. In order to tease apart the significance of 48℃-induced HbO changes, we relied on the linear mixed modeling analysis. The technical details on this method were described in section 5.3.4.4 . From Table 6-1 and Figure 6-3(b), we observe a trend for bilateral ΔHbO deactivation in the aPFC areas. It was interesting to note from Table 6-1 that the 48℃-induced HbO changes in the late phase of LH aPFC were significant with respect to associated baseline. This was promising given that we had only 5 healthy volunteers recruited for this study. Further, significant HbO changes in the LH aPFC also corroborates with a fMRI study that reported significant BOLD response from the LH medial prefrontal areas in response to noxious thermal stimulation (L. Becerra, Breiter, Wise, Gonzalez, & Borsook, 2001).

Now moving on to the second major sub-hypothesis (that is 6.2.2), from Table 6-2, we observed that no significant relationship was observed between the HbO-derived parameters

from aPFC and pain rating. Although the late phase HbO changes from LH aPFC were significant with respect to the baseline, the quantified parameters did not significantly correlate with the pain rating. A major striking difference between mechanical and 48℃ thermal stimulation was that the trend for ΔHbO deactivation in response to pain were observed in different phases. That is, for mechanical the ΔHbO deactivation was observed during the early phase while for 48℃ thermal stimulation, the ΔHbO deactivation was observed during the late phase. This could possibly stem from the peripheral factors such as *A-δ* fibers and *A-β* fibers (Treede, Meyer, & Campbell, 1998; Willis WD, 2005). In addition to *A-β* and *A-δ* fibers, slow conducting *C* fibers have also been shown to differentially impact the hemodynamic responses from deeper sub-cortical areas (Koltzenburg & Handwerker, 1994; Qiu, et al., 2006).

In light of the HbO changes in the DLPFC area, the sub-hypotheses 6.2.3 and 6.2.4 in section 6.2 were posited in this study. From Figure 6-7, we observed that the HbO changes induced by 48℃ thermal stimuli in the DLPFC area w ere opposite to that in the aPFC area during the late phase. In other words, during late phase, we observed a trend for HbO deactivation in the aPFC area and a trend for HbO activation in the DLPFC area. This could possibly be due to simultaneous depolarization-led vasodilation in the DLPFC areas while hyperpolarization-led vasoconstriction in the aPFC area (Devor, et al., 2007). Focusing on the HbO changes from the DLPFC area, we observe from Table 6-3 that pain-induced HbO changes were not significant with respect to the associated baseline. This could possibly be due to the limited subject pool (*N*=5) in this study and demands further investigation. Further, the HbO reconstructed image for early phase corroborates the finding from clustered-wise analysis that a trend for HbO deactivation was observed in the RH DLPFC area. Although the early phase HbO deactivation in the DLPFC was not significant as shown in Table 6-3, the HbO deactivation could possibly be invoked by pain induced synaptic inhibition and vasoconstriction (Devor, et al., 2007). In addition to pain induced synaptic inhibition and vasoconstriction, sex differences could also influence the negative HbO response and its magnitude. A recent fMRI study on gender role in pain perception has shown higher negative BOLD amplitude in RH DLPFC. This has been attributed to differences in baseline cerebral blood flow between the genders (Moulton, et al., 2006). Although

both male and female healthy volunteers were recruited for this study, they were not evenly balanced and hence the influence of gender on the magnitude of negative HbO response needs further investigation.

From the above discussion, we found that HbO changes in response to 48℃ thermal stimuli were not significant in the DLPFC area. However, given the preliminary nature of this study, we continued our investigation for correlates if any from the DLPFC area. It was interesting to find that the late phase HbO-derived PI from the LH DLPFC significantly correlated with the pain rating. From Figure 6-8(a), we observed a significant positive correlation between HbO-derived PI from the late phase of LH DLPFC and pain rating. This implies that at the group level, as the PI increases, it reflects an increase in the perception of pain. Further from Table 6-4, we observed that significant correlate was obtained only from the late phase of LH DLPFC. In the light of discriminating perception of two different kind of stimuli (that is mechanical and 48℃ thermal), it was interesting to observe that mechanical stimulation involved the aPFC area while the 48℃ thermal stimulation involved the LH DLPFC area.

A recent fMRI study has shown that the aPFC is significantly involved in the processing of anticipation under pain (Porro, et al., 2002). Although in this specific aim, we did not find significant correlates from the aPFC area (Table 6-2), given that we had only 5 subjects recruited for this study, we observed a strong correlation (r = 0.82) between late phase HbO-derived PI from the LH aPFC and pain rating. Hence it was imperative to investigate whether the correlate obtained from the aPFC area was affected by anticipation in response to noxious thermal stimuli. It was found that higher anticipation in response to the first stimulus did not interfere with the cognitive evaluation. However, these preliminary results must be verified for: (a) significance of correlates from LH aPFC area by recruiting more healthy subjects and (b) an experimental protocol design approach that disentangles anticipatory stress from cognitive evaluation of pain. Due to their periodic nature, block design experimental protocols result in habituation which may affect anticipation. Hence, further work is necessary to experimentally test for habituation and any of its effects on anticipation by incorporating event-related or mixed design protocols.

In conclusion, 48℃ thermal stimulation showed a tr end for late phase bilateral ΔHbO deactivation in the aPFC area. Specifically, the late phase HbO changes from the LH aPFC were significantly different from the associated baseline. In response to the same stimuli, we did not observe significant HbO changes in the DLPFC area with respect to associated baseline. Further from the regression analysis for correlation between pain rating and HbO-derived parameters, significant correlation was found only between HbO-derived PI from the late phase of LH DLPFC and pain rating. Although the correlates from the late phase of LH aPFC area were not significant, we observed a strong correlation between HbO-derived PI from the late phase of LH aPFC and pain rating. The investigation of anticipatory effects reasserted that the correlates obtained from LH aPFC area were robust in reflecting only the cognitive evaluation of pain. The next chapter discusses the investigation for correlates between HbO responses from prefrontal areas and cognitive evaluation of pain in response to a lesser noxious thermal pain (41℃).

CHAPTER 7

NEURAL CORRELATES FOR 41℃ THERMAL PAIN STIMULATION

7.1 Current Understanding

The observations from specific aims 1 and 2 (as described in Chapters 5 and 6 respectively) consistently showed significant role played by aPFC in cognitive evaluation of pain intensity. In the first specific aim, noxious pain was induced by pinching action, while in the second aim; the noxious pain was induced by thermal stimuli at 48℃. However in the first aim (that is pinching stimulation), the induced pain was not computer controlled at different levels of pain intensity. A recent fMRI study (Kong, et al., 2006) showed activation in medial prefrontal cortex mapped to cognitive evaluation of pain intensity, wherein they induced thermal pain at different levels with respect to neutral warm temperature at 34℃. Kong et.al protocol design incorporated randomized pain levels at three different levels interspersed with cognitive rating. However, the key interest of Kong et.al fMRI study was to separate sensory encoding from the cognitive evaluation.

In the first ever reported DOT study towards pain (L. Becerra, et al., 2008), the protocol incorporated fixed noxious temperature at 46℃. The major goal in Becerra et.al study was to investigate DOT's feasibility to measure hemodynamic changes in frontal and somatosensory areas in response to noxious pain.

The goals under this specific aim are multi-faceted. First, to validate consistency in correlates obtained from right hemispheric aPFC that were observed in response to 48℃ stimuli by inducing pain at a lower noxious (41℃) level. Secondly, to investigate the role played by prefrontal areas in cognitive discrimination of two different pain level (that is 48℃ and 41℃).

7.2 Sub-hypotheses

The major specific aim undertaken in this chapter is to investigate the detectability of fNIRS and the role of pre-frontal cortex to differentiate pain intensity. In order to methodically investigate the above specific aim, it is broken down in to sub-hypotheses as follows

1. Within the selected subject pool, **41℃** thermal stimulation will cause HbO change in the **anterior prefrontal cortex (BA 10)** during the **early (0.1 to 12sec)** and **late phase (12.1 to 25sec)** of the stimulation**.** 41℃-induced HbO changes are significantly different from the **baseline (-5 to 0sec)** HbO changes.
2. During the **late phase (12.1 to 25sec)** of the **41℃** thermal stimulation**,** the mean estimates from statistical testing for sub-hypothesis 7.2.1 show HbO deactivation in the **anterior prefrontal cortex**. The HbO-derived parameters **(PI and FWHM)** from the late phase have a **significant correlation** with the behaviorally measured **pain rating**.
3. Within the selected subject pool, **41℃** thermal stimulation will cause HbO change in the **dorsolateral prefrontal cortex (BA 46)** during the **early (0.1 to 12sec)** and **late phase (12.1 to 25sec)** of the thermal stimulation**.** 41℃-induced HbO changes are significantly different from the **baseline (-5 to 0sec)** HbO changes.
4. During the **late phase (12.1 to 25sec)** of the **41℃** thermal stimulation**,** the mean estimates from statistical testing for sub-hypothesis 7.2.3 show HbO activation in the **dorsolateral prefrontal cortex**. The HbO-derived parameters **(PI and FWHM)** from the late phase have a **significant correlation** with the behaviorally measured **pain rating**.
5. **HbO-quantified PI** from the **left hemispheric anterior prefrontal cortex** reflects the cognitive evaluation of pain perception. It is **not affected by anticipation** in response to the first pain stimulus.
6. The **late phase (12.1 to 25sec)** HbO-derived **time to peak (ttp)** obtained from the **left hemispheric aPFC** in response to **41℃** thermal stimuli is significantly

different from that obtained from the **left hemispheric aPFC** in response to **48℃** thermal stimuli.

7.3 Methods

In this section and subsequent subsections, the details on subjects, experimental protocol design, data acquisition and data analysis tailored for this specific aim are described.

7.3.1 Subjects

The same pool of subjects that were recruited for 48℃ study was continued for this specific aim. It has to be noted that the motivation here was to investigate the role of PFC in cognitive evaluation of pain perception under two different pain levels (that is 41℃ and 48℃). For consistency purposes, all other details remained the same as explained in sub-section 6.3.1 .

7.3.2 Experimental protocol

The details on experimental protocol are similar to that described in section 6.3.2 . However for this specific aim, the noxious stimulus intensity was changed from 48℃ to 41℃. The time period for each functional block was consistently maintained at 35sec. In order to do so, the slope for the thermode's rise and fall in temperature (from baseline temperature to the peak) was set at 1.34℃/sec for 41℃. However for 48℃, the r ise and fall slope was set at 3℃/sec. The entire 41℃ protocol was first completed followed b y the 48℃ protocol on each subject where the pain was induced on subject's dominant volar forearm. At the end of each protocol, the subjects were instructed to rate their pain level. The pain rating (0: no pain; 100: excruciating pain) was based on standard visual analog scale (VAS) which was available through the AVAS software (Marsh-Richard, et al., 2009). The two protocols were interspersed by sufficient resting time (approximately 10-15min) for two purposes: One was that the skin's thermoreceptors can desensitize during the resting time, and the second purpose was to ensure that the subject was rested comfortable enough to continue with the 48℃ protocol following the 41℃ protocol.

7.3.3 Data acquisition

The goal for this specific aim was to investigate fNIRS measured HbO changes in PFC in response to two different noxious pain intensities. In order to be consistent with specific aims 1 and 2, the data acquisition was carried out with the same probe design and acquisition procedures as described in section 5.3.3 .

7.3.4 Data analysis

As explained above, for consistency purposes, the data analysis procedures were similar to that for specific aims 1 and 2 as described in section 5.3.4 . In addition, linear mixed model analysis was also incorporated in this specific aim. The reason was that due to the repeated measurements on each subject, it was important to investigate the fixed effects of pain-induced changes in both aPFC and DLPFC areas across the subjects. The details on linear mixed model analysis are described in section 5.3.4.4 .

7.4 Results

The results shown here are based on clustered-wise analysis, and in addition, image reconstruction was also carried out for HbO changes in response to the pain stimuli. Details of the methodology are described in data analysis sub-section in Chapter 5. The motivation here was to quantify fNIRS measured parameters that correlated with subjective pain rating in response to 41℃ thermal stimulation.

7.4.1 Anterior Prefrontal Cortex (BA 10)

Figure 7-1(a) shows the selected channels of the aPFC area used in cluster-wise analysis. The sources covering the aPFC are denoted by the pink circles outlined in bold (from left to right: X3, X4, X8, and X7). The detectors collecting the signals from the aPFC are shown as solid green boxes, outlined in bold (from left to right, top to bottom: D4, D12, D8, and D16). The black, dashed lines denote the channels disabled for clustered-wise analysis of the aPFC. The red solid lines show the channels of contra-aPFC (X3-D4, X4-D4, X3-D8, X4-D8), and the solid blue lines show the channels of ipsi-aPFC (X8-D12, X7-D12, X8-D16, X7-D16).

Figure 7-1(b) below shows the averaged temporal plots from the aPFC (BA 10) area. Note that in response to the noxious heat stimuli, late phase from the ipsi/LH aPFC undergoes HbO deactivation (Figure 7-1(b)). The statistical verification of the above statement is explored in the following sub-section.

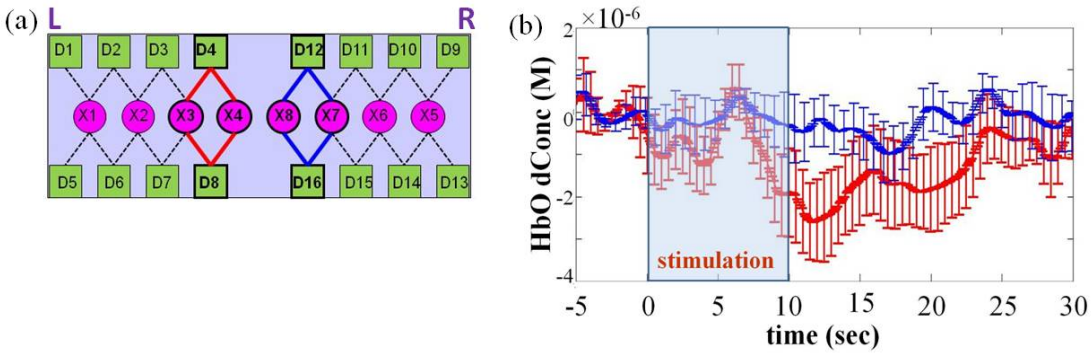

Figure 7-1: (a) Channels covering anterior PFC (b) Grand averaged temporal plots along with standard deviation shown by the error bars. The grand average included averaging across the 8 blocks for each subject, followed by group temporal averaging across the 5 subjects. Note: pink circles: sources; green box: detectors; dashed line: disabled channels; solid red line: contra aPFC; solid blue line: ipsi aPFC; L: left hemisphere and R: right hemisphere.

7.4.1.1 Significance of 41℃-induced HbO Changes in aPFC

The activation/deactivation changes observed in the temporal response need to be statistically verified for significance with respect to the associated baseline. In section 5.3.4.5 , the methodological details for statistical test for significance between the baseline and the pain-induced HbO changes were explained. The baseline time length was set at 5 sec (that is -5 to sec). The data sampling rate was set at a down-sampled rate of 10 data points/sec. This implied that for baseline, a time bin of 50 data points were obtained. The key focus of this dissertation work is to quantify ΔHbO changes. Hence, the time period that comprised of FWHM time period encompassing PI during activation/deactivation was compared with that of the baseline. The FWHM within the early (0.1-12sec) and late phase (12.1-25sec) was extracted for both ipsi- and contra- response as shown in Figure 7-2 within the parentheses. For the late phase, if necessary, the last 5sec of the functional block, that is 25-30sec, was incorporated for accurate quantification of the FWHM.

The data points from the baseline and from the 41℃-induced early and late phase HbO changes associated with the aPFC for each subject (*N*=5) were laid out continuously on a spread sheet and imported into the SAS software for mixed modeling analysis. The SAS code and results from the mixed modeling analysis for comparison between the baseline and 41℃-induced HbO changes are shown in Appendix E. Figure 7-2 below summarizes the mean estimates and associated standard errors for both baseline and 41℃-induced HbO changes from the aPFC cortical area.

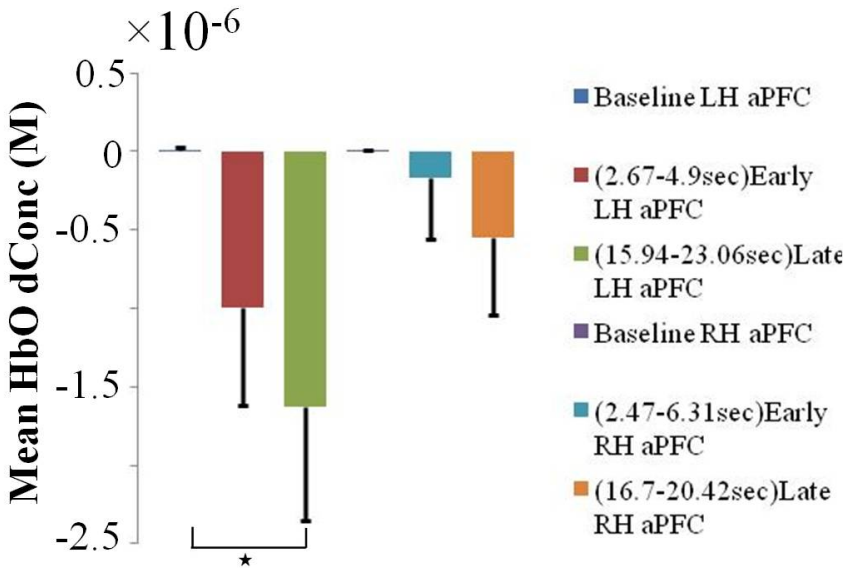

Figure 7-2: Summary of mean estimates and standard errors obtained for the baseline and 41℃-induced HbO changes in the aPFC area using Linear Mixed Model. Note: The baseline was fixed at -5 to 0sec and the * denotes significant difference at 0.05.

Looking at the mean estimates for the baseline from Figure 7-2, we observe that for both LH and RH aPFC, it was in the range of 10^{-9} M. Similarly, the mean estimates for the 41℃-induced changes were in the range of 10^{-7} except for the LH aPFC that showed an order higher at 10^{-6} M. This implies that 41℃ thermal stimulation induced a change in the HbO response magnitude by an order of at least 100. Specifically, we can also observe that the mean estimates for 48℃-induced change during the late phase are -1.63×10^{-6} M and -5.48×10^{-7} M in the LH and RH aPFC respectively. Comparing these values to the respective baseline values, we can clearly observe that the stimulus-induced HbO change had a trend for deactivation in response to the

41℃ thermal stimulation. Since both the LH and RH aPFC show negative HbO changes with respect to the baseline, we can deduce that during the late phase, a trend for bilateral deactivation was observed in the aPFC area. Another interesting observation was that early phase also shows a trend for bilateral ΔHbO deactivation while the 48℃ thermal stimulation displayed a trend for ΔHbO activation as shown in Figure 6-4.

The next important step was to investigate the significance of 41℃-induced changes with respect to the baseline. The observed p-values shown in Table 7-1 were obtained from the linear mixed model analysis for comparison between baseline and 41℃-induced HbO changes. From Table 7-1, we can clearly notice that significant 41℃-induced HbO changes were not observed with respect to the baseline except for the late phase in the LH aPFC area. This could probably be due to the small size of subject pool and also that in this preliminary study; we did not consider the between-subject variability or the random effects. However, it was promising to find late phase significance with respect to the baseline and hence the late phase of the HbO changes from the aPFC will be continued with further analyses for quantification for PI and FWHM and its correlation with cognitive evaluation of pain perception.

Table 7-1: Summary of significance of 41℃-induced HbO changes with respect to the baseline. Note: The critical value for significance is 0.05 and the green shade indicates the observed significance; LS stands for least square and the baseline was fixed at -5 to 0sec.

Baseline/Stimulation comparison	**LS Mean Difference(M)**	**Std. Error (M)**	**Pr > |t|**	**Significantly Induced Change**
LH aPFC (t=2.67 to 4.9 sec)$_{early}$	-1.00×10^{-6}	6.21×10^{-7}	$p = 0.113$	No change
LH aPFC (t=15.94 to 23.06 sec)$_{late}$	-1.64×10^{-6}	7.19×10^{-7}	**$p = 0.028$**	Deactivation
RH aPFC (t=2.47 to 6.31 sec)$_{early}$	-1.7×10^{-7}	3.95×10^{-7}	$p = 0.670$	No change
RH aPFC (t=16.7 to 20.42 sec)$_{late}$	-5.49×10^{-7}	4.87×10^{-7}	$p = 0.265$	No change

7.4.1.2 Correlates from the aPFC for Cognitive Evaluation

From Table 7-1, statistical significance was observed between baseline and late phase HbO changes from the LH aPFC area. Hence the group level linear regression was carried out between the late phase HbO-derived PI and FWHM extracted from the LH aPFC and subjective pain rating. As shown in Figure 7-3, for linear regression, pain rating was considered as the dependent variable and PI as the independent variable. Equation 7.1 below show the linear

relationship between pain rating and late phase HbO-derived FWHM from ipsi-aPFC (p=0.784, r=0.19, R^2=0.035). Similarly, Equation 7.2 shows the relationship between pain rating and the late phase HbO-derived PI from ipsi-aPFC (p=0.103, r=0.80 R^2=0.642). Each of the regression fittings passed the Shapiro-Wilk normality test and constant variance test.

$$Rating(41℃) = 42.32 - 2.86 * FWHM\_late\_\text{ipsi } aPFC \quad 7.1$$

$$Rating(41℃) = 16.33 - 5.19 \times 10^6 * PI\_late\_\text{ipsi } aPFC \quad 7.2$$

From Table 7-1, we can observe that 41℃ stimulatio n induced significant HbO changes only during the late phase of LH aPFC. However, the quantified parameters (that is PI and FWHM) from the late phase HbO changes does not show a significant relationship with the cognitive evaluation of pain. From this study with a limited number of subjects (N=5), we observe a significance of p=0.103 for ΔHbO-derived PI and pain rating, and a significance of p=0.784 for HbO-derived FWHM and pain rating. Although, the significance is greater than 0.05 for HbO-derived PI, it was promising to observe a correlation coefficient of 0.8 from this study. However, HbO-derived FWHM resulted in a poor correlation of 0.19 implying it cannot serve as a reliable correlate for clinical applications.

Although from Table 7-1, there was no significance observed between late phase HbO changes from RH aPFC, it was still imperative to explore whether the ΔHbO derived parameters from the RH aPFC significantly correlated with the pain rating. Table 7-2 below summarizes the correlation coefficient (r) and significance (p-value) for ΔHbO derived parameters from both LH and RH aPFC. We observe from the table below that no significant correlation was observed between ΔHbO derived parameters from the RH aPFC and pain rating. However, a strong correlation was observed between pain rating and HbO-derived PI from LH aPFC (r=0.8). This indicates that further investigation is necessary to validate the correlation observed from the current results in order to enhance the confidence that these HbO-derived parameters significantly reflect cognitive evaluation of pain perception.

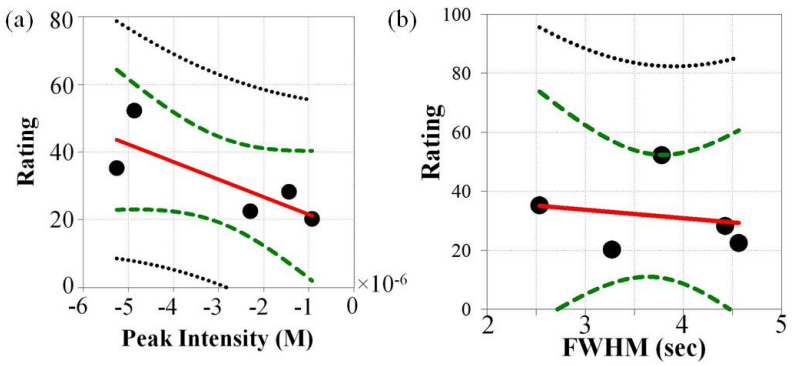

Figure 7-3: Linear regression between subjective pain rating and HbO-derived parameters from the *late* phase of LH aPFC. (a) Peak Intensity (p=0.103) (b) FWHM (p=0.764).Note: solid black dots denote raw data ; thick red lines denote the regression line ; dashed dark green lines denote the 95% confidence interval for regression ; and dotted black lines denote the 95% confidence interval for raw data.

Table 7-2: Summary of significance and correlation coefficient obtained for relationship between HbO-derived parameters from the late phase of aPFC and pain rating. Note: r: correlation coefficient obtained from linear regression analysis; p: significance of relationship between the two variables shown within the square brackets [].

Cortical area	[Peak Intensity, Pain Rating]	[FWHM, Pain Rating]
LH aPFC	r = 0.80	r = 0.19
	p = 0.103	p = 0.764
RH aPFC	r = 0.35	r = 0.41
	p = 0.561	p = 0.497

7.4.2 Dorsolateral Prefrontal Cortex (BA 46)

Figure 6-6(a) shows the selected channels of the DLPFC area used in cluster-wise analysis. The sources covering the DLPFC are denoted by the pink circles outlined in bold (from left to right: X1 and X5). The detectors collecting the signals from the DLPFC are shown as solid green boxes, outlined in bold (from left to right, top to bottom: D1, D2, D10, D9, D5, D6, D14, D13). The black, dashed lines denote the channels disabled for clustered-wise analysis of the DLPFC. The red solid lines show the channels of contra-DLPFC (X1-D1, X1-D2, X1-D5, X1-D6), and the solid blue lines show the channels of ipsi-DLPFC (X5-D10, X5-D9, X5-D14, X5-D13). Clustered-wise based grand-averaged (N=5) HbO temporal response from ipsi DLPFC for both 41°and 48℃ stimulation are shown in Figure 7-4(b) below.

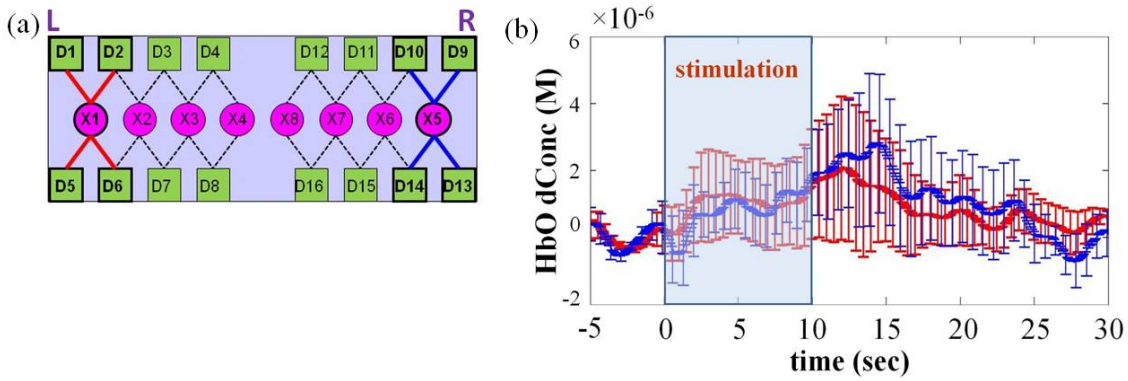

Figure 7-4: (a) Channels covering dorsolateral PFC (b) Grand averaged temporal plots along with standard deviation shown by the error bars. The grand average included averaging across the 8 blocks for each subject, followed by group temporal averaging across the 5 subjects. Note: pink circles: sources; green box: detectors; dashed line: disabled channels; solid red line: contra DLPFC; solid blue line: ipsi DLPFC; L: left hemisphere and R: right hemisphere.

7.4.2.1 Significance of 41℃-induced HbO Changes in DLPFC

The key focus of this dissertation work was to quantify the ΔHbO changes. Hence, the time period that comprised of FWHM time period encompassing PI during the stimulation-induced HbO changes was compared with that of the baseline. The FWHM within the early (0.1-12sec) and late phase (12.1-25sec) was extracted for both ipsi- and contra- response as shown within parentheses in Figure 7-5. For late phase, if necessary, the last 5sec of the functional block, that is 25-30sec, was incorporated for accurate quantification of the FWHM.

The data points from the baseline and from the 41℃-induced early and late phase HbO changes associated with the DLPFC for each subject (*N*=5) were laid out continuously on a spread sheet and imported into the SAS software for mixed modeling analysis. The SAS code and results from the mixed modeling analysis for comparison between the baseline and 48℃-induced HbO changes are shown in Appendix E. Figure 7-5 below summarizes the mean estimates and associated standard errors for both baseline and 41℃-induced HbO changes from the DLPFC cortical area.

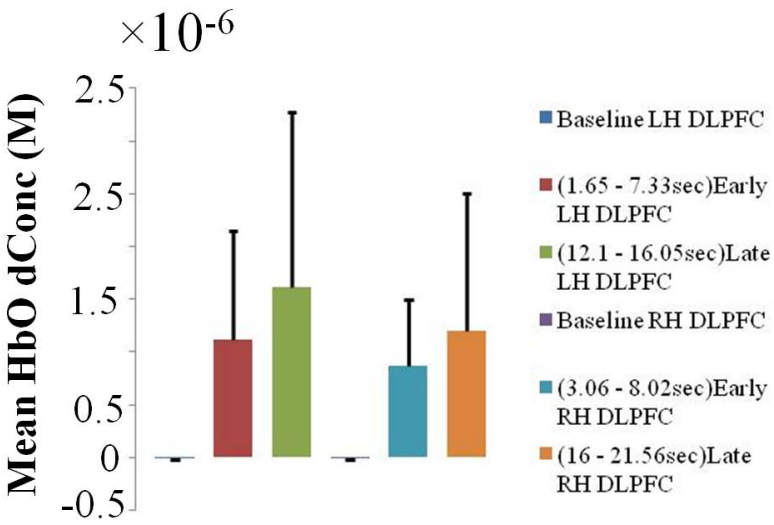

Figure 7-5: Summary of mean estimates and standard errors obtained for the baseline and 41℃-induced HbO changes in the DLPFC area using Linear Mixed Model. Note: The baseline was fixed at -5 to 0sec.

The mean estimates for the baseline from Figure 7-5 show that for the LH DLPFC it was in the range of 10^{-9} M for both the LH and RH DLPFC areas. Further, the standard errors for baseline HbO changes were higher than the mean estimates by an order of 10. The mean estimates for the 41℃ -induced changes, specifical ly in the late phase HbO changes, were in the range of 10^{-6} M in both the LH and RH DLPFC. This implies that 41℃ thermal stimulation induced a change in the ΔHbO response magnitude by an order of at least 1000. The mean estimates for 41℃-induced ΔHbO change during the late phase were 1.61×10^{-6} M and 1.2×10^{-6} M in the LH and RH DLPFC respectively. Comparing these values to the respective baseline values, we can clearly observe that the 41℃ stimuli induced activ ation in the ΔHbO response. Since both the LH and RH DLPFC show activation with respect to the baseline, we can deduce that bilateral activation was observed in the DLPFC area in response to 41℃ thermal stimulation during the late phase of the stimulation. Another interesting observation from this specific aim is that we observe opposite pattern in stimulus-induced HbO changes between the aPFC and DLPFC areas. From the above Figure 7-5 we notice a trend for activation in the DLPFC areas while from Figure 7-2 we observed a trend for deactivation in the aPFC area.

The next important step was to investigate the significance of 41℃ -induced changes with respect to the baseline in the DLPFC area. The observed p-values shown in Table 7-3 were obtained from the linear mixed model analysis for comparison between the baseline and 48℃-induced HbO changes. From Table 7-3, we can clearly notice that significant HbO changes were not observed in the DLPFC area in response to 41℃ thermal stimuli. This could probably be due to the small size of subject pool and also that in this preliminary study; we did not consider the between-subject variability or the random effects.

Table 7-3: Summary of significance of 41℃-induced HbO changes with respect to the baseline in the DLPFC area. Note: The critical value for significance is 0.05; LS stands for least square and the baseline was fixed at -5 to 0sec.

Baseline/Stimulation comparison	**LS Mean Difference (M)**	**Std. Error (M)**	**Pr > |t|**	**Significantly Induced Change**
LH DLPFC (t=1.65 to 7.33 sec)$_{early}$	1.13×10^{-6}	1.03×10^{-6}	$p = 0.282$	No change
LH DLPFC (t=12.1 to 16.05 sec)$_{late}$	1.61×10^{-6}	1.66×10^{-6}	$p = 0.338$	No change
RH DLPFC (t=3.06 to 8.02 sec)$_{early}$	8.69×10^{-7}	6.37×10^{-7}	$p = 0.179$	No change
RH DLPFC (t=16 to 21.56 sec)$_{late}$	1.21×10^{-6}	1.31×10^{-6}	$p = 0.360$	No change

7.4.2.2 Correlates from the DLPFC for Cognitive Evaluation

From Table 7-3 above, we observed that there was no significant HbO changes induced in the DLPFC area in response to the 48℃ thermal stimuli. Although the late phase does not show significant HbO changes, the mean estimates showing the magnitude change (Figure 7-5) are larger than that from the baseline by an order of at least 1000. Given the preliminary nature of this study and that we had only 5 subjects; correlation between the ΔHbO-derived parameters (that is PI and FWHM) from DLPFC area and the behaviorally measured pain rating was investigated in this study. The following figures below show the regression between HbO-derived PI and FWHM and pain rating during the late phase.

As shown in Figure 7-6, for linear regression, pain rating was considered as the dependent variable and PI as the independent variable. Equation 7.3 below show the linear relationship between pain rating and late phase HbO-derived FWHM from ipsi/LH DLPFC (p=0.089, r=0.82, R^2=0.67). Similarly, Equation 7.4 shows the relationship between pain rating

and the late phase HbO-derived PI from ipsi/LH DLPFC (p=0.006, r=0.97 R^2=0.94). Each of the regression fittings passed the Shapiro-Wilk normality test and constant variance test.

$$Rating(41℃) = -0.27 + 6.67 * FWHM\_late\_\text{ipsi DL}PFC \quad 7.3$$

$$Rating(41℃) = 26.03 + 2.63 \times 10^6 * PI\_late\_\text{ipsi DL}PFC \quad 7.4$$

From Table 7-3, we can observe that 41℃ stimulatio n induced HbO changes were not significant in the late phase of the DLPFC area. However, the quantified parameters (that is PI) from the late phase HbO changes from LH DLPFC show a significant relationship with the cognitive evaluation of pain. From this study with a limited number of subjects (N=5), we observe a significance of p=0.006 for ΔHbO-derived PI and pain rating, and a significance of p=0.089 for HbO-derived FWHM and pain rating. Unlike the mechanical stimulation, it was interesting to observe that a significant correlate was observed in the DLPFC area in response to both 48℃ and 41℃ thermal stimuli. Specifically in this aim, it was promising to observe a very significant positive correlation of 0.97 between HbO-derived PI and pain rating. The correlation between HbO-derived FWHM was also relatively strong at 0.82 but given the small subject size, it was not significant and hence demands further investigation. In addition, from Figure 7-6(b), we also observe that the right-most extreme data point appears to be an outlier. Since we did not observe significance for HbO-derived FWHM, investigation for significance in correlation excluding the right-most extreme data point was not considered in this study.

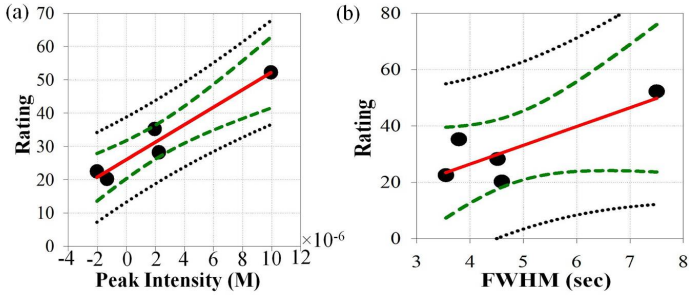

Figure 7-6: Linear regression between subjective pain rating and HbO-derived parameters from the late phase of ipsi/LH DLPFC. (a) Peak Intensity (p=0.006) (b) FWHM (p=0.089).Note: solid black dots denote raw data ; thick red lines denote the regression line ; dashed dark green lines denote the 95% confidence interval for regression ; and dotted black lines denote the 95% confidence interval for raw data.

From Table 7-4, we observed that there was no significance observed between late phase stimulation-induced HbO changes from the RH DLPFC area. Since we investigated for correlates from the LH DLPFC area that also did not had significant HbO changes in response to the thermal stimuli, it was imperative to explore whether the ΔHbO derived parameters from the RH DLPFC significantly correlated with the pain rating. Equation 7.5 below show the linear relationship between pain rating and late phase HbO-derived FWHM from contra/RH DLPFC (p=0.297, r=0.59, R^2=0.35). Similarly, Equation 7.6 shows the relationship between pain rating and the late phase HbO-derived PI from contra/RH DLPFC (p=0.004, r=0.98 R^2=0.96). Each of the regression fittings passed the Shapiro-Wilk normality test and constant variance test.

$$Rating(41℃) = 20.0 + 2.1 * FWHM\_late\_\text{contra DL}PFC \quad 7.5$$

$$Rating(41℃) = 28.36 + 2.27 \times 10^6 * PI\_late\_\text{contra DL}PFC \quad 7.6$$

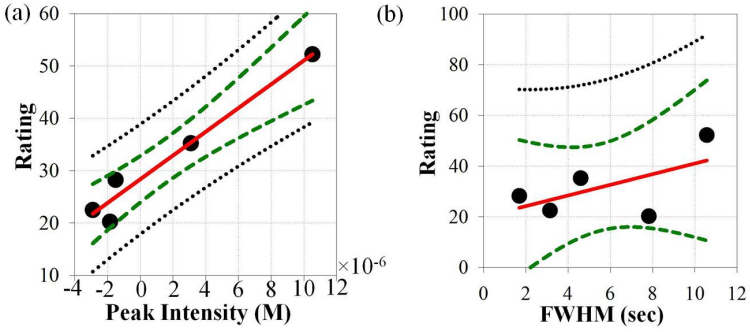

Figure 7-7: Linear regression between subjective pain rating and HbO-derived parameters from the late phase of contra/RH DLPFC. (a) Peak Intensity (p=0.004) (b) FWHM (p=0.297).Note: solid black dots denote raw data ; thick red lines denote the regression line ; dashed dark green lines denote the 95% confidence interval for regression ; and dotted black lines denote the 95% confidence interval for raw data.

Table 7-4 below summarizes the correlation coefficient (r) and significance (p-value) for ΔHbO derived parameters from both LH and RH DLPFC. One of the key observations from this specific aim was that we observed significant correlate from the RH DLPFC that was not observed from 48℃ thermal stimulation study. The H bO-derived PI shows a significant positive correlation of 0.98 with the pain rating. Comparing Equations 7.4 and 7.6, we observe that the correlation between HbO-derived PI and pain rating is more significant and also displays a higher correlation in the RH DLPFC area compared to the LH DLPFC area. In addition, a strong

correlation was observed between pain rating and HbO-derived FWHM from LH DLPFC (r=0.82), pain rating and HbO-derived FWHM from RH DLPFC (r=0.59). These results indicate that further investigation is necessary to validate the correlation observed from the current results in order to enhance the confidence that these HbO-derived parameters significantly reflect cognitive evaluation of pain perception.

Table 7-4: Summary of significance and correlation coefficient obtained for relationship between HbO-derived parameters from the *late* phase of DLPFC and pain rating. Note: r: correlation coefficient obtained from linear regression analysis; p: significance of relationship between the two variables shown within the square brackets []; the critical value for significance is 0.05 and the green shade indicates the observed significance.

Cortical area	[Peak Intensity, Pain Rating]	[FWHM, Pain Rating]
LH DLPFC	r = 0.97	r = 0.82
	p = 0.006	p = 0.089
RH DLPFC	r = 0.98	r = 0.59
	p = 0.004	p = 0.297

7.4.3 Significant Difference between aPFC and DLPFC HbO Changes

Sub-hypotheses 7.2.1 and 7.2.3 were solely based on investigating the significance of 41℃-induced HbO changes with respect to baseline in the aPFC and DLPFC areas respectively. We observed from Table 7-1 and Table 7-3 that significance was observed between the baseline and 41℃-induced HbO changes only in the LH aPFC area. However, given that we obtained measurements simultaneously from both the aPFC and DLPFC areas, we assume that inherently there exists a correlation between the measurements from the two different cortical areas for each subject. This was modeled in the covariance structure of the linear mixed model by assuming equi-correlation between all the measurements which refers to the compound symmetry structure.

From Table 7-1, we observe that there was significance (p<0.05) between the HbO changes before and after the thermal stimuli only during the late phase of the aPFC area. Further, from Table 7-4, we observed significant correlation between HbO-derived PI quantified from the late phase of both the LH and DLPFC area. Since our interest in this study was to quantify correlates, we focused on the late phase HbO changes from the DLPFC area (shown by yellow shade in Table 7-5). We observed that there was no significant difference between the estimates from the late phase of aPFC and the late phase of DLPFC HbO changes. Non-significance could

possibly be due to the limited size of our subjects and the variability between the subjects. However, it could also be possible that both the areas are coherently involved to some extent in the processing of pain. These possibilities need further investigation that is currently not investigated in this study.

Table 7-5: Summary of significance between 41℃-ind uced HbO changes from aPFC and DLPFC areas. Note: LH: Left hemispheric; RH: Right hemispheric; LS: Least square; the yellow shade indicates the areas and associated phase from which significant correlates were obtained in section 7.4.2.2 .

aPFC	DLPFC	LS Mean Difference (M)	Std. Error (M)	Pr > |t|
LH_{late}	LH_{late}	-3.24×10^{-6}	2.30×10^{-6}	p=0.167
RH_{late}	LH_{late}	2.15×10^{-6}	1.61×10^{-6}	p=0.189
LH_{late}	RH_{late}	-2.83×10^{-6}	1.96×10^{-6}	p=0.156
RH_{late}	RH_{late}	-1.75×10^{-6}	1.27×10^{-6}	p=0.176

7.4.4 Are the Correlates from the LH aPFC Biased by Anticipation?

Similar to the 48℃ stimulation study as described in the previous chapter, the anticipation effects in response to 41℃ thermal st imuli were explored for this specific aim. The details on analysis approach undertaken in this study to investigate anticipation effects are described in section 5.3.4.7 . Recalling from the previous chapter, for 48℃ stimuli, the results showed that anticipation did not affect the HbO-derived PI that correlated with the pain rating. Since the goal of this study was to extract correlates for cognitive evaluation of pain, our interest was to investigate whether anticipation significantly interferes with the cognitive evaluation as seen through the HbO-derived parameters measured from the LH aPFC area under 41℃ stimuli.

Although we did not find significant correlates from the late phase of LH aPFC, the stimulation-induced HbO changes were significant with respect to the baseline (Table 7-1). Further from Table 7-2, we also observed a strong correlation of r=0.8 between HbO-derived PI from LH aPFC and pain rating. Therefore, it was necessary to tease out the anticipation effects, if any, on the HbO-derived PI from the LH aPFC area. Thus, the PI was derived from the LH aPFC derived grand averaged HbO response, where the first block was excluded (shown by solid pink temporal plot in Figure 7-8), and statistically compared with the HbO-derived PI, where the first block was included (shown by solid red temporal plot in Figure 7-8). The analysis for anticipation

effects as described in section 5.3.4.7 was carried out on the LH aPFC derived HbO measurements (that is with the first block disabled and averaging of the remaining blocks). A paired t-test between the PI (with and without the first block included) values resulted in a significance of p=0.160. The p-value greater than 0.05 between the mean values for PI implied that anticipation did not influence the cognitive evaluation of pain reflected through PI.

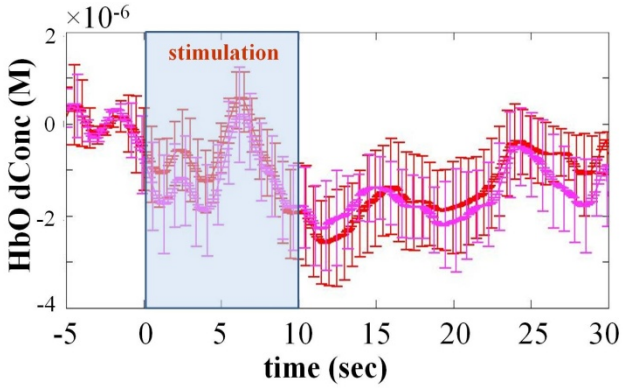

Figure 7-8: Grand averaged ΔHbO temporal plots (N=5) with and without the first block included into the block averaging to explore the anticipation effect in *ipsi/LH* aPFC. Note: solid red line: first block included; solid pink line: first block excluded; error bars denote the standard deviation across the subjects.

7.4.5 Summary of Correlates

Table 7-6 below summarizes the correlates between the HbO-derived parameters and the behaviorally measured pain rating under the 41°C thermal stimulation. One of the key observations is that the correlates were observed only during the late phase of the DLPFC area. Further from Figure 7-5, during the late phase, we observed bilateral ΔHbO activation in the DLPFC area. This implies that from this preliminary study, the HbO activation observed in the DLPFC area through fNIRS measurements; significantly reflect the cognitive evaluation of pain perception.

Table 7-6: Summary of *significant* correlates between ΔHbO-derived parameters and pain rating under 41℃ thermal stimulation. Note: RH: right hem ispheric; LH: left hemispheric; (+): positive correlation; (-): negative correlation; --: no correlates; PI: ΔHbO-derived Peak Intensity.

	Early phase	**Late phase**
RH aPFC	--	--
LH aPFC	--	--
RH DLPFC	--	(+)PI
LH DLPFC	--	(+)PI

7.4.6 HbO-derived time to peak (ttp) Reflecting Discrimination of Pain Levels

In addition to the HbO-derived PI and FWHM, which have been extensively discussed as a key parameter in reflecting the cognitive evaluation of pain, time to peak (ttp) was another HbO-derived parameter that was quantified in this dissertation study. A graphical sketch for quantifying ttp is shown in Figure 5-4. In this study, time to peak was defined as the time length between time point 0 when stimulation was started and the time point at which the ΔHbO response reaches the maximum change in magnitude (that is peak) in either positive or negative direction. As can seen from Figure 5-4, the ttp for late phase would be the segment AB and AF for early and late phase respectively.

Under thermal stimulation, the results from Table 6-1 and Table 7-1 show that the late phase HbO changes from the LH aPFC area were significant in response to 48℃ and 41℃ thermal stimuli. Hence, the HbO-derived ttp was quantified from the late phase of LH aPFC for each subject and Figure 7-9 shows a bar plot for mean and standard error across the subjects. From the same figure, we can observe that the mean ttp for higher noxious stimuli (that is 48℃) is longer compared to lesser noxious 41℃ stimuli. A paired t-test between the two mean values resulted in a significance of p=0.044. These results suggest the role played by LH aPFC in the discrimination of two different pain levels and an fNIRS based quantified parameter that can be potentially useful in clinical applications for discrimination of pain levels.

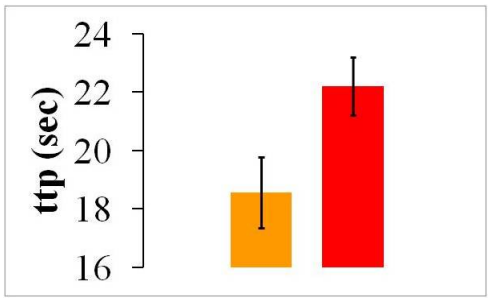

Figure 7-9: Average ΔHbO-derived time to peak (ttp) along with ± standard error during late phase from LH aPFC area in response to 41°and 48℃ thermal stimulations. Note: solid red denotes 48℃ while solid orange denotes 41℃. Signi ficance at p=0.044 was observed between the two mean values.

In addition to the HbO-derived ttp, the other two parameters that are the HbO-derived PI and HbO-derived FWHM were also statistically compared to investigate whether those parameters reveal discrimination of pain levels. A paired t-test between the mean values showed a significance of p=0.66 for HbO-derived PI and p=0.378 for HbO-derived FWHM respectively. The following table summarizes the above mentioned results.

Table 7-7: Summary of observed significant difference between late phase HbO-derived parameters from the LH aPFC area in response to 41°C and 48℃ thermal stimulation. Note: the green shade indicates the observed significance at 0.05.

HbO-derived parameter	Observed significance
ttp	***p* = 0.044**
PI	p = 0.66
FWHM	p = 0.378

7.4.7 Reconstructed HbO Images

Figure 7-10 shows the reconstructed images for grand-averaged (N=5) ΔHbO changes in response to both 41℃ thermal stimulation. Also in order to generate an image separately for early and late phase as shown in Figure 7-10(a) and (b), the image at each time point were temporally averaged between 0.1 and 12sec for early and between 12.1 and 25sec for late phase respectively. In the aPFC (selected channels as shown in Figure 5-3(a)), a weak bilateral ΔHbO deactivation (shown by blue) can be observed during both the early and late phase of the HbO changes. However in the DLPFC areas (selected channels as shown in Figure 5-3(b)), antagonistic pattern can be observed. That is, ΔHbO activation (shown by red) can be observed

in the DLPFC areas. The pattern for ΔHbO activation and deactivation observed from Figure 7-10 are consistent with the clustered-wise analysis on selected channels covering the aPFC and DLPFC areas. Although, reconstructed images are helpful in displaying scientifically meaningful information and could have clinical applications, the current results are limited by a smaller subject pool and also by the inherent drawbacks of the backprojection algorithm as applied to diffuse optics.

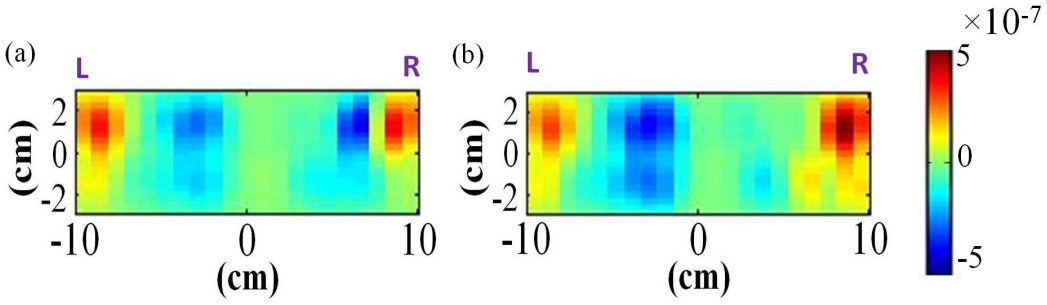

Figure 7-10: Reconstructed for grand-averaged (*N*=5) ΔHbO responses for 41℃ thermal stimulation. (a) early response (b) late response Note: the color bar range shows blue for deactivation and red for activation; the image for early response is the temporal average across 0.1-12sec while that for late response is the temporal average across 12.1-25sec; L: left hemisphere and R: right hemisphere.

7.5 Discussion

The specific aim delineated in this chapter focused on HbO changes in response to 41℃ thermal stimulation. The major goals of this specific aim were: (1) to investigate whether significant HbO-derived correlates for cognitive evaluation of pain can be obtained under 41℃ thermal stimulation. (2) To examine whether fNIRS has the feasibility to quantify cognitive discrimination of two different pain levels (that is 41℃ and 48℃). The following two sub-sections incorporate a detailed discussion on each of the major goals mentioned above.

7.5.1 Cognitive Evaluation of Pain under 41℃ Stimu li

Section 7.2 describes the major sub-hypotheses that were investigated for this specific aim. In the first two sub-hypotheses we focused on significance for 41℃-induced HbO changes in the aPFC area, and whether the correlates quantified from the same area significantly reflects cognitive evaluation of pain. In order to tease apart the significance of 41℃-induced HbO

changes, we relied on the linear mixed modeling analysis. The technical details on this method were described in section 5.3.4.4 . From Table 7-1 and Figure 7-1(b), we observed a trend for bilateral ΔHbO deactivation in the aPFC areas. It was interesting to note from Table 7-1 that the 41℃-induced HbO changes in the late phase of LH aPFC was significant with respect to associated baseline. In addition, please recall that the late phase HbO changes from the LH aPFC was also significant in response to the 48℃ thermal stimuli. These results indicate that under thermal stimulation, irrespective of the noxious pain level, the late phase HbO changes from the LH aPFC plays a significant role in processing the perception of pain

Now moving on to the second major sub-hypothesis (that is 7.2.2), from Table 7-2, we observed that there was no significant relationship observed between the HbO-derived parameters from the aPFC area and the pain rating. In consistence with the previous two specific aims, regression analysis was carried out between pain rating and HbO-derived PI and also between pain rating and HbO-derived FWHM. Although, we did not find significant correlation, one promising observation was that the HbO-derived PI from LH aPFC showed a strong correlation (r=0.8) with the pain rating in spite of only 5 subjects recruited for this study. This implies that HbO-derived PI is a promising correlate that needs further investigation with a larger subject pool.

In light of the HbO changes from DLPFC area in response to 41℃ thermal stimuli, the sub-hypotheses 7.2.3 and 7.2.4 in section 7.2 were posited in this study. From Figure 7-5, we observed that the HbO changes induced by 41℃ thermal stimuli in the DLPFC area had a trend for activation. However from Figure 7-2, in the aPFC area, we observed a trend for HbO deactivation. This implies that the 41℃ stimuli induced antagonistic HbO changes in the aPFC and DLPFC areas during the late phase of the stimulation. Further, the HbO reconstructed images shown in Figure 7-10 corroborates the findings from the clustered-wise analysis. This antagonistic pattern could possibly be due to simultaneous depolarization-led vasodilation in the DLPFC areas while hyperpolarization-led vasoconstriction in the aPFC area (Devor, et al., 2007). Focusing on the HbO changes from the DLPFC area, we observe from Table 7-3 that 41℃-

induced HbO changes were not significant with respect to the associated baseline. This could possibly be due to the limited subject pool (*N*=5) in this study and demands further investigation.

From the above discussion, we found that HbO changes in response to 41℃ thermal stimuli were not significant in the DLPFC area. However, given the preliminary nature of this study, we continued our investigation for correlates if any from the DLPFC area. It was interesting to find from Table 7-4 that the late phase HbO-derived PI both from the LH and RH DLPFC significantly correlated with the pain rating. From Figure 7-6(a), we observed a significant positive correlation between HbO-derived PI from the late phase of LH DLPFC and pain rating. In addition, similar results can be observed from Figure 7-7(a) for RH DLPFC with a higher significance. At this point, it has to be recalled that for 48℃ stimuli, only LH DLPFC showed significant correlate for pain rating. However, under 41℃ thermal stimuli, in addition to LH DLPFC, significant correlate was also found from the RH DLPFC. This implies that under a lesser noxious pain level, both LH and RH DLPFC areas are involved in the processing of cognitive evaluation of pain perception.

A key tool that was incorporated in the data analysis of this study was the linear mixed modeling analysis. The details on linear mixed modeling analysis were described previously in section 5.3.4.4 . For this specific aim, the SAS results for linear mixed modeling analysis are shown in Appendix E. It can be observed from the SAS results that the overall significance for fixed effects was not significant for this specific aim. However, given that our interest was to investigate the significance for comparison between baseline and 41℃-induced HbO changes in each cluster or cortical area, the non-significance from overall model fit for fixed effects was not a major concern. The reason is that the residuals obtained for fixed effects model showed a close to normal distribution as can be seen from Figure E-1 and Figure E-2. We also believe that the non-significance for overall model fit for fixed effects can be mitigated by incorporating more number of subjects in further investigation for this study.

In addition to cognitive evaluation of pain, a recent fMRI study has shown that the aPFC is also involved in the processing of anticipation due to pain (Porro, et al., 2002). Although in this specific aim, we did not find significant correlates from the aPFC area (Table 7-2), given that we

had only 5 subjects recruited for this study, we observed a strong correlation (r = 0.8) between late phase HbO-derived PI from the LH aPFC and pain rating. Hence it was imperative to investigate whether the correlate obtained from the aPFC area was affected by anticipation in response to noxious thermal stimuli. It was found that higher anticipation in response to the first stimulus did not interfere with the cognitive evaluation. However, these preliminary results must be verified for: (a) significance of correlates from LH aPFC area by recruiting more healthy subjects and (b) an experimental protocol design approach that disentangles anticipatory stress from the cognitive evaluation of pain. Due to their periodic nature, block design experimental protocols result in habituation which may affect anticipation. Hence, further work is necessary to experimentally test for habituation and any of its effects on anticipation by incorporating event-related or mixed design protocols.

7.5.2 Discrimination of Pain Intensity

One of the major experimental limitations of the mechanical stimulation study was that the pinching action could not be controlled to different pain levels. This drawback was compensated in the thermal study where the pain level was computer-controlled to two different levels that aided in the investigation for cognitive discrimination of pain levels. An optimal approach to tease apart the cognitive discrimination would be an event-related or mixed design. This approach would allow for incorporating randomized 41℃ and 48℃ stimuli within the protocol. However, this preliminary study that incorporated 41℃ protocol followed by the 48℃ protocol, is the first study to our best knowledge to investigate the feasibility of fNIRS to discriminate pain levels.

HbO-derived time to peak (ttp) was another parameter that was quantified in this study and proved to be a potential indicator for cognitive discrimination of two different pain levels. Figure 7-9 shows that the mean HbO-derived ttp from the late phase of LH aPFC for 48℃ was longer compared to that in response to the 41℃ thermal stimuli. Further, we also observed from Table 7-7 that the two mean values were significantly different at p=0.044. From a neurophysiological perspective, a possible reason for different lag times could be the preferential response from innervating nociceptive fibers in specific cortical area at different pain levels.

Another possible reason could be the localized neurovascular coupling that possibly leads to different lag times in the HbO response under different pain levels. However, further investigation is necessary for a deeper scientific understanding of the underlying physiological cause for different lag times observed at the two different pain levels. From the fNIRS perspective, this preliminary result was promising for its potential clinical use in cognitive discrimination of different pain levels. A more general discussion on discrimination of pain intensity based on this study is given in section 8.4 .

In conclusion, 41℃ thermal stimulation displayed a trend for late phase bilateral ΔHbO deactivation in aPFC area. Specifically, the late phase HbO changes from the LH aPFC were significantly different from the associated baseline. In response to the same stimuli, we did not observe significant HbO changes in the DLPFC area with respect to associated baseline. Further from the regression analysis for correlated between pain rating and HbO-derived parameters, significant correlation was found only between HbO-derived PI from the late phase of both LH and RH DLPFC and pain rating. Although the correlates from the late phase of LH aPFC area were not significant, we observed a strong correlation between HbO-derived PI from the late phase of LH aPFC and pain rating. In addition, fNIRS was found to be feasible in providing objective measures for cognitive discrimination of pain levels. The HbO-derived time to peak from the late phase of LH aPFC were significantly different between 41℃- and 48℃-induced HbO responses. Finally, the next chapter will comprehensively discuss the similarities and differences of findings observed across the mechanical and thermal stimulation studies.

CHAPTER 8

COMPREHENSIVE DISCUSSION OF FINDINGS ACROSS MECHANICAL AND THERMAL (41℃ AND 48℃) STIMULATIONS

To my best knowledge, the field of functional NIRS has only a few documented pain-related studies. Most of these reports focus on testing the feasibility of NIRS to measure the hemodynamic changes in the somatosensory and frontal areas in response to thermal pain (L. Becerra, et al., 2009; L. Becerra, et al., 2008). Another published work from our group (Krishnamurthy, et al., 2010) focused on the feasibility of a high density optical imager to detect the hemodynamic changes in the pre-frontal area in response to thermal pain. As a proof of principle, the above mentioned studies have demonstrated the feasibility of DOT to detect pain-induced hemodynamic changes. The next innovative step undertaken in this study was quantification of the neural correlates of pain perception using fNIRS measurements.

In Chapters 5 through 7, the results and discussion for each of the specific aims of this study were detailed. Since this study incorporated two different kinds of stimulation, it is imperative to discuss the similarities and differences in the observed results. The comprehensive discussion across the two different kinds of stimulations described in this chapter not only gives a contrast between fNIRS-based observations for mechanical and thermal stimulation, but also unveils an understanding of the prefrontal area's role in pain processing, irrespective of the type of stimulation.

8.1 Early versus Late Phase

In addition to the role played by nociceptive pathways and fibers on the cortical systems, neurovascular coupling that involves localized hemodynamic activity coupled into the neuronal activity further complicates the temporal variability and latencies in the measured hemodynamic response. Hence some of the researchers in the neuroimaging field explored the approach of parsing out the measured pain evoked hemodynamic response into early and late phase (L. Becerra, et al., 2001; L. Becerra, et al., 2008) as the first step to understand the localized neurovascular and neuro-metabolic coupling in cortical areas under noxious stimulation.

Table 5-1, Table 6-1, and Table 7-1 summarize the significant pain induced HbO changes in the aPFC area with respect to the associated baseline in response to mechanical and thermal (41℃ and 48℃) stimulation respectively. D uring the early phase of mechanical stimulation, a trend for bilateral deactivation was observed in the aPFC area. However, under thermal stimulation, a trend for bilateral deactivation was observed during the late phase in the same aPFC area. Further, from Table 5-1, Table 6-1, and Table 7-1 we observed that the pain-induced HbO changes in the aPFC area were not significant with respect to the baseline in response to the mechanical stimulation, but were significant in response to both the thermal stimuli. As far as the DLPFC area is concerned, we did not observe significant pain-induced HbO changes with respect to its associated baseline in response to either mechanical or thermal stimulation. The observed non-significance could be due to a small size of subject pool or it could also be the assumptions and limitations of linear mixed model analysis that needs further investigation.

Table 5-4, Table 6-6, and Table 7-6 summarize the correlates for cognitive evaluation of pain under mechanical and thermal stimulation (41℃ and 48℃) respectively. Under mechanical stimulation, correlates (that is PI and FWHM) were observed only in the early phase. However, for thermal stimulation, significant correlates were observed only during the late phase of the DLPFC area. A recent study has shown that laser induced burning pain resulted in right hemispheric (RH) DLPFC activation mediated by the *C* nociceptive fibers (Veldhuijzen, et al., 2009). Another fMRI study reported both 41 and 46℃ thermal stimuli causing increased BOLD

activation in the DLPFC area only during the late phase (L. Becerra, et al., 2001). In conjunction with these reports, it could be inferred that the correlates observed in the DLPFC during the late phase may be due to preferential innervations of the *C* nociceptive fibers in the dorsolateral areas.

Some of the recent studies have explored the temporal profile for changes in hemodynamic activation/deactivation at different time points of noxious stimulation (L. Becerra, et al., 2001; Lui, et al., 2008). It has been reported that in response to noxious stimuli, the peripheral factors such as *A-δ* fibers (that conduct nociceptive information) and *A-β* fibers (that conduct non-noxious information) should equally affect the responses of cortical regions (Treede, et al., 1998; Willis WD, 2005). In addition to *A-β* and *A-δ* fibers, slow conducting *C* fibers have also been shown to differentially impact the hemodynamic responses from deeper sub-cortical areas (Koltzenburg & Handwerker, 1994; Qiu, et al., 2006). It has also been reported that the conduction velocities of different spino-thalamocortical pathways targeting specific cortical areas have an impact on the peak latencies of the hemodynamic response(Tsuji, Inui, Kojima, & Kakigi, 2006). However, the influence of *A-β, A-δ* and *C* fibers on the hemodynamic response from the prefrontal areas has not been well understood.

8.2 Similarities between Mechanically and Thermally Induced Pain-Correlates

In this section, some of the similarities in the prefrontal response under both mechanical and thermal stimulation will be discussed. The analysis for each specific aim involved parsing out the data into the early and late phase. Irrespective of mechanical or thermal stimulation, a trend for HbO deactivation was observed in the aPFC area. Specifically, a trend for HbO deactivation was observed during early phase for mechanical stimulation while the same was observed during the late phase for thermal stimulation.

In the context of aPFC, the second similarity was that irrespective of mechanical or thermal stimulation, HbO-derived PI derived from the left hemispheric aPFC strongly correlated with the pain rating. This can be observed from Figure 5-9, Table 6-2, and Table 7-2 for mechanical, 48℃ and 41℃ thermal stimulation, resp ectively. A significant correlation was

observed only under mechanical stimulation, but the correlation coefficients obtained from the thermal study were greater than or equal to 0.8. As mentioned above, the respective phase from which the correlates were derived underwent HbO deactivation in response to either mechanical or thermal stimulation. Similar trend showing negative BOLD response in the aPFC area has also been reported in a fMRI study for mechanical (Lui, et al., 2008) and thermal stimulation (Kong, et al., 2010; Kong, et al., 2006).

The third similarity observed from this study was that the anticipation did not affect cognitive evaluation as seen through the HbO-derived parameters derived from the aPFC areas. Since a previous fMRI study had reported that the aPFC area is also involved in anticipation of pain (Porro, et al., 2002), it was imperative to verify the robustness of the derived correlates for cognitive evaluation for pain. The post-hoc analysis approach undertaken in this study showed that anticipation in response to the first pain stimulus did not affect the cognitive evaluation of pain perception as seen through the HbO-derived PI.

8.3 Differences between Mechanically and Thermally Induced Pain-Correlates

This section discusses some of the major differences between observations for mechanical and thermal stimulation. An understanding for the differences not only aides in a deeper scientific information for pain perception, but from a technology perspective, it also gives the rich information of fNIRS sensitivity in discriminating different types of pain stimuli.

One of the major differences between mechanical and thermal stimulation was that the correlates were found in different phase of the pain-induced HbO changes. This could possibly stem from the peripheral factors such as *A-δ* fibers and *A-β* fibers (Treede, et al., 1998; Willis WD, 2005). In addition to *A-β* and *A-δ* fibers, slow conducting *C* fibers have also been shown to differentially impact the hemodynamic responses from deeper sub-cortical areas (Koltzenburg & Handwerker, 1994; Qiu, et al., 2006). From Table 5-4, we observed that in response to pinch stimulation, HbO-derived PI from the early phase of aPFC significantly correlated with the pain rating. However, please recall that for thermal study we did not observe significant correlates from

the aPFC area, but the correlation between HbO-derived PI and pain rating was relatively strong (r >=0.8), as shown in Table 6-2 and Table 7-2.

Within the aPFC area, the second major difference was that significant correlates in the RH aPFC area were observed only in response to mechanical stimulation. Table 5-4 shows that from the RH aPFC area, both HbO-derived PI and HbO-derived FWHM significantly correlated with the pain rating. The significance of left hemispheric prefrontal areas in the processing of pain perception in response to thermal stimulation had also been observed in fMRI studies (L. Becerra, et al., 2001). However, the cause for right hemispheric PFC activity in response to mechanical stimulation and in general the neurophysiological underpinning in preferential PFC laterality in response to different pain stimuli needs further investigation. From fNIRS perspective, it was promising to observe HbO-derived FWHM correlating with pain rating in addition to HbO-derived PI. These results together shows that fNIRS has a promising potential in quantifying pain and also differentiate different types of pain stimuli.

The third major difference was that the LH DLPFC was found to play a significant role in cognitive evaluation of pain under thermal stimulation which was not observed for mechanical stimulation. From Table 6-6 and Table 7-6, we can observe that under thermal stimulation, the HbO-derived PI derived from LH DLPFC significantly correlated with the pain rating. Dorsolateral activation/deactivation in response to thermally induced noxious painful stimuli has also been reported by PET(Lorenz, et al., 2003) and fMRI studies(L. Becerra, et al., 2001; Moulton, et al., 2006).

From an experimental approach, we had another major difference between the protocols for mechanical and thermal stimulation. Please recall that all the subjects recruited for this study were right-handed. Under mechanical stimulation, the pain was induced on subject's non-dominant (left) volar forearm while for the thermal stimulation protocol (41℃ and 48℃), the pain was induced on subject's dominant (right) volar forearm. The reason we planned for this difference was to investigate the PFC activity in the processing of pain perception, irrespective of hand dominance. It was interesting to find the similarities in PFC activity irrespective of dominant/non-dominant volar forearm or mechanical/thermal stimulation as described in the

section above. However, the preferential laterality such as right hemispheric PFC role under mechanical stimulation could also stem from hand dominance that needs further investigation.

8.4 Discrimination of Pain Levels (Thermal)

One of the major experimental limitations of the mechanical stimulation study was that the pinching stimulation was manual and hence could not be controlled accurately to different pain levels. This drawback was compensated in the thermal study where the pain level was computer-controlled to two different levels (that is 41℃ and 48℃) that aided in the investigation for cognitive discrimination of pain levels. In this aspect, HbO-derived time to peak (ttp) that was quantified in this study proved to be a potential indicator for cognitive discrimination of two different pain levels. Figure 7-9 shows that the mean HbO-derived ttp from the late phase of LH aPFC for 48℃ was longer compared to that in response to the 41℃ thermal stimuli. Further, we also observed that the two mean values were significantly different at p=0.044. From a neurophysiological perspective, a possible reason for different lag times could be the preferential response from innervating nociceptive fibers in specific cortical area at different pain levels. Another possible reason could be the localized neurovascular coupling that possibly leads to different lag times in the HbO response under different pain levels. However, further investigation is necessary for a deeper scientific understanding of the underlying physiological cause for different lag times observed at the two different pain levels.

Another difference observed between the HbO responses from 41℃ and 48℃ thermal stimulation was that the RH DLPFC also played a significant role under 41℃ thermal stimuli that was not found under 48℃ thermal stimuli. From Figure 7-7(a), we observed that the HbO-derived PI from the RH DLPFC area significantly correlated with the pain rating under 41℃ thermal stimuli. It has to be recalled that both the 41℃ and 48℃ thermal stimuli were induced on right-handed subjects' dominant volar forearm. However, the RH DLPFC activity was found to be significant only under the lesser noxious 41℃ stimuli. The preferential role of RH DLPFC activity in addition to LH DLPFC under lesser noxious thermal stimuli needs further investigation.

As far as pain-induced HbO changes in the aPFC area are concerned, from Figure 6-4, we observe a trend for early phase HbO activation and late phase HbO deactivation in response to 48℃ thermal stimulation. However, under 41℃ th ermal stimulation, from Figure 7-2, we observed a trend for HbO deactivation both in the early and late phase in the aPFC area. Although the early phase HbO changes were not significant with respect to the baseline in both 41℃ and 48℃ thermal stimuli, it was intriguing to observe opposite pattern in HbO changes that needs further investigation. In the same lines, the DLPFC area also showed different patterns of HbO changes. From Figure 6-7, we observed that 48℃ stimuli induced negative HbO changes during early phase and HbO activation during the late phase. However under 41℃ stimuli, from Figure 7-5, we observe HbO activation both during the early and late phase. Once again, the early phase HbO changes in the DLPFC area were not significant with respect to the baseline in both 41℃ and 48℃ thermal stimuli. The non-signifi cance of HbO changes from the early phase of both aPFC and DLPFC areas does not imply that these areas are not involved in the processing of cognitive or affective components during the early phase of a painful experience. Instead, they could be involved in a process other than rating pain during this time period. The behavioral measure, that is pain rating, aided only in investigating cognitive evaluation of pain. Hence, further work should incorporate behavioral measures tailored to cognitive discrimination of pain levels to uncover the role played by the PFC areas specifically during the early phase of induced painful stimuli.

In the context of cognitive discrimination of pain levels, an optimal approach to tease apart this component would be to incorporate an event-related or mixed design. This approach would allow for randomizing both 41℃ and 48℃ stim uli within the protocol. This way, other confounding factors associated with typical block design such as anticipation and habituation can also be minimized to obtain a higher functional signal to noise ratio. However, this preliminary study, that incorporated 41℃ protocol followed by the 48℃ protocol, is the first study to our best knowledge to investigate the feasibility of fNIRS in discrimination of two different pain levels.

8.5 Plausible Cortical-physiology behind Cognitive Evaluation

In functional brain imaging studies, typically, the observation of interest is the task invoked increased neuronal activity that leads to increased blood flow and oxygen metabolism. However, in the field of fMRI, it has been intriguing to occasionally observe negative BOLD response. The early seminal work towards understanding the physiology behind negative BOLD response was shown in (Shmuel, et al., 2002). Later, another group carried out invasive optical studies on animal model to further explore the physiological interpretation of negative BOLD and negative HbO changes (Devor, et al., 2007). Specifically in this invasive optical study, they also reported a center-surround antagonistic pattern in the HbO changes due to a continuous phase of vasodilation and vasoconstriction.

In this study, consistent trend for HbO deactivation in the anterior prefrontal area was observed under both mechanical and thermal stimulation. This observation is consistent with the Devor et.al study where they observed HbO deactivation caused by synaptic inhibition coupled with concurrent arterial vasoconstriction (Devor, et al., 2007). In the same study, they also observed HbO activation was caused by depolarization coupled with arterial vasodilation. In conjunction with the Devor et.al optical study, HbO deactivation observed in this study implies that the pain stimulation possibly induces vasoconstriction, leading to decreased localized blood flow and oxygen supply (Shmuel, et al., 2002).

Recent studies have also shown that the decreased voltage sensitive calcium channels in the astrocytes coupled with neuronal inhibition leads to arterial vasoconstriction (Gordon, Choi, Rungta, Ellis-Davies, & MacVicar, 2008; Lauritzen, 2005). Further in another animal study, Ji et.al observed that the basolateral amygdala driven polysynaptic *GABA*ergic inhibition causes feed forward inhibition in the medial PFC pyramidal cells, reflecting cognitive impairment in pain (Ji, et al., 2010). These invasive studies in animal models along with non invasive fMRI human studies (Lui, et al., 2008) (Kong, et al., 2010) (Shmuel, et al., 2002) support the results of this study that the HbO deactivation reflecting cognitive evaluation of pain is probably caused by localized vasoconstriction and synaptic inhibition in the specific prefrontal areas.

CHAPTER 9

SUMMARY AND FURTHER WORK

Pain is a multi-dimensional experience that has been functionally categorized into sensory, adaptive, and affective components(McMahon & Koltzenberg, 2005). Although, several studies have explored the sensory mechanism of pain, in recent years, there is a growing interest to enhance our understanding of the cognitive and affective aspects of the pain experience. In this direction, there have been a growing number of reports from functional brain imaging studies to explore the “what” and “where” functional networks, but not much light has been shone on the “how much” module of the brain network involved in the pain processing.

To this date, the routine clinical practice in pain assessment is the verbal or numeric rating based on a specific scale. This approach does not give an objective assessment of the patient’s pain experience. Hence there is a growing interest to improve the clinical diagnosis and treatment through objective quantification of pain perception. Given that pain is a subjective experience, it is further challenging to quantify a state based on a specific biophysical sub-system of the brain whose presence regularly correlates with the pain experience.

Functional NIRS and DOT are budding neuroimaging tools that are gaining popularity in several clinical applications. The advantages offered by fNIRS or DOT over other currently available neuroimaging tools such as PET, and fMRI are that they provide a cheaper, mobile, and accessible method to measure brain hemodynamics in clinical settings. The motivation of this study was to steer the current fNIRS technology in the direction of quantifying neural correlates of pain perception from its measurements.

9.1 Synopsis of Findings

The major findings of this dissertation work are summarized in the following points:

1) Through this study, by incorporating two different pain stimulations (that is mechanical and thermal), it is shown that the fNIRS has the feasibility to quantify cognitive evaluation of pain perception.

2) The correlates obtained from the left hemispheric (LH) prefrontal areas across both mechanical and thermal stimulations implied that the left hemisphere plays a significant role in the processing of cognitive evaluation of pain.

3) Under mechanically stimulation, significant difference was not observed between the baseline and pinch-induced HbO changes. However, the HbO-derived PI from both the LH and right hemispheric (RH) aPFC were observed to significantly correlate with the pain rating during the early phase. In addition, the HbO-derived FWHM from RH aPFC significantly correlated with the pain rating.

4) Under both 41° and 48℃ thermal stimuli, only th e late phase HbO changes from the LH aPFC area were observed to be significant with respect to the associated baseline. Further, the HbO-derived PI from the late phase of LH aPFC highly correlated with the pain rating although the level of significance was not found at 0.05.

5) Specifically for thermal stimulation at both levels, significant correlates were observed in the DLPFC area. Although thermally-induced HbO changes were not significant with respect to the baseline from the DLPFC area, the HbO-derived PI from the LH DLPFC area significantly correlated with the pain rating under both 41℃ and 48℃ thermal stimuli. In addition, under 41℃ thermal stimuli alone, the HbO -derived PI from the RH DLPFC area significantly correlated with the pain rating.

6) Under mechanical stimulation, the correlates were significant during the early phase, while for thermal stimulation (both 41° and 48℃), the correlates were significant during the late phase of the pain stimulation.

7) Discrimination of the two different pain levels (that is 41℃ and 48℃) was observed in the late phase HbO-derived time to peak from the LH aPFC area. The HbO

response was found to have a longer lag in response to the relatively higher noxious (that is 48℃) thermal stimuli.

8) The HbO-derived parameters from the aPFC area reflect the cognitive evaluation of pain perception. Since aPFC area is also known to be involved in the processing of anticipation due to pain, we observed that the anticipation in response to the first pain stimulus did not affect the cognitive evaluation of pain revealed by the HbO-derived parameters from the aPFC area.

9.2 Drawbacks of this Study

Although the results observed from this study are promising and innovative, realistically, one specific scientific work cannot address all the questions due to the limitations of resources, scope, and time. Hence it is important to discuss the major drawbacks and limitations of this study with the hope that the reader is motivated to either validate the current results or to enhance the current cutting-edge scientific findings.

One of the major limitations of this study was that the subject population was relatively small for statistical robustness. The thermal study incorporated even a smaller subject pool of only 5 subjects compared to 8 subjects recruited for mechanical study. Although the nature of this study was preliminary investigation, observations from linear mixed model and regression analysis showed lower significance due to a small subject pool. From a clinical application perspective, this limitation calls for further verification of the current results by recruiting a larger population of healthy volunteers.

The protocol design of this study incorporated a two-condition block design, wherein the baseline was a no-stimulation condition. During the baseline, the subjects rested comfortably with their eyes closed and without any pain stimulation. The drawback of this design was that the baseline measurements from prefrontal area cannot be well-controlled in terms of variability stemming from several cognitive or affective components other than the desired cognitive component. For the pain discrimination protocol, the drawback was that on each subject, the 48℃ measurements were acquired after completing the entire 41℃ protocol. Although the two

protocols were interspersed by a sufficient time gap, the dynamics of the cognitive evaluation and discrimination cannot be well captured with the above approach. A better design for future study would be an event-related design that incorporates randomized 41 and 48℃ with jittered inter-stimulus interval. The event-related approach would enhance the temporal sensitivity to each of the different pain level and also aides in minimizing the habituation effects.

In the context of experimental protocol design, the pain stimulation was induced on the subject's non-dominant volar forearm for mechanical study; while for thermal study, the pain stimulation was induced on the dominant volar forearm. Recall that all the subjects recruited for both the mechanical and thermal studies were right-handed subjects. Irrespective of the kind of stimulation, consistent left hemispheric PFC activity was observed to be involved in the cognitive evaluation of pain. However, comparison of results across mechanical and thermal stimulation warrants caution in this study, since each kind of stimulation was induced on different volar forearms. A recent study has shown the role of hand dominance in the perception of pain (Pud, Golan, & Pesta, 2009). In regard with hand dominance, further work is necessary to explore the role played by prefrontal areas in the perception of pain.

The independent 6 minute long resting-state baseline measurements were carried out to explore the stability of the fNIRS-based baseline measurements. Since functional brain imaging involves quantification of relative changes, the resulting quantified measures depend on the baseline. Our preliminary study showed that a long resting-state baseline is not appropriate when the interest lies in quantification for 'functional' changes in response to a stimulus such as pain. Literature survey indicated that resting-state involves the phenomenon of spontaneous brain activity (Shmuel & Leopold, 2008) (He, et al., 2009) such that the hemodynamic-based measurements result in fluctuations of the signal. Hence, quantification for relative change in magnitude becomes challenging such that advanced and rigorous statistical and mathematical approaches are necessary to obtain unbiased measures for relative changes in the magnitude. In this study, baseline was set at 5 seconds to quantify HbO changes in response to pain stimuli. Further work is necessary to evaluate an optimal length for the baseline such that the quantification for functional changes is reliable.

In functional brain studies, blocked design is still a popular approach along with event-related and mixed designs that are also gaining importance in the recent years. Regardless of the experimental protocol design, t-test can be an appropriate univariate approach if the hypothesis testing requires comparing two groups for significant difference in the mean values. However, for the two-condition blocked design, since the t-test combines all the time points within a condition, it is insensitive to the shape of the hemodynamic response. In addition, t-test is also inherently insensitive to the differences in variability between the two groups. Another drawback with the t-test applied on task and non-task blocked design is that it is insensitive to the correlation between random noise (physiological or instrumentation) and task-induced cortical responses.

Given that this study involved repeated measurements, univariate tests were not the optimal approach as it assumes independence between the measurements. Hence, we relied on a more robust general linear mixed model approach to test the significance between baseline and pain-induced HbO changes. The mixed model is an extension of fixed effect model wherein the model allows for estimation of between-subjects variance at the group level (Beckmann, Jenkinson, & Smith, 2003). However in this study, the random effects were not investigated as the degree of freedom to estimate robust error variance was expected to be small due to the small size of subject pool. Within the fixed effect model, it comes down to the choice of the investigator to appropriately model the covariance structure of the residuals. In this study compound symmetry was chosen as it is mathematically a simple and parsimonious model that assumes equal correlation between the measurements within a cluster (cortical area) and across the subjects. Although the compound symmetry has been implemented in other studies (Ng, et al., 2010), from a practical perspective, first order autoregressive model, AR (1), is another reasonable choice. However in this study, since the preprocessing data analysis step involved high-pass filtering of the raw data, AR(1) was not an optimal choice as one of the recent fMRI study has shown that estimation of covariance using AR(1) is not robust if the covariance is estimated after the filtering step (Mumford & Nichols, 2008). Hence, having a larger subject population would allow to investigate for random effects and in addition, the covariance structure

for both the fixed and random effects can also be modeled using models other than compound symmetry such as AR(1) or unstructured to verify the current results of this study.

The primary goal of this dissertation work was to explore the cognitive evaluation of pain. In section 3.4 the role of anticipatory stress and anxiety in response to the painful stimuli were discussed. However, to explore the interaction between the cognitive evaluation and affective factor such as anticipatory stress, a post hoc analyses approach was undertaken as described in section 5.3.4.7 . Briefly, this approach statistically compares the HbO-derived parameters (that act as correlates) with and without the first stimulus block. To be more specific, 'with' first block implies that the temporal block averaging included all the 8 blocks while 'without' the first block means that the temporal block averaging was carried out on 2nd through the 8th block. The assumptions here were that (1) the anticipation in response to the first stimuli is higher than that in response to subsequent train of painful stimuli. (2) Excluding the first functional block from temporal averaging would minimize the effects of anticipation to negligible level. The post hoc analysis approach does not explicitly measure or quantify for anticipatory stress factor. A better approach for further study would be an experimental approach such as mixed or event-related design (Huettel Scott A, 2008) wherein before the painful stimuli, a 'cue' input (Kong, et al., 2006) can aide in exploring effects of anticipatory stress and its onset in response to incoming noxious pain stimuli. In addition, galvanic skin conductance measurements for arousal and anxiety (Williams, et al., 2001) should also be simultaneously acquired with the hemodynamic based optical measurements to investigate the influence of arousal and anxiety in the event of perception of pain.

9.3 Future Work

The advantages offered by fNIRS were explained in the Introduction chapter. However, it has its own major limitations such as depth sensitivity and spatial resolution. In the previous section, some of the limitations primarily associated with the design and methodology of this study were discussed. In this section, feasible further development of the fNIRS/DOT technology

and experimental methodologies towards a better approach in the investigation of cognitive aspects of pain and its objective quantification are discussed.

Optode geometry plays an important role in determining the spatial resolution and spatial distribution of fNIRS/DOT measured brain activity. In this direction, promising results are coming out for a balance between the probe density and spatial resolution(Tian, Alexandrakis, & Liu, 2009). Due to the diffuse nature of the photons traversing through the cortical tissue, depth sensitivity has always been a challenge in the DOT field. Recently developed depth compensation algorithms have proven to probe deeper into the cortical areas (Niu, Lin, Tian, Dhamne, & Liu, 2010). DOT/fNIRS and fMRI are complimentary under simultaneous measurements as DOT/fNIRS offers good temporal resolution while fMRI offers good spatial resolution. Simultaneous fNIRS/fMRI study towards understanding the principle behind neurovascular coupling (Boorman, et al., 2010) is a promising step towards investigation for neurovascular coupling underlying the cognitive and affective components of pain perception.

In surgical settings, in most of the cases, patients are induced with anesthetics. For clinicians, quantification for pain is very valuable information in monitoring analgesic efficacy. Recent simultaneous MEG (Magnetoencephalography) /DOT (Ou, et al., 2009) or EEG (Electroencephalography) /DOT (Franceschini, et al., 2010) studies have shown a progressive step in the field towards understanding the neurovascular dynamics under anesthesia. Quantification for pain and a deeper understanding for its neurovascular dynamics are very important in understanding the cause and mechanisms underlying drug addiction and related psychiatric conditions.

Functional connectivity is a developing and popular methodology for understanding a network of cortical and sub-cortical areas functionally involved in the processing of a specific task. This methodology was first developed in the fMRI field (Biswal, Yetkin, Haughton, & Hyde, 1995) and has also been recently implemented for DOT measurements (White, et al., 2009). In this current study, aPFC and DLPFC were observed to share a significant role in the cognitive evaluation of pain under thermal stimulation. In order to understand their connectivity, along with other cortical or sub-cortical areas, functional connectivity methods coupled with simultaneous

NIRS/fMRI studies would be a prospective future work to elicit the brain networks involved in cognitive and affective components of pain.

In typical functional brain imaging studies, it is quite uncommon to observe negative HbO changes in optical studies or negative BOLD responses in fMRI studies. The results from this current study are yet another torch bearer for the importance of a deeper scientific understanding for negative HbO changes and its implications in clinical diagnosis and therapy. In this direction, further experimental and quantitative approaches are necessary to elicit the physiological and physical processes underlying this elusive phenomenon.

Our current understanding of the cortical processing in cognitive and affective components of pain is in its infancy. Initiated by Wall and Melzack in the 1960s, several researchers over the years have converged upon the doctrine that pain perception is comprised of three major psychological dimensions: sensory-discriminative, motivational-affective and cognitive-evaluative. Understanding the role of nociceptive fibers and its innervations in prefrontal areas in the processing of cognitive and affective aspects of pain is not very well understood and was not within the scope of this study. Further invasive or non-invasive animal studies incorporating simultaneous electrophysiological and optical brain imaging studies are necessary to unravel some of these scientific mysteries.

This dissertation work was one little step taken towards quantification for cognitive-evaluation aspect of pain. Given that pain is a multi-dimensional phenomenon, it begs for further scientific work to objectively quantify for other dimensions such as cognitive-emotional component across both normal and patient population, and factors such as gender, age, culture etc. Further work towards innovative experimental protocol design and development of novel methods for objective quantification of pain is necessary in getting closer to mitigate pain.

APPENDIX A

MATLAB CODE TO OBTAIN '*.NIRS'* FILES

This MATLAB code was downloaded the from David Boas' PMI Lab website (Huppert & Boas, 2003) as a registered user and modified to the needs of probe configuration incorporated in this study.

```
function select_sd_CW5(filenm)
%select_sd_CW5('030917_00031_tapL1')

%Program written by T. Huppert  Oct 31st 2003
% Modified for pain measurements by Giri Krishnamurthy 01/10/2010
%%
%*********************************************************
%  THESE ARE THE ONLY PARTS THAT NEED TO BE CHANGED
%Specify the downsample fraction.
%down sample value starting from 100Hz (actually 100.159) (for final rate
%of 10Hz use a value of "10" or for final 100Hz use "1" etc...)
downSample=10;   %define 10 or 1

%Specify which lasers were plugged into to which optodes
%
%Define which lasers were in each source position
%PosLasers(1) =[#of 690nm laser  #of 830nm laser]
%i.e.  PosLasers(1)= [1 2]  means lasers 1 and 2 were plugged in at
%source optode position #1
PosLasers(1,:)=[1 2];
PosLasers(2,:)=[3 4];
PosLasers(3,:)=[5 6];
PosLasers(4,:)=[7 8];
PosLasers(5,:)=[9 10];
PosLasers(6,:)=[19 12];
PosLasers(7,:)=[13 14];
PosLasers(8,:)=[15 16];
 %Specify the Probe Layout and wavelengths used
SD.Lambda=[830 690];
 %Source Positions [X Y Z] in centimeters
SD.SrcPos(1,:)=[ -8.4 0 0];
SD.SrcPos(2,:)=[ -6.0 0 0];
```

```
SD.SrcPos(3,:)=[ -3.6 0 0];
SD.SrcPos(4,:)=[ -1.2 0 0];
SD.SrcPos(5,:)=[ 8.4 0 0];
SD.SrcPos(6,:)=[ 6.0 0 0];
SD.SrcPos(7,:)=[ 3.6 0 0];
SD.SrcPos(8,:)=[ 1.2 0 0];

%Detector Positions [X Y Z] in centimeters
SD.DetPos(1,:)  =[  -9.6    2.8 0];
SD.DetPos(2,:)  =[  -7.2    2.8 0];
SD.DetPos(3,:)  =[  -4.8    2.8 0];
SD.DetPos(4,:)  =[  -2.4    2.8 0];
SD.DetPos(5,:)  =[  -9.6    -2.8    0];
SD.DetPos(6,:)  =[  -7.2    -2.8    0];
SD.DetPos(7,:)  =[  -4.8    -2.8    0];
SD.DetPos(8,:)  =[  -2.4    -2.8    0];

SD.DetPos(9,:)   =[ 9.6 2.8 0];
SD.DetPos(10,:)  =[ 7.2 2.8 0];
SD.DetPos(11,:)  =[ 4.8 2.8 0];
SD.DetPos(12,:)  =[ 2.4 2.8 0];
SD.DetPos(13,:)  =[ 9.6 -2.8    0];
SD.DetPos(14,:)  =[ 7.2 -2.8    0];
SD.DetPos(15,:)  =[ 4.8 -2.8    0];
SD.DetPos(16,:)  =[ 2.4 -2.8    0];

% Specify which src-det combinations to save
%if you want to use an explicit Mlst change this to "if 1" and enter
%the SD_pairs structure.  SD_pair<laser pos number> = [list of all detectors that will see
this laser]
%
% SD_pairs(#)= [list of all detectors to connect to source #]

if 1
   flag=1;
   SD_pairs1=[1 2 5 6];
   SD_pairs2=[2 3 6 7];
```

```
   SD_pairs3=[3 4 7 8];
   SD_pairs4=[4 8];

   SD_pairs5=[9 10 13 14];
   SD_pairs6=[10 11 14 15];
   SD_pairs7=[11 12 15 16];
   SD_pairs8=[12 16];

else
   %Do this by a voltage threshhold
   flag=0;
   threshold=10^-11;        %Sets the threshold for which detectors to include for each source pair.
end

%Specify the channel that the stimmulus was on (1-8)
stimChan=2;

% this is set for the default outputs of CW5Filter- this needs to be
%modified if you use a different output structure
fileina = sprintf( '%s0A.cw5', filenm );
fileinb = sprintf( '%s0B.cw5', filenm );
fileinc = sprintf( '%s0C.cw5', filenm );
fileind = sprintf( '%s0D.cw5', filenm );
filein2A= sprintf( '%s_2A00000.bin', filenm);    %this may depend on the CW5 system used
%---------------------------------------

%*************************************************************************
%*************************************************************************
%%


%This loads in the data files- and displays an error if it can't find one-
%if this file doesn't exist then just ignore the error- its just a warning
freq=downSample;
numfiles=0;
```

```
%Read in the four DAQ cards A-D
if exist(fileina)~=0
   [Sa,da]=readPMIData(fileina);
   [na,ma]=size(Sa.MeasList);
   L=length(da);
   numfiles=numfiles+1;
else
   %disp('cannot find file %s', fileina)
   na=0;
   ma=0;
end

if exist(fileinb)~=0
   [Sb,db]=readPMIData(fileinb);
   [nb,mb]=size(Sb.MeasList);
   L=length(db);
   numfiles=numfiles+1;
else
   %disp('cannot find file %s', fileinb)
   nb=0;
   mb=0;
end

if exist(fileinc)~=0
   [Sc,dc]=readPMIData(fileinc);
   [nc,mc]=size(Sc.MeasList);
   L=length(dc);
   numfiles=numfiles+1;
else
   %disp('cannot find file %s', fileinc)
   nc=0;
   mc=0;
end

if exist(fileind)~=0
```

```
    [Sd,dd]=readPMIData(fileind);
    [nd,md]=size(Sd.MeasList);
    L=length(dd);
    numfiles=numfiles+1;
else
    %disp('cannot find file %s', fileind)
    nd=0;
    md=0;
end

if numfiles==0
    error('No files found')
    return
end
%%
%%Now contatinate the data into a single variable
S=zeros(na+nb+nc+nd,L);
idx=1;
if na~=0
    S(idx:na,:)=da(:,:);
    Mlst(idx:na,:)=Sa.MeasList(:,1:2);
    idx=idx+na;
end
if nb~=0
    S(idx:idx+nb-1,:)=db(:,:);
    Mlst(idx:idx+nb-1,1:2)=Sb.MeasList(:,1:2);
    idx=idx+nb;
end
if nc~=0
    S(idx:idx+nc-1,:)=dc(:,:);
    Mlst(idx:idx+nc-1,1:2)=Sc.MeasList(:,1:2);
    idx=idx+nc;
end
if nd~=0
     S(idx:idx+nd-1,:)=dd(:,:);
     Mlst(idx:idx+nd-1,1:2)=Sd.MeasList(:,1:2);
end
```

```
%%
%Sort the measurement list
counter=1;
if flag==1;
   for idx=1:length(PosLasers)
      if exist(sprintf('%s%d','SD_pairs',idx))~=0
         DetList=eval(sprintf('%s%d','SD_pairs',idx));
         lst1=find(Mlst(:,1)==PosLasers(idx,1));   %list of detectors for 830nm laser
         lst2=find(Mlst(:,1)==PosLasers(idx,2));
         for idx2=1:length(DetList)
            lst_idx1=find(Mlst(lst1,2)==DetList(idx2));    %830nm laser
            lst_idx2=find(Mlst(lst2,2)==DetList(idx2));     %690nm laser
            if isempty(lst_idx2) | isempty(lst_idx1)
               %warning('Couldn''t find source %d and detector %d pair',idx,DetList(idx2))
            else
               Measlist2(counter,:)=[idx DetList(idx2) 1 1];
               data2(counter,:)=abs(S(lst2(lst_idx2),:));
               Measlist1(counter,:)=[idx DetList(idx2) 1 2];
               data1(counter,:)=abs(S(lst1(lst_idx1),:));
               counter=counter+1;
            end
         end
         lst=[];
         lst2=[];
         lst_idx1=[];
         lst_idx2=[];
      end
   end
else

   for idx=1:length(PosLasers)
     lst=[];
      lst2=[];
      %for 1 to the num of laser positions find all the detectors that could
      %''see'' this laser-
      lst=find(Mlst(:,1)==PosLasers(idx,1));   %list of detectors for 830nm laser
```

```
      lst2=find(Mlst(:,1)==PosLasers(idx,2));

       for idx2=1:length(lst2)
         lst_idx=find(Mlst(lst(:),2)==Mlst(lst2(idx2),2));
         if mean(abs(S(lst2(idx2),26:end-25)))>threshold & mean(abs(S(lst(lst_idx),26:end-
25)))>threshold
            srcnum=[Mlst(lst2(idx2),1),Mlst(lst(lst_idx),1)];
            detnum=Mlst(lst2(idx2),2);
            Measlist1(counter,:)=[idx detnum 1 1];
            data2(counter,:)=abs(S(lst2(idx2),:));
            Measlist2(counter,:)=[idx detnum 1 2];
            data1(counter,:)=abs(S(lst(lst_idx),:));
            counter=counter+1;
         end
       end
   end
end
%%
%Now clean up the data and downsample.
n=length(Measlist1);
[a b]=size(data1);
SD.MeasList=zeros(n*2,4);
datar=[];
datar=ones(a*2,b);
datar(1:a,:)=data2(:,:);
datar(a+1:2*a,:)=data1(:,:);
SD.MeasList(1:n,:)=Measlist2;
SD.MeasList(n+1:2*n,:)=Measlist1;


d2= resample(datar',1,freq);

[L V]=size(d2);
t2=[1:L]'.*freq/(100.159);

ml=SD.MeasList;
```

```
clear data1 data2 data Measlist1 Measlist2 Sa Sb Sc Sd S da db dc dd;
%%
%Now we will deal with the Aux10 files
%this makes a call to the dac() file which unpacks the Cw5 structure

%Right now it DOESN'T correct for offset/delay time
if exist(filein2A)~=0
   [da,header]=dac(filein2A);
%The part of code to identify the start of the light channel and rearrange
%aux channels accordingly.
            drng=da(1,1:2*25000);%Assuming that the clock is in channel 1.Also delay is
no more than 2 sec
   zindx=find(drng==0);
   %zindx=find(drng<thres);
   for i=1:size(zindx,2)
     if(zindx(i+1)-zindx(i)>1)
       lcn=zindx(i)
       break;
     end
   end

    aux=da(:,lcn:end); %The new output doesn't contain the clock but all other channels
    %header.data_rate;
    %trunsec=lcn/ans;
    clear da,drng,zindx,lcn;
%End of code to identify the start of the light channel
   aux_temp=resample(aux',1,25);
   clear aux;
   [m n]= size(aux_temp);
   aux_temp2=zeros(ceil(m*1.00159)-2,n);
   %this assumes that time zero is the same for both
   %This does a linear extraplotion between points to find the
   %intermediate values.
   for idx=2:ceil(m*1.00159)-2
      change=(aux_temp(floor(idx/1.00159),:)-
aux_temp(ceil(idx/1.00159),:)).*(idx/1.00159-floor(idx/1.00159));
      aux_temp2(idx,:)=aux_temp(floor(idx/1.00159),:)-change(:)';
```

```
    end
    clear aux_temp;
    aux_temp3=resample(aux_temp2,1,freq*10);
else

    %disp('no aux file exists')
    aux_temp3=zeros(length(d2),1);
end
%%
%make all the variables the same length
%throw out first 20 and last 20 points

freq2=100/freq;

aux10=aux_temp3(20:end-80,:);
d=d2(20:length(aux10)+19,:);
t=t2(20:length(aux10)+19);

if size(aux10,2)>=stimChan
    s=aux10(:,stimChan);
else
    s=zeros(size(t));
end

fileout = sprintf( '%s_%dhz.nirs', filenm, freq2 );
save(fileout,'t','d','s','aux10','ml','SD','-MAT');
```

APPENDIX B

MATLAB CODE FOR QUANTIFICATION

The below MATLAB code is modified from (Furi Andi Karnapi, 2003) work that is publicly made available on the Mathworks website. The code is written to run the cursor over the temporal plot to obtain the accurate abscissa and ordinate values for quantification purpose.

```
function GTrace(select)
%GTRACE     Graph tracing utility
%
%To start: click or focus the plot you want to trace, then type GTrace in Matlab environment
%To stop: one click on the plot you're tracing
%
%If there're more than one plot in an axes, you can select which line to trace by
%selecting the listbox at the lower left corner
%
%Furi Andi Karnapi and Lee Kong Aik
%DSP Lab, School of EEE
%Nanyang Technological University
%Singapore
%March 2002
% Modified Giri Krishnamurthy 01/16/2010
%%

if nargin==0;
   currFcn = get(gcf, 'windowbuttonmotionfcn');
   currFcn2 = get(gcf, 'windowbuttondownfcn');
   currTitle = get(get(gca, 'Title'), 'String');

   handles = guidata(gca);
   if (isfield(handles,'ID') & handles.ID==1)
      disp('GTrace is already active.');
      return;
   else
      handles.ID = 1;
      disp('GTrace started.');
   end
```

```
    theDot = text(0, 0, '\leftarrow');
    set(theDot, 'FontWeight', 'bold', 'FontSize', 10);

    handles = createListBox(handles);
    handles.currFcn = currFcn;
    handles.currFcn2 = currFcn2;
    handles.currTitle = currTitle;
    handles.theDot = theDot;
    handles.theState = uisuspend(gcf);
    guidata(gca, handles);

    set(gcf, 'windowbuttonmotionfcn', 'GTrace(''OnMouseMove'')');
    set(gcf, 'windowbuttondownfcn', 'GTrace(''OnMouseDown'')');
else
   switch select

   case 'OnListBoxCallBack'
      GTrace_ListBoxCallback;
   case 'OnMouseMove'
      GTrace_OnMouseMove;
   case 'OnMouseDown'
      GTrace_OnMouseDown;
   end
end

%--------------------------------------------------------------------------------
function [out] = createListBox(handles)
ListBoxPost = [2 2 60 20];
Hc_listbox = uicontrol(gcf,'style','listbox','position',ListBoxPost);
lineObj = findobj(gca, 'Type', 'line');
numOfLines = max(size(lineObj));
if numOfLines > 0
    dispString = '1';
else
    return;
end
for i=2:numOfLines
```

```
    dispString = [dispString sprintf('|%d',i)];
end
set(Hc_listbox,'string',dispString);
set(Hc_listbox,'callback','GTrace(''OnListBoxCallBack'')');
handles.whichOne = 1;
handles.ListBox = Hc_listbox;
out = handles;

GTrace_ListBoxCallback(Hc_listbox);

%--------------------------------------------------------------------------------
function GTrace_OnMouseMove

global xData yData;

pt = get(gca, 'CurrentPoint');
xInd = pt(1, 1);
lineObj = findobj(gca, 'Type', 'line');
xLim = get(gca, 'XLim');
yLim = get(gca, 'YLim');
numOfLines = max(size(lineObj));

handles = guidata(gca);
whichOne = handles.whichOne;

if ((xInd < xLim(1)) | (xInd > xLim(2)) | (xInd < min(xData)) | (xInd > max(xData)))
    title('Out of X limit');
    return;
end

yInd = interp1(xData, yData, xInd);
if ((yInd < yLim(1)) | (yInd > yLim(2)))
    title('Out of Y limit');
    return;
end

set(handles.theDot, 'Position', [xInd, yInd]);
```

```
title(['LINE ' num2str(whichOne) ' of ' num2str(numOfLines) '; X = ' num2str(xInd) ...
      ', Y = ' num2str(yInd)]);

%--------------------------------------------------------------------------------
function GTrace_ListBoxCallback(aData)

global xData yData

handles = guidata(gca);
if (nargin ~= 1)
   handles.whichOne = get(gcbo,'value');
else
   handles.whichOne = get(aData,'value');
end

whichOne = handles.whichOne;
guidata(gca,handles);

lineObj = findobj(gca, 'Type', 'line');
lineObj = lineObj(whichOne);
xData = get(lineObj, 'xData');
yData = get(lineObj, 'yData');
xLim = get(gca, 'XLim');
yLim = get(gca, 'YLim');
reqInd = find((xData >= xLim(1)) & (xData <= xLim(2)));
if (length(reqInd) < 2) %Suppose the user zoom the data until the reqInd = []
   i1 = find(xData < xLim(1)); %Let the reqInd(1) = the last indice before min x axis
   i2 = find(xData > xLim(2)); %Let the reqInd(2) = the first indice after max x axis
   reqInd = [i1(end):i2(1)];
end
xData = xData(reqInd);
yData = yData(reqInd);

%--------------------------------------------------------------------------------
function GTrace_OnMouseDown

handles = guidata(gca);
```

```
set(gcf, 'windowbuttonmotionfcn', handles.currFcn);
set(gcf, 'windowbuttondownfcn', handles.currFcn2);
title(handles.currTitle);
delete(handles.theDot);
delete(handles.ListBox);
uirestore(handles.theState);
handles.ID=0;
guidata(gca,handles);
clear xData yData;
disp('GTrace ended.');
```

APPENDIX C

SAS CODE AND RESULTS: PINCH DATA

SAS Code:

```
libname saslib 'C:\Users\rowe\Documents\consult\giri\f060911\';

data one;
  set saslib.pinch;
  pinch_scaled=pinch*10000;

proc mixed data=one empirical;
  class code subject;
  model pinch_scaled=code/s outp=m_one;
  repeated / subject=subject type=cs;
  lsmeans code/pdiff;
  title 'CS';

proc univariate data=m_one plot normal;
  var resid;
  run;
```

Key Notations:

bLHaPFC : baseline data from LH aPFC

bRHaPFC : baseline data from RH aPFC

bLHdlPFC : baseline data from LH DLPFC

bRHdlPFC : baseline data from RH DLPFC

LHaPFC_E : Early phase data from LH aPFC

RHaPFC_E : Early phase data from RH aPFC

LHdlPFC_E : Early phase data from LH DLPFC

RHdlPFC_E : Early phase data from RH DLPFC

LHaPFC_L : Late phase data from LH aPFC

RHaPFC_L : Late phase data from RH aPFC

Yellow shade: highlights the comparison for significance between baseline and stimulus-induced HbO changes.

Green shade: highlights the significance of interest ($p<0.05$)

SAS Results:

10:42 Wednesday, June 15, 2011 1

The Mixed Procedure

Model Information

Data Set	WORK.ONE
Dependent Variable	pinch_scaled
Covariance Structure	Compound Symmetry
Subject Effect	subject
Estimation Method	REML
Residual Variance Method	Profile
Fixed Effects SE Method	Empirical
Degrees of Freedom Method	Between-Within

Class Level Information

Class	Levels	Values
code	10	LHaPFC_E LHaPFC_L LHdlPFC_E RHaPFC_E RHaPFC_L RHdlPFC_E bLHaPFC bLHdlPFC bRHaPFC bRHdlPFC
subject	8	S01 S20 S21 S22 S23 S25 S26 S27

Dimensions

Covariance Parameters	2
Columns in X	11
Columns in Z	0
Subjects	8
Max Obs Per Subject	430

Number of Observations

Number of Observations Read	3440
Number of Observations Used	3440
Number of Observations Not Used	0

Iteration History

Iteration	Evaluations	-2 Res Log Like	Criterion
0	1	-17961.25724091	
1	1	-18330.89704337	0.00000000

Convergence criteria met.

CS 10:42 Wednesday, June 15, 2011 2

The Mixed Procedure

Covariance Parameter Estimates

Cov Parm	Subject	Estimate
CS	subject	0.000038
Residual		0.000273

Fit Statistics

-2 Res Log Likelihood	-18330.9
AIC (smaller is better)	-18326.9
AICC (smaller is better)	**-18326.9**
BIC (smaller is better)	-18326.7

Null Model Likelihood Ratio Test

DF	Chi-Square	Pr > ChiSq
1	369.64	<.0001

Solution for Fixed Effects

Effect	code	Estimate	Standard Error	DF	t Value	Pr > |t|
Intercept		-0.00006	0.000101	7	-0.58	0.5808
code	LHaPFC_E	-0.00884	0.005295	63	-1.67	0.1001
code	LHaPFC_L	0.008988	0.008807	63	1.02	0.3114
code	LHdlPFC_E	0.001253	0.008903	63	0.14	0.8885
code	RHaPFC_E	-0.00539	0.003916	63	-1.38	0.1732
code	RHaPFC_L	0.007600	0.007705	63	0.99	0.3277
code	RHdlPFC_E	0.000880	0.004790	63	0.18	0.8548
code	bLHaPFC	0.000137	0.000104	63	1.32	0.1933
code	bLHdlPFC	0.000242	0.000237	63	1.02	0.3107
code	bRHaPFC	0.000072	0.000107	63	0.68	0.5001
code	bRHdlPFC	0	.	.	.	.

Type 3 Tests of Fixed Effects

Effect	Num DF	Den DF	F Value	Pr > F
code	7	63	2.45	0.0275

The Mixed Procedure

Least Squares Means

Effect	code	Estimate	Standard Error	DF	t Value	Pr > |t|
code	LHaPFC_E	-0.00889	0.005287	63	-1.68	0.0974
code	LHaPFC_L	0.008930	0.008883	63	1.01	0.3186
code	LHdlPFC_E	0.001195	0.008916	63	0.13	0.8938
code	RHaPFC_E	-0.00545	0.003939	63	-1.38	0.1711
code	RHaPFC_L	0.007542	0.007786	63	0.97	0.3364
code	RHdlPFC_E	0.000822	0.004739	63	0.17	0.8629
code	bLHaPFC	0.000078	0.000040	63	1.96	0.0550
code	bLHdlPFC	0.000183	0.000260	63	0.70	0.4840
code	bRHaPFC	0.000014	0.000056	63	0.25	0.8056
code	bRHdlPFC	-0.00006	0.000101	63	-0.58	0.5647

Differences of Least Squares Means

Effect	code	_code	Estimate	Standard Error	DF	t Value	Pr > |t|
code	LHaPFC_E	LHaPFC_L	-0.01782	0.01069	63	-1.67	0.1004
code	LHaPFC_E	LHdlPFC_E	-0.01009	0.009396	63	-1.07	0.2870
code	LHaPFC_E	RHaPFC_E	-0.00344	0.004019	63	-0.86	0.3951
code	LHaPFC_E	RHaPFC_L	-0.01644	0.009455	63	-1.74	0.0870
code	LHaPFC_E	RHdlPFC_E	-0.00972	0.007030	63	-1.38	0.1718
code	LHaPFC_E	bLHaPFC	-0.00897	0.005276	63	-1.70	0.0939
code	LHaPFC_E	bLHdlPFC	-0.00908	0.005331	63	-1.70	0.0935
code	LHaPFC_E	bRHaPFC	-0.00891	0.005269	63	-1.69	0.0958
code	LHaPFC_E	bRHdlPFC	-0.00884	0.005295	63	-1.67	0.1001
code	LHaPFC_L	LHdlPFC_E	0.007735	0.01043	63	0.74	0.4612
code	LHaPFC_L	RHaPFC_E	0.01438	0.008912	63	1.61	0.1115
code	LHaPFC_L	RHaPFC_L	0.001388	0.002686	63	0.52	0.6070
code	LHaPFC_L	RHdlPFC_E	0.008108	0.01179	63	0.69	0.4942
code	LHaPFC_L	bLHaPFC	0.008852	0.008866	63	1.00	0.3219
code	LHaPFC_L	bLHdlPFC	0.008747	0.008787	63	1.00	0.3233
code	LHaPFC_L	bRHaPFC	0.008916	0.008875	63	1.00	0.3189
code	LHaPFC_L	bRHdlPFC	0.008988	0.008807	63	1.02	0.3114
code	LHdlPFC_E	RHaPFC_E	0.006648	0.009182	63	0.72	0.4717
code	LHdlPFC_E	RHaPFC_L	-0.00635	0.009448	63	-0.67	0.5042
code	LHdlPFC_E	RHdlPFC_E	0.000373	0.008563	63	0.04	0.9654
code	LHdlPFC_E	bLHaPFC	0.001117	0.008908	63	0.13	0.9006
code	LHdlPFC_E	bLHdlPFC	0.001012	0.009003	63	0.11	0.9109
code	LHdlPFC_E	bRHaPFC	0.001181	0.008922	63	0.13	0.8951
code	LHdlPFC_E	bRHdlPFC	0.001253	0.008903	63	0.14	0.8885
code	RHaPFC_E	RHaPFC_L	-0.01299	0.007279	63	-1.79	0.0790
code	RHaPFC_E	RHdlPFC_E	-0.00627	0.006734	63	-0.93	0.3550
code	RHaPFC_E	bLHaPFC	-0.00553	0.003948	63	-1.40	0.1661
code	RHaPFC_E	bLHdlPFC	-0.00564	0.003845	63	-1.47	0.1477
code	RHaPFC_E	bRHaPFC	-0.00547	0.003957	63	-1.38	0.1719

The Mixed Procedure

Differences of Least Squares Means

Effect	code	_code	Estimate	Standard Error	DF	t Value	Pr > |t|
code	RHaPFC_E	bRHdlPFC	-0.00539	0.003916	63	-1.38	0.1732
code	RHaPFC_L	RHdlPFC_E	0.006720	0.01111	63	0.60	0.5474
code	RHaPFC_L	bLHaPFC	0.007463	0.007774	63	0.96	0.3407
code	RHaPFC_L	bLHdlPFC	0.007358	0.007690	63	0.96	0.3423
code	RHaPFC_L	bRHaPFC	0.007528	0.007785	63	0.97	0.3373
code	RHaPFC_L	bRHdlPFC	0.007600	0.007705	63	0.99	0.3277
code	RHdlPFC_E	bLHaPFC	0.000744	0.004752	63	0.16	0.8762
code	RHdlPFC_E	bLHdlPFC	0.000639	0.004781	63	0.13	0.8942
code	RHdlPFC_E	bRHaPFC	0.000808	0.004754	63	0.17	0.8656
code	RHdlPFC_E	bRHdlPFC	0.000880	0.004790	63	0.18	0.8548
code	bLHaPFC	bLHdlPFC	-0.00010	0.000282	63	-0.37	0.7108
code	bLHaPFC	bRHaPFC	0.000065	0.000030	63	2.13	0.0370
code	bLHaPFC	bRHdlPFC	0.000137	0.000104	63	1.32	0.1933
code	bLHdlPFC	bRHaPFC	0.000170	0.000289	63	0.59	0.5592
code	bLHdlPFC	bRHdlPFC	0.000242	0.000237	63	1.02	0.3107
code	bRHaPFC	bRHdlPFC	0.000072	0.000107	63	0.68	0.5001

The UNIVARIATE Procedure
Variable: Resid (Residual)

Moments

N	3440	Sum Weights	3440
Mean	0	Sum Observations	0
Std Deviation	0.01747462	Variance	0.00030536

Skewness	0.57344423	Kurtosis	2.87118706
Uncorrected SS	1.05014166	Corrected SS	1.05014166
Coeff Variation	.	Std Error Mean	0.00029794

Basic Statistical Measures

Location		Variability	
Mean	0.00000	Std Deviation	0.01747
Median	-0.00044	Variance	0.0003054
Mode	.	Range	0.14104
		Interquartile Range	0.01660

Tests for Location: Mu0=0

Test	-Statistic-		-----p Value------	
Student's t	t	0	Pr > |t|	1.0000
Sign	M	-46	Pr >= |M|	0.1208
Signed Rank	S	-125472	Pr >= |S|	0.0312

Tests for Normality

Test	--Statistic---		-----p Value------	
Kolmogorov-Smirnov	D	0.092222	Pr > D	<0.0100
Cramer-von Mises	W-Sq	8.788283	Pr > W-Sq	<0.0050
Anderson-Darling	A-Sq	54.60622	Pr > A-Sq	<0.0050

Quantiles (Definition 5)

Quantile	Estimate
100% Max	0.07166474
99%	0.05925128
95%	0.02789170
90%	0.01714566
75% Q3	0.00764403
50% Median	-0.00044472
25% Q1	-0.00895962
10%	-0.01871762

The UNIVARIATE Procedure
Variable: Resid (Residual)

Quantiles (Definition 5)

Quantile	Estimate
5%	-0.02898987
1%	-0.04409293
0% Min	-0.06937733

Extreme Observations

-------Lowest------		------Highest------	
Value	Obs	Value	Obs
-0.0693773	2898	0.0693010	956
-0.0685513	2899	0.0699507	955
-0.0679219	2897	0.0705583	954

-0.0657084	2900	0.0711286	953
-0.0640892	2896	0.0716647	952

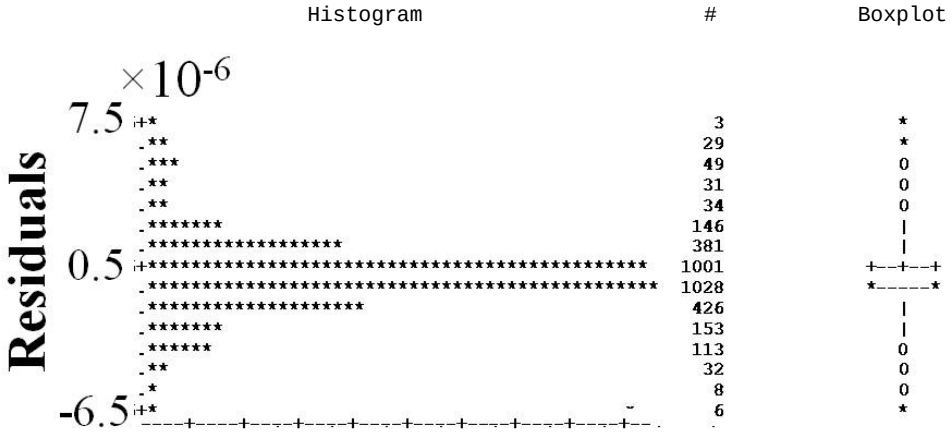

Figure C-1: Histogram and box plot of the residuals obtained from the linear mixed model analysis on the mechanical stimulation data. Note: * : data points; 0: outliers in the box plot.

The SAS System 10:44 Thursday, June 9, 2011 11

The UNIVARIATE Procedure
Variable: Resid (Residual)

Normal Probability Plot

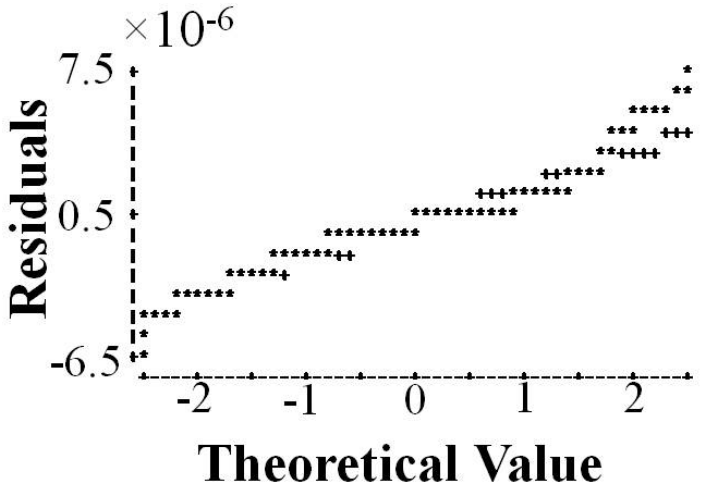

Figure C-2: Normal Probability plot of the residuals obtained from the linear mixed model analysis on the mechanical stimulation data. Note: * : data points; and the theoretical normal values are derived with standard normal distribution of mean 0 and variance of 1 and denoted by '+' in the above plot.

APPENDIX D

SAS CODE AND RESULTS: 48℃ THERMAL DATA

SAS Code:

```
libname saslib 'C:\Users\rowe\Documents\consult\giri\f060911\';

data one;
  set saslib.basevstem;
  forty8_thr_scaled=forty_eight_thermal*10000;

proc mixed data=one empirical;
  class code subject;
  model forty8_thr_scaled=code/s outp=m_one;
  repeated / subject=subject type=cs;
  lsmeans code/pdiff;
  title 'repeated CS';

proc univariate data=m_one plot normal;
  var resid;
  run;
```

Key Notations:

bLHaPFC : baseline data from LH aPFC

bRHaPFC : baseline data from RH aPFC

bLHdlPFC : baseline data from LH DLPFC

bRHdlPFC : baseline data from RH DLPFC

LHaPFC_E : Early phase data from LH aPFC

RHaPFC_E : Early phase data from RH aPFC

LHdlPFC_E : Early phase data from LH DLPFC

RHdlPFC_E : Early phase data from RH DLPFC

LHaPFC_L : Late phase data from LH aPFC

RHaPFC_L : Late phase data from RH aPFC

LHdlPFC_L : Late phase data from LH DLPFC

RHdlPFC_L : Late phase data from RH DLPFC

Yellow shade: highlights the comparison for significance between baseline and stimulus-induced HbO changes.

Green shade: highlights the significance of interest ($p<0.05$)

SAS Results:

10:49 Wednesday, June 15, 2011 1

The Mixed Procedure

Model Information

Data Set	WORK.ONE
Dependent Variable	forty8_thr_scaled
Covariance Structure	Compound Symmetry
Subject Effect	subject
Estimation Method	REML
Residual Variance Method	Profile
Fixed Effects SE Method	Empirical
Degrees of Freedom Method	Between-Within

Class Level Information

Class	Levels	Values
code	12	LHaPFC_E LHaPFC_L LHdlPFC_E LHdlPFC_L RHaPFC_E RHaPFC_L RHdlPFC_E RHdlPFC_L bLHaPFC bLHdlPFC bRHaPFC bRHdlPFC
subject	5	S20 S23 S25 S26 S28

Dimensions

Covariance Parameters	2
Columns in X	13
Columns in Z	0
Subjects	5
Max Obs Per Subject	518

Number of Observations

Number of Observations Read	2590
Number of Observations Used	2590
Number of Observations Not Used	0

Iteration History

Iteration	Evaluations	-2 Res Log Like	Criterion
0	1	-6299.51259017	
1	1	-6301.83975549	0.00000000

Convergence criteria met.

repeated CS 10:49 Wednesday, June 15, 2011 2

The Mixed Procedure

Covariance Parameter Estimates

Cov Parm	Subject	Estimate
CS	subject	0.000014
Residual		0.004949

Fit Statistics

-2 Res Log Likelihood	-6301.8
AIC (smaller is better)	-6297.8
AICC (smaller is better)	-6297.8
BIC (smaller is better)	-6298.6

Null Model Likelihood Ratio Test

DF	Chi-Square	Pr > ChiSq
1	2.33	0.1271

Solution for Fixed Effects

Effect	code	Estimate	Standard Error	DF	t Value	Pr > |t|
Intercept		0.000078	0.000049	4	1.60	0.1854
code	LHaPFC_E	0.009977	0.009472	44	1.05	0.2979
code	LHaPFC_L	-0.01685	0.006971	44	-2.42	0.0198
code	LHdlPFC_E	-0.00659	0.01564	44	-0.42	0.6756
code	LHdlPFC_L	0.03786	0.03263	44	1.16	0.2523
code	RHaPFC_E	0.002382	0.003999	44	0.60	0.5545
code	RHaPFC_L	-0.00313	0.006439	44	-0.49	0.6297
code	RHdlPFC_E	-0.1414	0.1094	44	-1.29	0.2031
code	RHdlPFC_L	0.03849	0.03783	44	1.02	0.3145
code	bLHaPFC	-0.00008	0.000023	44	-3.36	0.0016
code	bLHdlPFC	-0.00008	0.000034	44	-2.24	0.0305
code	bRHaPFC	-0.00006	0.000052	44	-1.24	0.2208
code	bRHdlPFC	0	.	.	.	.

Type 3 Tests of Fixed Effects

Effect	Num DF	Den DF	F Value	Pr > F
code	4	44	3.87	0.0089

The Mixed Procedure

Least Squares Means

Effect	code	Estimate	Standard Error	DF	t Value	Pr > |t|
code	LHaPFC_E	0.01006	0.009455	44	1.06	0.2934
code	LHaPFC_L	**-0.01677**	0.007012	44	-2.39	0.0211
code	LHdlPFC_E	-0.00651	0.01568	44	-0.42	0.6800
code	LHdlPFC_L	0.03793	0.03259	44	1.16	0.2508
code	RHaPFC_E	0.002460	0.003964	44	0.62	0.5381
code	RHaPFC_L	-0.00305	0.006472	44	-0.47	0.6399
code	RHdlPFC_E	-0.1413	0.1094	44	-1.29	0.2035
code	RHdlPFC_L	0.03857	0.03779	44	1.02	0.3130
code	bLHaPFC	**-1.22E-7**	0.000059	44	-0.00	0.9984
code	bLHdlPFC	1.59E-6	0.000058	44	0.03	0.9784
code	bRHaPFC	0.000013	0.000064	44	0.21	0.8359
code	bRHdlPFC	0.000078	0.000049	44	1.60	0.1173

Differences of Least Squares Means

Effect	code	_code	Estimate	Standard Error	DF	t Value	Pr > |t|
code	LHaPFC_E	LHaPFC_L	0.02683	0.01460	44	1.84	0.0728
code	LHaPFC_E	LHdlPFC_E	0.01657	0.02229	44	0.74	0.4614
code	LHaPFC_E	LHdlPFC_L	-0.02788	0.02602	44	-1.07	0.2898
code	LHaPFC_E	RHaPFC_E	0.007596	0.009913	44	0.77	0.4476
code	LHaPFC_E	RHaPFC_L	0.01310	0.01289	44	1.02	0.3150
code	LHaPFC_E	RHdlPFC_E	0.1513	0.1173	44	1.29	0.2036
code	LHaPFC_E	RHdlPFC_L	-0.02851	0.03148	44	-0.91	0.3700
code	LHaPFC_E	bLHaPFC	0.01006	0.009473	44	1.06	0.2943
code	LHaPFC_E	bLHdlPFC	0.01005	0.009485	44	1.06	0.2950
code	LHaPFC_E	bRHaPFC	0.01004	0.009494	44	1.06	0.2960
code	LHaPFC_E	bRHdlPFC	0.009977	0.009472	44	1.05	0.2979
code	LHaPFC_L	LHdlPFC_E	-0.01026	0.01245	44	-0.82	0.4141
code	LHaPFC_L	LHdlPFC_L	-0.05471	0.03915	44	-1.40	0.1693
code	LHaPFC_L	RHaPFC_E	-0.01923	0.01055	44	-1.82	0.0752
code	LHaPFC_L	RHaPFC_L	-0.01372	0.007975	44	-1.72	0.0923
code	LHaPFC_L	RHdlPFC_E	0.1245	0.1037	44	1.20	0.2363
code	LHaPFC_L	RHdlPFC_L	-0.05534	0.04440	44	-1.25	0.2192
code	LHaPFC_L	bLHaPFC	-0.01677	0.006976	44	-2.40	**0.0205**
code	LHaPFC_L	bLHdlPFC	-0.01677	0.006957	44	-2.41	0.0201
code	LHaPFC_L	bRHaPFC	-0.01679	0.006981	44	-2.40	0.0205
code	LHaPFC_L	bRHdlPFC	-0.01685	0.006971	44	-2.42	0.0198
code	LHdlPFC_E	LHdlPFC_L	-0.04444	0.04624	44	-0.96	0.3418
code	LHdlPFC_E	RHaPFC_E	-0.00897	0.01711	44	-0.52	0.6027
code	LHdlPFC_E	RHaPFC_L	-0.00346	0.01139	44	-0.30	0.7626
code	LHdlPFC_E	RHdlPFC_E	0.1348	0.09576	44	1.41	0.1663
code	LHdlPFC_E	RHdlPFC_L	-0.04508	0.05147	44	-0.88	0.3859
code	LHdlPFC_E	bLHaPFC	-0.00651	0.01563	44	-0.42	0.6791

The Mixed Procedure

Differences of Least Squares Means

Effect	code	_code	Estimate	Standard Error	DF	t Value	Pr > |t|
code	LHdlPFC_E	bLHdlPFC	-0.00651	0.01565	44	-0.42	0.6794
code	LHdlPFC_E	bRHaPFC	-0.00652	0.01564	44	-0.42	0.6787
code	LHdlPFC_E	bRHdlPFC	-0.00659	0.01564	44	-0.42	0.6756
code	LHdlPFC_L	RHaPFC_E	0.03548	0.03057	44	1.16	0.2521
code	LHdlPFC_L	RHaPFC_L	0.04098	0.03576	44	1.15	0.2580
code	LHdlPFC_L	RHdlPFC_E	0.1792	0.1415	44	1.27	0.2119
code	LHdlPFC_L	RHdlPFC_L	-0.00063	0.005534	44	-0.11	0.9097
code	LHdlPFC_L	bLHaPFC	0.03793	0.03263	44	1.16	0.2513
code	LHdlPFC_L	bLHdlPFC	0.03793	0.03264	44	1.16	0.2515
code	LHdlPFC_L	bRHaPFC	0.03792	0.03263	44	1.16	0.2514
code	LHdlPFC_L	bRHdlPFC	0.03786	0.03263	44	1.16	0.2523
code	RHaPFC_E	RHaPFC_L	0.005508	0.007958	44	0.69	0.4925
code	RHaPFC_E	RHdlPFC_E	0.1437	0.1111	44	1.29	0.2026
code	RHaPFC_E	RHdlPFC_L	-0.03611	0.03561	44	-1.01	0.3162
code	RHaPFC_E	bLHaPFC	0.002460	0.003991	44	0.62	0.5409
code	RHaPFC_E	bLHdlPFC	0.002458	0.004016	44	0.61	0.5436
code	RHaPFC_E	bRHaPFC	0.002446	0.003984	44	0.61	0.5424
code	RHaPFC_E	bRHdlPFC	0.002382	0.003999	44	0.60	0.5545
code	RHaPFC_L	RHdlPFC_E	0.1382	0.1061	44	1.30	0.1992
code	RHaPFC_L	RHdlPFC_L	-0.04161	0.04100	44	-1.01	0.3157
code	RHaPFC_L	bLHaPFC	-0.00305	0.006419	44	-0.47	0.6371
code	RHaPFC_L	bLHdlPFC	-0.00305	0.006451	44	-0.47	0.6386
code	RHaPFC_L	bRHaPFC	-0.00306	0.006420	44	-0.48	0.6358
code	RHaPFC_L	bRHdlPFC	-0.00313	0.006439	44	-0.49	0.6297
code	RHdlPFC_E	RHdlPFC_L	-0.1798	0.1465	44	-1.23	0.2260
code	RHdlPFC_E	bLHaPFC	-0.1413	0.1094	44	-1.29	0.2033
code	RHdlPFC_E	bLHdlPFC	-0.1413	0.1094	44	-1.29	0.2033
code	RHdlPFC_E	bRHaPFC	-0.1413	0.1094	44	-1.29	0.2033
code	RHdlPFC_E	bRHdlPFC	-0.1414	0.1094	44	-1.29	0.2031

code	RHdlPFC_L	bLHaPFC	0.03857	0.03783	44	1.02	0.3135
code	RHdlPFC_L	bLHdlPFC	0.03856	0.03784	44	1.02	0.3137
code	RHdlPFC_L	bRHaPFC	0.03855	0.03782	44	1.02	0.3136
code	RHdlPFC_L	bRHdlPFC	0.03849	0.03783	44	1.02	0.3145
code	bLHaPFC	bLHdlPFC	-1.71E-6	0.000050	44	-0.03	0.9727
code	bLHaPFC	bRHaPFC	-0.00001	0.000044	44	-0.31	0.7594
code	bLHaPFC	bRHdlPFC	-0.00008	0.000023	44	-3.36	0.0016
code	bLHdlPFC	bRHaPFC	-0.00001	0.000051	44	-0.23	0.8200
code	bLHdlPFC	bRHdlPFC	-0.00008	0.000034	44	-2.24	0.0305
code	bRHaPFC	bRHdlPFC	-0.00006	0.000052	44	-1.24	0.2208

The UNIVARIATE Procedure
Variable: Resid (Residual)

Moments

N	2590	Sum Weights	2590
Mean	0	Sum Observations	0
Std Deviation	0.07027806	Variance	0.00493901
Skewness	-3.1671692	Kurtosis	30.1964529
Uncorrected SS	12.7870864	Corrected SS	12.7870864
Coeff Variation	.	Std Error Mean	0.00138092

Basic Statistical Measures

Location		Variability	
Mean	0.00000	Std Deviation	0.07028
Median	-0.00076	Variance	0.00494
Mode	.	Range	0.89857
		Interquartile Range	0.02214

Tests for Location: Mu0=0

Test	-Statistic-		-----p Value------	
Student's t	t	0	Pr > |t|	1.0000
Sign	M	-87	Pr >= |M|	0.0007
Signed Rank	S	-144776	Pr >= |S|	0.0001

Tests for Normality

Test	--Statistic---		-----p Value------	
Kolmogorov-Smirnov	D	0.244139	Pr > D	<0.0100
Cramer-von Mises	W-Sq	58.67483	Pr > W-Sq	<0.0050
Anderson-Darling	A-Sq	300.1085	Pr > A-Sq	<0.0050

Quantiles (Definition 5)

Quantile	Estimate
100% Max	0.300352729
99%	0.197808008
95%	0.125775901
90%	0.038237767
75% Q3	0.007928571
50% Median	-0.000755025
25% Q1	-0.014209159
10%	-0.040763285

The UNIVARIATE Procedure
Variable: Resid (Residual)

Quantiles (Definition 5)

Quantile	Estimate
5%	-0.052941293
1%	-0.333301949
0% Min	-0.598217720

Extreme Observations

Lowest		Highest	
Value	Obs	Value	Obs
-0.598218	2535	0.280911	2547
-0.596273	2534	0.286153	2546
-0.596067	2536	0.291159	2545
-0.590602	2533	0.295901	2544
-0.589585	2537	0.300353	2543

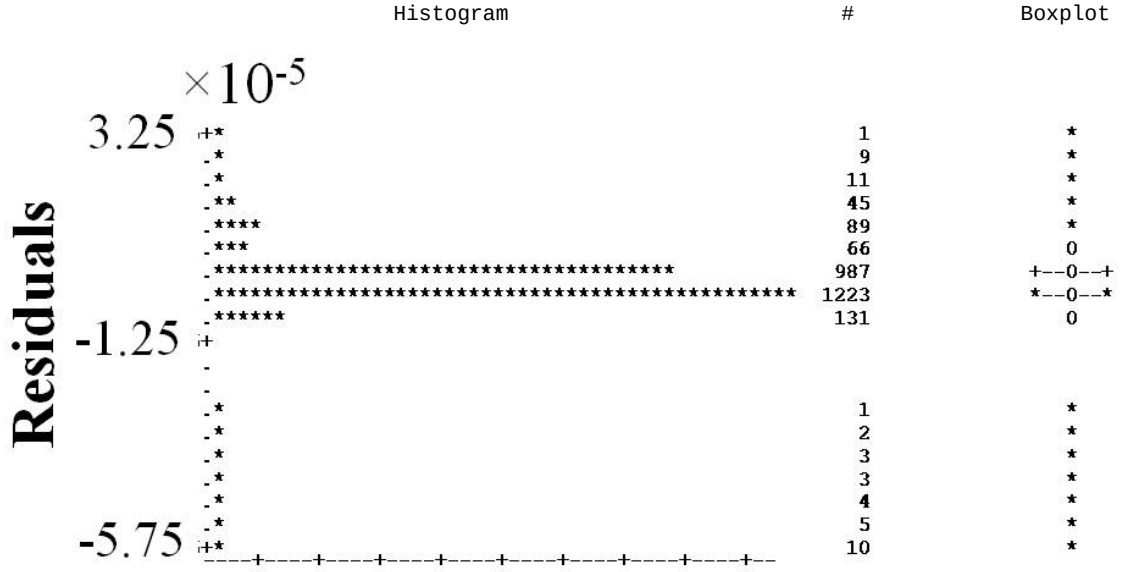

Figure D-1: Histogram and box plot of the residuals obtained from the linear mixed model analysis on the 48℃ thermal stimulation data. Note : * : data points; 0: outliers in the box plot.

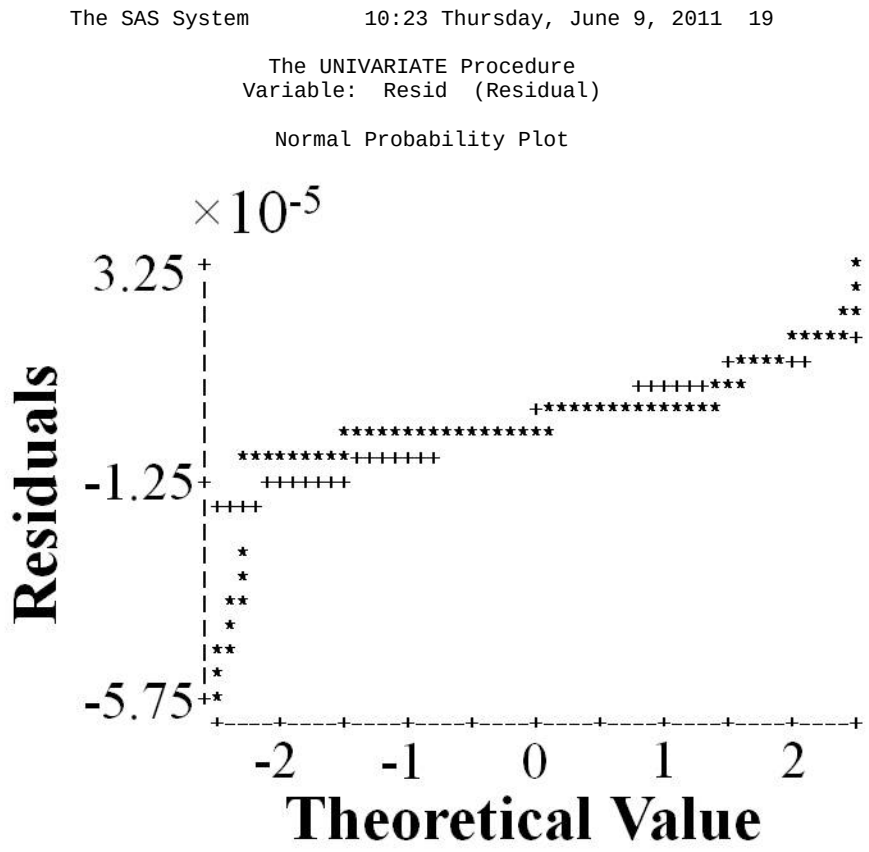

Figure D-2: Normal Probability plot of the residuals obtained from the linear mixed model analysis on the 48℃ thermal stimulation data. Note: * : dat a points; and the theoretical normal values are derived with standard normal distribution of mean 0 and variance of 1 and denoted by '+' in the above plot.

APPENDIX E

SAS CODE AND RESULTS: 41℃ THERMAL DATA

SAS Code:

```
libname saslib 'C:\Users\rowe\Documents\consult\giri\f061511\';

data one;
  set saslib.baseline_forty_one;
  forty1_thr_scaled=forty_one_thermal*10000;

proc mixed data=one empirical;
  class code subject;
  model forty1_thr_scaled=code/s outp=m_one;
  repeated / subject=subject type=cs;
  lsmeans code/pdiff;
  title 'repeated CS';

proc univariate data=m_one plot normal;
  var resid;
  run;
```

Key Notations:

bLHaPFC : baseline data from LH aPFC

bRHaPFC : baseline data from RH aPFC

bLHdlPFC : baseline data from LH DLPFC

bRHdlPFC : baseline data from RH DLPFC

LHaPFC_E : Early phase data from LH aPFC

RHaPFC_E : Early phase data from RH aPFC

LHdlPFC_E : Early phase data from LH DLPFC

RHdlPFC_E : Early phase data from RH DLPFC

LHaPFC_L : Late phase data from LH aPFC

RHaPFC_L : Late phase data from RH aPFC

LHdlPFC_L : Late phase data from LH DLPFC

RHdlPFC_L : Late phase data from RH DLPFC

Yellow shade: highlights the comparison for significance between baseline and stimulus-induced HbO changes.

Green shade: highlights the significance of interest ($p<0.05$)

SAS Results:

```
          11:04 Wednesday, June 15, 2011   1

                  The Mixed Procedure

                  Model Information

   Data Set                     WORK.ONE
   Dependent Variable           forty1_thr_scaled
   Covariance Structure         Compound Symmetry
   Subject Effect               subject
   Estimation Method            REML
   Residual Variance Method     Profile
   Fixed Effects SE Method      Empirical
   Degrees of Freedom Method    Between-Within


                Class Level Information

    Class      Levels    Values

    code           12    LHaPFC_E LHaPFC_L LHdlPFC_E
                         LHdlPFC_L RHaPFC_E RHaPFC_L
                         RHdlPFC_E RHdlPFC_L bLHaPFC
                         bLHdlPFC bRHaPFC bRHdlPFC
    subject         5    S20 S23 S25 S26 S28


                     Dimensions

           Covariance Parameters            2
           Columns in X                    13
           Columns in Z                     0
           Subjects                         5
           Max Obs Per Subject            580


                Number of Observations

        Number of Observations Read          2900
        Number of Observations Used          2900
        Number of Observations Not Used         0


                  Iteration History

Iteration    Evaluations    -2 Res Log Like       Criterion

        0              1    -14483.10773151
        1              1    -14799.33892995      0.00000000


               Convergence criteria met.

repeated CS         11:04 Wednesday, June 15, 2011   2

                  The Mixed Procedure

              Covariance Parameter Estimates

             Cov Parm     Subject    Estimate

             CS           subject    0.000052
             Residual                0.000338
```

Fit Statistics

-2 Res Log Likelihood	-14799.3
AIC (smaller is better)	-14795.3
AICC (smaller is better)	-14795.3
BIC (smaller is better)	-14796.1

Null Model Likelihood Ratio Test

DF	Chi-Square	Pr > ChiSq
1	316.23	<.0001

Solution for Fixed Effects

Effect	code	Estimate	Standard Error	DF	t Value	Pr > |t|
Intercept		-0.00005	0.000147	4	-0.31	0.7738
code	LHaPFC_E	-0.00988	0.006163	44	-1.60	0.1161
code	LHaPFC_L	-0.01625	0.007135	44	-2.28	0.0277
code	LHdlPFC_E	0.01124	0.01031	44	1.09	0.2813
code	LHdlPFC_L	0.01611	0.01661	44	0.97	0.3374
code	RHaPFC_E	-0.00164	0.003836	44	-0.43	0.6720
code	RHaPFC_L	-0.00543	0.004815	44	-1.13	0.2653
code	RHdlPFC_E	0.008692	0.006369	44	1.36	0.1793
code	RHdlPFC_L	0.01207	0.01305	44	0.92	0.3601
code	bLHaPFC	0.000156	0.000087	44	1.78	0.0821
code	bLHdlPFC	-2.15E-6	0.000052	44	-0.04	0.9674
code	bRHaPFC	0.000060	0.000146	44	0.42	0.6797
code	bRHdlPFC	0	.	.	.	.

Type 3 Tests of Fixed Effects

Effect	Num DF	Den DF	F Value	Pr > F
code	4	44	1.22	0.3143

The Mixed Procedure

Least Squares Means

Effect	code	Estimate	Standard Error	DF	t Value	Pr > |t|
code	LHaPFC_E	-0.00993	0.006217	44	-1.60	0.1175
code	LHaPFC_L	**-0.01629**	0.007194	44	-2.26	0.0285
code	LHdlPFC_E	0.01120	0.01026	44	1.09	0.2812
code	LHdlPFC_L	0.01607	0.01657	44	0.97	0.3377
code	RHaPFC_E	-0.00168	0.003918	44	-0.43	0.6701
code	RHaPFC_L	-0.00548	0.004906	44	-1.12	0.2702
code	RHdlPFC_E	0.008647	0.006340	44	1.36	0.1796
code	RHdlPFC_L	0.01202	0.01304	44	0.92	0.3614
code	bLHaPFC	**0.000110**	0.000160	44	0.69	0.4944
code	bLHdlPFC	-0.00005	0.000128	44	-0.37	0.7126
code	bRHaPFC	0.000015	0.000064	44	0.24	0.8124
code	bRHdlPFC	-0.00005	0.000147	44	-0.31	0.7600

Differences of Least Squares Means

Effect	code	_code	Estimate	Standard Error	DF	t Value	Pr > |t|
code	LHaPFC_E	LHaPFC_L	0.006368	0.004471	44	1.42	0.1615
code	LHaPFC_E	LHdlPFC_E	-0.02112	0.01352	44	-1.56	0.1252
code	LHaPFC_E	LHdlPFC_L	-0.02599	0.02029	44	-1.28	0.2068
code	LHaPFC_E	RHaPFC_E	-0.00825	0.004370	44	-1.89	0.0658
code	LHaPFC_E	RHaPFC_L	-0.00445	0.005534	44	-0.80	0.4259
code	LHaPFC_E	RHdlPFC_E	-0.01857	0.01226	44	-1.52	0.1369
code	LHaPFC_E	RHdlPFC_L	-0.02195	0.01717	44	-1.28	0.2079
code	LHaPFC_E	bLHaPFC	-0.01004	0.006214	44	-1.62	0.1134
code	LHaPFC_E	bLHdlPFC	-0.00988	0.006167	44	-1.60	0.1164
code	LHaPFC_E	bRHaPFC	-0.00994	0.006243	44	-1.59	0.1184
code	LHaPFC_E	bRHdlPFC	-0.00988	0.006163	44	-1.60	0.1161
code	LHaPFC_L	LHdlPFC_E	-0.02749	0.01541	44	-1.78	0.0814
code	LHaPFC_L	LHdlPFC_L	-0.03236	0.02303	44	-1.41	0.1669
code	LHaPFC_L	RHaPFC_E	-0.01461	0.003570	44	-4.09	0.0002
code	LHaPFC_L	RHaPFC_L	-0.01082	0.007559	44	-1.43	0.1595
code	LHaPFC_L	RHdlPFC_E	-0.02494	0.01324	44	-1.88	0.0662
code	LHaPFC_L	RHdlPFC_L	-0.02832	0.01960	44	-1.44	0.1556
code	LHaPFC_L	bLHaPFC	-0.01640	0.007194	44	-2.28	**0.0275**
code	LHaPFC_L	bLHdlPFC	-0.01625	0.007116	44	-2.28	0.0273
code	LHaPFC_L	bRHaPFC	-0.01631	0.007227	44	-2.26	0.0291
code	LHaPFC_L	bRHdlPFC	-0.01625	0.007135	44	-2.28	0.0277
code	LHdlPFC_E	LHdlPFC_L	-0.00487	0.009641	44	-0.50	0.6161
code	LHdlPFC_E	RHaPFC_E	0.01288	0.01326	44	0.97	0.3368
code	LHdlPFC_E	RHaPFC_L	0.01668	0.009374	44	1.78	0.0821
code	LHdlPFC_E	RHdlPFC_E	0.002551	0.008780	44	0.29	0.7728
code	LHdlPFC_E	RHdlPFC_L	-0.00082	0.008289	44	-0.10	0.9212
code	LHdlPFC_E	bLHaPFC	0.01109	0.01023	44	1.08	0.2843

The Mixed Procedure

Differences of Least Squares Means

Effect	code	_code	Estimate	Standard Error	DF	t Value	Pr > |t|
code	LHdlPFC_E	bLHdlPFC	0.01125	0.01031	44	1.09	0.2815
code	LHdlPFC_E	bRHaPFC	0.01118	0.01021	44	1.09	0.2795
code	LHdlPFC_E	bRHdlPFC	0.01124	0.01031	44	1.09	0.2813
code	LHdlPFC_L	RHaPFC_E	0.01775	0.02014	44	0.88	0.3830
code	LHdlPFC_L	RHaPFC_L	0.02154	0.01613	44	1.34	0.1885
code	LHdlPFC_L	RHdlPFC_E	0.007419	0.01244	44	0.60	0.5539
code	LHdlPFC_L	RHdlPFC_L	0.004043	0.004597	44	0.88	0.3839
code	LHdlPFC_L	bLHaPFC	0.01596	0.01654	44	0.96	0.3398
code	LHdlPFC_L	bLHdlPFC	0.01611	0.01664	44	0.97	0.3380
code	LHdlPFC_L	bRHaPFC	0.01605	0.01653	44	0.97	0.3367
code	LHdlPFC_L	bRHdlPFC	0.01611	0.01661	44	0.97	0.3374
code	RHaPFC_E	RHaPFC_L	0.003798	0.005538	44	0.69	0.4964
code	RHaPFC_E	RHdlPFC_E	-0.01033	0.009849	44	-1.05	0.3001
code	RHaPFC_E	RHdlPFC_L	-0.01370	0.01650	44	-0.83	0.4107
code	RHaPFC_E	bLHaPFC	-0.00179	0.003900	44	-0.46	0.6484
code	RHaPFC_E	bLHdlPFC	-0.00163	0.003823	44	-0.43	0.6713
code	RHaPFC_E	bRHaPFC	-0.00170	0.003951	44	-0.43	0.6699
code	RHaPFC_E	bRHdlPFC	-0.00164	0.003836	44	-0.43	0.6720
code	RHaPFC_L	RHdlPFC_E	-0.01413	0.008714	44	-1.62	0.1122
code	RHaPFC_L	RHdlPFC_L	-0.01750	0.01272	44	-1.38	0.1757
code	RHaPFC_L	bLHaPFC	-0.00559	0.004787	44	-1.17	0.2493
code	RHaPFC_L	bLHdlPFC	-0.00543	0.004840	44	-1.12	0.2679
code	RHaPFC_L	bRHaPFC	-0.00549	0.004870	44	-1.13	0.2654
code	RHaPFC_L	bRHdlPFC	-0.00543	0.004815	44	-1.13	0.2653
code	RHdlPFC_E	RHdlPFC_L	-0.00338	0.008546	44	-0.40	0.6947
code	RHdlPFC_E	bLHaPFC	0.008537	0.006302	44	1.35	0.1825
code	RHdlPFC_E	bLHdlPFC	0.008694	0.006384	44	1.36	0.1802
code	RHdlPFC_E	bRHaPFC	0.008632	0.006297	44	1.37	0.1774
code	RHdlPFC_E	bRHdlPFC	0.008692	0.006369	44	1.36	0.1793

code	RHdlPFC_L	bLHaPFC	0.01191	0.01297	44	0.92	0.3635
code	RHdlPFC_L	bLHdlPFC	0.01207	0.01308	44	0.92	0.3611
code	RHdlPFC_L	bRHaPFC	0.01201	0.01298	44	0.92	0.3601
code	RHdlPFC_L	bRHdlPFC	0.01207	0.01305	44	0.92	0.3601
code	bLHaPFC	bLHdlPFC	0.000158	0.000110	44	1.43	0.1585
code	bLHaPFC	bRHaPFC	0.000095	0.000122	44	0.78	0.4398
code	bLHaPFC	bRHdlPFC	0.000156	0.000087	44	1.78	0.0821
code	bLHdlPFC	bRHaPFC	-0.00006	0.000137	44	-0.46	0.6493
code	bLHdlPFC	bRHdlPFC	-2.15E-6	0.000052	44	-0.04	0.9674
code	bRHaPFC	bRHdlPFC	0.000060	0.000146	44	0.42	0.6797

The UNIVARIATE Procedure
Variable: Resid (Residual)

Moments

N	2900	Sum Weights	2900
Mean	0	Sum Observations	0
Std Deviation	0.01945538	Variance	0.00037851
Skewness	0.77539466	Kurtosis	2.16797726
Uncorrected SS	1.0973052	Corrected SS	1.0973052
Coeff Variation	.	Std Error Mean	0.00036128

Basic Statistical Measures

Location		Variability	
Mean	0.00000	Std Deviation	0.01946
Median	-0.00067	Variance	0.0003785
Mode	.	Range	0.13250
		Interquartile Range	0.02061

Tests for Location: Mu0=0

Test	-Statistic-		-----p Value------	
Student's t	t	0	Pr > |t|	1.0000
Sign	M	-71	Pr >= |M|	0.0088
Signed Rank	S	-110398	Pr >= |S|	0.0143

Tests for Normality

Test	--Statistic---		-----p Value------	
Kolmogorov-Smirnov	D	0.075654	Pr > D	<0.0100
Cramer-von Mises	W-Sq	4.410575	Pr > W-Sq	<0.0050
Anderson-Darling	A-Sq	26.93664	Pr > A-Sq	<0.0050

Quantiles (Definition 5)

Quantile	Estimate
100% Max	0.083447589
99%	0.057821799
95%	0.031324171
90%	0.020992398
75% Q3	0.009368717
50% Median	-0.000667835
25% Q1	-0.011237609
10%	-0.023667653

The UNIVARIATE Procedure
Variable: Resid (Residual)

Quantiles (Definition 5)

Quantile	Estimate
5%	-0.030261091
1%	-0.041028217
0% Min	-0.049056205

Extreme Observations

Lowest		Highest	
Value	Obs	Value	Obs
-0.0490562	2136	0.0829661	2704
-0.0490094	2135	0.0830937	2708
-0.0486976	2137	0.0833402	2705
-0.0486235	2134	0.0833446	2707
-0.0479894	2133	0.0834476	2706

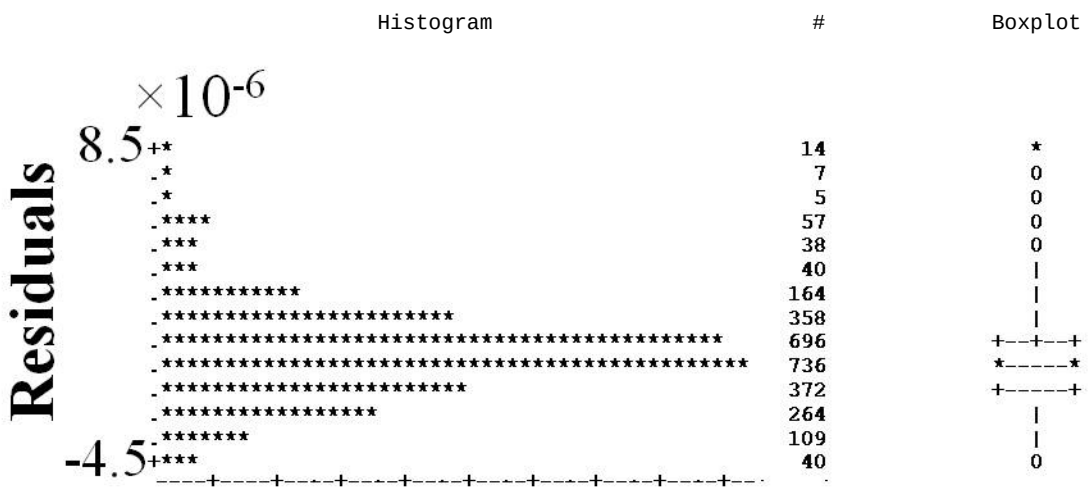

Figure E-1: Histogram and box plot of the residuals obtained from the linear mixed model analysis on the 41℃ thermal stimulation data. Note: * : dat a points; 0: outliers in the box plot.

repeated CS 11:04 Wednesday, June 15, 2011 11

The UNIVARIATE Procedure
Variable: Resid (Residual)

Normal Probability Plot

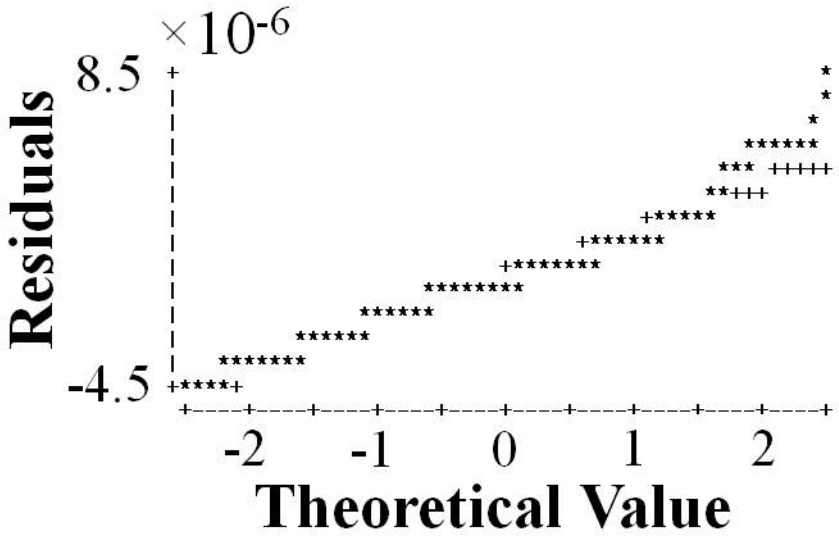

Figure E-2: Normal Probability plot of the residuals obtained from the linear mixed model analysis on the 41℃ thermal stimulation data. Note: * : dat a points; and the theoretical normal values are derived with standard normal distribution of mean 0 and variance of 1 and denoted by '+' in the above plot.

REFERENCES

Apkarian, A. V., Bushnell, M. C., Treede, R. D., & Zubieta, J. K. (2005). Human brain mechanisms of pain perception and regulation in health and disease. *Eur J Pain, 9*(4), 463-484.

Apkarian, A. V., Darbar, A., Krauss, B. R., Gelnar, P. A., & Szeverenyi, N. M. (1999). Differentiating cortical areas related to pain perception from stimulus identification: temporal analysis of fMRI activity. *J Neurophysiol, 81*(6), 2956-2963.

Apkarian, A. V., Sosa, Y., Sonty, S., Levy, R. M., Harden, R. N., Parrish, T. B., et al. (2004). Chronic back pain is associated with decreased prefrontal and thalamic gray matter density. *J Neurosci, 24*(46), 10410-10415.

Arridge, S. R. (1999). Optical tomography in medical imaging. *Inverse Problems, 15*, R41-R93.

Arridge, S. R., & Schweiger, M. (1997). Image reconstruction in optical tomography. *Philos Trans R Soc Lond B Biol Sci, 352*(1354), 717-726.

Baliki, M. N., Geha, P. Y., & Apkarian, A. V. (2009). Parsing pain perception between nociceptive representation and magnitude estimation. *J Neurophysiol, 101*(2), 875-887.

Bandura, A., O'Leary, A., Taylor, C. B., Gauthier, J., & Gossard, D. (1987). Perceived self-efficacy and pain control: opioid and nonopioid mechanisms. *J Pers Soc Psychol, 53*(3), 563-571.

Bantick, S. J., Wise, R. G., Ploghaus, A., Clare, S., Smith, S. M., & Tracey, I. (2002). Imaging how attention modulates pain in humans using functional MRI. *Brain, 125*(Pt 2), 310-319.

Barbour, R. L., Graber, H. L., Pei, Y., Zhong, S., & Schmitz, C. H. (2001). Optical tomographic imaging of dynamic features of dense-scattering media. *J Opt Soc Am A Opt Image Sci Vis, 18*(12), 3018-3036.

Becerra, L., Breiter, H. C., Wise, R., Gonzalez, R. G., & Borsook, D. (2001). Reward circuitry activation by noxious thermal stimuli. *Neuron, 32*(5), 927-946.

Becerra, L., Harris, W., Grant, M., George, E., Boas, D., & Borsook, D. (2009). Diffuse optical tomography activation in the somatosensory cortex: specific activation by painful vs. non-painful thermal stimuli. *PLoS One, 4*(11), e8016.

Becerra, L., Harris, W., Joseph, D., Huppert, T., Boas, D. A., & Borsook, D. (2008). Diffuse optical tomography of pain and tactile stimulation: activation in cortical sensory and emotional systems. *Neuroimage, 41*(2), 252-259.

Becerra, L., Morris, S., Bazes, S., Gostic, R., Sherman, S., Gostic, J., et al. (2006). Trigeminal neuropathic pain alters responses in CNS circuits to mechanical (brush) and thermal (cold and heat) stimuli. *J Neurosci, 26*(42), 10646-10657.

Becerra, L. R., Breiter, H. C., Stojanovic, M., Fishman, S., Edwards, A., Comite, A. R., et al. (1999). Human brain activation under controlled thermal stimulation and habituation to noxious heat: an fMRI study. *Magn Reson Med, 41*(5), 1044-1057.

Beckmann, C. F., Jenkinson, M., & Smith, S. M. (2003). General multilevel linear modeling for group analysis in FMRI. *Neuroimage, 20*(2), 1052-1063.

Biswal, B., Yetkin, F. Z., Haughton, V. M., & Hyde, J. S. (1995). Functional connectivity in the motor cortex of resting human brain using echo-planar MRI. *Magn Reson Med, 34*(4), 537-541.

Boas, D. (1997). A fundamental limitation of linearized algorithms for diffuse optical tomography. *Opt Express, 1*(13), 404-413.

Boas, D. A. (1996). *Diffuse photon probes of structural and dynamic properties of turbid media: Theory and biomedical applications.* Unpublished Ph.D. dissertation, University of Pennsylvania.

Boas, D. A., Chen, K., Grebert, D., & Franceschini, M. A. (2004). Improving the diffuse optical imaging spatial resolution of the cerebral hemodynamic response to brain activation in humans. *Opt Lett, 29*(13), 1506-1508.

Boas, D. A., Dale, A. M., & Franceschini, M. A. (2004). Diffuse optical imaging of brain activation: approaches to optimizing image sensitivity, resolution, and accuracy. *Neuroimage, 23 Suppl 1*, S275-288.

Boorman, L., Kennerley, A. J., Johnston, D., Jones, M., Zheng, Y., Redgrave, P., et al. (2010). Negative blood oxygen level dependence in the rat: a model for investigating the role of suppression in neurovascular coupling. *J Neurosci, 30*(12), 4285-4294.

Brodmann, K. (1908). Beitraege zur histologischen Lokalisation der Grosshirnrinde. VI. Mitteilung: Die Cortex-gliederung des Menschen. *J. Psychol. Neurol. (Lzp), 10*, 231-246T.

Brodmann, K. (1909). *Vergleichende localisationslehre der grosshirnrinde in ihren dargestellt auf grund des zellenbaues*: Leipzig: Barth.

Burgess, P. W., Gilbert, S. J., & Dumontheil, I. (2007). Function and localization within rostral prefrontal cortex (area 10). *Philos Trans R Soc Lond B Biol Sci, 362*(1481), 887-899.

Bushnell, M. C., Duncan, G. H., Hofbauer, R. K., Ha, B., Chen, J. I., & Carrier, B. (1999). Pain perception: is there a role for primary somatosensory cortex? *Proc Natl Acad Sci U S A, 96*(14), 7705-7709.

Buxton, R. B., & Frank, L. R. (1997). A model for the coupling between cerebral blood flow and oxygen metabolism during neural stimulation. *J Cereb Blood Flow Metab, 17*(1), 64-72.

Chalmers, D. J. (1996). *The Conscious Mind: In Search of a Fundamental Theory*: Oxford University Press.

Chance, B., Zhuang, Z., UnAh, C., Alter, C., & Lipton, L. (1993). Cognition-activated low-frequency modulation of light absorption in human brain. *Proc Natl Acad Sci U S A, 90*(8), 3770-3774.

Cope, M. (1991). *The application of near infrared spectroscopy to non invasive monitoring of cerebral oxygenation in the newborn infant.* Unpublished Ph.D. dissertation, University College London.

Cowan, N. (2001). The magical number 4 in short-term memory: a reconsideration of mental storage capacity. *Behav Brain Sci, 24*(1), 87-114; discussion 114-185.

Crombez, G., Eccleston, C., Baeyens, F., & Eelen, P. (1998). When somatic information threatens, catastrophic thinking enhances attentional interference. *Pain, 75*(2-3), 187-198.

Davis, K. D., Wood, M. L., Crawley, A. P., & Mikulis, D. J. (1995). fMRI of human somatosensory and cingulate cortex during painful electrical nerve stimulation. *Neuroreport, 7*(1), 321-325.

de, C. W. A. C., Davies, H. T., & Chadury, Y. (2000). Simple pain rating scales hide complex idiosyncratic meanings. *Pain, 85*(3), 457-463.

Demidenko, E. (2004). *Mixed Models Theory and Applications*. Hoboken, New Jersey: John Wiley & Sons, Inc.

Devor, A., Tian, P., Nishimura, N., Teng, I. C., Hillman, E. M., Narayanan, S. N., et al. (2007). Suppressed neuronal activity and concurrent arteriolar vasoconstriction may explain negative blood oxygenation level-dependent signal. *J Neurosci, 27*(16), 4452-4459.

di Pellegrino, G., & Wise, S. P. (1991). A neurophysiological comparison of three distinct regions of the primate frontal lobe. *Brain, 114 (Pt 2)*, 951-978.

Essenpreis, M., Elwell, C. E., Cope, M., van der Zee, P., Arridge, S. R., & Delpy, D. T. (1993). Spectral dependence of temporal point spread functions in human tissues. *Appl Opt, 32*(4), 418-425.

Feng, W., Haishu, D., Fenghua, T., Jun, Z., Qing, X., & Xianwu, T. (2001). Influence of overlying tissue and probe geometry on the sensitivity of a near-infrared tissue oximeter. *Physiol Meas, 22*(1), 201-208.

Fowles, G. R. (1989). *Introduction to moder optics* (2nd ed.): Dover Publications, Inc.

Franceschini, M. A., Joseph, D. K., Huppert, T. J., Diamond, S. G., & Boas, D. A. (2006). Diffuse optical imaging of the whole head. *J Biomed Opt, 11*(5), 054007.

Franceschini, M. A., Radhakrishnan, H., Thakur, K., Wu, W., Ruvinskaya, S., Carp, S., et al. (2010). The effect of different anesthetics on neurovascular coupling. *Neuroimage, 51*(4), 1367-1377.

Franceschini, M. A., Toronov, V., Filiaci, M., Gratton, E., & Fantini, S. (2000). On-line optical imaging of the human brain with 160-ms temporal resolution. *Opt Express, 6*(3), 49-57.

Friston, K. J., Holmes, A. P., Price, C. J., Buchel, C., & Worsley, K. J. (1999). Multisubject fMRI studies and conjunction analyses. *Neuroimage, 10*(4), 385-396.

Frostig, R. D. (Ed.). (2009). *In Vivo Optical Imaging of Brain Function* (2nd ed. ed.): CRC press.

Furi Andi Karnapi, L. K. A. (2003). http://www.mathworks.com/matlabcentral/fileexchange/3832-matlab-plot-tracing-utility

Fuster, J. M. (2002). Frontal lobe and cognitive development. *J Neurocytol, 31*(3-5), 373-385.

Gagliese, L., & Melzack, R. (1997). Chronic pain in elderly people. *Pain, 70*(1), 3-14.

Gordon, G. R., Choi, H. B., Rungta, R. L., Ellis-Davies, G. C., & MacVicar, B. A. (2008). Brain metabolism dictates the polarity of astrocyte control over arterioles. *Nature, 456*(7223), 745-749.

Gundel, H., Valet, M., Sorg, C., Huber, D., Zimmer, C., Sprenger, T., et al. (2008). Altered cerebral response to noxious heat stimulation in patients with somatoform pain disorder. *Pain, 137*(2), 413-421.

Hale, G. M., & Querry, M. R. (1973). Optical Constants of Water in the 200-nm to 200-microm Wavelength Region. *Appl Opt, 12*(3), 555-563.

Halliday, D., & Resnick, R. (1962). *Physics Part II*: John Wiley & Sons, Inc.

He, Y., Wang, J., Wang, L., Chen, Z. J., Yan, C., Yang, H., et al. (2009). Uncovering intrinsic modular organization of spontaneous brain activity in humans. *PLoS One, 4*(4), e5226.

Hecht, E., & Zajac, A. (1997). *Optics* (3rd ed.): Addison Wesley Publishing Company.

Huettel, S. A., Song, A. W., & McCarthy, G. (2008). *Functional Magnetic Resonance Imaging* (2nd ed.): Sinauer Associates, Inc.

Huettel Scott A, S. A. W., McCarthy Gregory. (2008). *Functional Magnetic Resonance Imaging* (2nd sedition ed.). Sunderland, Massachusetts U.S.A.: Sinauer Associates, Inc.

Huppert, T. J., & Boas, D. A. (2003). from http://www.nmr.mgh.harvard.edu/PMI/resources/homer/home.htm

Huppert, T. J., Diamond, S. G., Franceschini, M. A., & Boas, D. A. (2009). HomER: a review of time-series analysis methods for near-infrared spectroscopy of the brain. *Appl Opt, 48*(10), D280-298.

Huppert, T. J., Franceschini, M. A., & Boas, D. A. (Eds.). (2009). *Noninvasive Imaging of Cerebral Activation with Diffuse Optical Tomography* (2nd ed.): CRC press.

Huppert, T. J., Hoge, R. D., Diamond, S. G., Franceschini, M. A., & Boas, D. A. (2006). A temporal comparison of BOLD, ASL, and NIRS hemodynamic responses to motor stimuli in adult humans. *Neuroimage, 29*(2), 368-382.

Irani, F., Platek, S. M., Bunce, S., Ruocco, A. C., & Chute, D. (2007). Functional near infrared spectroscopy (fNIRS): an emerging neuroimaging technology with important applications for the study of brain disorders. *Clin Neuropsychol, 21*(1), 9-37.

Jensen M.P., K. P. (Ed.). (2001). *Self-report scales procedures for assessing pai in adults* (2nd ed.). New York: Guilford Press.

Jensen, M. P., & Karoly, P. (1991). Control beliefs, coping efforts, and adjustment to chronic pain. *J Consult Clin Psychol, 59*(3), 431-438.

Ji, G., Sun, H., Fu, Y., Li, Z., Pais-Vieira, M., Galhardo, V., et al. (2010). Cognitive impairment in pain through amygdala-driven prefrontal cortical deactivation. *J Neurosci, 30*(15), 5451-5464.

Jobsis, F. F. (1977). Non-invasive, infra-red monitoring of cerebral O2 sufficiency, bloodvolume, HbO2-Hb shifts and bloodflow. *Acta Neurol Scand Suppl, 64*, 452-453.

Jones, A. K., Brown, W. D., Friston, K. J., Qi, L. Y., & Frackowiak, R. S. (1991). Cortical and subcortical localization of response to pain in man using positron emission tomography. *Proc Biol Sci, 244*(1309), 39-44.

Kerns, R. D., & Rosenberg, R. (2000). Predicting responses to self-management treatments for chronic pain: application of the pain stages of change model. *Pain, 84*(1), 49-55.

Koltzenburg, M., & Handwerker, H. O. (1994). Differential ability of human cutaneous nociceptors to signal mechanical pain and to produce vasodilatation. *J Neurosci, 14*(3 Pt 2), 1756-1765.

Kong, J., Loggia, M. L., Zyloney, C., Tu, P., Laviolette, P., & Gollub, R. L. (2010). Exploring the brain in pain: activations, deactivations and their relation. *Pain, 148*(2), 257-267.

Kong, J., White, N. S., Kwong, K. K., Vangel, M. G., Rosman, I. S., Gracely, R. H., et al. (2006). Using fMRI to dissociate sensory encoding from cognitive evaluation of heat pain intensity. *Hum Brain Mapp, 27*(9), 715-721.

Krane, K. (1998). *Modern Physics* (2nd ed.): John Wiley & Sons, Inc.

Krishnamurthy, V., Kavuri, V., Tian, F., & Liu, H. (2010). *Detectability of Hemodynamic Response to Thermal Pain in Pre-Frontal Cortex Using Diffuse Optical Tomography.* Paper presented at the Biomedical Optics; Optical Society of America, Miami, FL.

Lauritzen, M. (2005). Reading vascular changes in brain imaging: is dendritic calcium the key? *Nat Rev Neurosci, 6*(1), 77-85.

Liu, H., Chance, B., Hielscher, A. H., Jacques, S. L., & Tittel, F. K. (1995). Influence of blood vessels on the measurement of hemoglobin oxygenation as determined by time-resolved reflectance spectroscopy. *Med Phys, 22*(8), 1209-1217.

Lorenz, J., Minoshima, S., & Casey, K. L. (2003). Keeping pain out of mind: the role of the dorsolateral prefrontal cortex in pain modulation. *Brain, 126*(Pt 5), 1079-1091.

Lucchetti, C., Lui, F., & Bon, L. (1998). Neglect syndrome for aversive stimuli in a macaque monkey with dorsomedial frontal cortex lesion. *Neuropsychologia, 36*(3), 251-257.

Lui, F., Duzzi, D., Corradini, M., Serafini, M., Baraldi, P., & Porro, C. A. (2008). Touch or pain? Spatio-temporal patterns of cortical fMRI activity following brief mechanical stimuli. *Pain, 138*(2), 362-374.

Mai, J. K., Assheuer, J., & Paxinos, G. (1997). *Atlas of the Human Brain*: Acaedemic Press.

Maihofner, C., Handwerker, H. O., & Birklein, F. (2006). Functional imaging of allodynia in complex regional pain syndrome. *Neurology, 66*(5), 711-717.

Maihofner, C., Schmelz, M., Forster, C., Neundorfer, B., & Handwerker, H. O. (2004). Neural activation during experimental allodynia: a functional magnetic resonance imaging study. *Eur J Neurosci, 19*(12), 3211-3218.

Mansouri, C., L'Huillier J, P., Kashou, N. H., & Humeau, A. (2010). Depth sensitivity analysis of functional near-infrared spectroscopy measurement using three-dimensional Monte Carlo modelling-based magnetic resonance imaging. *Lasers Med Sci, 25*(3), 431-438.

Marsh-Richard, D. M., Hatzis, E. S., Mathias, C. W., Venditti, N., & Dougherty, D. M. (2009). Adaptive Visual Analog Scales (AVAS): a modifiable software program for the creation, administration, and scoring of visual analog scales. *Behav Res Methods, 41*(1), 99-106.

McMahon, S., & Koltzenberg, M. (Eds.). (2005). *Wall and Melzack's Textbook of Pain* (5 edition ed.): Churchill Livingstone.

Meichenbaum, D., & Turk, D. C. (Eds.). (1976). *The cognitive-behavioral management of anxiety, anger, and pain*. New York: Bruner/Mazel.

Melzack, R., & Wall, P. D. (1965). Pain mechanisms: a new theory. *Science, 150*(699), 971-979.

Miller, G. A. (1956). The magical number seven plus or minus two: some limits on our capacity for processing information. *Psychol Rev, 63*(2), 81-97.

Moulton, E. A., Keaser, M. L., Gullapalli, R. P., Maitra, R., & Greenspan, J. D. (2006). Sex differences in the cerebral BOLD signal response to painful heat stimuli. *Am J Physiol Regul Integr Comp Physiol, 291*(2), R257-267.

Mumford, J. A., & Nichols, T. E. (2008). Power calculation for group fMRI studies accounting for arbitrary design and temporal autocorrelation. *Neuroimage, 39*(1), 261-268.

Myers, R. H., Montgomery, D. C., Vining, G. G., & Robinson, T. J. (2010). *Generalized Linear Models with Applications in Engineering and the Sciences* (2nd ed.). Hoboken, New Jersey: John Wiley & Sons, Inc.

Newton C.R., B. H. E. (1987). Cognitive changes accompanying headache treatment: the use of a thought-sampling procedure. *Cognitive Therapy and Research, 11*, 635-652.

Ng, C. S., Raunig, D. L., Jackson, E. F., Ashton, E. A., Kelcz, F., Kim, K. B., et al. (2010). Reproducibility of perfusion parameters in dynamic contrast-enhanced MRI of lung and liver

tumors: effect on estimates of patient sample size in clinical trials and on individual patient responses. *AJR Am J Roentgenol, 194*(2), W134-140.

Niu, H., Lin, Z. J., Tian, F., Dhamne, S., & Liu, H. (2010). Comprehensive investigation of three-dimensional diffuse optical tomography with depth compensation algorithm. *J Biomed Opt, 15*(4), 046005.

Niu, H., Tian, F., Lin, Z. J., & Liu, H. (2010). Development of a compensation algorithm for accurate depth localization in diffuse optical tomography. *Opt Lett, 35*(3), 429-431.

Ongur, D., Ferry, A. T., & Price, J. L. (2003). Architectonic subdivision of the human orbital and medial prefrontal cortex. *J Comp Neurol, 460*(3), 425-449.

Oshiro, Y., Quevedo, A. S., McHaffie, J. G., Kraft, R. A., & Coghill, R. C. (2009). Brain mechanisms supporting discrimination of sensory features of pain: a new model. *J Neurosci, 29*(47), 14924-14931.

Ou, W., Nissila, I., Radhakrishnan, H., Boas, D. A., Hamalainen, M. S., & Franceschini, M. A. (2009). Study of neurovascular coupling in humans via simultaneous magnetoencephalography and diffuse optical imaging acquisition. *Neuroimage, 46*(3), 624-632.

Palermo, T. M., & Drotar, D. (1996). Prediction of children's postoperative pain: the role of presurgical expectations and anticipatory emotions. *J Pediatr Psychol, 21*(5), 683-698.

Pandya D.N., B. C. L. (1987). Architecture and connections of the fontal lobe. In E. Perecman (Ed.), *The frontal lobes revisted* (pp. 41-72): New York: IRBN.

Petrides, M. (2005). Lateral prefrontal cortex: architectonic and functional organization. *Philos Trans R Soc Lond B Biol Sci, 360*(1456), 781-795.

Petrides, M., & Pandya, D. N. (Eds.). (1994). *Comparative architectonic analysis of the human and the macaque frontal cortex* (Vol. 9): Amsterdam: Elsevier.

Peyron, R., Laurent, B., & Garcia-Larrea, L. (2000). Functional imaging of brain responses to pain. A review and meta-analysis (2000). *Neurophysiol Clin, 30*(5), 263-288.

Piazza, M., Pinel, P., Le Bihan, D., & Dehaene, S. (2007). A magnitude code common to numerosities and number symbols in human intraparietal cortex. *Neuron, 53*(2), 293-305.

Porro, C. A., Baraldi, P., Pagnoni, G., Serafini, M., Facchin, P., Maieron, M., et al. (2002). Does anticipation of pain affect cortical nociceptive systems? *J Neurosci, 22*(8), 3206-3214.

Pud, D., Golan, Y., & Pesta, R. (2009). Hand dominancy--a feature affecting sensitivity to pain. *Neurosci Lett, 467*(3), 237-240.

Qiu, Y., Noguchi, Y., Honda, M., Nakata, H., Tamura, Y., Tanaka, S., et al. (2006). Brain processing of the signals ascending through unmyelinated C fibers in humans: an event-related functional magnetic resonance imaging study. *Cereb Cortex, 16*(9), 1289-1295.

Reesor, K. A., & Craig, K. D. (1988). Medically incongruent chronic back pain: physical limitations, suffering, and ineffective coping. *Pain, 32*(1), 35-45.

Rosen, B. R., Buckner, R. L., & Dale, A. M. (1998). Event-related functional MRI: past, present, and future. *Proc Natl Acad Sci U S A, 95*(3), 773-780.

Semendeferi, K., Armstrong, E., Schleicher, A., Zilles, K., & Van Hoesen, G. W. (2001). Prefrontal cortex in humans and apes: a comparative study of area 10. *Am J Phys Anthropol, 114*(3), 224-241.

Serway, R. A., & Jewett, J. W. J. (2004). *Physics for scientists and engineers* (6th ed.): Thomson Vrooks/Cole.

Shmuel, A., & Leopold, D. A. (2008). Neuronal correlates of spontaneous fluctuations in fMRI signals in monkey visual cortex: Implications for functional connectivity at rest. *Hum Brain Mapp, 29*(7), 751-761.

Shmuel, A., Yacoub, E., Pfeuffer, J., Van de Moortele, P. F., Adriany, G., Hu, X., et al. (2002). Sustained negative BOLD, blood flow and oxygen consumption response and its coupling to the positive response in the human brain. *Neuron, 36*(6), 1195-1210.

Siegel, A. M., Culver, J. P., Mandeville, J. B., & Boas, D. A. (2003). Temporal comparison of functional brain imaging with diffuse optical tomography and fMRI during rat forepaw stimulation. *Phys Med Biol, 48*(10), 1391-1403.

Spanos, N. P., Radtke-Bodorik, H. L., Ferguson, J. D., & Jones, B. (1979). The effects of hypnotic susceptibility, suggestions for analgesia, and the utilization of cognitive strategies on the reduction of pain. *J Abnorm Psychol, 88*(3), 282-292.

Strangman, G., Franceschini, M. A., & Boas, D. A. (2003). Factors affecting the accuracy of near-infrared spectroscopy concentration calculations for focal changes in oxygenation parameters. *Neuroimage, 18*(4), 865-879.

Sullivan, M. J., & D'Eon, J. L. (1990). Relation between catastrophizing and depression in chronic pain patients. *J Abnorm Psychol, 99*(3), 260-263.

Talbot, J., Marrett, S., Evans, A., Meyer, E., Bushnell, M., & Duncan, G. (1991). Multiple representations of pain in human cerebral cortex. *Science, 251*(4999), 1355-1358.

TechEn. (2006). Continuous wave model CW5: User manual documentation, safety service and operational instructions. Milford, MA.

Tian, F., Alexandrakis, G., & Liu, H. (2009). Optimization of probe geometry for diffuse optical brain imaging based on measurement density and distribution. *Appl Opt, 48*(13), 2496-2504.

Tian, F., Chance, B., & Liu, H. (2009). Investigation of the prefrontal cortex in response to duration-variable anagram tasks using functional near-infrared spectroscopy. *J Biomed Opt, 14*(5), 054016.

Tian, F., Sharma, V., Kozel, F. A., & Liu, H. (2009). Functional near-infrared spectroscopy to investigate hemodynamic responses to deception in the prefrontal cortex. *Brain Res, 1303*, 120-130.

Tracey, I., Ploghaus, A., Gati, J. S., Clare, S., Smith, S., Menon, R. S., et al. (2002). Imaging attentional modulation of pain in the periaqueductal gray in humans. *J Neurosci, 22*(7), 2748-2752.

Treede, R. D., Meyer, R. A., & Campbell, J. N. (1998). Myelinated mechanically insensitive afferents from monkey hairy skin: heat-response properties. *J Neurophysiol, 80*(3), 1082-1093.

Tsuji, T., Inui, K., Kojima, S., & Kakigi, R. (2006). Multiple pathways for noxious information in the human spinal cord. *Pain, 123*(3), 322-331.

Turk, D. C., Meichenbaum, D., & Genest, M. (1983). *Pain and behavioral medicine: a cognitiv-behavioral perspective*. New York: Guilford Press.

Veldhuijzen, D. S., Nemenov, M. I., Keaser, M., Zhuo, J., Gullapalli, R. P., & Greenspan, J. D. (2009). Differential brain activation associated with laser-evoked burning and pricking pain: An event-related fMRI study. *Pain, 141*(1-2), 104-113.

Villringer, A., & Chance, B. (1997). Non-invasive optical spectroscopy and imaging of human brain function. *Trends Neurosci, 20*(10), 435-442.

Vlaeyen, J. W., De Jong, J. R., Onghena, P., Kerckhoffs-Hanssen, M., & Kole-Snijders, A. M. (2002). Can pain-related fear be reduced? The application of cognitive-behavioural exposure in vivo. *Pain Res Manag, 7*(3), 144-153.

Wager, T. D., Rilling, J. K., Smith, E. E., Sokolik, A., Casey, K. L., Davidson, R. J., et al. (2004). Placebo-induced changes in FMRI in the anticipation and experience of pain. *Science, 303*(5661), 1162-1167.

Walker, S. A., Fantini, S., & Gratton, E. (1997). Image reconstruction by backprojection from frequency-domain optical measurements in highly scattering media. *Appl Opt, 36*(1), 170-174.

Walsh, D. A., & Radcliffe, J. C. (2002). Pain beliefs and perceived physical disability of patients with chronic low back pain. *Pain, 97*(1-2), 23-31.

Walsh, V. (2003). A theory of magnitude: common cortical metrics of time, space and quantity. *Trends Cogn Sci, 7*(11), 483-488.

White, B. R., Snyder, A. Z., Cohen, A. L., Petersen, S. E., Raichle, M. E., Schlaggar, B. L., et al. (2009). Resting-state functional connectivity in the human brain revealed with diffuse optical tomography. *Neuroimage, 47*(1), 148-156.

Wiech, K., Kalisch, R., Weiskopf, N., Pleger, B., Stephan, K. E., & Dolan, R. J. (2006). Anterolateral prefrontal cortex mediates the analgesic effect of expected and perceived control over pain. *J Neurosci, 26*(44), 11501-11509.

Williams, L. M., Phillips, M. L., Brammer, M. J., Skerrett, D., Lagopoulos, J., Rennie, C., et al. (2001). Arousal dissociates amygdala and hippocampal fear responses: evidence from simultaneous fMRI and skin conductance recording. *Neuroimage, 14*(5), 1070-1079.

Willis WD, C. R. (2005). *Sensory mechanisms of the spinal chord* (3rd ed. Vol. 2): New York: Kluwer.

Witting, N., Kupers, R. C., Svensson, P., & Jensen, T. S. (2006). A PET activation study of brush-evoked allodynia in patients with nerve injury pain. *Pain, 120*(1-2), 145-154.

Wolff, L. B. (1994). *On the relative brightness of specular and diffuse reflection.* Paper presented at the IEEE Seattle, WA.

Yamashita, Y., Maki, A., & Koizumi, H. (2001). Wavelength dependence of the precision of noninvasive optical measurement of oxy-, deoxy-, and total-hemoglobin concentration. *Med Phys, 28*(6), 1108-1114.

Zeff, B. W., White, B. R., Dehghani, H., Schlaggar, B. L., & Culver, J. P. (2007). Retinotopic mapping of adult human visual cortex with high-density diffuse optical tomography. *Proc Natl Acad Sci U S A, 104*(29), 12169-12174.

Zhang, H., Duan, L., Zhang, Y. J., Lu, C. M., Liu, H., & Zhu, C. Z. (2011). Test-retest assessment of independent component analysis-derived resting-state functional connectivity based on functional near-infrared spectroscopy. *Neuroimage, 55*(2), 607-615.

BIOGRAPHICAL INFORMATION

Venkatagiri Krishnamurthy obtained his Bachelors of Engineering degree in Electronics and Communication from Bangalore University. His keen interest and motivation to pursue graduate school brought him to The University of Texas at Arlington, to continue his pursuit for knowledge in Wireless and Telecommunication Systems. During his pursuit for Master's degree, he also earned an opportunity to intern with the RF circuit design research and development group at Nokia Mobile Phones, Irving, Texas. After graduating with a Master's degree in Electrical Engineering and a brief period of absence from the graduate school, he came back to pursue Ph.D. degree in the joint Biomedical Engineering program at The University of Texas at Arlington and UT Southwestern Medical Center at Dallas. In 2005, he got inspired by a stimulating lecture from Nobel Laureate Dr. Eric Kandel on cellular and physiological mechanisms underlying learning and memory. This inspiring lecture cultivated his interests for a deeper understanding in Cognitive Neuroscience, specifically using cutting edge noninvasive brain imaging techniques. Over the years of his Ph.D. training, he has gained extensive training and experience in applying fMRI, EEG, and fNIRS techniques and methodologies to explore the physiological and biophysical aspects of human cognition and emotions. Given that at the current state, how little knowledge we have about the brain, combined with the impact of rapid growth in technology in the last few decades, he is motivated to continue research work in multimodal functional brain imaging, and foster breakthroughs in bringing some of the scientifically fictitious concepts into reality.